University of Southampton

Faculty of Engineering and Physical Sciences

Department of Aeronautical and Astronautical Engineering

Aerodynamic Noise from a High Speed Train Pantograph and Recess

by

Hogun Kim

A thesis submitted for the degree of

Doctor of Philosophy

October 2019

UNIVERSITY OF SOUTHAMPTON

ABSTRACT

FACULTY OF ENGINEERING AND PHYSICAL SCIENCES

DEPARTMENT OF AERONAUTICAL AND ASTRONAUTICAL ENGINEERING

Thesis for the degree of Doctor of Philosophy

AERODYNAMIC NOISE FROM A HIGH SPEED TRAIN PANTOGRAPH AND RECESS

by Hogun Kim

As high speeds bring higher levels of noise, noise reduction has become an important consideration for high-speed train design. In this study, the flow behaviour of a simplified geometry representing a high-speed train roof and cavity with pantographs at 1/10 scale is investigated. Computational Fluid Dynamics simulations are used based on the Improved Delayed Detached-Eddy simulation method to determine the near-field flow behaviours. The equivalent source terms are then used to predict the far-field acoustic pressure using the Ffowcs Williams-Hawkings acoustic analogy.

The effect of the pantograph cavity is studied by comparing the flow behaviour and radiated noise from cases with two pantographs, one raised and one retracted, mounted either in a cavity or on a flat surface. In comparison with case with the flat surface, the flow around the pantographs with the cavity has slightly different characteristics. The cavity slightly reduces the flow velocity upstream of the raised pantograph, and changes the unsteady flow and its interactions with the pantographs, which leads to reduced surface pressure fluctuations and noise radiated from the raised pantograph. The trailing edge of the cavity also generates a highly unsteady flow.

The highly unsteady flow over the cavity is significantly reduced by introducing modified leading and trailing cavity edges, which are rounded or angled. Consequently, noise radiated from the cavity is reduced compared to a rectangular cavity. Furthermore, the effect of rounded cavity edges on the flow over the pantographs is also investigated by comparing the flow features and noise contributions from the cases without rounded cavity edges. A slightly lower flow speed occurs around the upper parts of the raised pantograph, whereas the flow velocity in the cavity is slightly increased compared to the rectangular cavity. It is shown that, by rounding the cavity edges, a reduction in radiated noise can be obtained.

The influence of three different roof configurations is also studied by comparing the flow behaviour, including flow separations, reattachment and vortex shedding, which are potential noise sources. A highly unsteady flow occurs downstream when the train roof has a cavity or ramped cavity due to flow separation at the cavity trailing edge, while vortical flow is generated by the side insulation plates. When the retracted pantograph is located inside the ramped cavity, its noise contribution is less important. Furthermore, the insulation plates also generate tonal components in the noise spectra. For the three configurations considered,

the roof configuration with a conventional cavity radiates the least A-weighted noise at the side receiver.

Table of Contents

List of Figures

List of Tables

Declaration of Authorship

I, Hogun Kim, declare that this thesis entitled *Aerodynamic Noise from a High Speed Train Pantograph and Recess* and the work presented in it are my own and have been generated by me as the result of my own original research.

I confirm that:

1. This work was done wholly or mainly while in candidature for a research degree at this University;

2. Where any part of this thesis has previously been submitted for a degree or any other qualification at this University or any other institution, this has been clearly stated;

3. Where I have consulted the published work of others, this is always clearly attributed;

4. Where I have quoted from the work of others, the source is always given. With the exception of such quotations, this thesis is entirely my own work;

5. I have acknowledged all main sources of help;

6. Where the thesis is based on work done by myself jointly with others, I have made clear exactly what was done by others and what I have contributed myself;

7. Parts of this work have been published as:

   - H. Kim, Z. Hu, D.J. Thompson, "Unsteady aerodynamics of high speed train pantograph cavity flow control for noise reduction", In *22nd AIAA/CEAS Aeroacoustics Conference*, p. 2848, 2016.

   - H. Kim, Z. Hu, D.J. Thompson, "Effect of Cavity Flow on High Speed Train Pantograph Aerodynamic Noise", In *INTER-NOISE and NOISE-CON Congress and Conference Proceedings* Vol. 255, No. 7, pp. 906-915, 2017.

   - H. Kim, Z. Hu, D.J. Thompson, "Numerical Investigation of the Effect of various High-Speed Train Roof Configurations on Aerodynamic Noise", In *25th AIAA/CEAS Aeroacoustics Conference*, p. 2645, 2019.

Signed:

Date:

Journal publications:

- H. Kim, Z. Hu, D.J. Thompson, "Numerical Investigation of the Effect of Cavity Flow on High Speed Train Pantograph Aerodynamic Noise" (submitted to Journal).

- H. Kim, Z. Hu, D.J. Thompson, "Effect of Cavity Flow Control on High Speed Train Pantograph and Roof Aerodynamic Noise" (submitted to Journal).

- H. Kim, Z. Hu, D.J. Thompson, "Numerical Investigation of the Effect of Various High Speed Train Roof Configuration on Aerodynamic Noise" (submitted to Journal).

Awards:

- The Best poster, In *Europe-Korea Conference on Science and Technology 2019 (EKC 2019)*.

- The Best Poster, In *Europe-Korea Conference on Science and Technology 2017 (EKC 2017)*.

Acknowledgements

Nomenclature

Symbols

A	Area
c_0	Speed of sound
C_D	Drag coefficient
C_D^{rms}	Root mean square of drag coefficient
C_L	Lift coefficient
C_L^{rms}	Root mean square of lift coefficient
C_p	Pressure coefficient
C_s	Side force coefficient
C_s^{rms}	Root mean square of side force coefficient
D	Depth of cavity
d	Wall distance
$\tilde{d}$	Modified length scale in DDES model
f	Frequency
$f_B, \tilde{f}_d, f_e$	Blending functions in the IDDES turbulence model
f_{v1}, f_{v2}, f_w	Damping functions in the S-A turbulence model
G	Green's function
G_0	Green's function in free space
h	Radius
h/D	Cavity edge rounding ratio
$H(f)$	Heaviside function
k	Turbulence kinetic energy
L	Length of cavity
L_i	Dipole source term (Sound source strength)
L/D	Length-to-depth ratio
l_{DES}	Length scale used in DES method
l_{DDES}	Length scale used in DDES method
l_{IDDES}	Length scale used in IDDES method
l_{LES}	Length scale used in LES method

m	Mass
M	Freestream Mach number
M_r	Source Mach number in radiation direction
p	Pressure
P	Mean pressure
p'	Pressure fluctuation
P_{ij}	Compressive stress tensor
p_{ref}	Reference pressure
Q	Q criterion (Second invariant of the velocity gradient)
Q_i	Monopole source term (Sound source strength)
Q_{norm}	Normalized Q-criterion
Re	Reynolds number ($\rho U_\infty D/\mu$)
r	Distance between source surface and observer point
S_{ij}	Strain-rate tensor
$\overline{S}_{ij}$	Mean strain-rate tensor
t	Time
T_{ij}	Lighthill tensor
U_i	Mean velocity
U_t	Transition speed
U_∞	Freestream velocity
u, u_i, u_j	Instantaneous flow velocity components
u_τ	Friction velocity
W	Width of cavity
W/D	Width-to-depth ratio
x, y, z	Cartesian coordinate system
y^+	Dimensionless wall distance

Greek symbols

Δt	Time step
$\Delta x, \Delta y, \Delta z$	Cell dimensions in x, y, z directions
Δ	Filter width
δ_{ij}	Kronecker delta
ϵ	Turbulent energy dissipation rate
θ	Azimuthal angle, cavity edge angle
λ	Wavelength
μ	Molecular dynamic viscosity
μ_t	Eddy viscosity
ν_T	Kinematic viscosity
ν_t	Turbulent viscosity

$\tilde{\nu}$	Modified turbulent eddy viscosity
ρ	Density
ρ_0	Non-perturbed density of medium
ρ'	Density fluctuation
τ_{ij}	Viscous stress tensor
ϕ	Polar angle
ω	Specified dissipation rate
ω_{norm}	non-dimensional vorticity

Abbreviations

2D	Two-dimensional
3D	Three-dimensional
CAA	Computational Aeroacoustics
CAD	Computational Aid Design
CFD	Computational Fluid Dynamics
CFL	Courant number
CRH	China Railway High-speed (Chinese high speed train)
dB	Decibel
DES	Detached Eddy Simulation
DDES	Delayed Detached Eddy Simulation
DNS	Direct Numerical Simulation
IDDES	Improved Delayed Detached Eddy Simulation
LES	Large Eddy Simulation
FEM	Finite element method
FFT	Fast Fourier Transform
FW-H	Ffowcs Williams-Hawkings
KTX	Korean train express (Korean high speed train)
LIC	Line Integral Convolution
N-S	Navier-Stokes
OASPL	Overall Sound Pressure Level
PIMPLE	Merged PISO-SIMPLE
PISO	Pressure-Implicit Split Operator
PIV	Particle Image Velocimetry
PSD	Power spectral density
RANS	Reynolds Averaged Navier-Stokes
rms	Root-mean-square
RTRI	Railway Technical Research Institute
S-A	Spalart-Allmaras
SGS	Sub-grid scale

SIMPLE	Semi-implicit Method for Pressure-Linked Equations
SPL	Sound Pressure Level
TGV	Train á Grande Vitesse (French high speed train)
URANS	Unsteady Reynolds Averaged Navier Stokes

Subscripts

∞	Freestream quantities
i	spatial or summation index
max	Maximum value
min	Minimum value

Superscripts

$\bar{\ }$	Mean value
$'$	Fluctuating component

Chapter 1

Introduction

1.1 Background and motivation

In recent years, high-speed rail transportation has evolved into a thriving industry. Energy efficiency and environmental impact as well as journey time and price are the most important factors to consider when attempting to compete with air and road transport. High-speed trains have more capacity compared to other means of transport and, when travelling at approximately 300 km/h, are one of the most attractive forms of transport [1]. However, high-speed train noise increases considerably as its speed increases. With high speed comes higher levels of noise; therefore, noise reduction has become an essential consideration in high-speed train design, and is critical to future development, expansion, and operation of high-speed train systems.

The noise from trains is dominated by rolling noise when trains operate below a certain speed, which may be referred to as the transition speed (U_t). Rolling noise is generated by the interaction between the wheel and rail [2]. Aerodynamic noise has a higher speed dependence and becomes dominant when the train speed exceeds the transition speed [2, 3]. A reduction of the rolling noise lowers the transition speed. Many researches have shown that aerodynamic noise could become predominant over rolling noise above approximately 300 km/h (see Figure 1.1) [2–5].
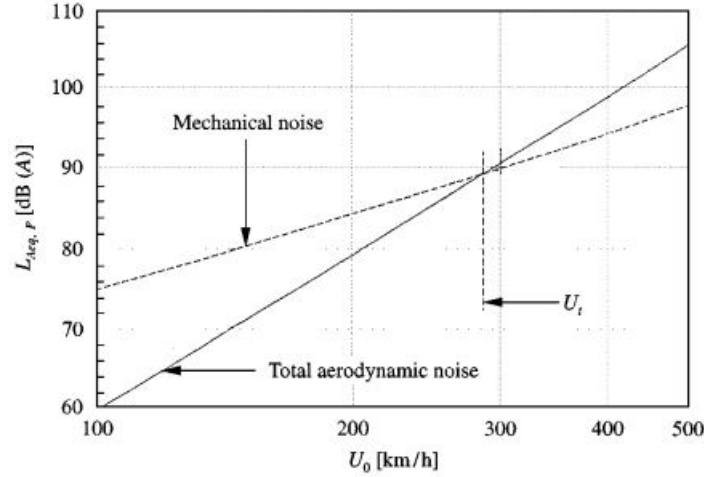
Figure 1.1: Transition speed U_t for a high-speed wheeled train (ICE or TGV) with an average level of rolling and aerodynamic noise [3]. - - -, rolling noise; —, aerodynamic noise.

The aerodynamic noise from high-speed trains is comes from several sources: the bogies, inter-coach gaps, the nose of the power car, the pantograph, and the recess of the pantograph [2, 3, 6, 7]. Noise from the bogies, the inter-coach gaps and the front nose can be shielded by conventional noise barriers; however, it is more difficult to shield the noise from the pantograph and the pantograph recess as they are located at the top of the train. Therefore, a number of investigations on noise from the pantograph and its recess have been carried out in order to identify the dominant noise sources and to find ways to reduce the radiated noise.

Many studies have been carried out to identify pantograph noise sources [8–10] and to attempt to reduce its noise [11–18]. By comparison, the generation of aerodynamic noise from the pantograph recess, representing a rectangular cavity, and its flow interacting with pantograph components are less well understood even though the noise from the pantograph recess may have a similar level to that from the pantograph [7]. Therefore, improved understanding of aerodynamic phenomena and noise generation mechanisms from cavity flow is required.

1.2   Aim and objectives

As mentioned above, most previous studies on pantograph noise have focused on the pantograph itself, such as the panhead and arms, whereas work on the pantograph recess is limited. Of relevance to the pantograph recess, a large number of experimental and theoretical studies have been carried out on cavity flow over a wide range of speeds and length-to-depth (L/D) ratios. However, no clear noise control techniques have been developed for 'closed' cavities

(i.e. $L/D \geq 10$) at low Mach number or for a cavity with objects inside. Therefore, the aim of this research is to investigate the noise sources and the flow features of a rectangular 'closed' cavity with two pantographs (one raised and one folded) and analyse the interaction between the cavity flow and the pantographs, and the noise radiated from them. Furthermore, recommendations should be established for noise reduction. To investigate noise from the pantographs and the recess, computational fluid dynamics (CFD) using Improved Delayed Detached-Eddy Simulations (IDDES) and Computational aeroacoustics (CAA) using the Ffowcs Williams-Hawkings (FW-H) acoustic analogy are used to resolve details of the turbulent structures and enable sufficiently accurate noise prediction.

The specific objectives of this research are as follows:

- To develop a numerical approach for train roof cavity and pantograph noise predictions, and after validating the method, to apply the method to cavity and pantograph noise predictions.

- To investigate the effect of the cavity flow on the pantographs by comparing with results of the pantographs without the cavity configuration.

- To study the effects of the cavity flow control by modifying the cavity edges to investigate reduction of the noise from the pantographs and its recess.

- To study unsteady flow behaviour for different high speed train roof configurations including a cavity containing two pantographs and a flat roof with side insulation plates to quantify and describe the mean and unsteady flow behaviour in the cavity and predict the noise radiated from the roof configurations.

The thesis contains eight chapters. Chapter 2 reviews studies of aerodynamic noise from high-speed trains, the fundamentals of cavity flows and the resulting noise. Chapter 3 describes the methodologies employed including numerical schemes and acoustic analogies. Chapter 4 presents flow-field and far-field measurements for a cavity used for validation and describes the mesh, numerical set-up and simulation results of flow over cavities. The results are analysed in order to validate the accuracy of the numerical methodology used and a benchmark case is used to demonstrate the applicability of the numerical method for the pantograph case. Chapter 5 presents an analysis of the effects of the cavity flow on the noise radiated from the pantographs. Chapter 6 focuses on computational results with different cavity flow control for noise reduction from cavities and analyse the effect on simplified pantograph components. An investigation of flow features and the acoustic characteristics of three different high-speed train roof configurations is provided in Chapter 7. Finally, conclusions of the current research and a discussion on recommendation for future works are

summarised in Chapter 8.

Chapter 2

Literature Review

This chapter presents a review of recent relevant studies. This includes an introduction to aerodynamic noise from high-speed trains, followed by a discussion of the fundamental principles related to the flow and acoustic features of cavities.

2.1 A brief overview of aeroacoustics of high speed trains

A number of researchers have investigated the aerodynamic noise sources of high-speed trains by full-scale measurements [7, 19–21, 23–25], wind tunnel tests with scaled models [20, 26] and using computational simulations [21, 22, 27]. Moritoh et al. [19] measured noise sources of a Shinkansen high-speed train operating at a speed of between 220 and 240 km/h by using a microphone array and parabola microphone. They identified the main sources of aerodynamic noise from the high-speed train as the pantograph, the louvre intake, the nose of the leading car, inter-coach gaps, windows and doors. They suggested that modification of train surfaces and design was necessary in order to reduce the radiated noise from high speed trains.

Noh et al. [7] investigated noise sources of a Korean high-speed train (Korean Train eXpress, KTX) operating at speeds between 150 km/h and 300 km/h by using an array of 96 microphones placed 5 m away from the rail. They found that the leading power car and the trailing car generated most noise at both 150 km/h and 300 km/h, as shown in Figure 2.1. The dominant noise sources on the leading car were located at the first bogie, the pantograph and its recess, the side wall, the train doors and windscreen. Turbulent boundary layer noise is one of the dominate noise sources of the trailing car as the boundary layer is developing along the trailing car; it can be observed at low frequency (125 Hz). Furthermore, the spectrum of aerodynamic noise at 300 km/h was estimated for each main source of noise, as summarized in Table 2.1.

Table 2.1: Spectra of aerodynamic noise sources of KTX at 300 km/h from A-weighted beampower (dB(A)), 500 Hz bandwidth [7].

	500 Hz	1000 Hz	1500 Hz	2000 Hz	2500 Hz	3000 Hz
Front nose	71	68	64	62	62	55
Pantograph	70	73	71	66	68	65
Pantograph recess	67	70	68	65	63	62
Inter-coach gap	68	63	68	62	66	62
Bogie in the leading car	77	75	72	68	64	62
Bogie in intermediate cars	76	77	73	67	66	63
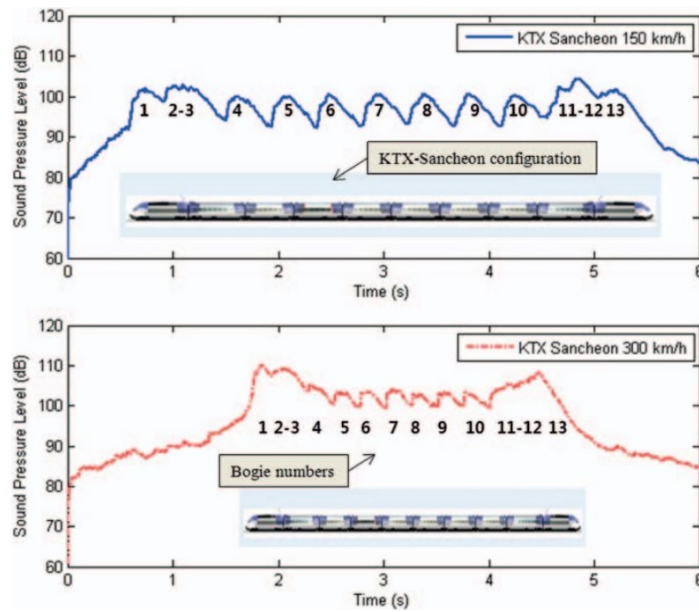
Figure 2.1: Time history of A-weighted sound pressure level from a full-scale high-speed train (KTX) measured with a microphone array at 5 m from rail for train speeds of 150 and 300 km/h [7].

Noh [23] also carried out field tests for a high-speed train using a beamforming method at a speed of 390 km/h. Noise-source maps were produced to identify noise sources on the train at different frequencies as shown in Figure 2.2. It was found that the pantograph is the main noise source at 500 Hz. In addition, it was detected that the panhead is the primary noise source at 1 kHz and the sound pressure level (SPL) emitted by the pantograph was 108.3 dB(A) at 390 km/h measured by microphones located 8 m away from the train.
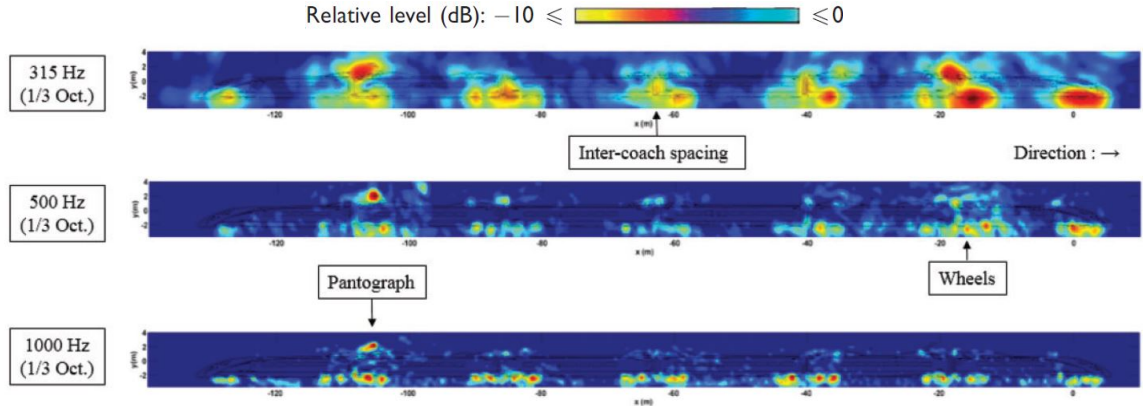
Figure 2.2: Noise source map of high-speed train travelling at 390 km/h [23].

Nagakura [26] carried out wind tunnel tests at the Maibara Wind Tunnel in Japan using a 1/5 scale train model using an acoustic mirror in order to find the characteristics of aerodynamic noise. In addition, field tests for a full-scale train at a speed of 300 km/h were carried out. It was found from the full-scale test results that the dominant noise source at 2 kHz was the front bogie of the leading car, whereas the pantograph was the primary noise source at 4 kHz as shown in Figure 2.3. Furthermore, other noise sources such as the wiper and the door were also detected.
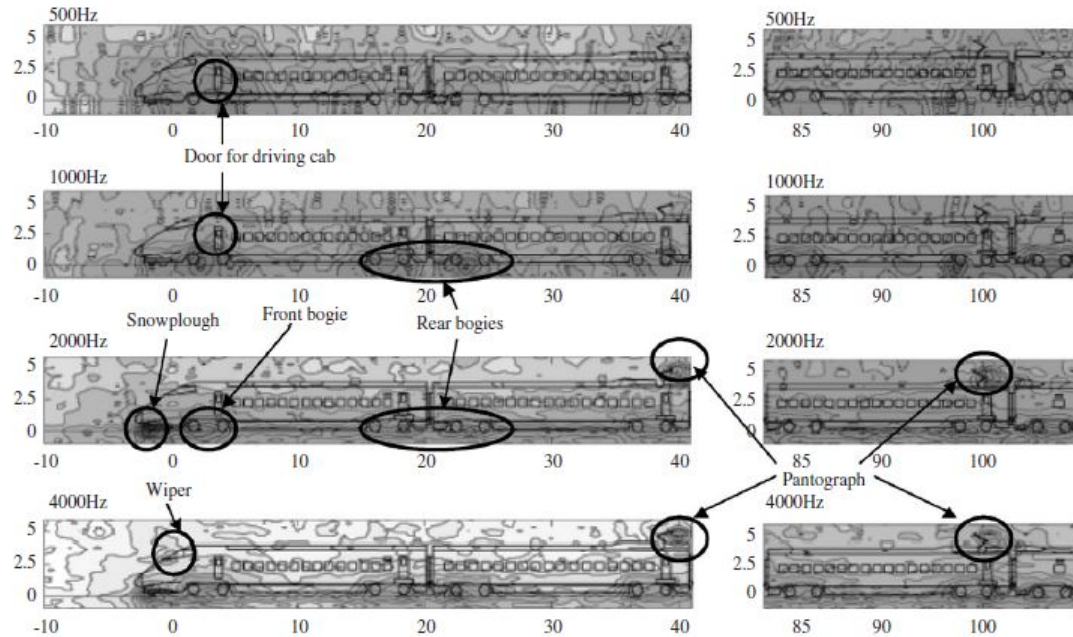
Figure 2.3: Aerodynamic noise source map of full-scale high-speed train Shinkansen at various frequencies by using acoustic mirror [26].

Zhu et al. [27] studied a three-coach 1/8 scale high speed train without pantographs at speeds of 60 and 67 m/s (216 km/h and 241.2 km/h) using a numerical method. It was found that highly unsteady flow occurred in the nose, the gap between the train and ground, and rear wake regions. The high-speed train mainly produces dipole noise sources, which represent the noise generated by the force to the fluid at the surface. Most of the sound pressure occurs at low frequency between 10 Hz and 300 Hz where a peak at 10 Hz can be seen. Moreover, it was shown that the dominant noise source was the leading coach and the bogies of the leading coach.

Another numerical study aimed at predicting the radiated noise from high speed trains was carried out by Zhang et al. [21]. They investigated a full-scale high speed train with six bogies, two windscreen wipers, and two pantographs (one raised and one folded). They identified highly turbulent flow downstream of the raised pantograph and the flow interacted with inter-coach gap where highly unsteady flow occurs. They stated that the nose of the first coach, the windscreen wipers, the pantographs, the bogies (especially on the first coach) and the inter-coach gaps are the main contributors to aerodynamic noise for high speed trains.

Dai et al. [22] carried out numerical investigations for the flow features and far-field acoustics of the inter-coach gap for a two-coach full-scale Chinese high speed train (CRH) at a speed of 350 km/h. They found that the flow features of the inter-coach gap have a characteristic similar to an 'open' cavity and the noise radiated from the inter-coach gaps is broadband without any strong tonal components. The inter-coach gap generates most noise in the low frequency region.

Despite the different test conditions, it has generally been concluded that the main aerodynamic noise sources of high-speed trains are the pantograph, its recess, the bogies and the inter-coach gaps.

2.1.1   Pantograph noise studies

As the location of the pantograph is at train roof level (see Figure 2.4) its noise cannot be easily shielded by noise barriers along the track. Therefore, more attention has been paid to the noise from the pantograph than to other aerodynamic sources and experimental and numerical methods have been employed to investigate its noise reduction. Several studies, especially [6, 9, 23, 25], emphasise the importance of pantograph noise.

Figure 2.4: Pantograph and recess on TGV train [28].

2.1.1.1 Pantograph noise identification studies

Lölgen [29] carried out tests on full-scale DSA350SEK, ASP and PS206 pantographs in a wind tunnel at flow speeds ranging from 115 km/h to 400 km/h. Radiated noise spectra were analysed in detail, see for example Figure 2.6. As the pantograph consists of slender bodies, it generates Aeolian tones, which are characterised by periodic vortex shedding [3]. Peaks at 550 Hz, 900 Hz and 3500 Hz in the noise spectrum of the DSA350SEK measured at 330 km/h were identified as being generated by the contact strip, the pantograph horn and the stroke limiting cage, respectively. Furthermore, there was no significant difference between the noise radiated from pantograph configurations with the knee (joint) either upstream or downstream.

Grosche et al. [9] performed measurements for a full-scale DSA350 pantograph (see Figure 2.5) in a wind tunnel at DLR Göttingen to obtain its noise source distribution. Three main noise sources were identified which are the foot, the panhead and the knee connector.
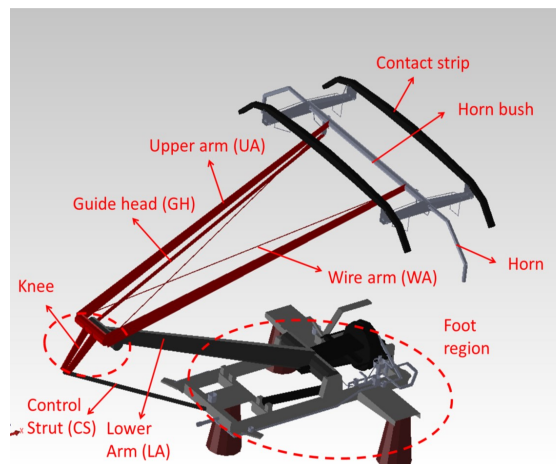
Figure 2.5: DSA350 pantograph configuration [31].
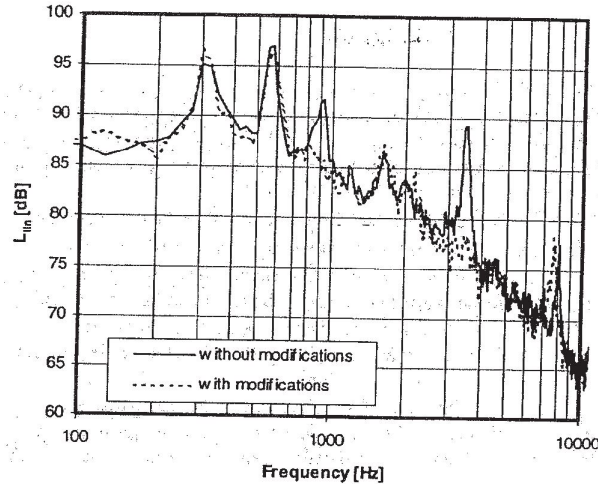
Figure 2.6: The radiated noise from DSA350SEK and with head modification at a speed of 330 km/h [29].

Brick et al. [30] conducted a wind tunnel test using a full-scale DSA350SEK pantograph installed in the recess on part of the roof, as shown in Figure 2.7 in order to measure the noise radiated from both the folded and the raised pantograph. Spires were installed upstream of the pantograph to generate a similar turbulent boundary layer to the real case. They found that the SPL of the raised pantograph was 8 dB higher than the noise radiated from the folded pantograph at a speed of 280 km/h. The noise radiated from both the raised and folded pantographs was reduced by the presence of the spires which generated a turbulent inflow. Therefore, it is noted that the incoming boundary layer thickness can be important fact of the radiated noise from the pantograph. Furthermore, the Overall SPL (OASPL) followed a sixth power law in terms of the flow speed, i.e. $L_p \sim 60\log_{10}N$, which is typical of dipole sound [69].

(a) Folded pantograph

(b) Raised pantograph
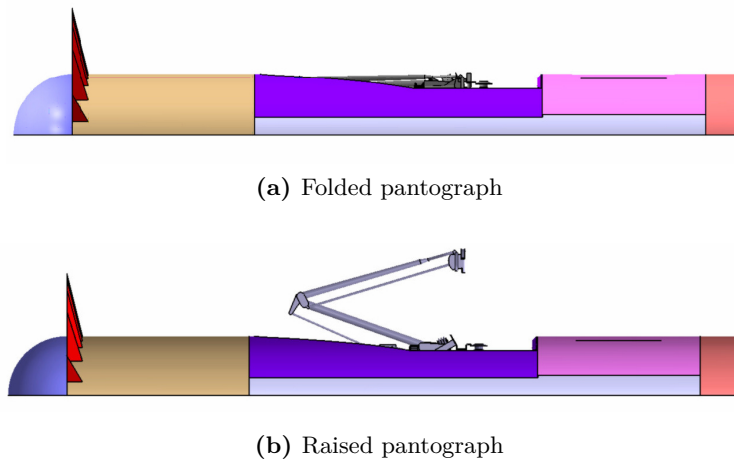
Figure 2.7: Pantograph and its recess configurations used for measurement by Brick et al. [30].

Yu et al. [10] predicted the aerodynamic noise emission of a pantograph system at 350 km/h using a hybrid method of non-linear acoustic solver (NLAS) and FW-H. They found that the main mechanism is the periodic vortex shedding, which generates Aeolian tones [3] around the pantograph structures, especially the panhead. Moreover, unsteadiness in the wake caused by flow separation occurs downstream of the pantograph and generates broadband noise. Another computational study by Lei et al. [8] also indicated that the main noise sources from the pantograph were the strong vortices shed from its body. The strongest turbulent flows appeared around the panhead, knee and oblique arm region generate mainly low and mid-frequency noise.

To predict the aerodynamic noise generated by a high-speed train pantograph, Latorre Iglesias et al. [31] introduced a semi-empirical component-based model. The predictions from the model were compared with radiated noise measured for two different full-scale pantographs, giving good agreement for OASPL, speed dependence and spectral shape.

Noh [32] investigated numerically the aerodynamic noise of a full-scale pantograph for the KTX train at a speed of 300 km/h using the lattice Boltzmann method. The time derivative of the pressure in the flow field was used to predict the radiated noise from the pantograph. Noh [32] indicated that the large pressure fluctuations mostly occurring in the regions of the panhead, the joint and the base frame, and are likely to be the main noise sources. The highest noise was radiated in the direction downstream of the panhead. Furthermore, a strong tonal peak at 242 Hz was observed at a receiver position above the panhead. This peak is generated by the vortex shedding of the panhead. However, Noh [32] only provided flow behaviour and the noise generation mechanism of the panhead. It would be necessary to provide detail of the flow behaviour of the other parts such as the frame and knee.

Zhang et al. [33] performed numerical simulations for a full-scale DSA380 pantograph at a speed of 350 km/h using Large Eddy Simulation (LES) for the flow field and FW-H acoustic analogy for the far-field pressure. Three peaks, at 305, 608 and 913 Hz, were found in the noise spectrum of the pantograph panhead at the top receiver position. They indicated that the first peak is associated with the oscillation of the lift force of the panhead contact strip and the second peak is generated by the interaction between the wake from the panhead contact strip and horn bush, and the panhead support. The noise source of the third peak and detail of those tonal noise generation mechanisms were not provided. They also compared different running directions of the train with the pantograph knee either downstream or upstream. They found that the radiated noise from the knee-downstream configuration was 3.4 dB lower than that from knee-upstream configuration at the side receiver position. However, they have not provided details of the noise generation mechanisms of the knee-upstream and knee-downstream configurations.

2.1.1.2   Pantograph noise reduction studies

A number of researchers have investigated noise reduction techniques applied to pantographs. Ikeda et al. [11] introduced an optimized shape of panhead and tests were carried out in a wind tunnel at the Railway Technical Research Institute (RTRI). Holes were made through the panhead along the span in order to decrease the intensity of the Aeolian tone. The optimized panhead significantly reduced the noise from an isolated panhead. However, they found that it did not effectively reduce the noise when it was installed on the articulated frame. The reason was that strong aerodynamic interference occurred between the optimised panhead design and the articulated frame. Ikeda and Mitsumoji [12, 13] investigated the details of this interference through computational simulations and they found that distinct vortex lines occurred from the panhead support toward the panhead. To prevent this aerodynamic interference, a new panhead support was developed which generates less vortical structures around the joint between panhead and its support. The new panhead and its support generated an OASPL approximately 4 dB less than the baseline case.

Another study aimed at reducing panhead noise was carried out numerically by Lee and Cho [14]. They showed that the noise from the panhead was reduced when a thin plate was attached on the crossbar in the panhead. Various configurations of the thin plate were studied in two dimensions and the far-field noise was predicted using a URANS model and the FW-H acoustic analogy. It was found that the thin plate reduced the SPL. By increasing its length, the noise was decreased until it reached a minimum at a length of 148 mm. Furthermore, the thin plate produced a lift force, which it was, claimed could provide better stability of the panhead.

Sato et al. [15] investigated inclined circular cylinders and tapered cylinders (see Figure 2.8) using experimental and computational methods at a speed of 30 m/s. They reported that tapered cylinders produce higher broadband noise than circular cylinders for both the knuckle upstream configurations (see Figure 2.8(b) and (c)), whereas tapered cylinders contribute less narrowband noise for the knuckle downstream configuration. This is because a wake flow is likely to be generated by the knuckle and the tapered shape causes a more widely separated flow around the knuckle. They presumed that the separated flow produced more vortex noise.

Liu et al. [16] used the Delayed Detached Eddy Simulation (DDES) method to investigate the effects of various yaw angles of cylinders representing pantograph arms. They found that by increasing the yaw angle of the cylinder, the vortex shedding was reduced and aerodynamic force fluctuations such as lift were also decreased. These phenomena caused a reduction in the sound levels and in the frequency of the peak.

With no geometry modification, Ikeda et al. [11] and Sueki et al. [18] used porous material on

pantograph surfaces in order to reduce noise. Using a wind tunnel at RTRI, they investigated the effect of covering cylinders and parts of the pantograph with various porous materials with about 95% porosity and 8 - 20 pores per inch, including urethane and metal foam. The result of the cylinder tests showed that the porous materials eliminated tonal noise and generated less overall broadband noise. They also covered the panhead support, knuckle and base frame of the pantograph with the porous materials. This treatment reduced the noise by up to 1.9 dB, especially the tonal noise, regardless of the shape of the pantograph. Thus, they suggested that porous materials could provide an alternative way of reducing noise for a wide range of pantograph shapes.
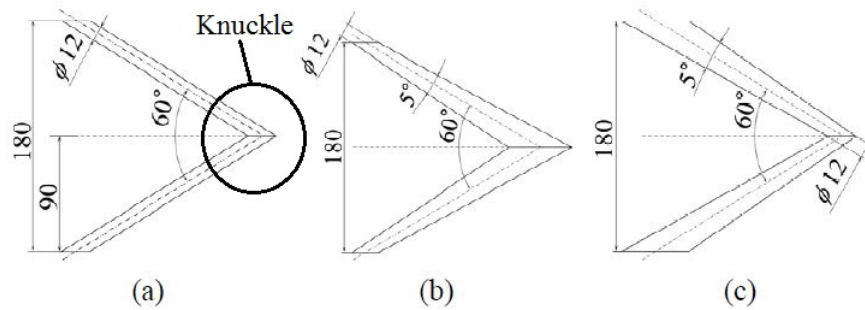
Figure 2.8: Experimental model studied by Sato et al. [15]: (a) inclined circular cylinder, (b) inclined tapered cylinder with increasing diameter to knuckle and (c) inclined tapered cylinder with increasing diameter from knuckle.

2.1.2 Pantograph recess studies

The pantograph is generally located in a recess on the train roof as shown in Figure 2.4. This is used to house the retracted pantograph and various electrical parts. Wind tunnel tests were performed by Noger et al. [34] to identify aerodynamic and acoustic features of a 1/7 scale model of a Train á Grande Vitesse (TGV) pantograph recess as shown in Figure 2.9. Noger measured the empty recess, which can be classified as a 'closed' cavity with a length-to-depth ratio of 11. He also studied a recess with two pantographs and one with an additional hood on the upstream region. It was found that most noise was generated in a region near the trailing edge of the cavity. Due to the presence of the pantograph in the recess, there were interactions between the wake of the pantographs and the downstream shear layer and Noger [34] showed that this interaction caused less turbulence intensity than the empty recess case. On the other hand, the pantograph surface was impinged by the upstream shear layer, increasing the turbulence intensity in the upstream region. Furthermore, it was found that the shield located on the side of the roof reduced the shear layer and broadband noise.
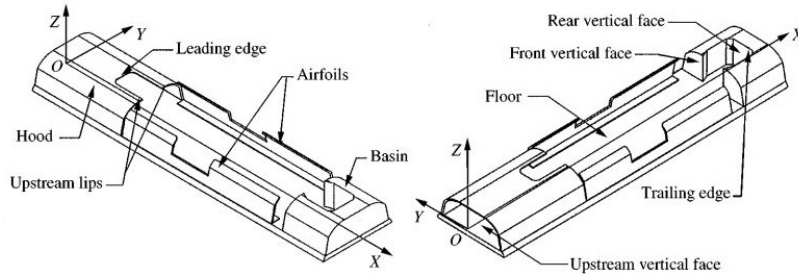
Figure 2.9: Configuration of pantograph recess on TGV train studied by Noger et al. [34].

Noh et al. [7] estimated the aerodynamic noise induced by the recess of a full-scale Korea high-speed train (KTX) using the beamforming method. The level was found to be similar to that from the pantograph itself at a speed of 300 km/h and the dominant frequency was below 1200 Hz (see Table 2.1). Although the noise level from the pantograph recess appears to be similar to that of the pantograph itself, much less attention has been given to noise reduction techniques for it.

Kurita et al. [17] introduced the so-called insulation plates or pantograph shields for the reduction of pantograph noise. These plates are attached to the side of the train roof where the pantograph is installed, thus shielding noise from the pantograph. However, these plates can also generate noise themselves. Kurita et al. [17] compared Z-shaped noise insulation plates with conventional plates on a Japanese high-speed train, as shown in Figure 2.10. They showed that the greatest noise sources were at the front and rear edges of the plates as well as around the pantograph head. When they tested the conventional plates with a 45 degree angle instead of vertical ends, the noise from the edges of the plates was significantly reduced compared with the Z-shaped plates. They also conducted a wind tunnel test using a 1/10 scale model in order to optimise the edge shape of conventional insulation plates as well as the shape of its cross-section. As a result of the optimisation, they achieved a 2 dB reduction of noise compared with the original conventional insulation plates.

Figure 2.10: Z-shaped (left) and conventional (right) insulation plates studied by Kurita et al. [17].

Yu et al. [10] modelled numerically various types of pantograph insulation cover, as shown in Figure 2.11. It was found that one case, which covered the sides of the pantograph (see Figure 2.11(a)), reduced the tonal noise by 3 dB, whereas all the other cases (See Figure 2.11(b), (c), (d)) performed poorly and produced more noise than the case without the cover. The radiated noise from the ramped cover case (Figure 2.11(b)) has the highest level compared with the other configurations. They indicated that the cover reduced the flow speed at the pantograph frame. Consequently, the noise radiated from the pantograph is reduced, but the covers generated extra cavity noise due to other aspects of the cover geometry such as the formation of cavities. The cases with and without the side insulation plates (case (a) in Figure 2.11 and baseline) were compared. They concluded that the case with side insulation-plate reduced the radiated noise from the pantograph. However, the information of the aerodynamic phenomena and the noise generation mechanism of the recess geometry was not given. Therefore, it is useful to investigate the phenomena.
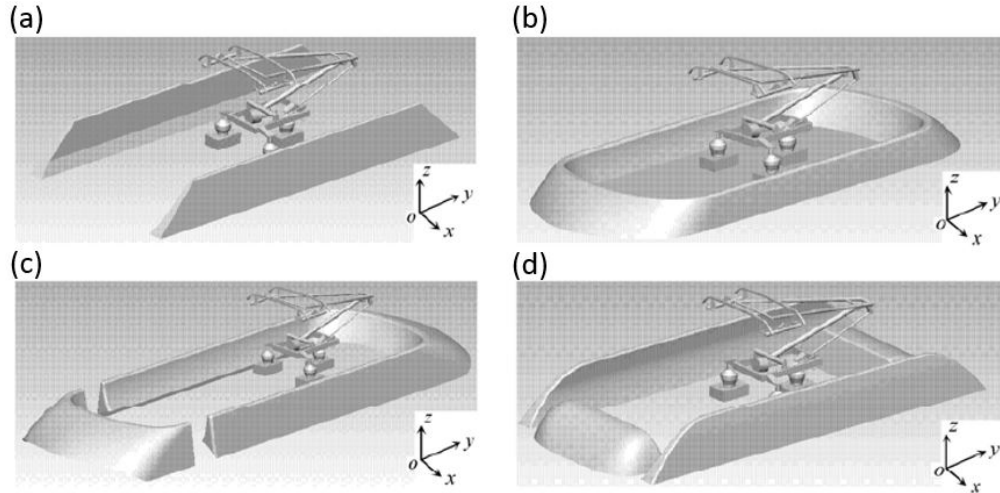
Figure 2.11: Pantograph insulation plates studied by Yu et al. [10]: (a) side insulation plates with half height of pantograph, (b) cover around pantograph, (c) spoiler cover and separated by an inter-coach spacing, and (d) combination of front and rear spoiler and side insulation plates.

Another numerical investigation of the recess with a pantograph has been carried out by Yao et al. [35]. They used LES and the acoustic finite element method (FEM) to investigate the aerodynamic noise characteristics of four pantograph installation configurations shown in Figure 2.12 at a speed of 350 km/h. Two pantographs at full-scale, one folded and one raised, were installed directly on the train roof (Figure 2.12(a) and (b)) and in an open cavity (Figure 2.12(c) and (d)). It was found that large pressure fluctuations appear downstream of the pantograph for all four configurations. Furthermore, they stated that the sound level for the configuration with the raised pantograph in the cavity is the lowest in all directions. This is because a large part of the pantograph is placed inside the cavity region.

(a) Folded pantograph

(b) Raised pantograph

(c) Folded pantograph in the recess (d) Raised pantograph in the recess
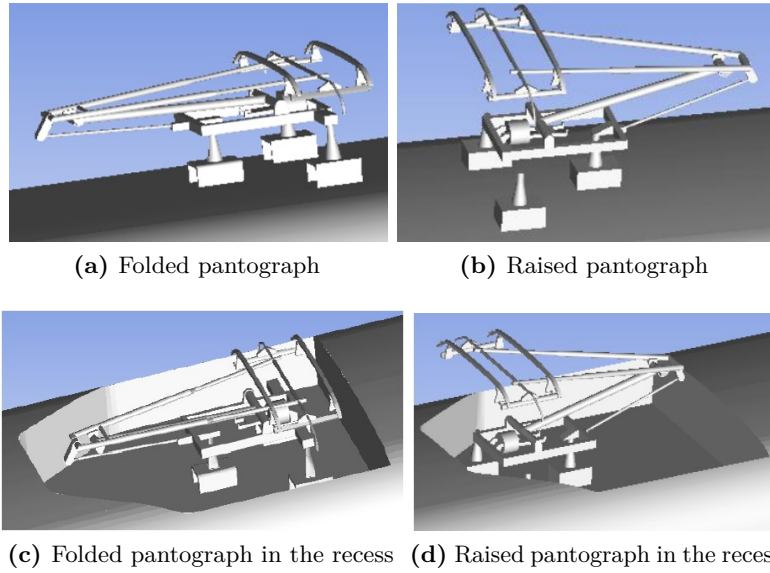
Figure 2.12: Four different pantograph installation types studied by Yao et al. [35].

2.2 Cavity flow and noise

The high-speed train pantograph recess can be simplified as a cavity. The flow and acoustic features of cavities are reviewed in this section.

Cavity flow has been studied for more than a century. The research began with Helmholtz as early as 1875 [51]. He established an expression for the flow resonance of a cavity. However, these early studies were not very clear about cavity flow characteristics. Research on cavity flow fields was not developed until the mid-twentieth century. Most of the early studies were motivated by aircraft weapon bay aerodynamic issues [36, 37]. In recent years, there have been many studies on cavity flow mainly because of noise from the cavity. Krishnamurty [38] carried out wind tunnel tests in the GALCIT transonic wind tunnel with various cavity models for a Mach number range of 0.5 to 1.5. He found that the cavity acoustic characteristics depend on the incoming boundary layer, the length of the cavity and the flow velocity. Furthermore, stronger acoustic radiation and higher frequencies occurred at increasing flow velocity.

2.2.1 Cavity flow types

Cavities can be categorised as deep or shallow with shallow cavities further divided into open, transitional and closed [36, 37, 40] as shown in Figure 2.13 [39]. Although the values of L/D have not been precisely classified, according to Rockwell et al. [41] deep cavity behaviour normally occurs for $L/D < 1$, whereas shallow cavity behaviour occurs for $L/D \geq 1$. The shallow cavity flows are generally sub-divided into four categories, depending on L/D.

(a) Deep cavity   **(b)** Open cavity

(c) Transitional cavity   **(d)** Closed cavity
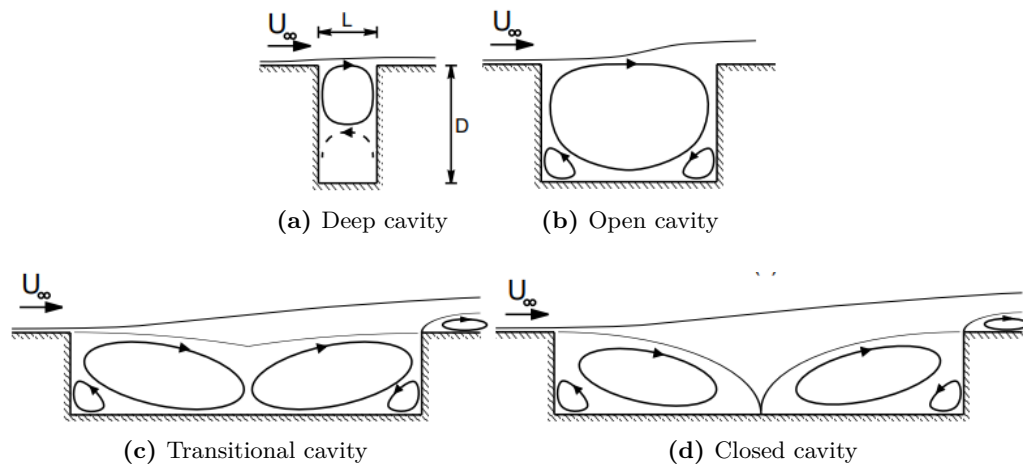
Figure 2.13: Flow features of deep and shallow cavities [39].

In an open cavity with small L/D, the shear layer separates at the leading edge of the cavity, bridges the cavity length and reattaches on the trailing edge; a distinct recirculation inside the cavity is observed. Open cavities show intense periodic pressure fluctuations caused by self-sustaining flow oscillations. These oscillations are a consequence of the direct interaction of the shear layer with the aft wall. Figure 2.14(a) shows a general open cavity flow field.

(a) Open cavity
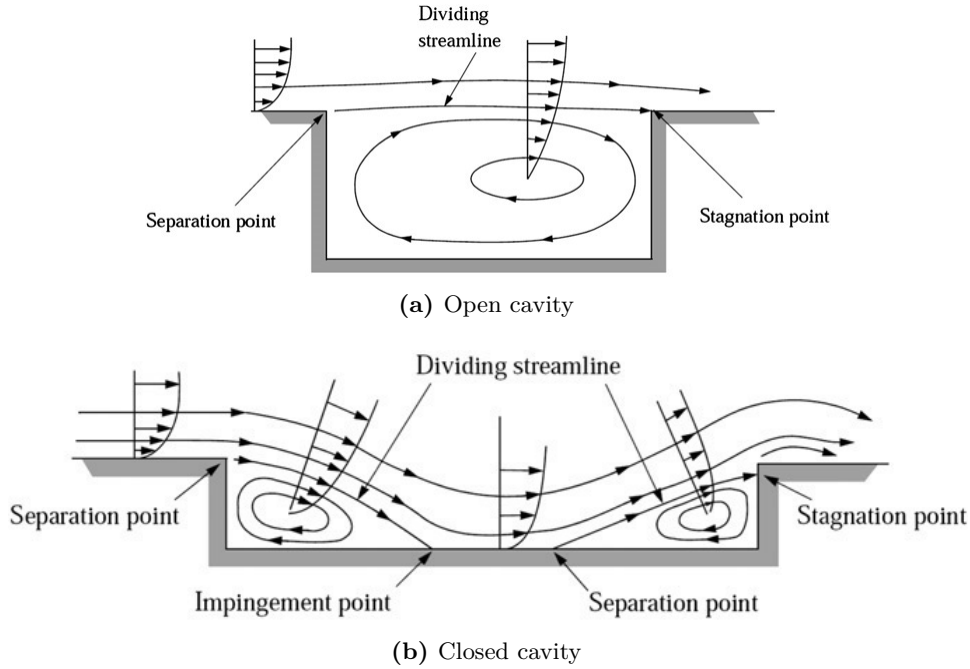
(b) Closed cavity

Figure 2.14: Comparison of open cavity (a) and closed cavity (b) flow for subsonic/transonic flow. [42].

Transitional cavity flow is an intermediate step between open and closed cavity flows and can be further divided into two stages as transitional-open and transitional-closed. For the transitional-open cavity flow, the shear layer might not bridge the cavity any more and impinges on the cavity rear wall. For the transitional-closed cavity, the shear layer starts to impinge on the floor and rear wall of the cavity [40].

Closed cavity flows are associated with cavities having L/D ratios generally higher than 9 at subsonic speed and 13 at supersonic speed. These dimensions are typical of the pantograph recess on a high-speed train. Figure 2.14(b) shows a general closed cavity flow field. In this type of flow regime, the shear layer, which forms as the incoming boundary layer separates at the cavity leading edge, reattaches along the cavity floor before separating again ahead of the downstream wall. As the shear layer touches and separates from the cavity floor, two distinct recirculation regions are created in a closed cavity flow.

Plentovich et al. [37] stated that $L/D < 6$ corresponded to an open cavity flow and 6 $< L/D < 8$ to a transitional cavity flow for subsonic speeds. The boundary of transitional and closed cavity flows was not so clearly defined due to strong dependency on the Mach number, and the width of the cavity (W) as well as L/D. However, the closed cavity flow appeared above somewhere from $L/D \geq 9$ up to $L/D \geq 15$. The boundary between an open and a transitional cavity flow is relatively independent of the Mach number. However, for W/D of 4 and 8, the boundary between a transitional and a closed cavity flow is not constant and the boundary occurs at higher values of L/D with increasing Mach number as shown in Figure 2.15.
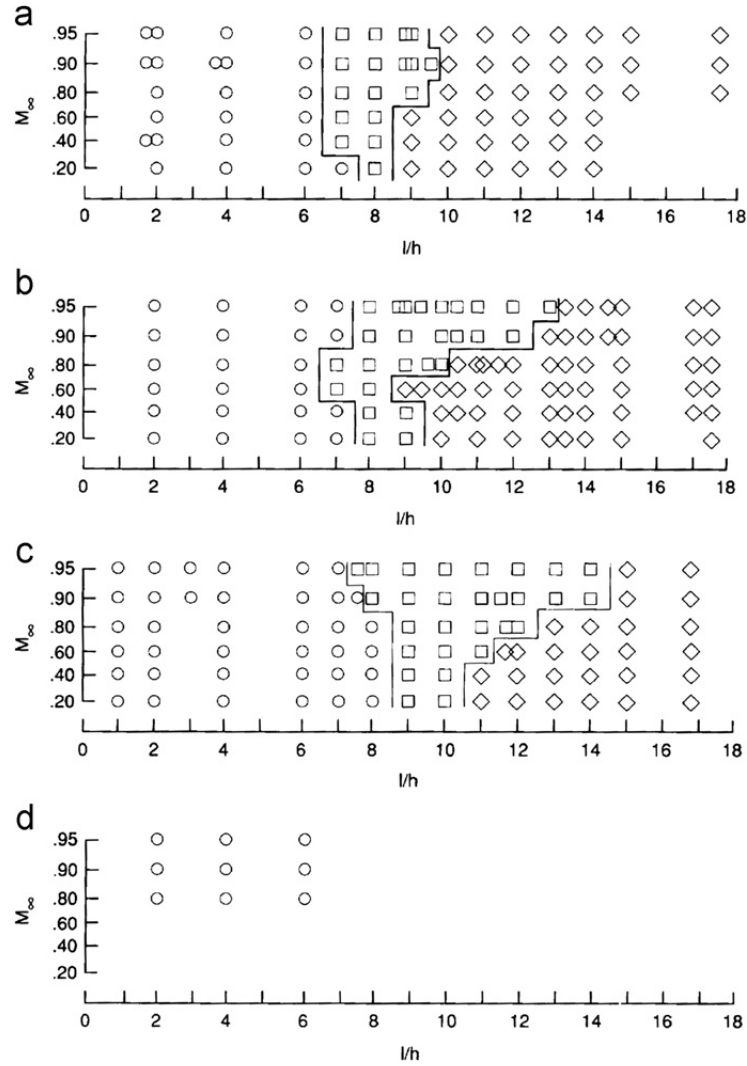
Figure 2.15: Boundaries of cavity flow regimes for a range of cavity variables and Mach numbers [37]. l/h indicates the cavity-to-depth ratio (L/D). (a) $W/D = 1$, (b) $W/D = 4$, (c) $W/D = 8$, (d) $W/D = 16$ (Data between $M = 0.2$ and 0.6, and for $6 < L/D$ were not provided). $\bigcirc$: open cavity flow, $\square$: transitional cavity flow, $\Diamond$: closed cavity flow.

Ng [40] classified cavity flow regimes, especially the regimes between transitional-open and transitional-closed, using measurements of the static pressure and the pressure fluctuations in a rectangular cavity with L/D of 3 to 20 at a very low Mach number ($M = 0.029$). He reported $L/D < 6.5$ for open, $6.5 < L/D < 10$ for transitional-open, $10 < L/D < 15$ for transitional-closed and $15 < L/D$ for closed cavity flow regimes.

However, due to various phenomena, cavity flow depends on a variety of parameters, especially flow velocity, in addition to the value of L/D and W/D. There are also other important parameters, such as boundary layer thickness, ambient density and viscosity.

2.2.2   Classification of cavity oscillations

A number of studies have been conducted to understand the fundamental fluid mechanics related with cavity flow oscillations, especially for an open cavity [38, 43–47]. Cavity flow fields show different flow oscillation characteristics according to the flow conditions and the cavity geometry. Rockwell et al. [46] divided these oscillation characteristics into two oscillation types: fluid dynamic oscillations and fluid resonant oscillations.

2.2.2.1   Fluid dynamic oscillations

Rockwell et al. [46] stated that fluid dynamic oscillations appear when the ratio of the cavity length (L) to the acoustic wavelength (λ) is much less than 1. These oscillations are sometimes referred to as feedback resonance. The frequencies of these oscillations can be traced to the selective amplification of the vorticity fluctuations inside the cavity shear layer. The mechanism for the excitation of the fluid dynamic oscillations is the amplification of the shear layer from the cavity leading edge disturbances and this process is strongly sustained by the presence of the trailing edge of the cavity [46]. During the shear layer impingement on the cavity trailing edge, pressure perturbations occur. Due to this, acoustic disturbances propagate upstream through the cavity which can amplify the shear layer disturbances at selected frequencies. This selective amplification is necessary for generating coherent oscillations. Rossiter developed an empirical equation for the frequencies of fluid dynamic cavity oscillations which can be written as [44],

$$f = \frac{U}{L} \frac{(m - \alpha)}{\left(\frac{1}{K} + M\right)} \tag{2.1}$$

where f is the frequency of the resonant, U is the freestream velocity, L is the cavity length, m is an integer ($m = 1, 2, ..$), α is the phase lag between the passage of a vortex and the emission of a sound pulse at the cavity downstream corner, K is the ratio of the convection velocity of vortices to the freestream velocity ($K = U_c/U$ where U_c is the convection velocity), M is the Mach number. The Rossiter formula can be used for fluid dynamic oscillation as

well as fluid resonant oscillations when effects of the resonating wave on the constants α and K are considered.

2.2.2.2 Fluid resonant oscillations

Fluid resonant oscillations occur when the shedding frequencies are sufficiently high and the acoustic wavelength (λ) is of the same order of magnitude or smaller than the cavity characteristic dimension, i.e. the cavity length (L) or width (W) [46]. Tracy et al. [47] performed measurements in a cryogenic transonic wind tunnel using a cavity model with $L/D = 4.4, 6.7$ and 20 and with $L/W = 4.5$ for a Mach number range of 0.2 to 0.9. They found that longitudinal standing waves may occur when L/D is sufficiently large (a shallow cavity), whereas transverse waves occur related with the cavity width for a deep cavity, i.e. $L/D < 1$.

2.2.3 Effect of boundary layer on cavity oscillations

In earlier years, studies on the effect of the boundary layer on cavity flow were focused on classifying the effect of laminar and turbulent incoming boundary layers on cavity oscillations. Koschatzky et al. [48] conducted a wind tunnel test using two-dimensional particle image velocimetry (PIV) and wall pressure measurement at speeds of 10 m/s, 12 m/s and 15 m/s. The cavity had 3 cm length and 1.5 cm depth ($L/D = 2$). They investigated the acoustic emission characteristics under the influence of incoming laminar and turbulent boundary layers. They found the presence of high amplitude tones for a laminar incoming boundary layer while these peaks did not occur with a turbulent incoming boundary layer. They also observed that the standing vortex inside the cavity became smaller for a turbulent boundary layer.

Ahuja and Mendoza [49] carried out experiments using a cavity model with $L/D = 3.75$ ($L = 0.048$ m) and $L/W = 0.468$ at $M = 0.4$ to investigate the effect of the turbulent boundary layer thickness on cavity noise. The boundary layer thickness was obtained at a location 3.18 mm ($x/L = 0.067$) upstream of the cavity leading edge and the acoustic data was obtained by a microphone located at 0.102 m above the cavity leading edge as shown in Figure 2.16. They found that an increase in boundary layer thickness δ from $L/\delta = 26.3$ to $L/\delta = 22.2$ eliminated the first and third mode feedback tones at 750 Hz and 4107 Hz, whereas it increased the amplitude of the second mode, which was the dominant one. By increasing the boundary layer thickness to $L/\delta = 15.1$, it was observed that the cavity tones were reduced to the broadband level with a reduction of 23 dB. The thickest boundary layer case ($L/\delta = 15.1$) eliminated completely the feedback tones and also reduced depth-mode acoustic resonances. No explanations were given for this reduction phenomenon. The turbulence levels and thickness of the boundary layer could also have considerable effects on the pressure gradients along the cavity floor.
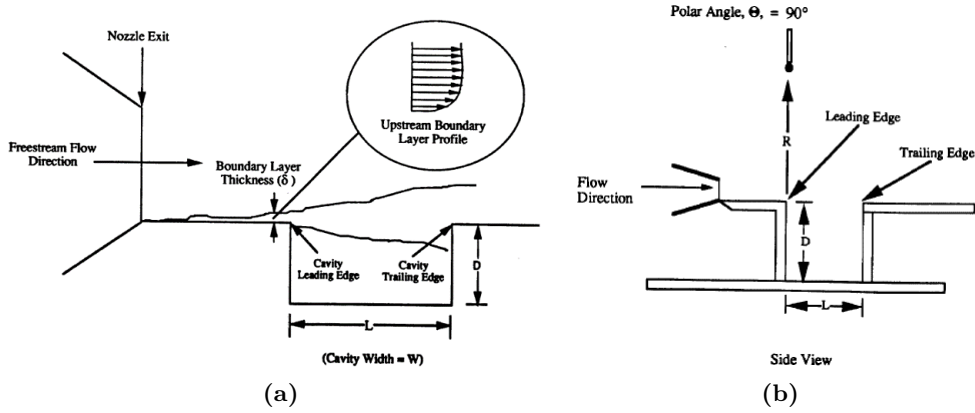
Figure 2.16: Experimental set up used by Ahuja and Mendoza [49]. (a) Upstream boundary layer approaching the cavity. (b) Microphone position.

2.2.4   Effect of cavity geometry on flow characteristics

A number of studies have been performed on the effects of cavity geometry parameters on the flow charateristics, both experimentally and computationally. Plentovich et al. [37] compared phenomena of cavity flows for the transonic/subsonic and supersonic regimes. They found a similar effect of the geometry on the pressure distribution on the cavity floor and on the cavity flow field between subsonic/transonic and supersonic cases, as shown in Figures 2.17. These figures show that with increasing L/D, the mean pressure downstream of the cavity leading edge becomes lower and a negative value occurs when it becomes transitional-open, whereas the mean pressure upstream of the cavity trailing edge increases. Furthermore, differences were found in the location of the peak pressure on the open cavity rear wall. The position was located near the trailing edge of the cavity for supersonic flow, with the particular locations depending on the flow regime.
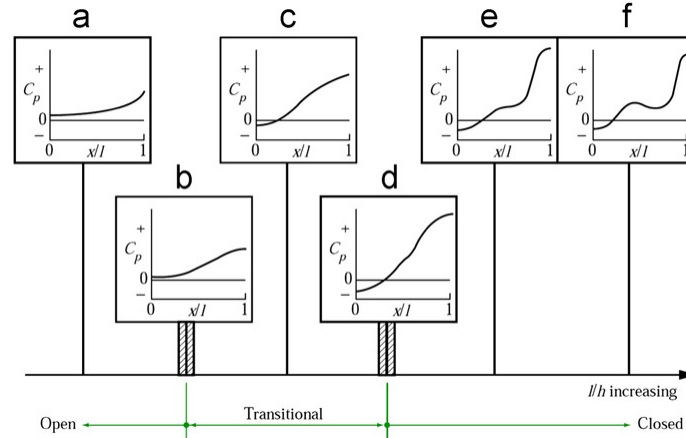
Figure 2.17: Pressure distribution on cavity floor for various types at subsonic and transonic flow speeds. Reproduced from ESDU [42], and original graphs from Plentovich et al. [37].

More recently, Ng [40] investigated the characteristics of transitional cavity flow at a low speed of 10 m/s (Mach number 0.029) using a subsonic wind tunnel. Results are summarised in Table 2.2. In the study, the cavity length was kept constant, while the depth was changed to obtain different L/D to give different flow region. This study attempted to distinguish between the transitional-open and the transitional-closed cavity flow regimes. Coefficients of mean pressure ($C_p = \frac{p_{mean}-p_\infty}{0.5\rho U^2}$, where p_{mean} is the mean pressure, p_∞ is the static pressure in the freestream, ρ is the density and U is the freestream velocity) and pressure fluctuation ($C_p' = \frac{p_{rms}}{0.5\rho U^2}$, where p_{rms} is the root-mean square pressure) on the cavity wall were shown. These helped to identify differences in the transitional cavity flow characteristics. It was stated that the average C_p distribution on the cavity aft wall for a transitional-open cavity showed a linear tendency with distance from the cavity floor, whereas for a transitional-closed cavity the average C_p distribution exhibited a non-linear trend. Furthermore, the distribution of C_p' for a transitional-open cavity showed a distinctive peak at the trailing edge of the cavity. On the other hand, the C_p' distribution in the floor of a transitional-closed cavity showed an additional low secondary peak near the leading edge.
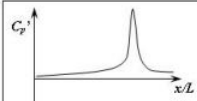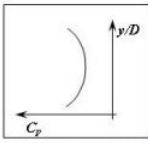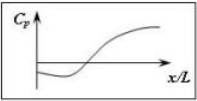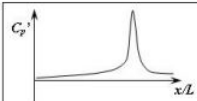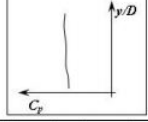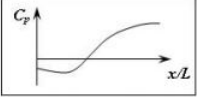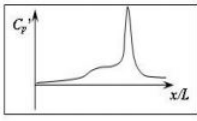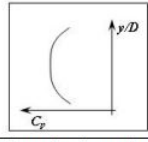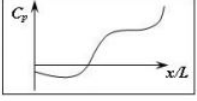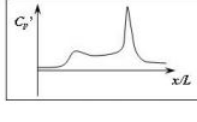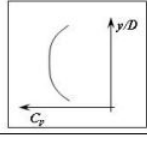
Ng [40] also provided instantaneous flow visualisations of four types of cavity using PIV as shown in Figure 2.18. Figure 2.18(a) shows the flow features of an open cavity. The shear layer bridges across the cavity and a vortex is observed within the cavity. Ng [40] stated that the shear layer was fluctuating in the downstream region of the cavity and this affected the formation of the vortex.

In the transitional-open cavity flow regime, unsteady flow in the cavity increased and the shear layer impingement occurred on the cavity trailing edge and the cavity downstream wall, as shown in Figure 2.18(b). Due to the impingement, the C_p distribution on the cavity downstream wall becomes higher than that for the open cavity and is relatively uniform (see

Table 2.2).

In the transitional-closed cavity in Figure 2.18(c), the shear layer impinges on the down-stream bottom edge and the direction of the shear layer is slightly downward. Furthermore, the shear layer reattaches intermittently on the cavity floor. Despite this, an inflection in the distribution of C_p cannot be seen for $0.4 < x/L < 1$, whereas such an inflection in C_p is seen for the closed cavity in Figure 2.18(d). The shear layer directly impinges on the cavity floor for the closed cavity flow regime. This slightly increases the pressure fluctuation (C_p') on the cavity floor at $0.4 < x/L < 0.6$. This can be seen in Figure 2.19 which shows C_p' plotted against x/L for cavities with different values of L/D.

Table 2.2: Distributions of C_p and C_p' on cavity floor and aft wall for different cavity flow regimes [40].

	Criteria for flow regime		
	Shape of C_p curve	Shape of C_p' curve	Shape of C_p curve over the rear face
Open cavity flow regime. (*L/D* < 6.5)	Concave up in the aft portion of the cavity.	No secondary peaks present.	With local minimum point.
Transition-open cavity flow regime. (6.5 < *L/D* < 10)	Concave down in the aft portion of the cavity.	No secondary peak present.	Relatively linear in shape.
Transition-closed cavity flow regime. (10 < *L/D* < 15)	Concave down in the aft portion of the cavity.	Slight secondary peak present.	With a local maximum point.
Closed cavity flow regime. (*L/D* > 15)	Inflection point present.	Secondary peak present	With a local maximum point.
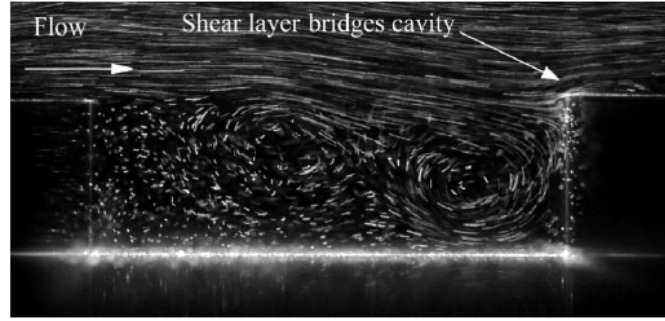
(a) Open cavity
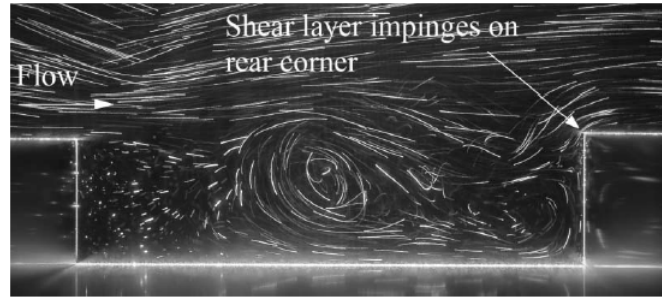
(b) Transitional-open cavity
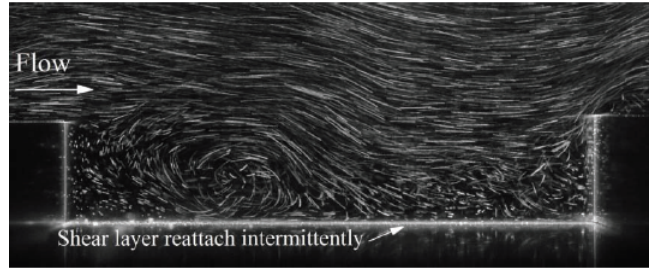
(c) Transitional-closed cavity
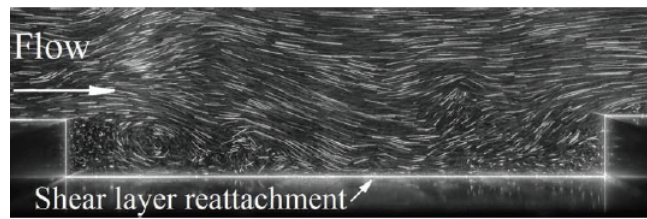
(d) Closed cavity

Figure 2.18: Instantaneous flow features obtained using PIV giving an indication of the shear layer impingement points for different types of cavities [40]. (L/D values were not given for each figure).
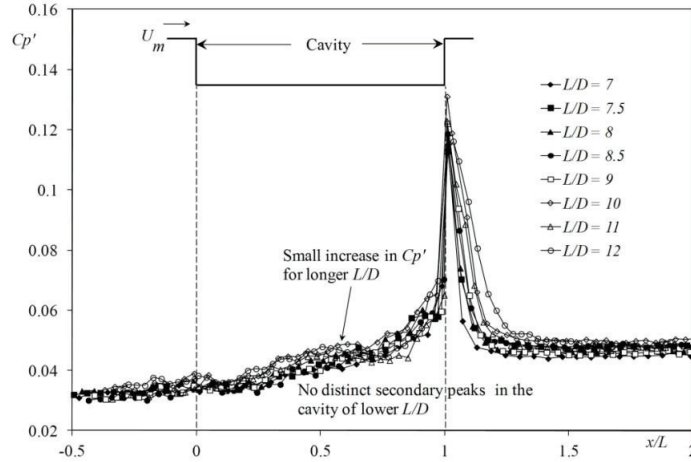
Figure 2.19: Distribution of coefficient of pressure fluctuation for different types of cavities [40].

Yang et al. [51] investigated the effect of the length-to-depth ratio L/D and the width-to-depth ratio W/D of cavities using low-speed wind tunnel tests. They tested various cavities with different values of L/D. They showed that as the value of L/D is increased, the SPL of the fluctuating wall pressure at the bottom centre of the cavity increases; the difference in maximum SPL measured at the centre point of the cavity floor for $L/D =$ 12 was 15 dB greater than for $L/D = 2$ for a constant cavity depth. Furthermore, the effect of flow velocity was tested at Mach numbers 0.03 to 0.14. The coefficient of mean pressure at the bottom of the cavity was not affected by increasing velocity, whereas the noise increased by 25 dB at $M = 0.14$ compared with that at $M = 0.03$. The results showed that the flow patterns do not seem to be affected by the flow velocity. Moreover, the effect of the W/D ratio was investigated, and when this ratio increased from $W/D = 1$ to W/D = 2 (for constant D), there was a large increase in the noise radiation by approximately 10 dB.

Tracy and Plentovich [53] measured the SPL at the cavity wall at subsonic and transonic speeds (Mach number from 0.2 to 0.95). It was found that, as the value of the length-to-depth ratio decreased, an initially non-resonant cavity gradually generated resonances with increasing peak amplitudes. Moreover, the resonance frequencies were reduced as L is increased.

The cavity geometry effects were investigated for supersonic flow by Stalling and Wilcox [36]. They showed different phenomena for open and closed cavity flows. For open cavity flow, the distribution of pressure along the cavity floor was shown to be uniform, and the pressure increased slightly at the downstream wall region.

A numerical study aimed at reducing noise from an open cavity at Mach number 1.5 and 2.5 was carried out by Zhang et al. [54]. They modelled two types of cavity leading edge

modifications (a compression ramp and an expansion surface) as shown in Figure 2.20. They showed that the compression ramp at the cavity leading edge gave a reduction of the SPL on the cavity wall at Mach number 2.5, but the change in SPL was negligible at Mach number 1.5. When the leading edge was modified as an expansion surface, this configuration reduced the SPL on the cavity wall at both Mach numbers.
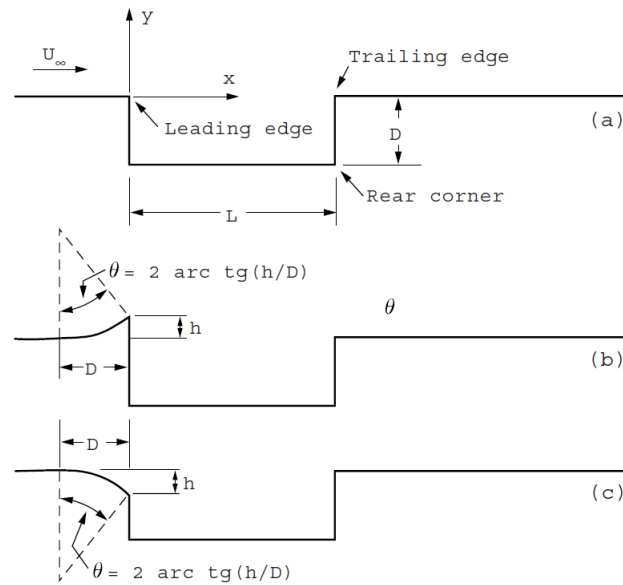
Figure 2.20: Numerical test geometry used by Zhang et al. [54]: (a) baseline; (b) compression ramp type; (c) expansion surface.

2.2.5 Cavity flow and noise studies

Wang et al. [55] investigated the mechanism of buffeting noise from an automobile sunroof with a simplified cavity model using CFD simulations at speeds of 15 m/s to 50 m/s and a wind tunnel test at speeds of 15 m/s to 25 m/s. They found that the sunroof buffeting noise is likely to be an open cavity noise mechanism. The sunroof buffeting noise occurs due to the periodicity of flow separation and vortex shedding from the leading edge of the cavity and vortex impingement on the trailing edge. These cause a feedback tone and fluid-resonant tone. Henderson [56] also found a similar noise mechanism from studies of automobile door gap cavities at low Mach numbers ($M = 0.058$ to $M = 0.18$). The cavity flow behaviour shows oscillation, which causes radiated noise when the flow passes over the cavity. Studies on cavity flow typically involve complex flow-sound-vortex interaction, unsteady characteristics and shear layer instability.

2.3   Summary

From the literature review, although there is some evidence that the pantograph recess causes high levels of noise, it has been found that there is a lack of knowledge of the mechanisms of noise generation from the pantograph recess, the effect of cavity flow on the radiated noise from the pantograph and suitable noise reduction techniques. Furthermore, most cavity noise research has focused on open cavities so that very few of the studies have investigated closed cavities that are more typical of the pantograph recess, which generally has $L/D = 11$. Therefore, this research will be devoted to an investigation of various cavity configurations, including cases containing two pantographs, in a subsonic flow regime (83.3 m/s corresponding to $M = 0.24$) in order to find the mechanism of noise generation of the pantograph recess, and the effect of the cavity flow on the pantograph noise.

Chapter 3

Methodology

This chapter presents the CFD simulation method used in this study and introduces the governing equations, including the continuity and Navier-Stokes (N-S) equations, and the turbulence modelling. The far-field noise prediction method, using the FW-H equation based on Farassat's Formulation 1A [78–80], is also described.

3.1 Governing equations

Turbulent flow fields can be solved with the N-S equations consisting of continuity, momentum and energy equations, which are given in tensor notation as:

$$\frac{\partial \rho}{\partial t} + \frac{\partial \rho u_i}{\partial x_i} = 0 \tag{3.1}$$

$$\frac{\partial \rho u_i}{\partial t} + \frac{\partial \rho u_j u_i}{\partial x_j} = -\frac{\partial p}{\partial x_i} + \frac{\partial \tau_{ij}}{\partial x_j} \tag{3.2}$$

$$\frac{\partial E_T}{\partial t} + u_j \frac{\partial E_T}{\partial x_j} = \dot{q} + \frac{1}{\rho}\left[\frac{\partial}{\partial x_j}(k\frac{\partial T}{\partial x_j}) - p\frac{\partial u_j}{\partial x_j} + u_j \frac{\partial \tau_{ij}}{\partial x_j} \right] \tag{3.3}$$

where ρ is the density of the fluid, t is time and the vectors u_i and x_i are the flow velocity and position, respectively. p is the pressure, μ is the dynamic viscosity, $\dot{q}$ is the heat transferred per unit time and area by thermal conduction, T is the temperature, k is thermal conductivity and E_T is total energy; δ_{ij} is the Dirac delta function ($\delta_{ij} = 1$ when $i = j$ and $\delta_{ij} = 0$ otherwise). τ_{ij} is the stress tensor, defined as:

$$\tau_{ij} = \left[2\mu\left(S_{ij} - \frac{1}{3}S_{kk}\delta_{ij} \right) \right] \tag{3.4}$$

where S_{ij} is the rate-of-strain tensor.

$$S_{ij} = \frac{1}{2}\left(\frac{\partial u_i}{\partial x_j} + \frac{\partial u_j}{\partial x_i}\right) \ \text{ with } \ S_{kk} = \frac{\partial u_k}{\partial x_k}. \tag{3.5}$$

For the typical operational speed of modern high-speed trains, the Mach number is generally less than 0.3, which allows the flow to be treated as incompressible [57]. The flow can therefore be considered as incompressible, which means the density is constant. Thus, Equation (3.1) reduces to the following:

$$\frac{\partial u_i}{\partial x_i} = 0 \tag{3.6}$$

Furthermore, since thermodynamic effects are not considered, the energy equation can be ignored. If the flow is incompressible, $S_{kk} = 0$ in Equation (3.4) and the momentum equation can be reduced to:

$$\frac{\partial u_i}{\partial t} + u_j \frac{\partial u_i}{\partial x_j} = -\frac{1}{\rho}\frac{\partial p}{\partial x_i} + \frac{1}{\rho}\frac{\partial \tau_{ij}}{\partial x_j} \tag{3.7}$$

where τ_{ij} is the viscous stress tensor defined as:

$$\tau_{ij} = 2\mu S_{ij} \tag{3.8}$$

3.2   Turbulence models

In principle, Direct Numerical Simulation (DNS) can be used to solve the full time-dependent N-S equations and resolve the whole spectrum of turbulence scales. Thus, it would not require any turbulence models and could provide the highest accuracy results. However, in order to capture the smallest turbulence scale, a very fine mesh is essential. Therefore, the computational cost is too high so it is generally used only for research purposes rather than industrial problems. To overcome this limitation, turbulence models should be used.

3.2.1   Reynolds-Averaged Navier Stokes with Spalart-Allmaras model

In the Reynolds-Averaged Navier-Stokes (RANS) approach, averaged (or time-averaged) N-S equations are solved. In this approach, all turbulent scales are represented by a model. It is the most widely used approach for practical engineering applications as the computational cost are significantly reduced. It is possible to calculate time-varying solutions using unsteady RANS (URANS). These unsteady simulations might be able to capture some slow-varying mean flow unsteadiness, such as vortex shedding, but they are generally

incapable of capturing unsteadiness arising from turbulence. Furthermore, their accuracy for recirculation simulations, especially cavity flow, shows poor results [58].

The time-averaged N-S equation is given by:

$$\rho \frac{\partial U_i}{\partial t} + \rho \frac{\partial U_j U_i}{\partial x_j} = -\frac{\partial P}{\partial x_i} + \frac{\partial (\tau_{ij} - \rho \overline{u'_j u'_i})}{\partial x_j} \tag{3.9}$$

where U_i is the mean velocity, and P is the mean pressure. The new term $-\rho \overline{u'_j u'_i}$ is the Reynolds-stress tensor, where u'_i is fluctuating velocity and $\overline{(\cdot)}$ indicates time average. This makes it difficult to close the time-averaged N-S equation. Thus, the Reynolds-stress tensor should be represented by a model. The RANS model can be closed by assuming the Reynolds stress is linked with mean flow quantities, e.g. through the Boussinesq approximation:

$$\tau_{ij} = -\rho \overline{u'_j u'_i} = \mu_T \left(\frac{\partial U_i}{\partial x_j} + \frac{\partial U_j}{\partial x_i} \right) \tag{3.10}$$

where τ_{ij} is viscous stress tensor. In this research, the Spalart-Allmaras (S-A) one-equation turbulence model based on the kinematic eddy viscosity $\nu_T = \mu_T/\rho$ will be used [59]:

$$\frac{D\tilde{\nu}}{Dt} = c_{b1} \tilde{S} \tilde{\nu} - c_{w1} f_w \left(\frac{\tilde{\nu}}{d} \right)^2 + \frac{1}{\sigma_{\tilde{\nu}}} \left[\frac{\partial}{\partial x_j} \left\{ (\mu + \rho \tilde{\nu}) \frac{\partial \tilde{\nu}}{\partial x_j} \right\} + c_{b2} \left(\frac{\partial \tilde{\nu}}{\partial x_j} \right)^2 \right] - c_{w1} \rho f_w \left(\frac{\tilde{\nu}}{d} \right)^2 \tag{3.11}$$

where $\tilde{\nu}$ is the modified turbulent viscosity, defined by:

$$\tilde{\nu} = \frac{\nu_T}{f_{\nu 1}} \tag{3.12}$$

The damping functions are defined by [59]:

$$f_{\nu 1} = \frac{\chi^3}{\chi^3 + c_{\nu 1}^3} \tag{3.13}$$

$$f_{\nu 2} = 1 - \frac{\chi}{1 + \chi f_{\nu 1}} \tag{3.14}$$

$$f_w = g \left[\frac{1 + c_{w3}^6}{g^6 + c_{w3}^6} \right]^{1/6} \tag{3.15}$$

where $\chi = \frac{\tilde{\nu}}{\nu}$, $g = r + c_{w2}(r^6 - r)$, $r = \frac{\tilde{\nu}}{\tilde{S} k^2 d^2}$. The closure coefficients are defined by [59]:

$$c_{w1} = \frac{c_{b1}}{k^2} + \frac{1 + c_{b2}}{\sigma_{\tilde{\nu}}} \tag{3.16}$$

$$\tilde{S} = S + \frac{\tilde{\nu}}{k^2 d^2} f_{v2} \tag{3.17}$$

and the constants are given as $c_{w2} = 0.3, c_{w3} = 2, k = 0.41, c_{b1} = 0.1335, c_{b2} = 0.622, \sigma_{\tilde{\nu}} = \frac{2}{3}$.

3.2.2   Large Eddy Simulation with a subgrid-scale model

LES solves the spatially averaged N-S equations. It directly resolves large energy-containing eddies, whereas small eddies the size of which is smaller than the mesh, are modelled using a sub-grid scale (SGS) model [58]. Thus, it is affordable compared with DNS and can predict turbulent flow away from the walls. However, LES still requires large computational resources due to the requirement for a very fine grid spacing in regions near the walls in order to achieve a high accuracy [60].

The LES models use a spatially filtered N-S equation where only smaller eddies are represented by a turbulence model. For incompressible flow, it can be defined as follows:

$$\frac{\partial \bar{u}_i}{\partial t} + \frac{\partial \bar{u}_i \bar{u}_j}{\partial x_j} = -\frac{1}{\rho} \frac{\partial \bar{p}}{\partial x_j} + \frac{\partial}{\partial x_j} \left(\nu \frac{\partial \bar{u}_i}{\partial x_j} \right) - \frac{\partial \tau_{ij}^{SGS}}{\partial x_j} \tag{3.18}$$

where:

$$\tau_{ij}^{SGS} = \overline{u_i u_j} - \bar{u}_i \bar{u}_j \tag{3.19}$$

These SGS stresses resulting from the space filtering operation need to be modelled. The purpose of the SGS model is to avoid accumulating energy and to help dissipate the energy at small scales. In this study, the Smagorinsky-Lilly SGS model [58] is used and the stress term τ_{ij} can be redefined in terms of the mean velocity vector:

$$\tau_{ij}^{SGS} - \frac{1}{3} \tau_{kk}^{SGS} \delta_{ij} = -2(C_s \Delta)^2 |\bar{S}| S_{ij} \tag{3.20}$$

where the grid spacing Δ is $\max(\Delta x, \Delta y, \Delta z), \bar{S} \equiv \sqrt{2 S_{ij} S_{ij}}$, S_{ij} is defined in Equation (3.4), and C_s is a Smagorinsky constant with a value between 0.1 and 0.2.

3.2.3   Detached Eddy Simulation

In order to achieve a reasonably high accuracy at reduced computational cost, a hybrid RANS-LES method called DES will be considered. This hybrid modelling approach combines the benefits of RANS and LES while minimising their disadvantages. It is useful to be able to relax the strong LES mesh constraints close to the wall. A sufficient number of grid points should be provided with a moderate expansion ratio in the direction normal to the wall to resolve the boundary layer [58, 60]. Near the walls, the URANS equation with the S-A model is used to represent the flow. By contrast, the LES with a one-equation model

for the SGS viscosity is used in regions dominated by large turbulence scales.

In order to employ the RANS model in parallel with the LES model, the two models are unified with a smooth interface by switching the length scale in the transport equation and the RANS model is used for modified eddy viscosity.

In DES, the length scale is replaced by:

$$l_{\mathrm{DES}} = d - f_d \mathrm{min}(d, C_{\mathrm{DES}}\Delta) \tag{3.21}$$

The eddy viscosity can be defined in the Smagorinsky-Lilly model by:

$$\mu_{sgs} = \rho(C_s\Delta)^2|\bar{S}| \tag{3.22}$$

where d is the distance to the wall, C_{DES} is a constant taken equal to 0.65 and $f_d = f(\nu_t, \nu, S_{ij}, k, d)$.

When $d < C_{\mathrm{DES}}\Delta$, the model will employ URANS mode to resolve the ensemble-averaged flow field and when $d > C_{\mathrm{DES}}\Delta$, LES will be used to calculate the filtered flow field. A hybrid RANS-LES method will be suitable for the current study, taking into account limitations on computational resources.

The DES method has some limitations within the attached boundary layer and unsteady turbulent structure development between the URANS and LES model. In the case of an ambiguous grid with high aspect ratios in the boundary layer, grids may be fine enough to activate the DES limiter to LES-mode, but not fine enough to support resolved fluctuating velocities within the boundary layer and this issue produces early separations, a so-called grid-induced separation [60].

As a result, the DES method has been improved by Spalart et al. [61] leading to the Delayed Detached Eddy Simulation (DDES) method. In this model, the DES length scale $\tilde{d}$ is redefined as:

$$\tilde{d} = d - f_d \mathrm{max}(0, d - C_{\mathrm{DES}}\Delta) \tag{3.23}$$

where d is the distance to the wall, f_d is delay function, given by:

$$f_d = 1 - \tanh([8r_d]^3) \tag{3.24}$$

where r_d is a parameter related to the eddy-viscosity and is defined as:

$$r_d = \frac{\nu_t + \nu}{\sqrt{U_{i,j}U_{i,j}}k^2 d^2} \tag{3.25}$$

where ν_t is the turbulent kinematic eddy viscosity, ν the molecular viscosity, $U_{i,j}$ is the velocity gradient, k is the Von Karman constant. The parameter r_d equals 1 away from the boundary layer, and falls gradually to 0 towards the edge of the boundary layer. if the function f_d equals 1 this yields the LES mode, while 0 finds the RANS mode. Later it was found that DDES may cause logarithmic-layer mismatch, resulting under-prediction of the skin friction [62]. Shur [62] introduced Improved DDES (IDDES) in order to solve this problem by using a new length-scale, combining the DDES and the Wall-Modeled LES (WMLES), is defined:

$$l_{\mathrm{IDDES}} = \widetilde{f}_d(1 + f_e)l_{\mathrm{RANS}} + (1 - \widetilde{f}_d)l_{\mathrm{LES}} \tag{3.26}$$

where $l_{\mathrm{RANS}} = d$, $l_{\mathrm{LES}} = C_{\mathrm{DES}}\Delta$, and $\widetilde{f}_d$ is a modified version of the DDES f_d blending function, is defined by:

$$\widetilde{f}_d = \max[(1 - f_{dt}), f_B] \tag{3.27}$$

where f_{dt} is delay function, define as $f_{dt} = 1 - \tanh[(8r_{dt})^3]$ and f_B is the empirical blending function, which provides switching of the model from RANS mode (when $f_B = 1.0$) to LES mode (when $f_B = 0$) within the range of wall distance $0.5\Delta < d < \Delta$, and and f_e is elevating-function, defined by [62]:

$$f_B = \min[2\exp(-9\alpha^2), 1.0] \ \text{ with } \ \alpha = 0.25 - d/\Delta \tag{3.28}$$

$$f_e = \max[(f_{e1} - 1), 0]f_{e2} \tag{3.29}$$

where:

$$f_{e1} = \begin{cases} 2\exp(-11.09\alpha^2) & \text{if } \alpha \geq 0 \\ 2\exp(-9\alpha^2) & \text{if } \alpha < 0 \end{cases} \tag{3.30}$$

$$f_{e2} = 1.0 - \max(f_t, f_l) \tag{3.31}$$

with

$$f_t = \tanh[(C_t^2 r_{dt})^3] \tag{3.32}$$

$$f_l = \tanh[(C_l^2 r_{dl})^{10}] \tag{3.33}$$

where C_t and C_l are constant, given as $C_t = 1.63$ and $C_l = 3.55$, r_{dl} and r_{dt} are parameters and are defined as:

$$r_{dt} = \frac{\nu_t}{k^2 d^2 \max\{\sqrt{\sum_{i,j}(\partial u_i/\partial x_j)^2}, 10^{-10}\}} \tag{3.34}$$

$$r_{dl} = \frac{\nu}{k^2 d^2 \max\{\sqrt{\sum_{i,j}(\partial u_i/\partial x_j)^2}, 10^{-10}\}} \tag{3.35}$$

For unsteady inflow turbulent content simulation, $r_{dt} \ll 1$, and f_{dt} is close to 1. Consequently, $\widetilde{f_d}$ is equal to f_B, Equation 3.26 is written as:

$$l_{\text{IDDES}} = l_{\text{WMLES}} = f_B(1 + f_e)l_{\text{RANS}} + (1 - f_B)l_{\text{LES}} \tag{3.36}$$

This allows the WMLES mode to be activated within the boundary layers. When f_e is equal to 0, and Equation 3.26 is written as:

$$l_{\text{IDDES}} = l_{\text{DDES}} = \widetilde{f_d}l_{\text{RANS}} + (1 - \widetilde{f_d})l_{\text{LES}} \tag{3.37}$$

This acts in DDES mode near the wall. In the present work the IDDES model is used.

3.3   Numerical schemes

A second-order central difference method, based on the Taylor series, is used in the current work to evaluate the spatial derivatives of equations (3.7). The central difference scheme used to evaluate the spatial derivative of a scalar function $f = \frac{dy}{dx}$ at point i, at time step n can be expressed as [63, 64]:

$$\frac{\partial y}{\partial x} \approx \left.\frac{dy}{dx}\right|_{x_i} = \frac{y_{i+1}^n - y_{i-1}^n}{2\Delta x} \tag{3.38}$$

This can be rearranged to obtain y_{i+1}^n from y_i^n:

$$y_{i+1}^n = y_{i-1}^n + 2\Delta x f(y_i^n, x_i) \tag{3.39}$$

For the temporal discretization, a second-order accuracy implicit backward Euler method is employed [64, 65]:

$$\frac{\partial y}{\partial t} \approx \left.\frac{dy}{dt}\right|_{t_{n+1}} = \frac{y_i^{n+1} - y_i^n}{\Delta t} \tag{3.40}$$

This can be rearranged in order to obtain y_i^{n+1} from y_i^n:

$$y_i^{n+1} = y_i^n + \Delta t f(y_i^{n+1}, t_{n+1}) \tag{3.41}$$

In order to resolve the governing equations using the above schemes, the algorithm PIMPLE is employed. This is a combination of SIMPLE (Semi-Implicit Method for Pressure-Linked Equation) and PISO (Pressure Implicit with Splitting of Operator) methods [66]. The SIMPLE algorithm evaluates the convective fluxes per unit mass through cell faces from guessed velocity components. The guessed pressure field is used to solve the momentum equation. A pressure correction equation is solved to gain a pressure correction field and to update the velocity and pressure fields. To begin the iteration process, initial guesses for the velocity and pressure fields are made. The process is iterated until the velocity and pressure fields converge. On the other hand, the PISO method solves a pressure correction equation and when the corrections are obtained, the velocity components are solved. Combining the two methods allows a large-time step to be used and less computational cost with robust convergence behaviour [66, 67]. Figure 3.1 describes the PIMPLE algorithm in the CFD procedure.
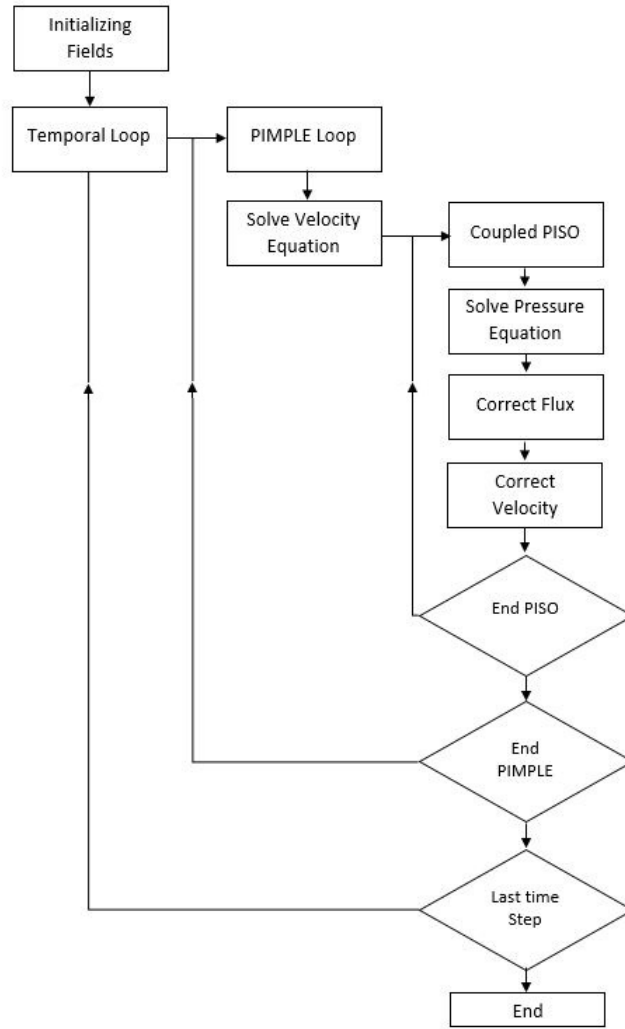
Figure 3.1: The PIMPLE algorithm [66]

3.4 Boundary conditions

In mathematical terms, there are two types of numerical boundary conditions: a value specified (or Dirichlet) and a flux specified (or Neumann) boundary conditions. The Dirichlet boundary condition prescribe the value of the variable on the boundary and the Neumann prescribe the gradient of a variable normal to the boundary. For incompressible flow, boundary conditions are velocity inlet boundary, pressure outlet boundary, no-slip wall, symmetry boundary and periodic boundary.

3.4.1   Velocity inlet

The inlet boundary is usually used when velocity distributions and fluid properties are known. The velocity field at the inlet is imposed (fixed value boundary condition) as $\mathbf{u} = \mathbf{U}(x, y, z)$, and used to calculate the inlet volume flux and the momentum flux.

3.4.2   Pressure outlet

The pressure outlet boundary is an outflow condition which prescribes the working pressure. The fixed value boundary condition is applied for the pressure. In normal outflow conditions, the values of all other variables such as velocity normal to the boundary are extrapolated from the interior of the domain on the assumption of zero gradient at the outlet plane.

3.4.3   Symmetry

The scalar flux normal to the boundary is set to zero and there is no flow across the boundary. velocities normal to the boundary are set to zero at the symmetry boundary. Furthermore, the values of all other properties from the cells adjacent to the boundary are projected to the boundary face, equivalent to zero normal gradient.

3.4.4   Periodic

A periodic boundary condition is applied when an infinite homogeneous flow field is approximated. To apply this boundary condition, the coupled boundaries are directly liked in the system. The flux of all variables adjacent to one periodic boundary is used to the flux entering the opposite periodic boundary.

3.4.5   No-slip wall

A wall boundary is regarded as an impermeable surface (solid region). For the no-slip conditions, the fluid attaches to the wall and the fluid velocity is zero at the wall.

3.5   Far-field noise prediction

3.5.1   Lighthill's analogy

To predict noise from turbulent flow, Lighthill [68] proposed an acoustic analogy in 1952. The analogy relates the non-linear fluid equation to the linear acoustic wave equation. This allows the sound radiated by turbulent flow in a fluid to be determined from flow modelling results, which serve as equivalent sources for far-field prediction. It is widely used for flow-generated noise analysis, i.e. jet noise. Lighthill's equation converts the compressible N-S equation into an exact inhomogeneous wave equation. This shows that source terms are important only within the turbulent region. In Lighthill's analogy, the fluid mechanical

process acts as an acoustic source.

To derive Lighthill's wave equation, first taking the time derivative of the mass conservation law (Equation (3.1)):

$$\frac{\partial}{\partial t}\left(\frac{\partial \rho}{\partial t} + \frac{\partial}{\partial x_i}(\rho u_i)\right) = 0 \tag{3.42}$$

Then the divergence of the momentum equation (Equation (3.2)):

$$\frac{\partial}{\partial x_i}\left(\frac{\partial}{\partial t}(\rho u_i) + \frac{\partial}{\partial x_j}(P_{ij} + \rho u_j u_i)\right) = 0$$
$$\implies \frac{\partial^2}{\partial t \partial x_i}(\rho u_i) = \frac{\partial^2}{\partial x_i \partial x_j}(P_{ij} + \rho u_j u_i) \tag{3.43}$$

Subtract Equation 3.42 from Equation 3.43 to give

$$\frac{\partial^2 \rho}{\partial t^2} = \frac{\partial^2}{\partial x_i \partial x_j}(P_{ij} + \rho u_j u_i) \tag{3.44}$$

where $P_{ij} = p\delta_{ij} - \tau_{ij}$ is the compressive stress tensor. $\rho = \rho_0 + \rho'$ is the density. Only the fluctuation of the density ρ' is variable with time. Hence, ρ in the left-hand term can be replaced by ρ', and by subtracting the term $c_0^2 \frac{\partial^2 \rho'}{\partial x_i^2}$ from both sides of the equation, Equation (3.44) can be reformulated to give:

$$\frac{\partial^2 \rho'}{\partial t^2} - c_0^2 \frac{\partial^2 \rho'}{\partial x_i^2} = \frac{\partial^2 T_{ij}}{\partial x_i \partial x_j} \tag{3.45}$$

where c_0 is the sound speed of the undisturbed medium, and T_{ij} is Lighthill's stress tensor. This stress tensor plays a major role in generating sound and can be written as:

$$T_{ij} = P_{ij} + \rho u_j u_i - (c_0^2 \rho' + p_0)\delta_{ij} \tag{3.46}$$

where p_0 is the atmospheric pressure and δ_{ij} is the Kronecker delta.

Equation (3.46) can be re-written using $c_0^2 \frac{\partial^2 \rho'}{\partial x_i^2} = \frac{\partial^2 c_0^2 \rho' \delta_{ij}}{\partial x_i \partial x_j}$ and $P_{ij} = p\delta_{ij} - \tau_{ij}$:

$$T_{ij} = \rho u_j u_i - \tau_{ij} + (p' - c_0^2 \rho')\delta_{ij} \tag{3.47}$$

where τ_{ij} is the viscous stress tensor, and $p' = p - p_0$. From Equation (3.46), it can be seen that the Lighthill stress tensor consists of three terms which produce noise. The first term is the Reynolds stress $\rho u_i u_j$, which is nonlinear. This occurs within the rotational source

region, such as the turbulent region. The second term is the viscous stress tensor τ_{ij}, which can be neglected in most flows at low Mach numbers. When there is no unsteady heat source in the fluid, the entropy source can be also negligible. The last term $(p' - c_0^2 \rho')\delta_{ij}$, is the surplus of momentum transfer through the pressure compared with a linear fluid with sound speed c_0 and density ρ_0. It occurs due to the variation of mean density and amplitude non-linearity of the wave in the source flow [68]. For low Mach number flow, the Lighthill stress tensor can be approximated by:

$$T_{ij} \simeq \rho u_i u_j \tag{3.48}$$

In order to solve Lighthill's wave equation (Equation (3.46)), the Green's function, which is the impulse response of the wave equation, can be used. It is the solution to:

$$\frac{\partial^2 G}{\partial t^2} - c_0^2 \frac{\partial^2 G}{\partial x_i^2} = \delta(\mathbf{x} - \mathbf{y})\delta(t - \tau) \tag{3.49}$$

In free space the Green's function can be written as:

$$G_0 = \frac{\delta(t - \tau - r/c_0)}{4\pi r c_0^2} \tag{3.50}$$

where r is the distance between source surface and observer point.

Using the above Green's function, the acoustic density perturbation can be obtained as:

$$\rho'(\mathbf{x}, t) = \int_{t_0}^{t} \iiint_V q(\mathbf{y}, \tau) G_0(\mathbf{x}, t|\mathbf{y}, \tau) \, d\mathbf{y} \, d\tau \tag{3.51}$$

By combining Equations (3.45) and (3.51) and using the free space Green's function G_0, the density perturbation can be defined as:

$$\rho'(\mathbf{x}, t) = \int_{-\infty}^{t} \iiint_V \frac{\partial^2 T_{ij}}{\partial y_i \partial y_j} G_0(\mathbf{x}, t|\mathbf{y}, \tau) \, d\mathbf{y} \, d\tau \tag{3.52}$$

As G_0 only consists of a function of $r = |\mathbf{x} - \mathbf{y}|$, then Equation (3.52) can be re-written as:

$$\rho'(\mathbf{x}, t) = \frac{\partial^2}{\partial x_i \partial x_j} \int_{-\infty}^{t} \iiint_V G_0(\mathbf{x}, t|\mathbf{y}, \tau) T_{ij}(\mathbf{y}, \tau) \, d\mathbf{y} \, d\tau \tag{3.53}$$

By combining Equation (3.50) and (3.53), the acoustic density perturbation at a far-field observer position $\mathbf{x}$ can be written as:

$$\rho'(\mathbf{x}, t) \simeq \frac{1}{4\pi c_0^2} \frac{\partial^2}{\partial x_i \partial x_j} \iiint_V \frac{T_{ij}(\mathbf{y}, t - |\mathbf{x} - \mathbf{y}|/c_0)}{|\mathbf{x} - \mathbf{y}|} \, d\mathbf{y} \tag{3.54}$$

in which the integration is performed over the volume of the domain V, where the sound sources are located.

3.5.2   Curle's theory for effects of solid bodies

Curle [69] extended the Lighthill analogy with additional source and force terms to include the influence of stationary solid boundaries. It is explained that when a solid object exists in a fluid, a sound wave radiated by a flow can be determined by the sum of Lighthill's quadrupole sound, which represent the noise generated by turbulent flow itself outside the solid surface, and sound due to dipole acoustic sources from the solid surface of the object. The Lighthill-Curle theory can be written as:

$$
\begin{aligned}
\rho'(\mathbf{x}, t) \simeq \ & \frac{1}{4\pi c_0^2} \frac{\partial^2}{\partial x_i \partial x_j} \iiint_V \frac{T_{ij}(\mathbf{y}, t - |\mathbf{x} - \mathbf{y}|/c_0)}{|\mathbf{x} - \mathbf{y}|} \, dV(\mathbf{y}) \\
& + \frac{1}{4\pi c_0^2} \frac{\partial}{\partial x_i} \iint_S \frac{P_i(\mathbf{y}, t - |\mathbf{x} - \mathbf{y}|/c_0)}{|\mathbf{x} - \mathbf{y}|} \, dS(\mathbf{y})
\end{aligned}
\tag{3.55}
$$

where $P_i = -n_j p_{ij}$, n_j is the unit outward normal on the surface, p_{ij} is the compressive stress tensor and S is the surface of the solid body.

3.5.3   Ffowcs Williams-Hawkings method for moving bodies

Ffowcs Williams and Hawkings [70, 71] further developed Curle's analogy to consider the influence of a moving solid surface in the fluid. This can be derived from the N-S and continuity equations. In order to take into account the effects of solid and porous surfaces with arbitrary motion, a Heaviside function $H(f)$ was introduced as:

$$
H(f) = \begin{cases} 1 & \text{for } f \geq 0 \\ 0 & \text{for } f < 0 \end{cases}
\tag{3.56}
$$

where $f = 0$ represents the surfaces. A new variable can be defined which vanishes within a finite volume V ($f < 0$) when any physical quantity is multiplied by the Heaviside function because $H(f) = 1$ in the fluid and $H(f) = 0$ inside the volume V. Multiplying the equations of mass conservation and momentum conservation by the Heaviside function, an equation can be derived as:

$$
H(f)\left[\frac{\partial \rho'}{\partial t} + \rho \frac{\partial u_i}{\partial x_i}\right] = 0
$$
$$
H(f)\left[\frac{\partial}{\partial t}(\rho u_i) + \frac{\partial}{\partial x_j}(P_{ji} + \rho u_j u_i)\right] = 0
\tag{3.57}
$$

By subtracting the divergence of the momentum equation from the time derivative of the continuity equation and using $\frac{\partial}{\partial t} H(f) = -\mathbf{v} \cdot \nabla H(f) = -\mathbf{v} \cdot \mathbf{n} \delta(f)$, where $\mathbf{v}$ is the velocity

of the moving surface, and $\mathbf{n}$ gives the unit outward normal vector to the surface. The following Ffowcs Williams-Hawkings (FW-H) equation can be obtained as:

$$
\frac{\partial^2}{\partial t^2}(\rho' H(f)) - c_0^2 \nabla^2 (\rho' H(f)) = \frac{\partial^2}{\partial x_i \partial x_j}\{[\rho u_i u_j - \tau_{ij} + (p' - c_0^2 \rho')\delta_{ij}]H(f)\}
$$
$$
+ \frac{\partial}{\partial t}\{[\rho(u_j - v_j) + \rho_0 v_j]n_j \delta(f)\} \qquad (3.58)
$$
$$
- \frac{\partial}{\partial x_i}\{[\rho u_i(u_j - v_j) + p'\delta_{ij} - \tau_{ij}]n_j \delta(f)\}
$$

From the above Equation (3.58), following some rearranging, the FW-H equation can be simplified as an differential form:

$$
\left(\frac{1}{c_0^2}\frac{\partial^2}{\partial t^2} - \nabla^2\right)(c_0^2 \rho' H(f)) = \frac{\partial^2}{\partial x_i \partial x_j}[T_{ij}H(f)] + \frac{\partial}{\partial t}[Q\delta(f)] - \frac{\partial}{\partial x_i}[F_i\delta(f)] \qquad (3.59)
$$

where $\delta(f)$ is the Dirac delta function, T_{ij} is given by Equation (3.47), Q is a monopole source term, given by $Q \equiv Q_j n_j = [\rho(u_j - v_j) + (\rho_0)v_j]n_j$ where u_j and v_j are the velocity components of the fluid and integration surface. F_i is a dipole source term, given by $F_i \equiv F_{ij}n_j = [\rho u_i(u_j - v_j) + (p - p_0)\delta_{ij} - \tau_{ij}]n_j$. These terms are for impermeable surfaces. The FW-H equation consists of three different source terms, identified as monopole (Q), dipole (F_i) and quadrupole sources (T_{ij}). The unsteady mass flux generates monopole sound which is generally referred to as thickness noise. The dipole noise source is generated by unsteady forces on the surface, which is generally known as loading noise. The quadrupole source, as found in Lighthill's analogy, is caused by nonlinearity and discontinuities in the fluid such as shock waves, wakes and vortices.

The integration form of Equation 3.59 can be obtained using the convolution of the free-space Green's function as:

$$
4\pi p'(\mathbf{x}, t) = \frac{\partial^2}{\partial x_i \partial x_j}\int_V \left[\frac{T_{ij}}{r(1 - M_r)}\right]_{ret} dy^3 + \frac{\partial}{\partial t}\int_S \left[\frac{\rho'(u_n - v_n) + \rho_0 u_n}{r(1 - M_r)}\right]_{ret} dS
$$
$$
+ \frac{\partial}{\partial x_i}\int_S \left[\frac{(p - p_0)\delta_{ij}n_j - \rho u_i(u_n - v_n)}{r(1 - M_r)}\right]_{ret} dS \qquad (3.60)
$$

where M_r is the Mach number in the observer direction, the brackets '$[\ ]_{ret}$' denote that

the quantities are evaluated at retarded time $\tau = t - |\mathbf{x} - \mathbf{y}|/c_0$, c_0 is the speed of sound, $r = |\mathbf{x} - \mathbf{y}|$ is the distance from a source point to the observer, u_n and v_n are the velocities of u_i and v_i projecting to the surface normal direction.

The FW-H equation is solved for far-field acoustic pressure by using the aerodynamic near-field data as input. As mentioned eailer, the FW-H analogy consists of two surface source terms, thickness (monopole) and loading (dipole) terms, and a volume source term, known as the quadrupole source. The quadrupole term can be neglected in general low subsonic applications because the contribution of this source is insignificant for low Mach number flow. This assumption has been used successfully for low Mach number flow noise predictions for high-lift devices [72, 73], aircraft landing gear [74, 75], and high-speed train noise prediction [76, 77]. The FW-H equation is solved to obtain the far-field acoustic pressure by using the aerodynamic near-field data as input.

Brentner and Farassat [78–80] developed the FW-H equations for use in predicting noise of subsonic motion, especially from helicopter rotors, to give an integral form. It is called Formulation 1A and expressed as follows:

$$p'(\mathbf{x}, t) = p'_T(\mathbf{x}, t) + p'_L(\mathbf{x}, t) \tag{3.61}$$

where $p'_T(\mathbf{x}, t)$ and $p'_L(\mathbf{x}, t)$ are the thickness and loading noise contributions respectively. In this study, as the integration surfaces are taken as the solid surfaces, $p'_T(\mathbf{x}, t) = 0$ and only loading noise contributions are considered, given by:

$$p'_L(\mathbf{x}, t) = \frac{1}{4\pi} \left(\frac{1}{c_0} \int_{f=0} \left[\frac{\dot{L}_r}{r(1 - M_r)^2} \right]_{ret} dS + \int_{f=0} \left[\frac{L_r - L_M}{r(1 - M_r)^2} \right]_{ret} dS \right.$$
$$\left. + \frac{1}{c_0} \int_{f=0} \left[\frac{L_r(r\dot{M}_r + c_0 M_r - c_0 M^2)}{r^2(1 - M_r)^3} \right]_{ret} dS \right) \tag{3.62}$$

with

$$L_r = L_i r_i \tag{3.63}$$

$$L_M = L_i M_i \tag{3.64}$$

$$L_i = P_{ij} n_i + \rho u_i (u_n - v_n) \tag{3.65}$$

$$P_{ij} = (p - p_0)\delta_{ij} - \sigma_{ij} \tag{3.66}$$

where M_i is the Mach number in the x_i direction and P_{ij} is the compressive stress tensor, σ_{ij} is the viscous stress tensor, and p_0 is ambient pressure.

URANS models can be used for noise predictions and are well established as numerical tools to satisfy industrial needs. However, these methods tend to under-predict the shear stress in the separated layer which may lead to inaccurate acoustic results. The URANS methods predict very regular oscillations for pressure perturbation with low amplitude compared with DES method [81, 82]. Furthermore, the URANS can predict discrete tone components but these can be associated with significant underestimation of the broadband noise level and also provide poor prediction at high frequency regions as only large-scale turbulent eddies are resolved [81, 82]. Therefore, hybrid RANS-LES methods are suitable for flow with large separations and noise prediction.

For the far-field noise prediction in this thesis, the solid surface term of the FW-H method based on Farassat's formulation 1A is used for all numerical cases. For near-field calculation of aerodynamic characteristics, the N-S equations are solved using the IDDES model using the software STAR-CCM+ and the Ffowcs Williams and Hawkings equations based on Farassat's Formulation 1A are implemented using the aeroacoustics module in STAR-CCM+.

Chapter 4

Experimental Validation

Experiments were carried out for both aerodynamic and aeroacoustic behaviours of a cavity in a wind tunnel and the ISVR's large anechoic chamber. The experimental results are analysed in order to validate the numerical methodology used. Furthermore, the methodology is also validated with other experiment results [37] for the near-field presence of the closed cavity and for the far-field pressure for an isolated pantograph [31]. All cases in this Chapter are listed in Table 4.1.

4.1 Pressure distribution on the cavity wall

4.1.1 Experimental set-up

The near-field experiments were carried out in the open wind tunnel in Boldrewood campus (Building 176) at the University of Southampton which provides a flow speed up to 38 m/s. An overall view of the wind tunnel is shown in Figure 4.1(a). It has a cross-section area of 0.6 m × 0.45 m. The cavity considered has a length $L = 0.36$ m and a depth $D = 0.0313$ m, giving $L/D = 11.5$, and a width $W = 0.125$ m, giving $W/D = 4$. The blockage ratio for the tested model is less than 1.5%. The upstream length from the wind tunnel nozzle to the cavity leading edge was $15D$ (0.525 m).

A removable cavity was installed in a base plate as shown in Figure 4.2. The material selected for both the base and the cavity was polymethly methacrylate, commonly known as acrylic plastic. A laser cutter machine was used to produce the cavity model including accurate size of holes (1.05 mm) for pressure taps. For the base, a precision drilling machine was used. The base was directly mounted on the bottom of the test section of the wind tunnel using bolts. The gaps between the edges of each component were sealed with tape to ensure flush-mounted and water-tight.

Table 4.1: Summary of the experimental and the numerical cases

Pressure distribution of cavity wall experimental cases		
Length-to-depth (L/D)	Velocity (m/s)	Re, based on D
11.5	10	2×10^4
11.5	20	4×10^4
11.5	30	6×10^4
Far-field noise of cavity experimental cases		
Length-to-depth (L/D)	Velocity (m/s)	Re, based on D
11.5	30	6×10^4
Numerical cases for validation		
Mesh $((\Delta x, \Delta z)_{max}/\Delta y)$	Velocity (m/s)	Re, based on D
120	30	6×10^4
200	30	6×10^4
300	30	6×10^4
500	30	6×10^4
Numerical cases for benchmark comparison of cavity floor pressure		
Mesh $((\Delta x, \Delta z)_{max}/\Delta y)$	Velocity (m/s)	Re, based on D
120	70.2	1.8×10^5
200	70.2	1.8×10^5
400	70.2	1.8×10^5
670	70.2	1.8×10^5
Numerical cases for pantograph far-field validation		
Mesh	Velocity (m/s)	Re, based on H
coarse	83.3	1.3×10^6
medium	83.3	1.3×10^6
fine	83.3	1.3×10^6

The current near-field measurements were carried out at three flow speeds, $U_\infty = 10$, 20 and 30 m/s (corresponding to $Re = 2 \times 10^4 - 6 \times 10^4$, based on the cavity depth). The mean pressure was obtained using an integrated pressure measurement device, the Scanivalve ZOC33. Stainless steel tubes with an outer diameter of 1.02 mm were flush mounted on the test rig (the cavity aft wall region) and the cavity floor. They were connected to the ZOC pressure scanner using rubber tubes as shown in Figure 4.1(d). 30 pressure taps were installed on the cavity floor and 20 on the aft wall. Before acquiring any data, air was allowed to flow in the tunnel for 5 seconds to avoid transient effects. A time signal of 10 s duration was acquired using a sampling frequency of 10 Hz. It is noted that the uncertainty of the pressure coefficient in the experimental is $\pm 0.15\%$. This uncertainty does not have an effect on the pressure distribution.
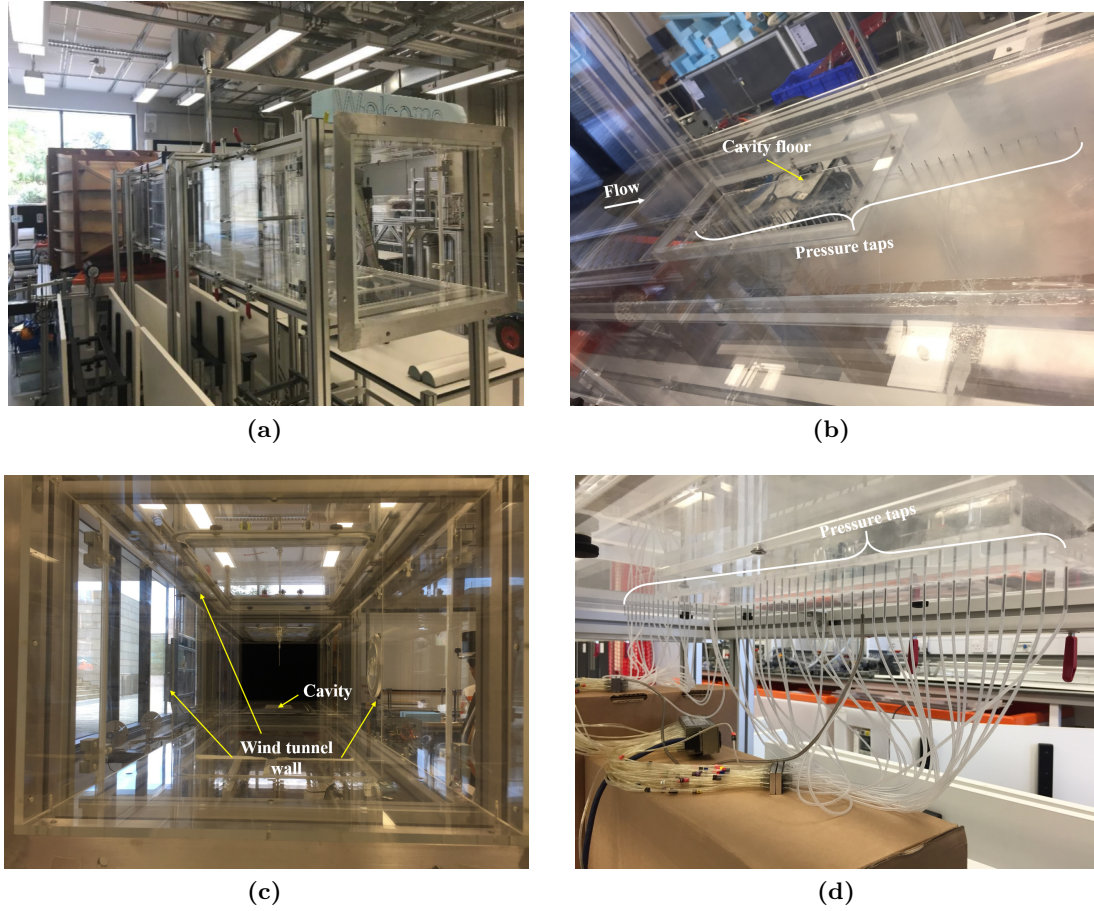
Figure 4.1: Experimental set-up for the pressure distributions measurements.
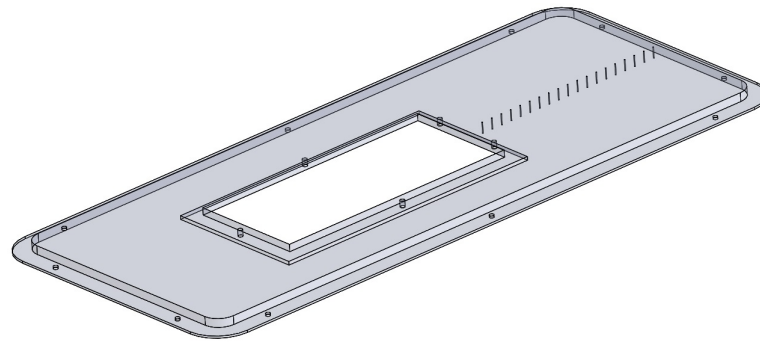
(a) Test rig
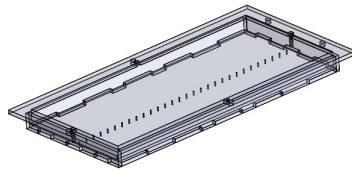
(b) Cavity
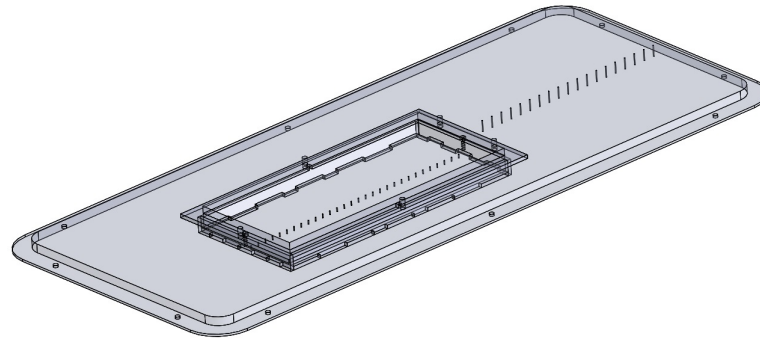
(c) Assembled model

Figure 4.2: The test rig and cavity model.

4.1.2   Numerical set-up

A numerical model was established in which the cavity has the same geometry (length, depth and width) as the wind tunnel model and the computational domain has the same height and width as the wind tunnel. A planar cavity is investigated. The computational domain extends $52D$ downstream of the cavity, $14.4D$ vertically and $7.1D$ laterally from the cavity edge to each side. An upstream length of $15D$ was used which is the same as the wind tunnel's upstream length. For the boundary conditions of the simulations, no-slip conditions are defined on all walls of the cavity and the floor; the two side and top boundaries of the domain are defined as slip-wall boundaries. An outflow boundary with zero gauge pressure

was used at the downstream boundary. A velocity inlet is specified at the inflow with a freestream speed of 30 m/s (corresponding to a Reynolds number $Re = 6 \times 10^4$ based on the cavity depth D).

In the present study, a hexa-dominant mesh was generated using the mesh generator of the commercial software STAR-CCM+ (called trimmed mesh in STAR-CCM+). For the purpose of the mesh dependence study, four meshes were generated with different mesh densities and sizes. Seven refinement blocks were used to generated the meshes with improved resolution in areas with strong flow variations and different cell sizes were applied for each refinement zone. As intensive turbulent and vortical flow are expected in the cavity region and at the cavity trailing edge, refined resolutions were used with a surface growth rate of 1.1 and a boundary layer stretching ratio of 1.12. The refinement zones and mesh are shown in Figure 4.3. As the S-A turbulence model is used in the near-wall region, it was ensured that y_1^+ values are limited to 1 along all solid walls [83], as shown in Figure 4.5; y_1^+ is the non-dimensional wall distance of the first off-wall grid points ($y_1^+ \equiv \frac{u_* y}{\nu}$, where u_* is the friction velocity, y_1 is the distance of the first grid point to the wall, and ν is the kinematic viscosity). The maximum Courant-Friedrichs-Lewy (CFL) number ($CFL = \frac{u \Delta t}{\Delta x}$, where u is the freestream velocity, Δt is the time step and Δx is the grid size in the streamwise direction) is set to 1 for simulation stability.

The strategy used in the mesh dependence study is that Δy, the first cell height from the wall, is kept constant whereas Δx and Δz, the cell lengths in the x-direction and the z-direction respectively, are refined. The maximum ratios of $(\Delta x, \Delta z)_{max}$ / Δy are given in Table 4.3 for each mesh along with the total number of cells.
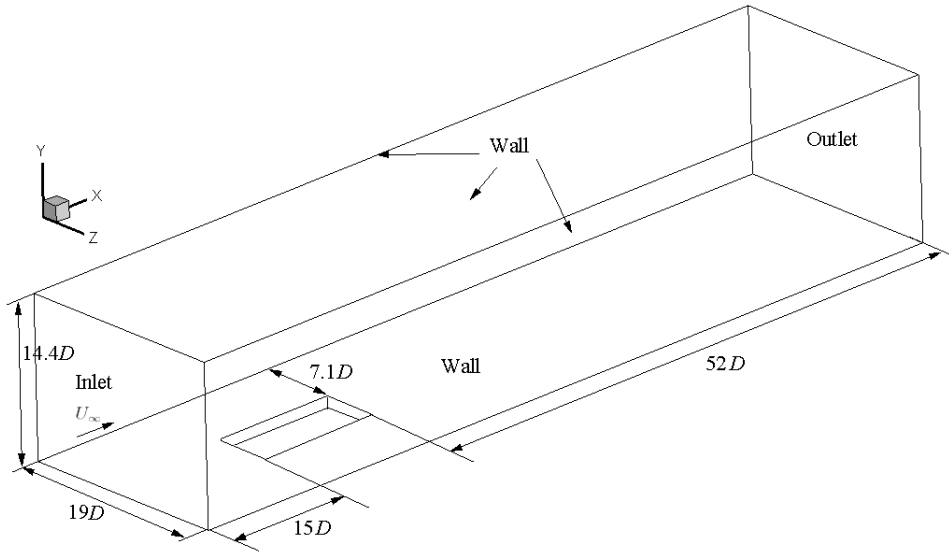
Figure 4.3: Computational domain and boundary conditions used for cavity model.

Table 4.2: The refinement zones and mesh criteria for each zone.

$(\Delta x,\ \Delta z)_{max}/\Delta y$	Refinement region	Number of zones	Min. cell size (mm)
120	Cavity leading edge	1	1.2
	Cavity trailing edge	2	1.2
	Cavity inside	1	1.2
	Cavity side edge	2	2
	Cavity overall	2	10
200	Cavity leading edge	1	2
	Cavity trailing edge	2	2
	Cavity inside	2	2
	Cavity side edge	2	3.5
	Cavity overall	2	10
300	Cavity leading edge	1	3
	Cavity trailing edge	2	3
	Cavity inside	2	3
	Cavity side edge	2	4
	Cavity overall	2	12
500	Cavity leading edge	1	5
	Cavity trailing edge	2	5
	Cavity inside	2	5
	Cavity side edge	2	4
	Cavity overall	2	12

Table 4.3: Mesh criteria for each cases for the cavity model.

	Coarse			Fine
$(\Delta x,\ \Delta z)_{max}/\Delta y$	500	300	200	120
Total number of cells	2 million	6 million	10 million	14 million
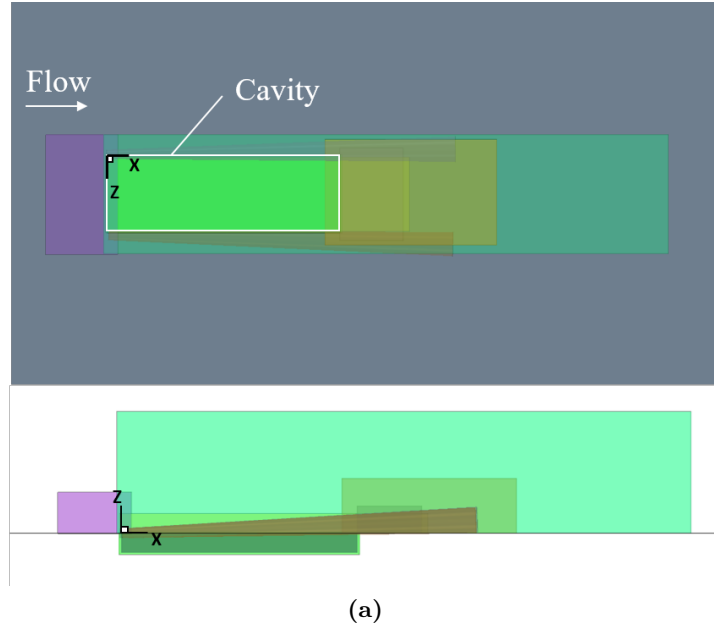
(a)
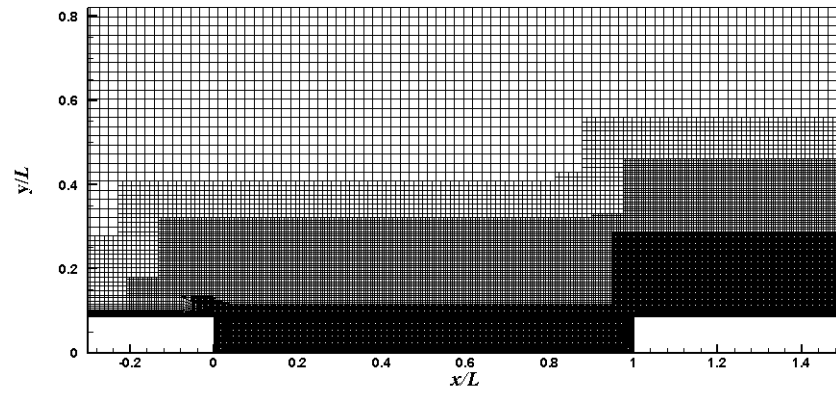
(b)

Figure 4.4: Mesh refinement zones (a) and overall mesh (b) for cavity model.
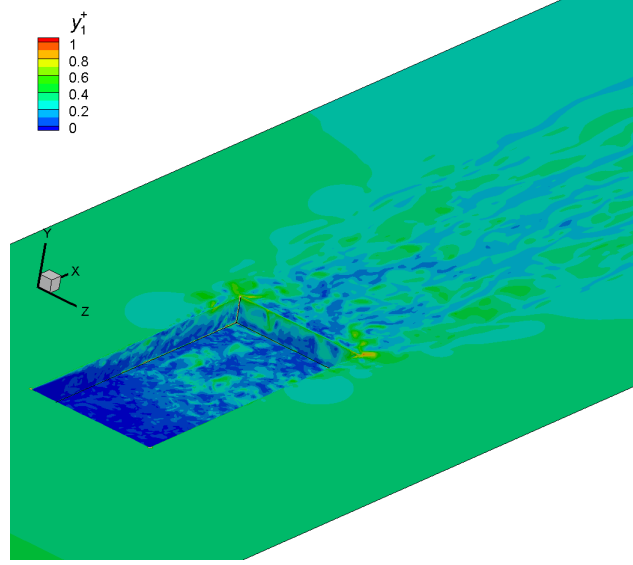
Figure 4.5: y_1^+ distribution of the cavity surface.

4.1.3   Experimental and numerical results

Figure 4.6 shows the measured mean pressure coefficient ($C_p = \frac{p - p_\infty}{\frac{1}{2}\rho_\infty U_\infty^2}$, where p is the surface pressure and p_∞ is the static pressure in the freestream) on the cavity floor and aft wall for three different freestream velocities. The origin of the physical coordinates is at the corner of the cavity leading edge as shown in Figure 4.4(a). In general, negative values of C_p appear at $x/L < 0.4$ and C_p increases rapidly for $x/L > 0.4$. The C_p of the cavity floor ($0 < x/L < 1$) decrease as increasing the flow speeds and there are large differences at $0.5 < x/L < 1$ between the results at different speeds. The coefficients of the pressure C_p on the aft wall ($1 < x/L < 1.6$) are similar for all three flow speeds.

The numerical results with four mesh resolutions are validated against the experimental results for $U_\infty = 30$ m/s as shown in Figure 4.7. The numerical results with the coarser mesh resolution $(\Delta x, \Delta z)_{max}/\Delta y \geq 300$ cannot provide a similar tendency on the surface pressure coefficient C_p of the cavity floor and aft wall compared to the experimental result. The numerical results of the cavity with the finer mesh aspect ratio $(\Delta x, \Delta z)_{max}/\Delta y = 120$ and 200 are similar to the experimental data and good agreements in C_p of the cavity floor and aft wall with experiment are demonstrated. Therefore, it is concluded that the current numerical procedure is able to give accurate prediction for flow over a cavity with adequate mesh resolution. Simulations conducted in the remainder of this mesh will have a mesh generated with similar resolution as the fine mesh aspect ratio $(\Delta x, \Delta z)_{max}/\Delta y = 200$.
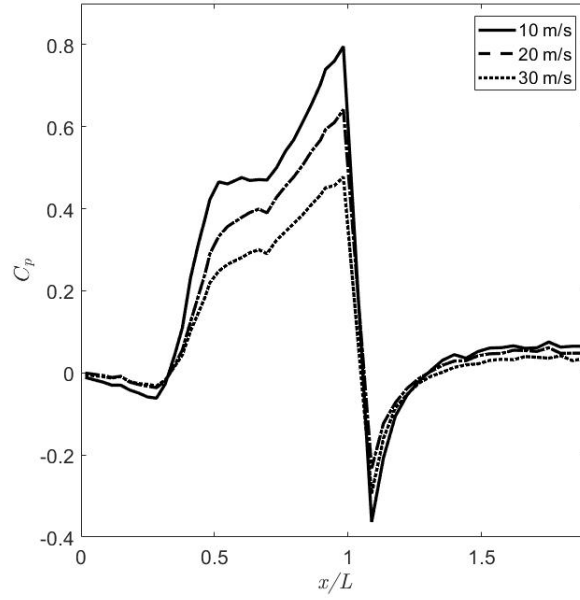
Figure 4.6: Mean pressure coefficient measured on cavity floor and aft wall at three different freestream velocities.
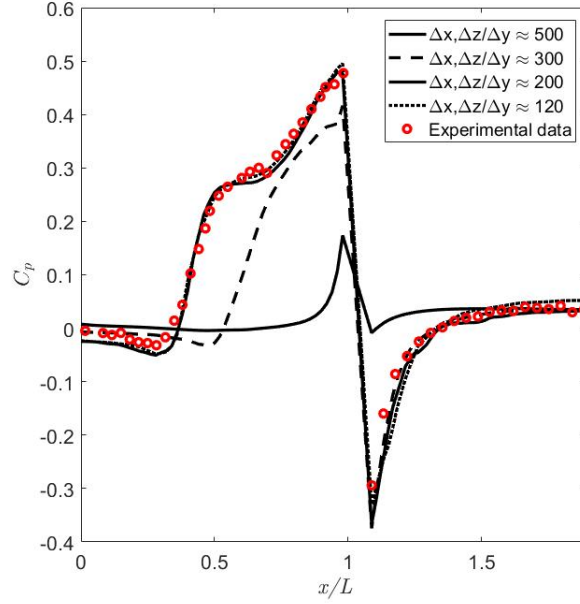
Figure 4.7: Comparison of the cavity floor and aft wall pressure distributions at $M = 0.09$ for numerical results and experimental results.

4.2   Far-field noise of the cavity

4.2.1   Experimental set-up

Far-field acoustic measurements were carried out in the ISVR's large anechoic chamber (8 m × 8 m × 8 m) for the same cavity model used in the previous wind tunnel tests measurements. As shown in Figure 4.8 an open jet wind tunnel is set up in the anechoic chamber. The rectangular nozzle is 0.35 m × 0.45 m. The facility provides a flow speed up to 40 m/s with low background noise and low turbulence intensity (0.1%). In the current work, measurements were performed at 30 m/s.

For this test, another plate was designed to attach to the nozzle and extend the flat region, as shown in Figure 4.9(a). The plate which held the cavity was attached to the bottom of the nozzle exit and also supported by two supports on the chamber floor. The plate was aligned with the bottom of the nozzle exit. In order to avoid interaction between the flow and supports, they were positioned away from the nozzle as shown in Figure 4.8(a). The cavity was positioned $15D$ away from the nozzle exit. The gaps between each component and the holes used for the pressure taps were sealed by using tape.

Eight microphones were placed in a plane parallel to the inflow direction and perpendicular to the cavity floor at a radial distance $R = 1.5$ m from the centre of the cavity floor. Three microphones were located at the side in a plane perpendicular to the inflow direction at $R = 1.2$ m and 0.1 m above the cavity floor. The microphones were distributed to cover a range of radiation angles, $\phi = 60°$ - $130°$ with an interval of $10°$ in the circumferential direction and $\theta = 60°$ - $120°$ with an interval of $30°$ in the azimuthal direction. A time signal of 10 seconds duration was acquired using a sampling frequency of 50 kHz. It is noted that the uncertainty of the SPL in the experimental is ±3%. This uncertainty does not have an effect on the spectrum trend.

4.2.2   Numerical set-up

The numerical domain and set-up are identical with the near-field numerical set-up in the previous Section. However, the test section excluded the wind tunnel top and side walls in these acoustic experiments and, therefore the boundary conditions of the top and two sides were set to symmetry, as shown in Figure 4.10. To calculate the far-field noise, the FW-H solver was used with the integration surface for the solver coinciding with the solid walls as discussed in Chapter 3. The sampling frequency for the far-field noise was 100 kHz.

(a)   (b)
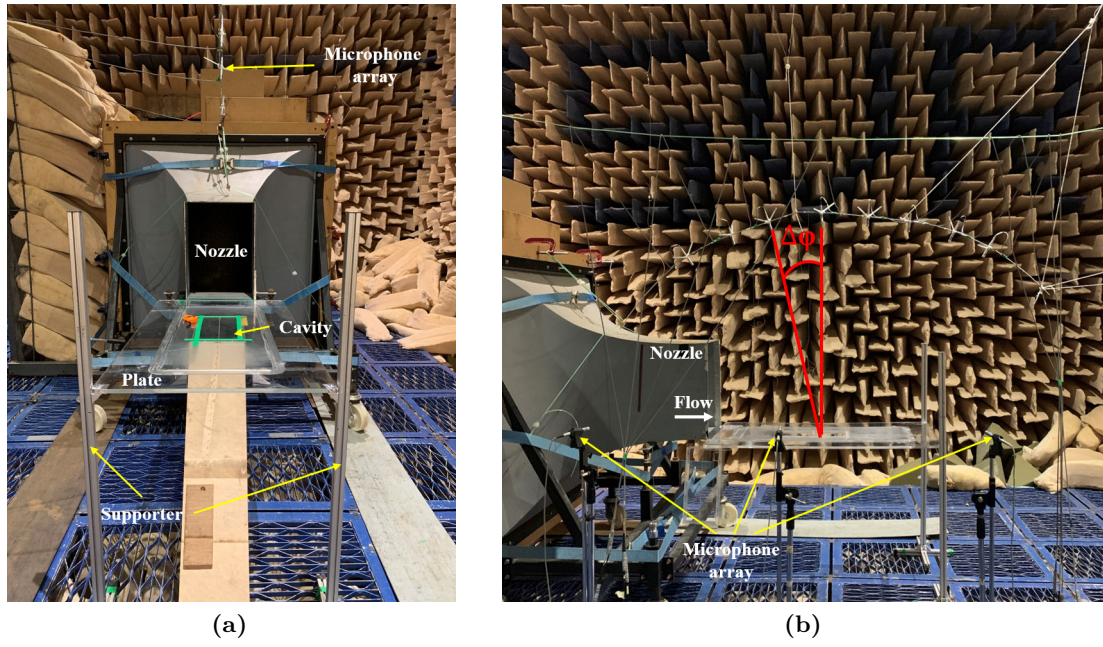
Figure 4.8: Experimental set-up for noise measurements.

(a)

(b)
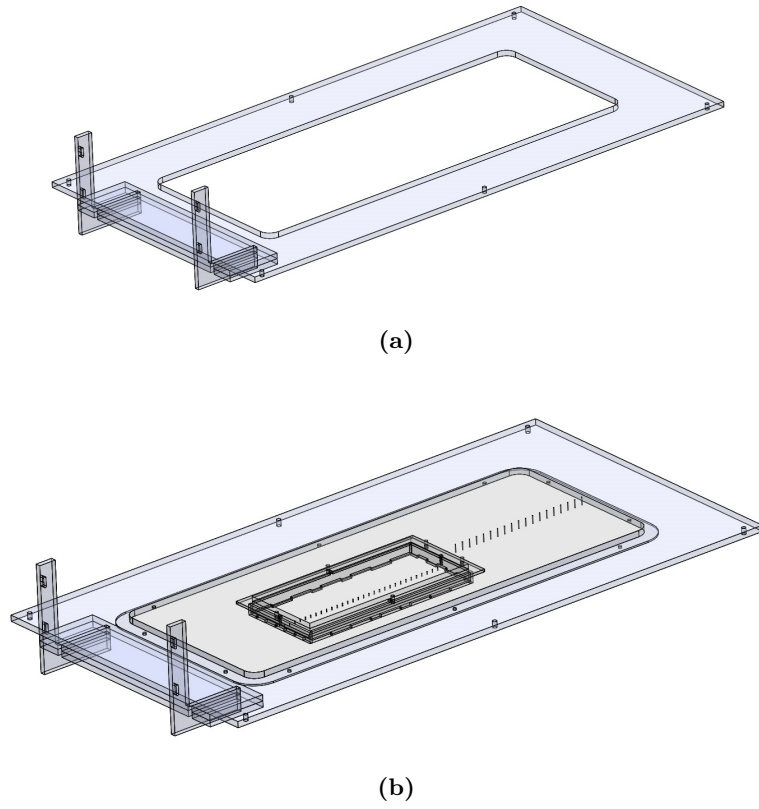
Figure 4.9: The test set-up for noise measurements of cavity.
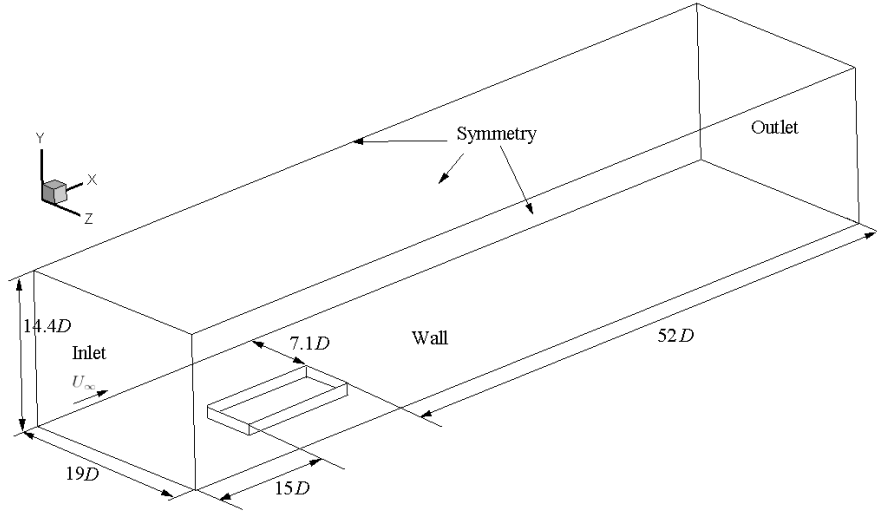
Figure 4.10: Computational domain and boundary conditions used for cavity model for far-field acoustic simulations.

4.2.3   Experimental and numerical results

The spectra for both experimental and numerical results are obtained by segmental average using a Hanning window with 50% overlap [92] and are shown as power spectral densities (PSDs). The background noise was measured when all the equipment was installed, except the cavity, which was replaced by a flat plate. The acoustic spectrum is corrected by subtracting the background noise, according to:

$$PSD_{corr} = 10\log_{10}(10^{\frac{\text{PSD}_{\text{origin}}}{10}} - 10^{\frac{\text{PSD}_{\text{BG}}}{10}}) \tag{4.1}$$

where, PSD_{origin} is the PSD in dB of the original measured noise and PSD_{BG} is the PSD in dB of the background noise. Figure 4.11 shows the noise spectra after correcting for the background noise for receivers at $\theta = 90°$ and $\phi = 90°$ for inflow speed of 30 m/s.

(a) $\theta = 90°$ **(b)** $\phi = 90°$
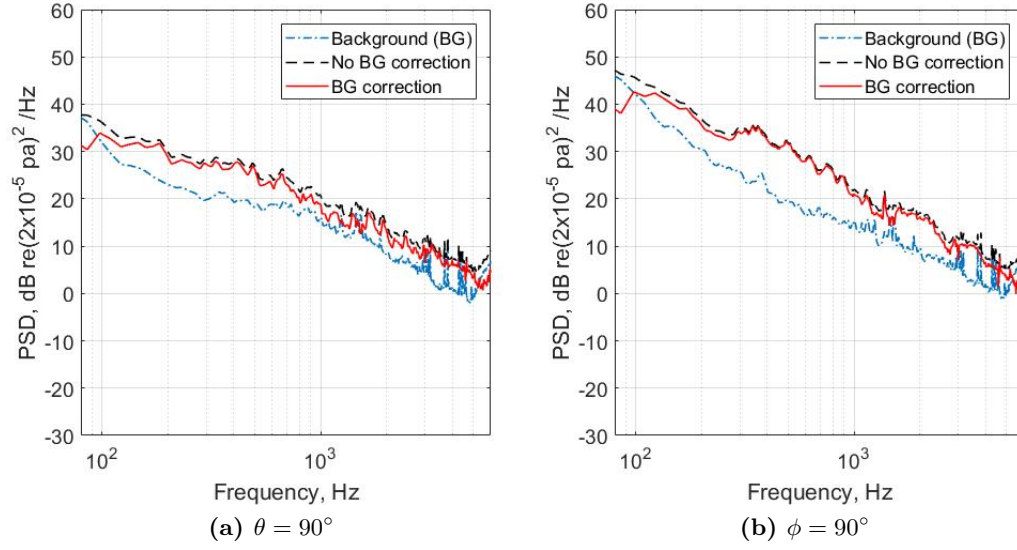
Figure 4.11: The spectra for the background noise and the noise radiated from the cavity with and without the background correction, (a) side position at $(x, y, z) =$(0.18 m, 0 ,1.563 m), (b) top position at $(x, y, z) =$(0.18 m, 1.2 m, 0).

Figure 4.12 shows a comparision of the numerical and experimental acoustic spectra at $\theta = 90°$ and $\phi = 90°$ for inflow speed of 30 m/s. In general, the PSDs of both the experimental and numerical data are broadband, and do not have any tonal components. The results for a cell aspect ratio of 500 poor agreement with the measurements. As the mesh densities are increased, the acoustic spectra are in good agreement with the experimental data in both of the side and top positions. However, the PSD from the mesh with the ratio 300 is slightly lower in the frequency region below 250 Hz at the side and below 200 Hz at top positions.
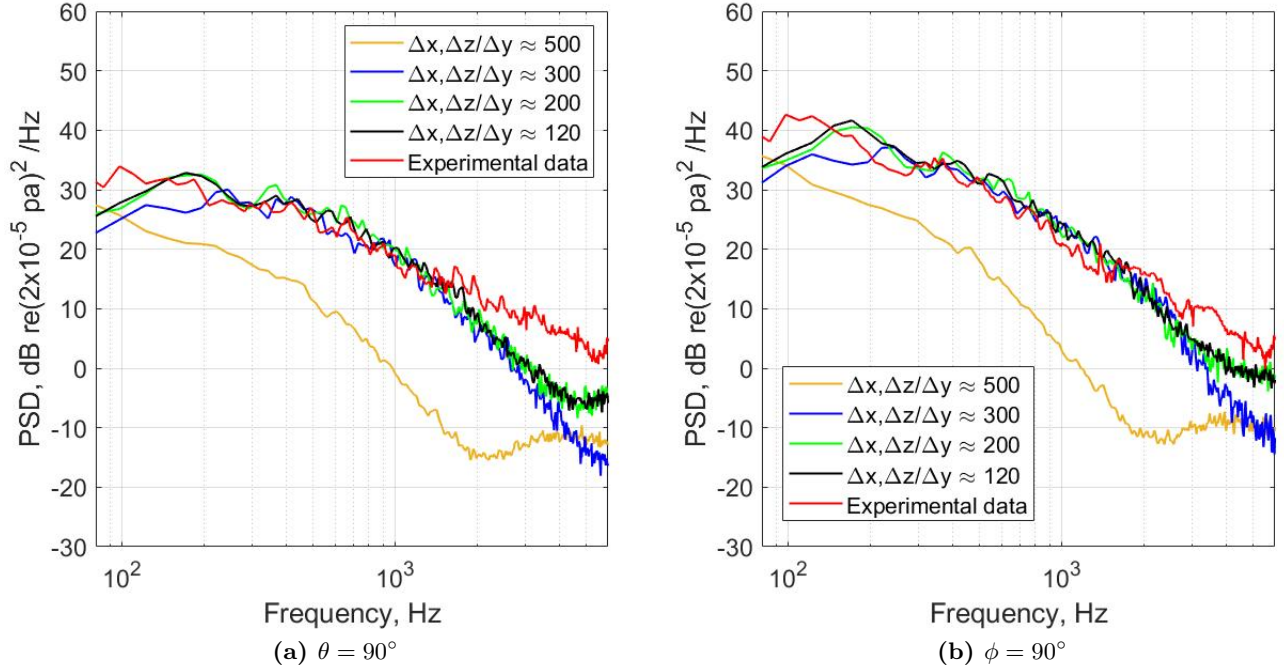
Figure 4.12: Comparisons of acoustic pressure spectra at different positions, (a) side position at $(x, y, z) =$(0.18 m, 0 ,1.563 m), (b) top position at $(x, y, z) =$(0.18 m, 1.2 m, 0).

Comparisons of the numerical and the experimental far-field acoustic directivity in the horizontal plane (a) and the vertical plane (b) are shown in Figure 4.13. The OASPL from both experimental and numerical data is calculated by integrating the mean-square pressure over the frequency range up to 6000 Hz. Good agreement is found in both Figure 4.13(a) and 4.13(b). The deviation of the level with the experiments is less than 2 dB and the maximum difference occurs at $\phi = 60°$. This may be due to the microphone at $\phi = 60°$ being located near the nozzle, which was not covered by acoustic foam so it might have caused extra noise due to retentions from the nozzle. The OASPL at the top position $\phi = 90°$ in Figure 4.13(b) is approximately 6.5 dB higher than that at the side at $\theta = 90°$ in Figure 4.13(a) in both the experimental and numerical results. This is mainly due to the noise spectra in the low frequency region as shown in Figure 4.12. For the side directivity, the maximum OASPL appears at $\theta = 60°$ for both the numerical and experimental data. For the top directivity, the maximum OASPL appears at $\phi = 110°$ in the numerical data, whereas for the experimental data, it is at $\phi = 60°$.

(a) Side directivity
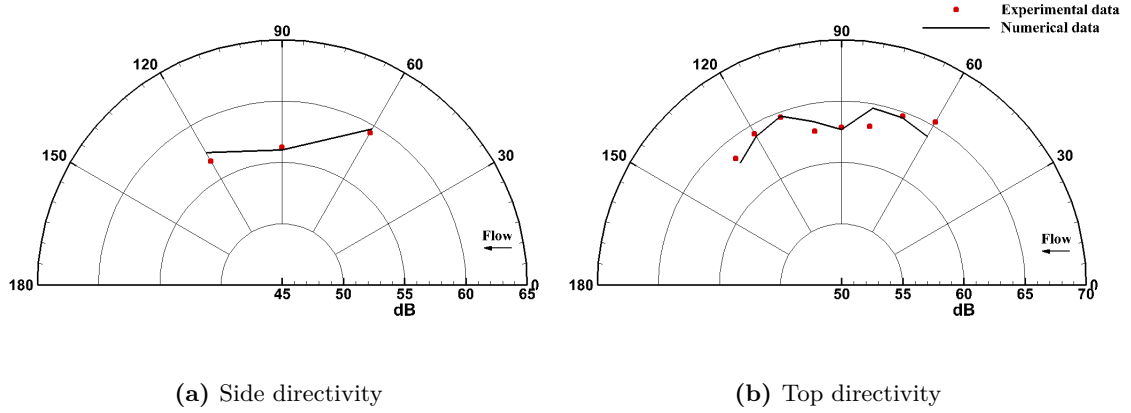
(b) Top directivity

Figure 4.13: Far-field acoustic directivity comparisons.

For the validation study, the maximum inflow velocity speed in the experiments is about 40 m/s due to safety reasons. Furthermore, the size of the cavity models was limited due to the wind tunnel size as well and the nozzle size for acoustic experiment hence the Reynolds number was limited in these validation studies. Therefore, validation studies are required at a higher Reynold number and carried out with the benchmark cases in the following section.

4.3 Benchmark comparison of cavity near-field pressure

In Sections 4.1 and 4.2, numerical results are validated and verified against experimental data in the comparisons of aerodynamic and acoustic characteristics at low Reynold number ($Re = 6 \times 10^4$). In this section, the numerical results of the cavity floor C_p are validated against other measurements at a higher Reynolds number ($Re = 1.8 \times 10^5$) [37].

The numerical procedure used is validated for a clean cavity against experiments of Plentovich et al. [37]. Plentovich et al. [37] investigated effect of the cavity length-to-depth ratio L/D on the cavity wall pressure distribution at Mach numbers of 0.2 to 0.95 using a transonic wind tunnel at NASA Langley. The cavities investigated had L/D ranging from 1 to 17.5. The test rig with a rectangular cavity was installed in the centre of the wind tunnel and the rig was supported by six supports. Furthermore, 128 static-pressure orifices with an inner diameter of 0.5 mm were used and connected to electronically scanned pressure (ESP) transducers from which the coefficient of pressure (C_p) was determined. It was ensured that the flow before the cavity leading edge was fully turbulent by using a strip in the upstream of the test rig. To validate the current calcuations, the case of a cavity with $L/D = 12$ and $W/D = 4$ at a Mach number $M = 0.2$ [37] was chosen because the geometry size and flow speed are similar to the current work. The simulations are carried out for this cavity and speed and compared with the experimental data [37].

4.3.1   Geometry and flow conditions

The cavity considered has a length $L = 0.731$ m and a depth $D = 0.061$ m, giving $L/D = 12$, and a width $W = 0.243$ m, giving $W/D = 4$. The computational domain is shown in Figure 4.14. It extends $36D$ downstream of the cavity, $16D$ vertically and $8D$ laterally from the cavity edge to each side. An upstream length of $12D$ was determined (and checked after the simulation was run) so that the computed boundary layer upstream of the cavity has approximately the same thickness ($\delta = 0.011$ m) as in the experiment ($\delta = 0.0125$ m) [37].
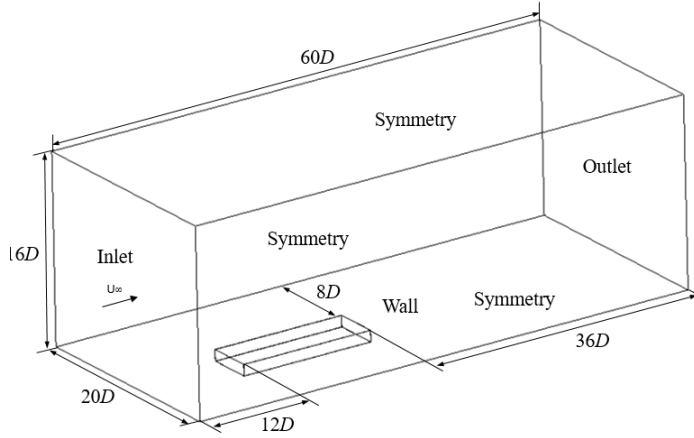
Figure 4.14: Computational domain and boundary conditions for validation study [37] (not to scale).

For the boundary conditions of the simulations, no-slip conditions are defined on all walls of the cavity and the floor; the two side and top boundaries of the domain are defined as symmetric boundaries. An outflow boundary with zero gauge pressure was used at the downstream boundary. A velocity inlet was specified at the inflow with a freestream Mach number of 0.2 (speed 70.2 m/s) corresponding to a Reynolds number of 1.8×10^5 based on the cavity depth.

The strategy of the mesh generation and refinement zones are the same as previous numerical validation case in Section 4.1, except the cell sizes for the refinement zones. Different cell sizes are applied for each refinement zone as summarised in Table 4.4. For the purpose of a mesh dependence study, four meshes were generated with different mesh densities. The strategy used in the mesh dependence study is the same as in Section 4.1. Δy, the first cell height from the wall, is kept constant whereas Δx and Δz, the cell lengths in the x-direction and the z-direction respectively, are refined. The maximum ratios $(\Delta x, \Delta z)_{max}$ / Δy are given in Table 4.4 for each mesh. y_1^+ values are limited to 1 along all solid walls. Figure 4.16 shows the y_1^+ distribution on the cavity surface, confirming that this criterion has been

achieved.

Table 4.4: The refinement zones and mesh criteria for each zone.

$(\Delta x,\ \Delta z)_{max}/\Delta y$	Refinement region	Number of zones	Min. cell size (mm)
120	Cavity leading edge	1	0.8
	Cavity trailing edge	2	0.8
	Cavity inside	1	0.8
	Cavity side edge	2	1.5
	Cavity overall	2	8
200	Cavity leading edge	1	1.2
	Cavity trailing edge	2	1.2
	Cavity inside	2	1.2
	Cavity side edge	2	2.5
	Cavity overall	2	9
400	Cavity leading edge	1	2.5
	Cavity trailing edge	2	2.5
	Cavity inside	2	2.5
	Cavity side edge	2	4
	Cavity overall	2	9
670	Cavity leading edge	1	4
	Cavity trailing edge	2	4
	Cavity inside	2	4
	Cavity side edge	2	4
	Cavity overall	2	9

Table 4.5: Mesh criteria for each cases for the cavity model.

	Coarse			Fine
$(\Delta x,\ \Delta z)_{max}/\Delta y$	670	400	200	120
Total number of cells	4 million	6 million	26 million	30 million

(a)

(b)
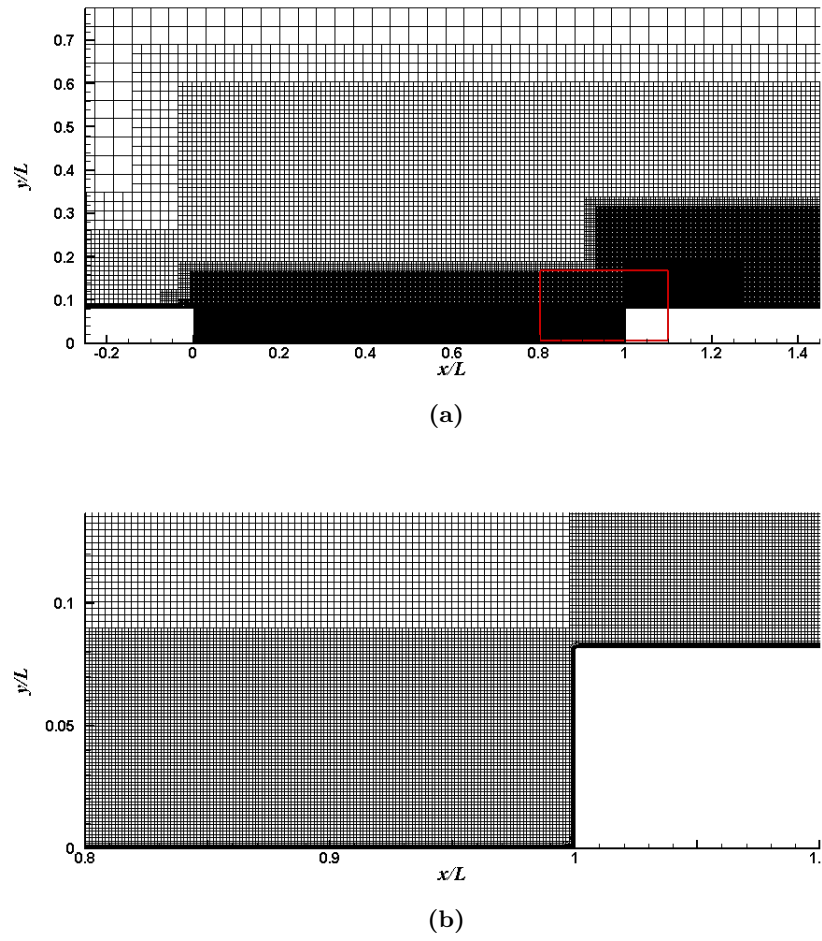
Figure 4.15: Overview (a) and detail (b) of the meshes for the cavity model i.e. aspect ratio 100.
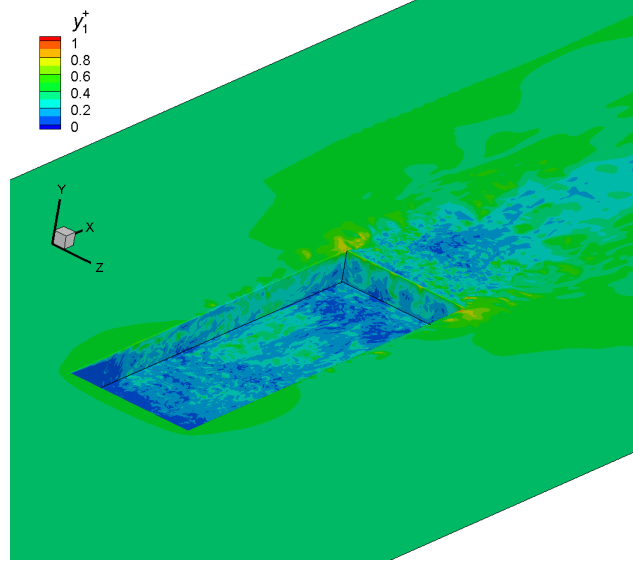
Figure 4.16: y_1^+ distribution of the cavity surface.

4.3.2 Validation of the numerical results

The mean surface pressure coefficients on the cavity floor calculated using the four meshes are compared with the experiment from [37] in Figure 4.17. As the mesh is refined (Δx / Δy, Δz / Δy become smaller), the pressure distribution converges. The distributions from the meshes with maximum cell aspect ratios 200 and 120 are in good agreement with the experimental data. Considering the balance between the accuracy of the result and the computational cost, the set-up based on the mesh aspect ratio 200 is chosen as the basis for generating meshes in subsequent chapters.
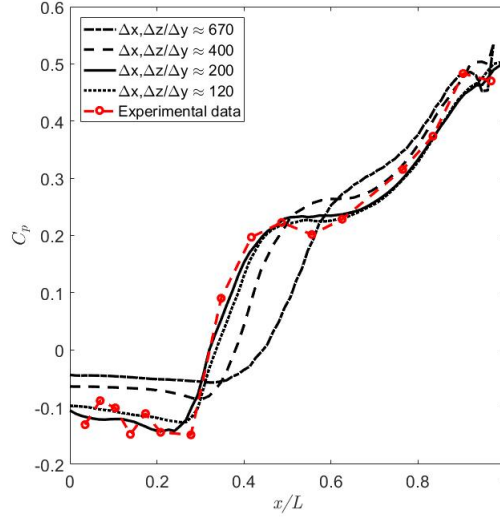
Figure 4.17: Comparison of the cavity floor pressure distributions at $M = 0.2$ from computational results using different meshes and experimental data [37].

4.4   Pantograph far-field validation

Prediction of the acoustic characteristic of the raised pantograph is also validated. To validate of the far-field acoustic pressure spectra for a raised DSA 350 pantograph, the calculated far-field sound pressure spectra are compared with measurements from a wind tunnel for a full scale DSA350 pantograph [31].

4.4.1   Geometry and flow conditions

Owing to the complexity of the actual pantograph, it is necessary to simplify its geometry to reduce the computational resource requirements. In the current study, most of the parts of the pantograph are retained, apart from small components such as straps, springs and wire arms. Table 4.6 gives a list of the retained and omitted parts of the pantograph. Figure 4.18 shows a comparison between actual pantograph model ((a) and (b)) used in the experiments [31] and the simplified model ((c) and (d)) used in the current simulations.

The computational domain is shown schematically in Figure 4.19. A velocity inlet is applied as inflow. The simulation is performed for a flow speed of 83.3 m/s (300 km/h). A hexa-dominated mesh is used for all cases, generated with several refinement zones. For the purpose of a mesh dependence study for the pantograph, three meshes were generated with different mesh densities and mesh sizes and different cell sizes are applied for each refinement zone as summarised in Table 4.7 and shown in Figure 4.20. Furthermore, 38 refinement regions were used for the pantograph, including regions around all components and in the wake of the panhead and the arms of the raised pantograph. All refinement

regions had a surface growth rate of 1.1. Furthermore, 14 - 30 prism layers were used to resolve the boundary layer near solid surfaces. The first layer non-dimensional wall distance y_1^+ is smaller than 1.0 as shown in Figure 4.21. A non-dimensional time step $U\Delta t/H = 0.00272$ is used, where H (0.245 m) is the height of the pantograph, which ensures that the CFL number is less than 1 for all cases.

(a) Overview   **(b)** Detail of the panhead

(c) Overview   **(d)** Detail of the panhead
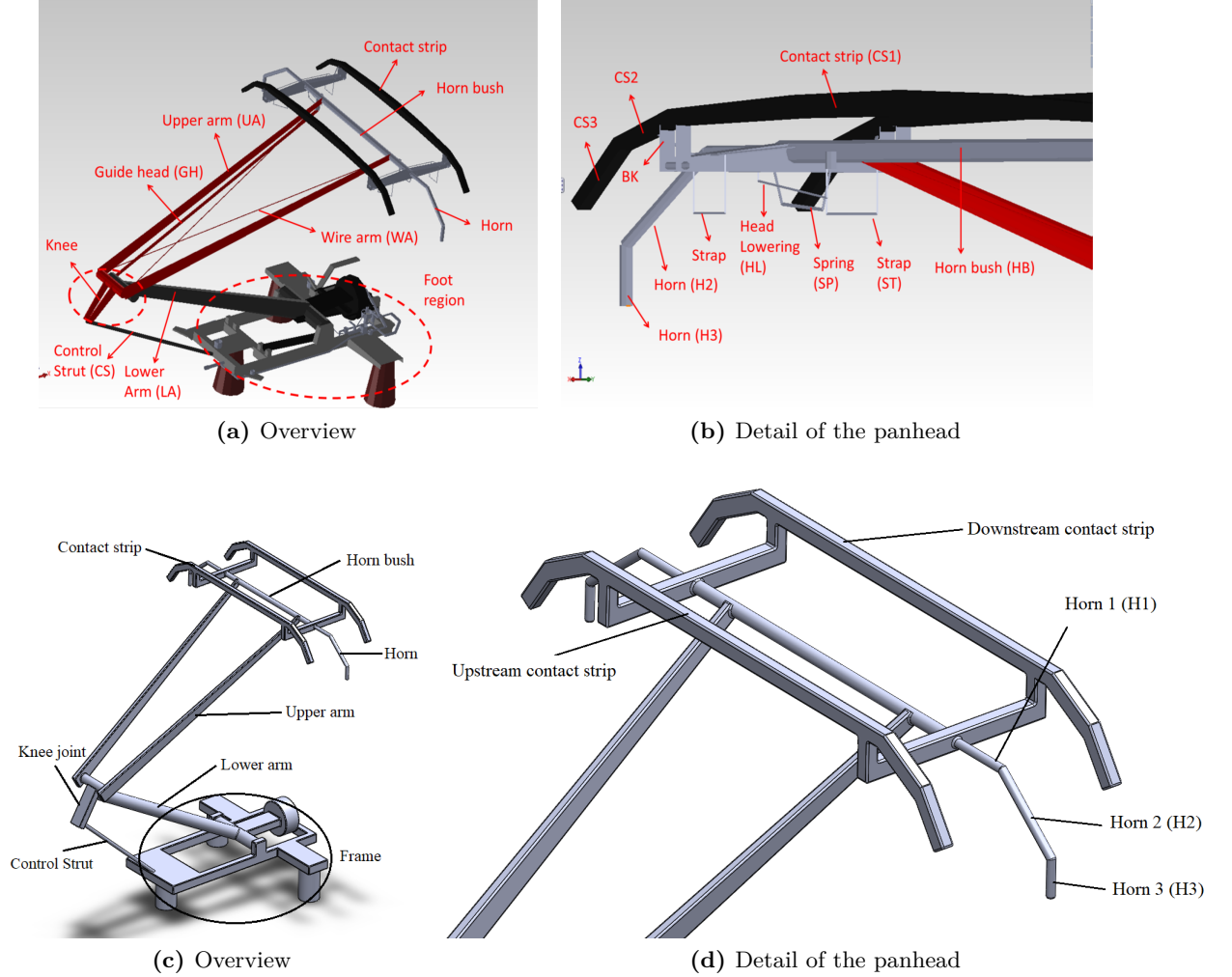
Figure 4.18: Comparison of the pantograph DSA350 model between the actual model ((a) and (b)) [31] and the simplified model ((c) and (d)).

Table 4.6: List of retained and omitted parts of pantograph.

Regions	Retained parts	Omitted parts
Panhead	Contact strip, horn bush, horn	Straps, head lowering, spring,
Upper arm	Upper arm, knee joint	Guide head, wire arms
Lower arm	Lower arm, control strut	

Table 4.7:   The refinement zones and minimum cell size for each zone on pantograph.

Refinement region	Number of zones	Coarse	Medium	Fine
Panhead wake	4	1.5 mm	0.8 mm	0.6 mm
Upper arm wake	2	1.5 mm	1.0 mm	0.8 mm
Joint wake	1	1.5 mm	1.0 mm	0.8 mm
Lower arm wake	1	1.8 mm	1.0 mm	0.8 mm
Components	30	1.0 mm	0.4 mm	0.25mm
Total number of cells		16 million	24 million	49 million
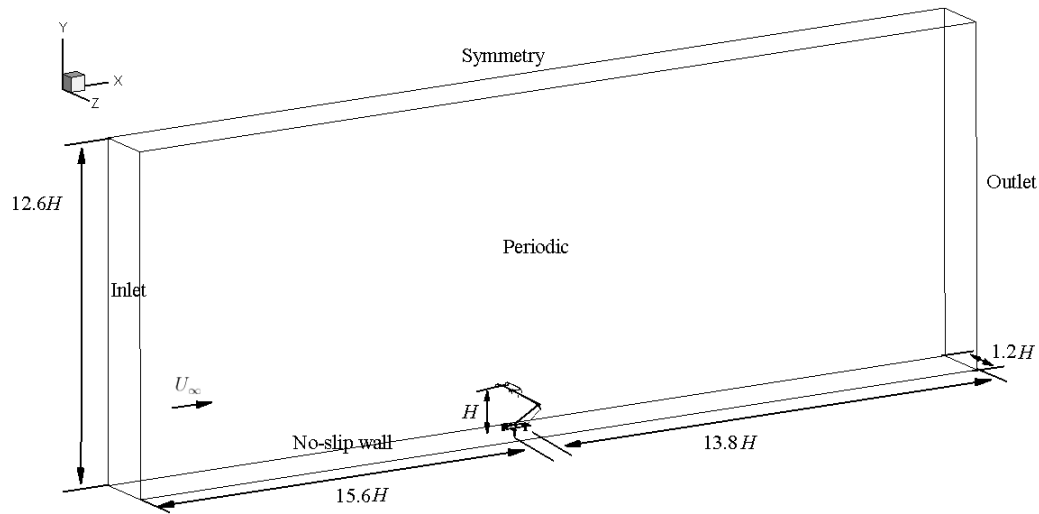
Figure 4.19: Computational domain and boundary conditions used for validation study of pantograph.

(a)

(b)

(c)
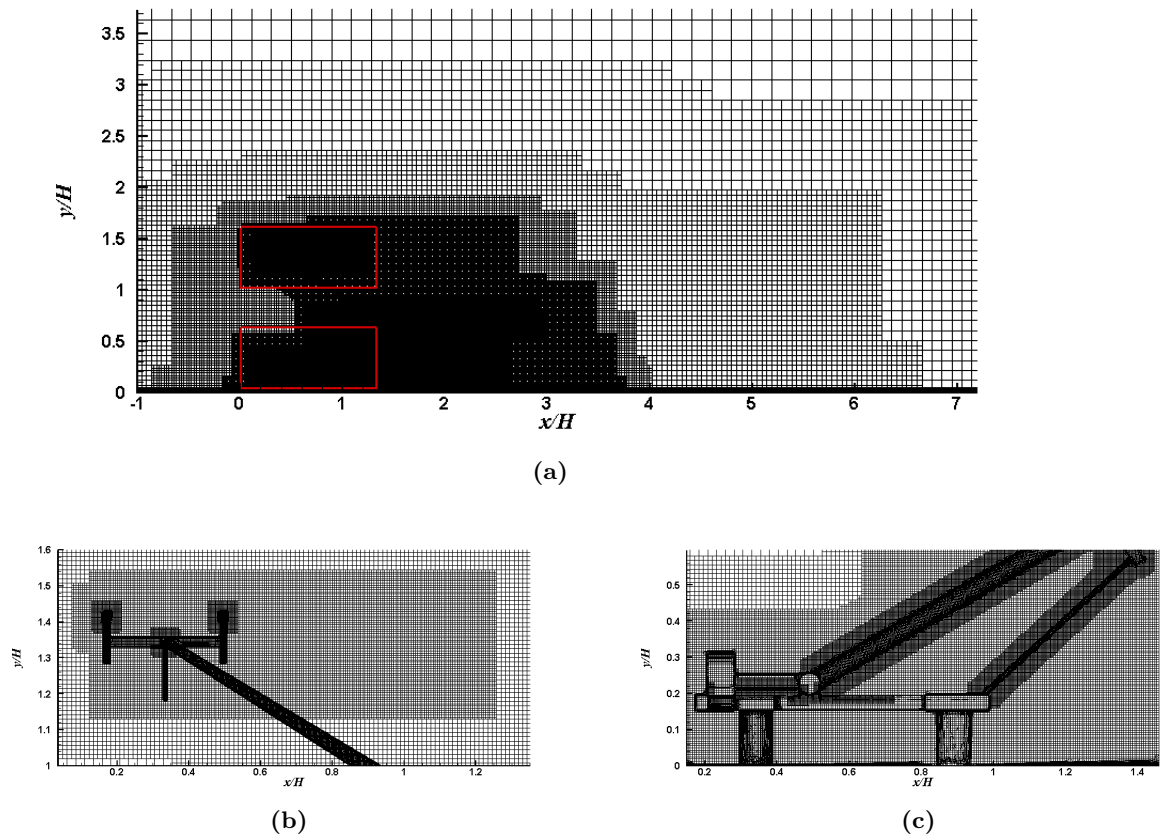
Figure 4.20: Overview (a) and detail (b) of the meshes of the pantograph.
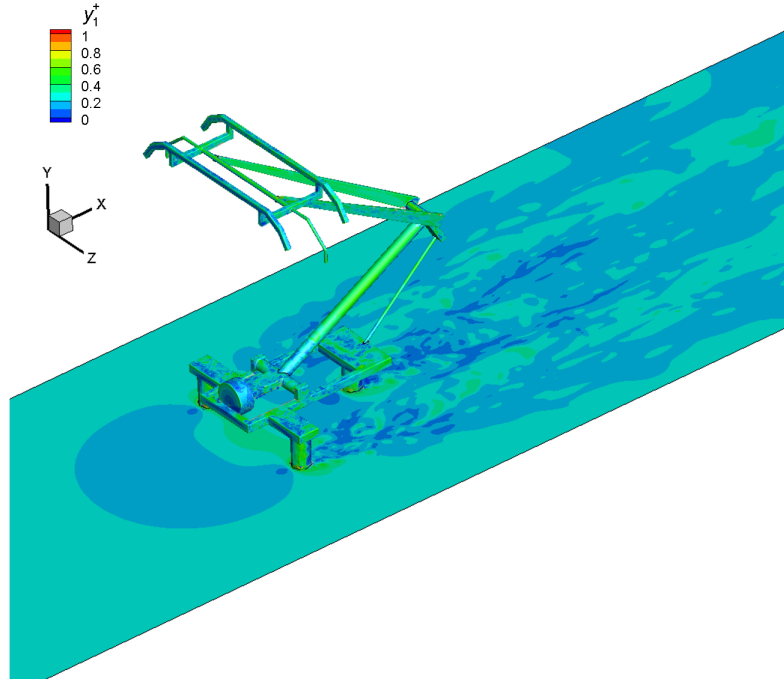
Figure 4.21: y_1^+ distribution of the pantograph and the ground.

4.4.2   Validation of the numerical results

The microphone was located at 5 m (full scale) from the centre of the panhead at a position normal to the flow direction which corresponds to the position used by Lölgen [29]. Lölgen [29] conducted tests on full-scale DSA350SEK pantograph in a wind tunnel at flow speeds ranging from 115 km/h to 400 km/h (31.0 m/s to 111 m/s). The sampling frequency was 125 kHz at 1/10 scale. The spectra are obtained by segmental average using a Hanning window with 50% overlap [92]. Iida et al. [89] derived the aeroacoustic similarity law for pantograph, based on Curle equation and validated the equation comparing scaled and full scale models in a wind tunnel at flow speed ranging from 108 km/h to 180 km/h (30 m/s to 50 m/s). To convert from the 1/10 scale, used for the current numerical simulations, to full scale the following aeroacoustics similarity law is used [89]:

$$L(f) = L_m(f_m) + 10\log\left(\frac{r_m D}{r D_m}\right)^2 + 10\log\left(\frac{U_\infty}{U_{\infty,m}}\right)^n \tag{4.2}$$

where f is the frequency, $L(f)$ is SPL at frequency f, D is a characteristic length of the model, r is the distance between the sound source and the observer, U_∞ is the flow speed (83.3 m/s for the current numerical results and 97.1 m/s for the experimental test) and n is the speed exponent of the sound power, which is taken as 5.8 for the current case [31]. The values with subscript m represent values for the scale model. Most of the cylindrical struts of the pantograph are in the sub-critical flow regime, except the lower arm of the

raised pantograph. The Reynolds number of the lower arm may be in the critical flow regime ($1.4 \times 10^5 < Re \leqslant 1.0 \times 10^6$) as it has the largest diameter ($D = 0.12$ m for full scale). However, the lower arm is located in the wake region of the control strut and folded pantograph. Therefore, the incoming flow velocity for the lower arm in this case is lower than the freestream velocity. Therefore, the Reynolds numbers of all components of the current pantographs are in the upper subcritical regimes ($Re \leqslant 1.4 \times 10^5$). The Strouhal number is relatively constant for a range of $10^3 < Re < 2 \times 10^5$ [89]. Hence, the full-scale frequency f can be obtained from the following equation:

$$St = \frac{fD}{U_\infty} = \frac{f_m D_m}{U_{\infty,m}} \qquad (4.3)$$

Figure 4.22 shows a comparison between numerical and experimental far-field spectra in 1/3 octave bands. Although numerical results for all cases are slightly over-predicted in the low frequency region, excellent agreement from the medium and fine meshes is seen up to 800 Hz and in particular the first peak at 315 Hz, produced by the contact strips, and the second peak at 630 Hz, generated by the horns, are in good agreement with the experimental data. However, because the pantograph geometry in the numerical study has been simplified by removing smaller components such as straps and springs, which generate the high frequency peaks, the numerical results do not match the measurements at high frequencies. The result from the coarse mesh shows under-estimation of the first peak at 315 Hz by 2.5 dB compared with the experimental data. According to this mesh dependence study, the medium mesh set-up is chosen as the basis for generating meshes for the pantographs in the remainder of this work. Besides, the difference between incoming flow speed in the middle of the panhead and side of the panhead is about 1%. Therefore, it can be assumed that the flow does not influence the incoming flow velocity of the panhead due to the domain width.
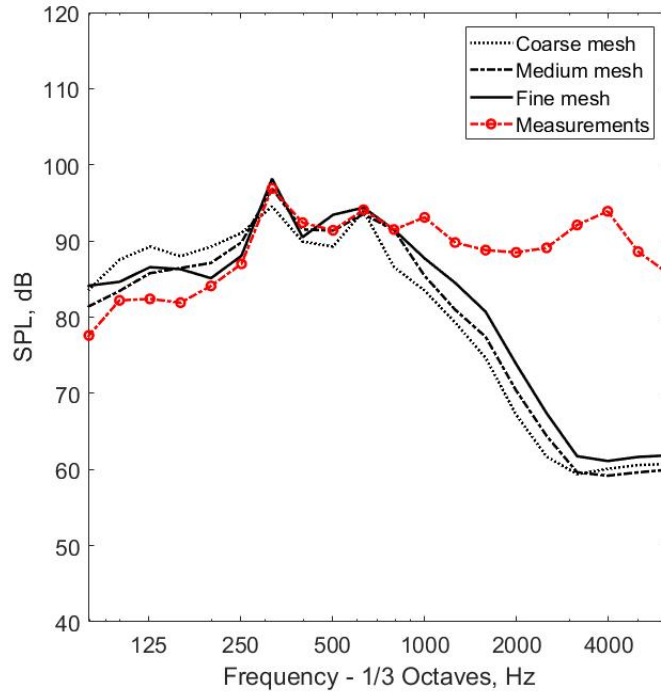
Figure 4.22: SPL comparison of experimental [31] and numerical results.

4.5   Summary

In this chapter, both numerical simulations and pressure distribution and noise measurements are carried out to validate of the numerical methodology used and a gird sensitivity study was carried out. The numerical data shows that the mesh aspect ratio $(\Delta x, \Delta z)_{max}/\Delta y = 120$ and 200 show good agreements in C_p of the cavity floor and aft wall with experiment data as well as benchmark experiment date. For far-field noise measurements, it is found that the spectrum of both the experimental and numerical data are found to be broadband, and do not include tonal components. Furthermore, the results with the mesh resolution $(\Delta x, \Delta z)_{max}/\Delta y = 120$ and 200 can also provide a similar tendency and good agreement between the numerical and the experiment data in terms of the far-field acoustic spectrum and directivity. Therefore, the mesh aspect ratio $(\Delta x, \Delta z)_{max}/\Delta y = 200$ for a cavity is used to provide accurate prediction for near-field flow and far-field noise in this thesis. In addition, the numerical data is validated for the radiated noise from the raised pantograph against experiments data. Good agreement is obtained between the simulations with medium and fine meshes and noise measurement in terms of the two peaks in the noise spectrum from the panhead.

In summary, the numerical predictions of the near-field pressure distribution of the cavity

wall and far-field acoustics show good agreements with the experimental data. However, there are some limitations of the experiments, such as measured flow speed, limited microphone positions, and lack of flow visualisations.

Chapter 5

Effect of cavity flow on high speed train pantograph noise

There have been many studies on the noise radiated from high speed train pantographs. However, much less attention has been given to the generation of aerodynamic noise from the pantograph recess and methods to reduce it. Moreover, interactions of the recess with pantograph components are less well understood. Therefore, this chapter aims to provide improved understanding of aerodynamic phenomena and noise generation mechanisms from cavity flow and its effect on the pantograph, using computational methods. The IDDES approach is used to resolve details of the turbulent structures and enable sufficiently accurate noise prediction using the FW-H equation. The Chapter is structured as follows: Section 5.1 describes the geometry and the mesh set-up used for this study. Section 5.2 presents the computational aerodynamics results, while aeroacoustic results are presented in section 5.3. A summary is given in Section 5.4.

5.1   Computational set-up

5.1.1   Geometry

The geometry is chosen to represent a simplified 1/10 scale high-speed train pantograph roof cavity of a TGV train with two DSA 350 pantographs (one raised and one retracted). The pantograph recess is simplified to a rectangular cavity with dimensions $L = 0.812$ m, $D = 0.07$ m and $W = 0.29$ m, giving $L/D = 11.5$, $W/D = 4.1$. The raised pantograph models are the same as the one in Section 4.4.

Since this study investigates the effect of the cavity on the flow, cases with the pantographs installed directly on a flat surface without the cavity are also studied (cases 3 and 4). An empty cavity (without pantographs in the cavity) is also considered for comparison (case

0). To consider effects of the train running direction, the freestream direction is set as the positive x-direction for cases 1 and 3, and the negative x-direction for cases 2 and 4 and the origin of the coordinate system is at the cavity floor and the upstream wall edge corner, as shown in Figure 5.1(a).

(a) Side view

(b) Top view
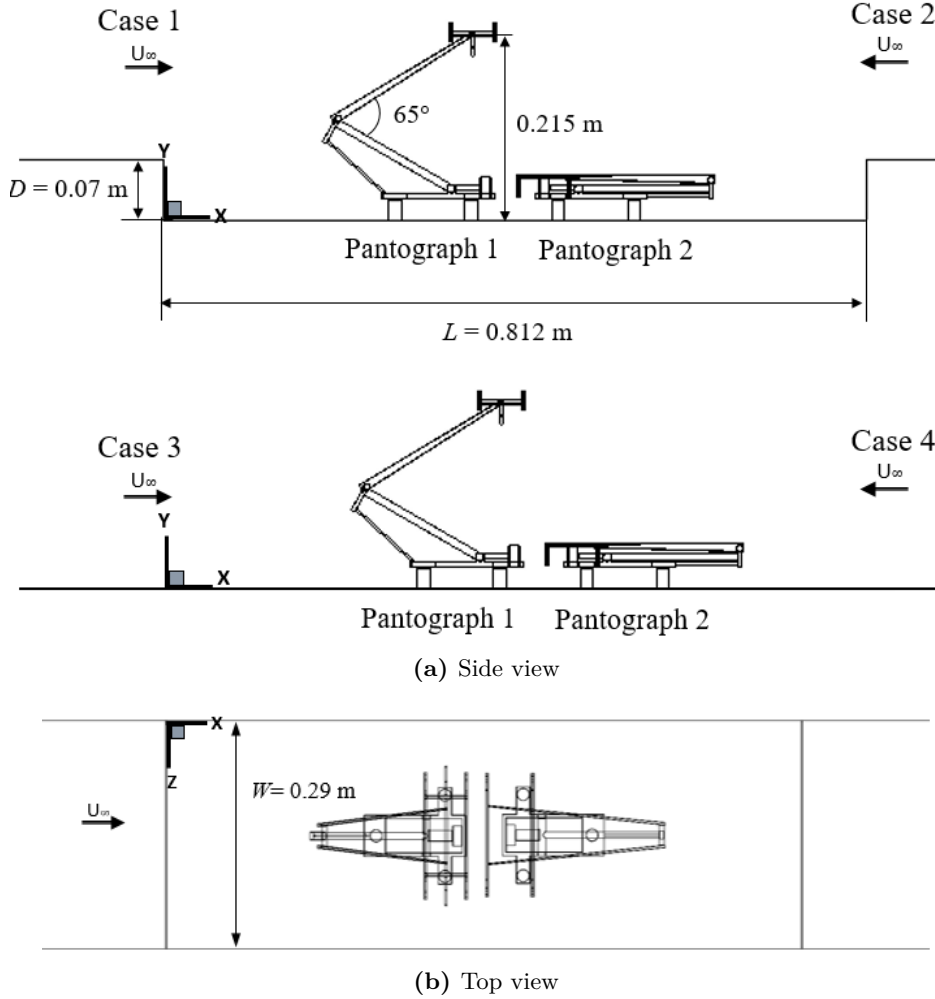
Figure 5.1: Description of the geometry

5.1.2   Numerical test section

The computational domain, as illustrated in Figure 5.2, extends over $71.5D$, $29D$ and $4.1D$ along the streamwise (x), vertical (y) and spanwise (z) directions, respectively. The upstream length was determined as $30D$ in order to have a fully-developed turbulent boundary layer at the cavity leading edge for all cases. The cavity and pantograph walls are defined as no-slip walls. The outlet and top boundaries are sufficiently far away to have negligible effect on the flow developed around the cavity. The top boundary is specified to have symmetry conditions and a pressure outlet is imposed at the outlet boundary. Periodic boundary conditions are applied to the two side surfaces of the domain. The inflow boundary is set

as a velocity inlet with incoming flow velocity $U_\infty = 83.3$ m/s (300 km/h), corresponding to a Reynolds number of 3.89×10^5 (based on the freestream properties and the cavity depth).

For all cases in this study, a hexa-dominated mesh is used and these meshes are generated using the STAR-CCM+ mesh generator with multiple refinement zones in regions where strong variations in flow quantities are expected . Different cell sizes are specified for each refinement zone; an example is shown in Figure 5.3. The same meshing strategy for the cavity is used as one in Section 4.1 and 4.3 and for the pantograph meshing, the same strategy is used as one in Section 4.4. As high gradients of pressure and velocity occur in the vicinity of the cavity trailing edge and the pantographs, these regions are refined with a minimum cell size of 1.2 mm in the cavity trailing edge region and 0.4 mm in the pantograph panhead region, and a surface growth rate of 1.1. The maximum cell aspect ratio is 200 (Δx / Δy, Δz / $\Delta y = 200$). In order to reduce the computational costs while retaining a sufficient accuracy, the boundary layer mesher is used. 25 - 40 layers are used in order to resolve the boundary layer region. The total number of cells for each case is listed in Table 5.1. It is verified that y_1^+ is less than 1 on all surfaces. In order to ensure a stable simulation, a non-dimensional time step $U\Delta t/D = 0.0095$ ($\Delta t = 8 \times 10^{-6}$) is used, where D is depth of cavity, which ensures that the CFL number is less than 1 for all cases. The numerical data was collected after 0.05 s when the flow was deemed to be statistically steady.
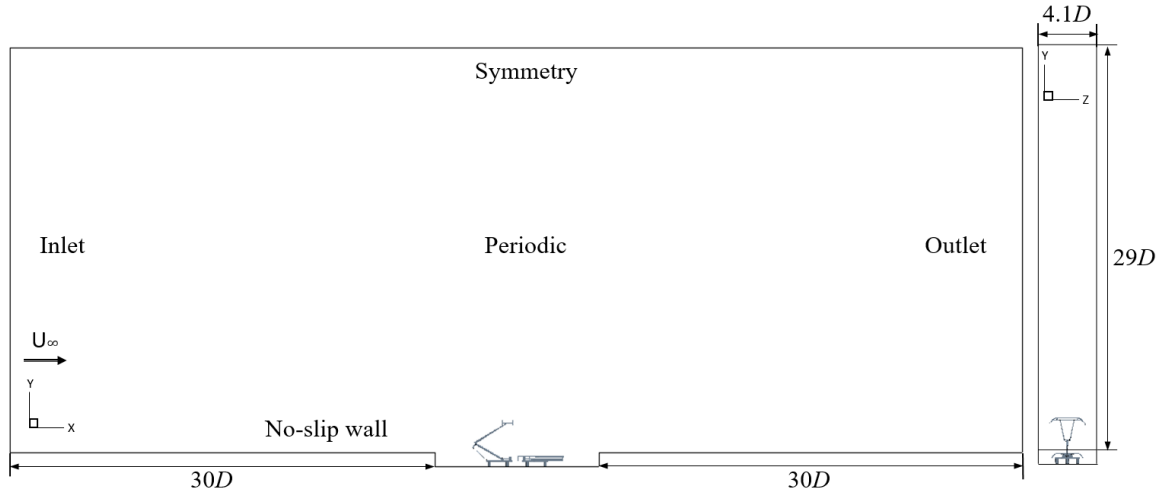
Figure 5.2: Computational domain and boundary conditions

(a) Overall view of the mesh

(b) Details view of the mesh

(c) Details view of the panhead mesh
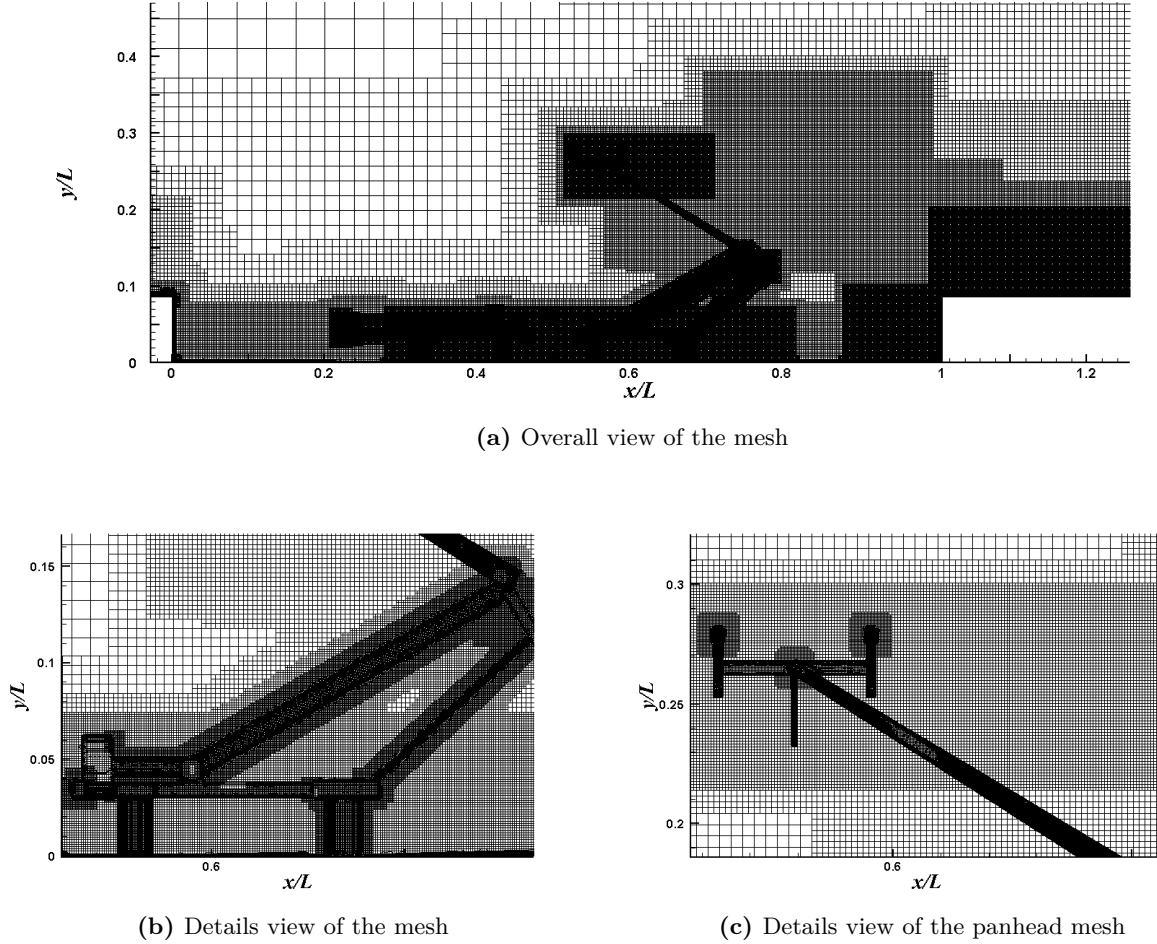
Figure 5.3: Overview and detail of the meshes

Table 5.1: Summary of the cases considered

Simulation cases	Description of the case	Number of cells
Case 0	Empty cavity	8.1 million
Case 1	Front pantograph raised with the cavity	30.4 million
Case 2	Rear pantograph raised with the cavity	29.4 million
Case 3	Front pantograph raised without the cavity	27.8 million
Case 4	Rear pantograph raised without the cavity	25.7 million

5.2   Aerodynamic results

In order to investigate the near-field flow characteristics and potential acoustic sources of the cavity and pantographs, the time-averaged velocity, wall pressure fluctuations and instantaneous flow fields are analysed and compared for the cavity without and with the pantographs.

5.2.1   Q-criterion

To provide an overview of the flow field and analyse its interaction with the pantographs, three-dimensional vortical structures are illustrated in Figure 5.4, based on the Q-criterion [93]. Q is the second invariant of the velocity gradient, and can be written as: $Q = \frac{1}{2}(\Omega_{ij}\Omega_{ij} - S_{ij}S_{ij})$, where Ω_{ij} is the vorticity tensor and S_{ij} is the rate-of-strain tensor. These can be defined as $\Omega_{ij} = \frac{1}{2}\left(\frac{\partial u_i}{\partial x_j} - \frac{\partial u_j}{\partial x_i}\right)$, $S_{ij} = \frac{1}{2}\left(\frac{\partial u_i}{\partial x_j} + \frac{\partial u_j}{\partial x_i}\right)$. $Q_{\mathrm{norm}} = \frac{QD^2}{U_\infty^2}$ is the normalized value of Q, where D is the cavity depth, and U_∞ is the freestream velocity. Q indicates the local balance between vorticity and shear strain rate magnitude. Regions of positive Q indicate the vortical flow dominates.

The iso-surface of the normalized Q-criterion is plotted for $Q_{\mathrm{norm}} = 2.5$ in Figure 5.4 and is coloured by the non-dimensional instantaneous velocity magnitude. In general, vortices are generated in the wakes of pantograph components, especially the panhead, the upper and lower arms, and also in front of the pantographs. When the pantographs are placed in the cavity (cases 1 and 2), the shear layer, due to the flow separation from the cavity leading edge, rolls up and generates spanwise vortical structures in a recirculation region between the upstream wall of the cavity and the front pantograph and these vortical structures evolve and become hairpin vortices. These vortical structures are seen in most of the upstream region of the cavity in case 2. In case 1, however, the vortical structure is dissipated after interacting with the raised pantograph. In case 2, stronger unsteady flow is observed in the region downstream of the cavity than in case 1. This is due to flow interactions between the raised pantograph and the cavity downstream wall. Furthermore, highly unsteady flows occur in the cavity downstream region, as seen in Figure 5.4(a) and (b). The trailing edge generates flow separation and highly unsteady flow. The streamwise vortical structures from the flow separated at the trailing edge rapidly develop into hairpin vortical structures, which will lead to large pressure fluctuations on the cavity trailing edge wall.

For cases 3 and 4, without the cavity, a highly unsteady flow is seen behind the panhead of the raised pantograph and the frame of both pantographs. The vortices from the upstream contact strip roll up and rapidly develop into hairpin vortices, similar to those in cases 1 and 2. For case 4 shown in Figure 5.4(d), the joint of the folded pantograph and the upper arms of the raised pantograph generate higher unsteady flow with stronger vortical structures than in case 3. Furthermore, most of the vortical structures become streamwise vortices in the downstream region. Compared with the cases with the cavity, strong vortices are generated by the frame of the raised pantograph and the whole folded pantograph in the cases without the cavity. These vortices strongly interact with the rear pantograph components.

These results suggest that the cavity (in cases 1 and 2), the folded pantograph and the frame of the raised pantograph (in cases 3 and 4) and the panhead of the raised pantograph in all cases produce a highly unsteady flow.

(a) Case 1   **(b)** Case 2

(c) Case 3   **(d)** Case 4
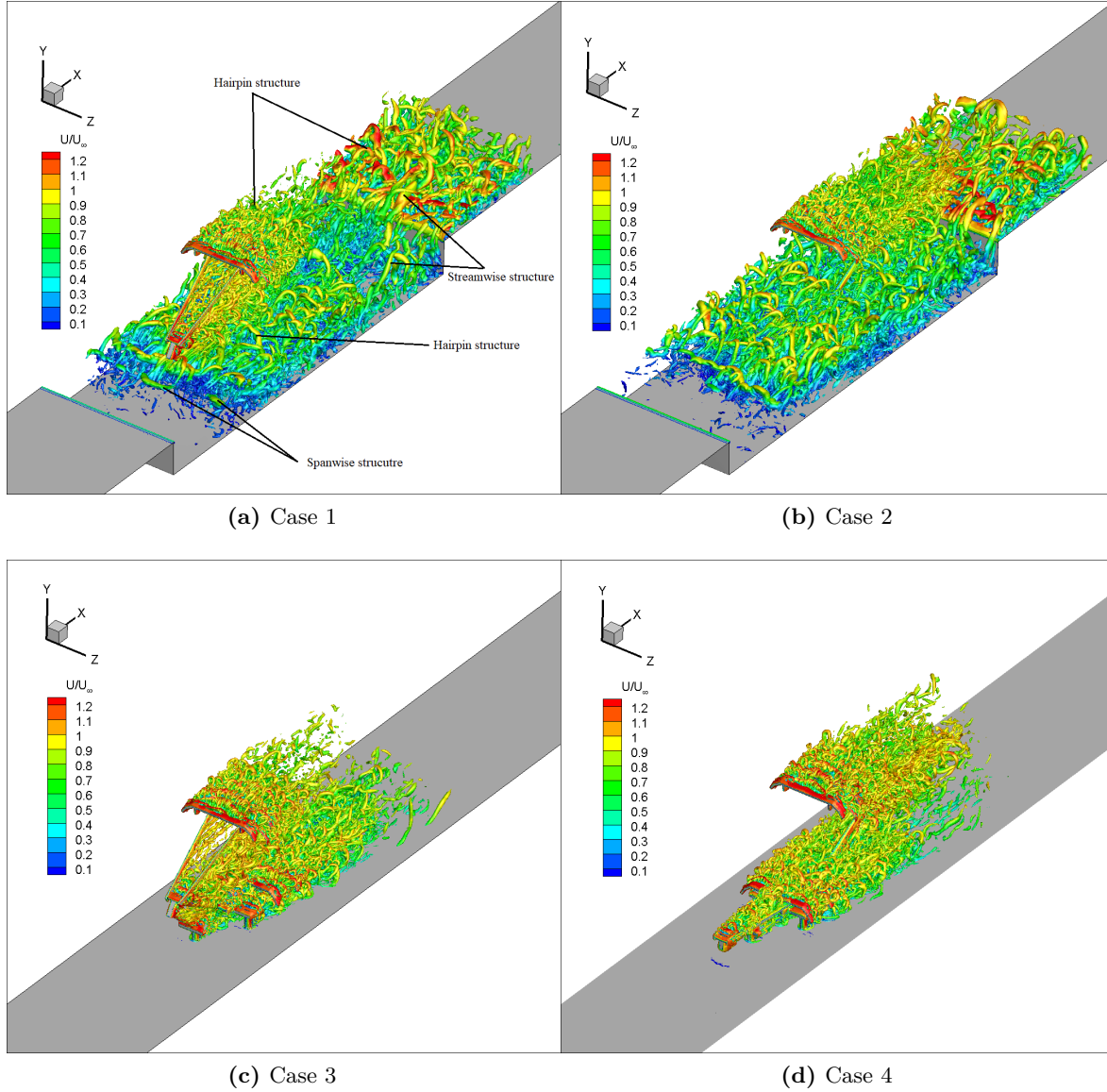
Figure 5.4: Flow structure demonstrated by iso-surface of Q-criterion with Q_{norm}=2.5

5.2.2   Time-averaged velocity field

Figure 5.5 displays contours of the mean streamwise velocity at the mid-span plane ($z = 0.145$ m) together with two-dimensional in-plane streamlines. For the two cases in which the pantographs are located inside the cavity (cases 1 and 2), the incoming flow boundary layer separates from the cavity leading edge, the shear layer from this separated flow impinges

around the middle of the cavity floor and the flow reattaches at $x/L = 0.6$. The cavity has a length-to-depth ratio $L/D = 11.5$ which is a classic closed cavity, as confirmed by the simulation shown in Figure 5.5(a). The shear layer impinges on the cavity floor and the pantographs in both cases 1 and 2. In case 1 (raised pantograph in front), the shear layer impinges on the front foot, frame and control strut of the raised pantograph, whereas for case 2 impingement of the shear layer occurs on the panhead region of the folded pantograph. This impingement may generate surface pressure fluctuations, which would produce noise.

In the region upstream of the cavity, the mean flow behaviours of the three cavity cases (cases 0, 1 and 2) are similar. In both cases, flow separation at the cavity leading edge introduces a recirculation region between the cavity leading edge and the front pantograph. Case 2 shown in Figure 5.5(c), has a smaller recirculation region than case 1 due to turbulent flow interaction with the front folded pantograph. For both cases 1 and 2, a small recirculation region appears at the upstream bottom edge and another small recirculation region can be observed in the gap between the two pantographs. Furthermore, another recirculation is found at the downstream bottom corner in all cavity cases (cases 0, 1 and 2). The shape and size of this separation region is altered by the installed pantographs. Flow separates again at the trailing edge and reattaches on the cavity aft wall further downstream, at $x/L = 1.10$ for case 1, and at $x/L = 1.15$ for case 2. The flow recirculation region at the aft wall is influenced by turbulent flow generated by the pantographs. The flow direction in the vicinity of the cavity trailing edge for case 1 (Figure 5.5(b)) is more upward than for case 2. This is due to the wake from the raised pantograph. When the knee is upstream in case 1 (raised pantograph in front) this generates a larger wake region than with the knee downstream in case 2.

Highly unsteady flow occurs in the vicinity of the cavity with low velocity in cases 1 and 2. The direction of the streamlines passing through the panhead of the raised pantograph is slightly more downward, which is associated with the cavity flow. Moreover, the incoming flow velocity in the vicinity of the panhead in cases 1 and 2 is slightly lower than for the cases without the cavity, which will be analysed in more detail later. The wake region around the panhead for cases 3 and 4 is slightly larger than that for cases 1 and 2. In cases 3 and 4, small recirculation regions are found at the back of the feet, joint and frame of the pantographs, which are similar to those found for cases 1 and 2. Furthermore, for cases 3 and 4, a large wake region is generated by the rear pantograph frame.
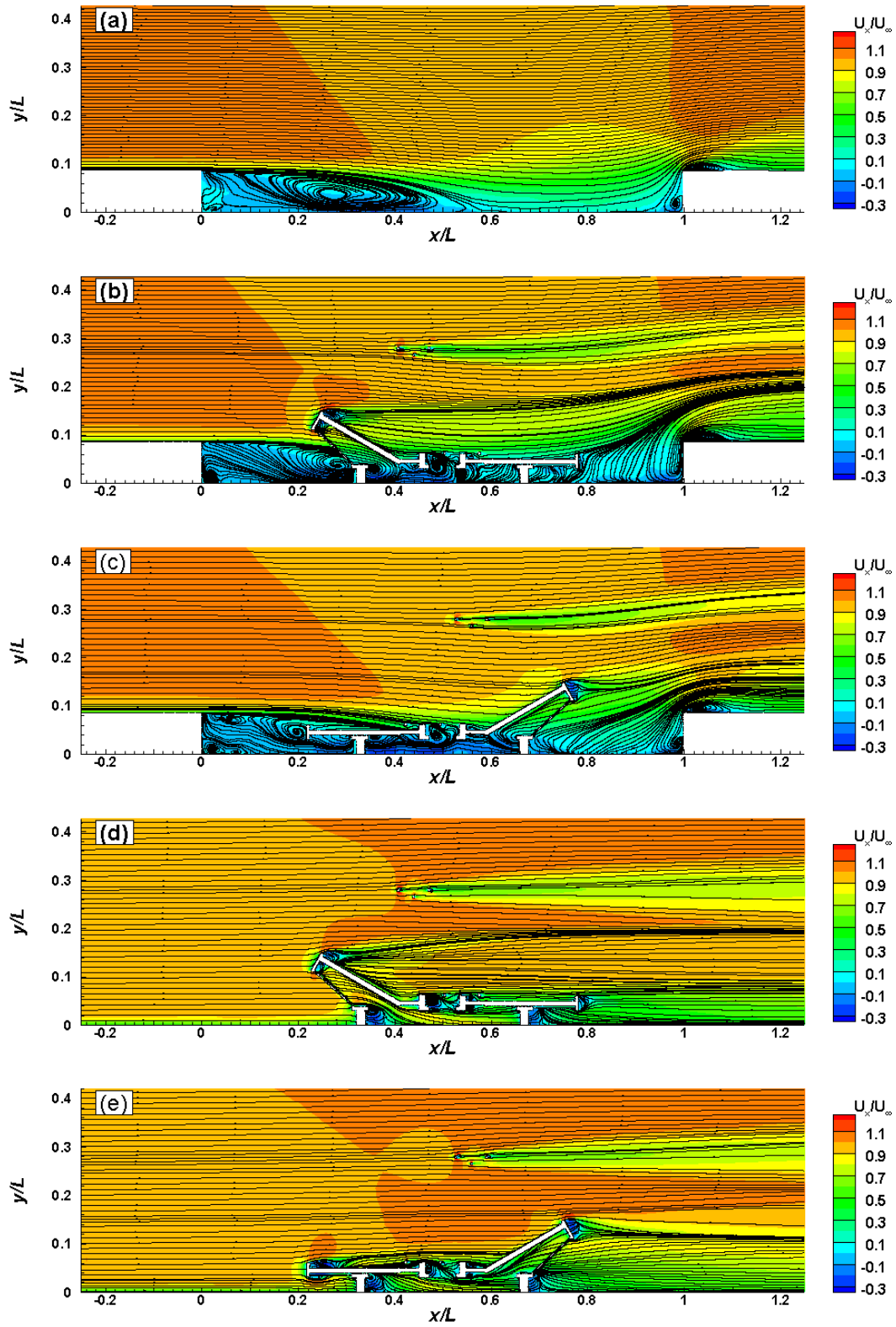
Figure 5.5: Mean streamlines with time-averaged velocity contours, (a) case 0 (empty cavity), (b) case 1, (c) case 2, (d) case 3, (e) case 4.

As the panhead of the raised pantograph is a major source of noise, the flow velocity ahead of the panhead is an important factor influencing the radiated noise. In order to investigate the development of the flow and the mean streamwise velocity U_x from the cavity leading edge to the panhead of the raised pantograph, the development of velocity for the empty cavity is investigated first. This is shown in Figure 5.6, which gives the profiles of U_x at different streamwise locations. A typical boundary layer profile is seen upstream of the cavity until flow separates at the leading edge ($x = 0$). Due to the recirculation zone formed at the front part of the cavity, here negative velocity is seen near the cavity bottom. It is also observed that U_x outside the cavity decreases slightly and the lowest velocity appears at $x/L = 0.451$. The streamwise velocity at a height of $y = 3D$, which is at a similar height to the panhead location, reduces by up to approximately 4% (from $1.01U_\infty$ to $0.97U_\infty$) away from the cavity leading edge. This is important for the noise generation as the flow speed has a strong influence on the noise generated.
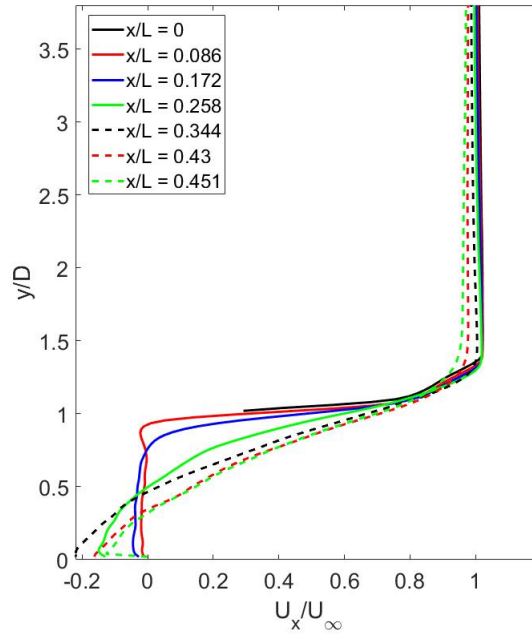
Figure 5.6: Time-averaged x-velocity on vertical lines at $z = 0.5W$ for empty cavity.

Figures 5.7 and 5.8 display the profiles of U_x at different streamwise and spanwise locations for the four cases with pantographs. The lines at $x/L = 0.43$ for cases 1 and 3 are located just before the upstream contact strip of the raised pantograph and the lines at $x/L = 0.45$ are just in front of the horn of the pantograph. In cases 2 and 4, the lines at $x/L = 0.52$ and at $x/L = 0.54$ are located at the upstream contact strip and the horn of the raised pantograph.

The profiles in cases 1 and 2 are similar upstream of the pantographs ($x/L = 0 \sim 0.26$) within the cavity ($y/D = 0 \sim 1$); negative values of the streamwise velocity U_x start to

appear after the cavity leading edge between $y/D = 0$ and 1 due to the cavity recirculation. In general, the flow speed in the cavity region is smaller than the corresponding cases without the cavity. This means that although the cavity causes unsteady flow around the cavity, it reduces the flow speed at the folded pantographs and lower parts of the raised pantograph. The slightly lower flow speed, seen in Figure 5.6, is also observed outside the cavity region in cases 1 and 2 away from the leading edge of the cavity. At $x/L = 0.43$ (before the panhead of the raised pantograph) and $x/L = 0.45$ (before the horn of the raised pantograph), the values of U_x between $y/D = 3$ and 3.5 in case 1 are about 5% lower than in case 3 due to the cavity flow. A similar tendency can be seen at $x/L = 0.52$ and 0.54 in cases 2 and 4 as shown in Figure 5.8(g) and (h).

The influence of the cavity on the flow upstream of the panhead suggests that the noise from the upper part of the raised pantograph (including panhead and upper arms) will be different between the cases with the cavity (cases 1 and 2) and the cases without (cases 3 and 4). This will be discussed in more detail in Section 5.3.
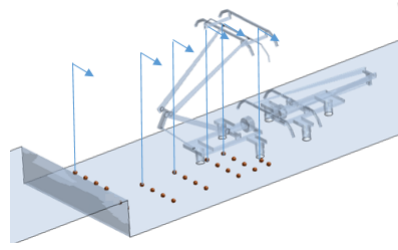
(a) Line positions
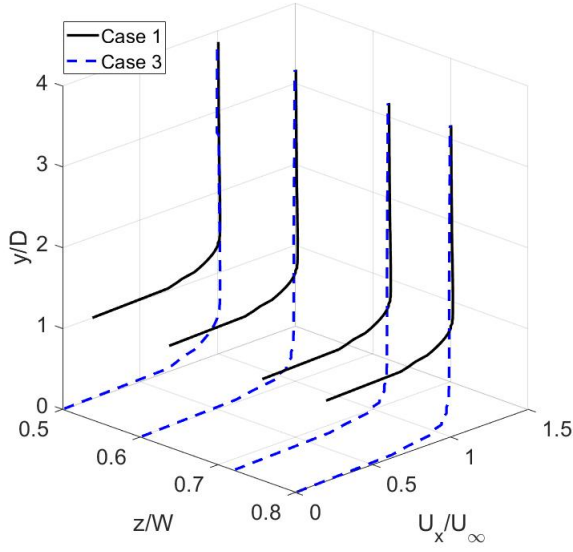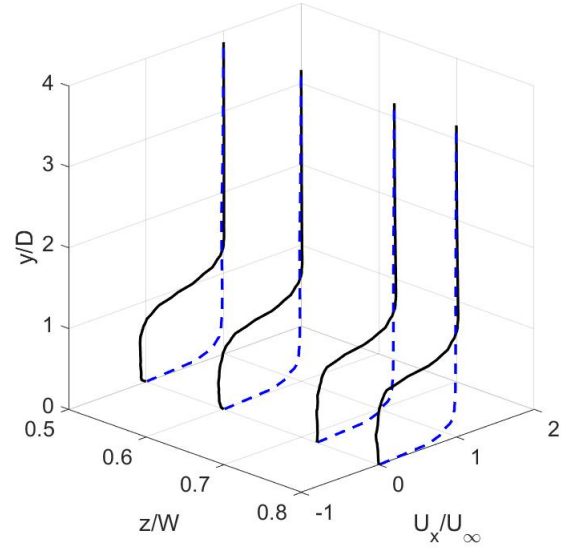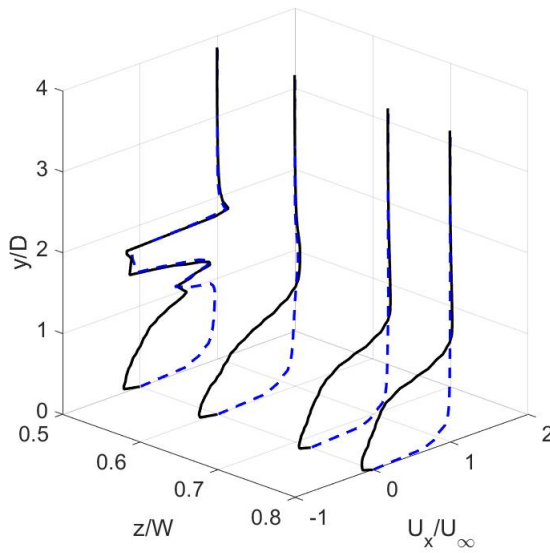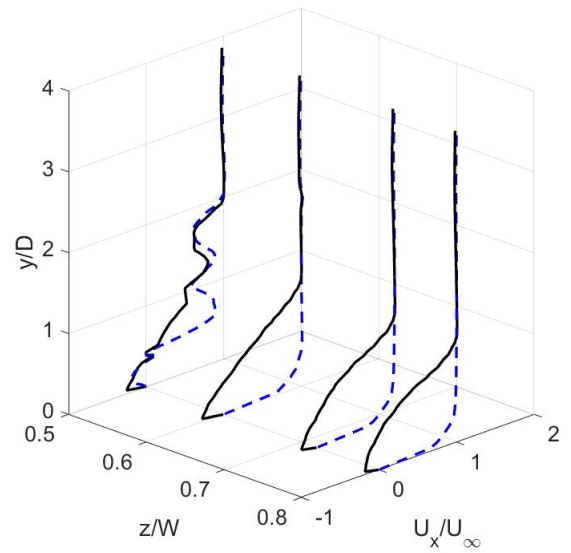
(b) $x/L = 0$

(c) $x/L = 0.17$
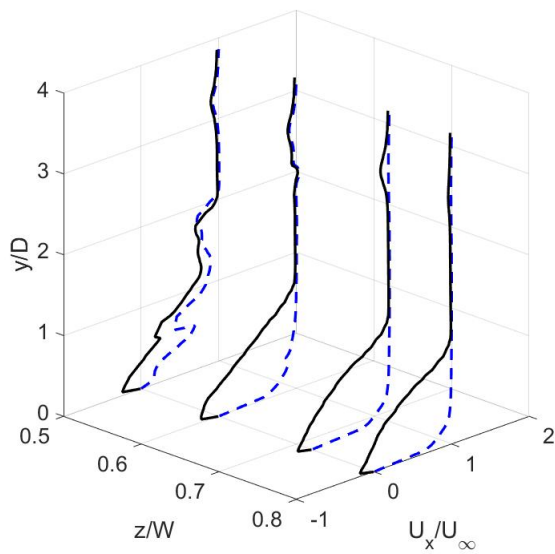
(d) $x/L = 0.26$

(e) $x/L = 0.34$

(f) $x/L = 0.43$
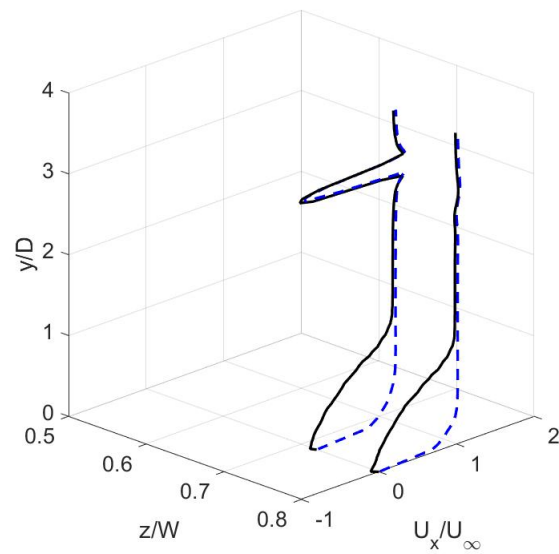
(g) $x/L = 0.45$

Figure 5.7: Streamwise time-averaged velocity U_x from cases 1 and 3.

(a) Line positions

(b) $x/L = 0$

(c) $x/L = 0.17$

(d) $x/L = 0.26$

(e) $x/L = 0.34$

(f) $x/L = 0.43$

(g) $x/L = 0.52$
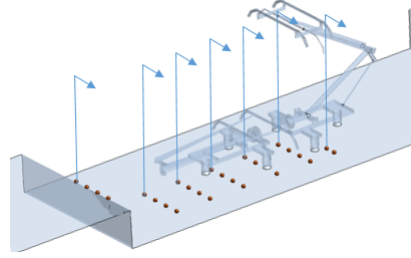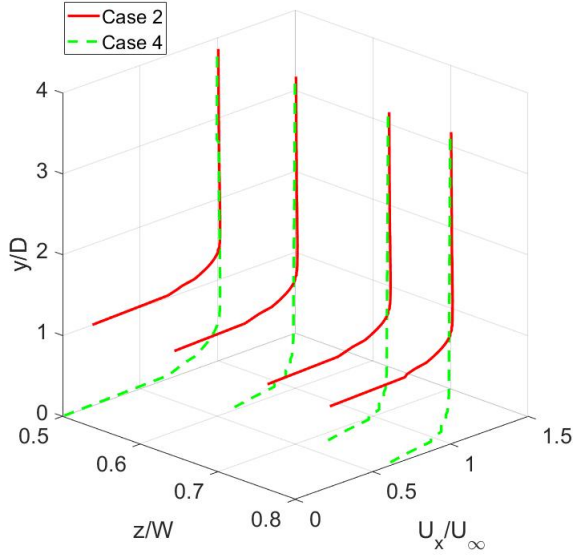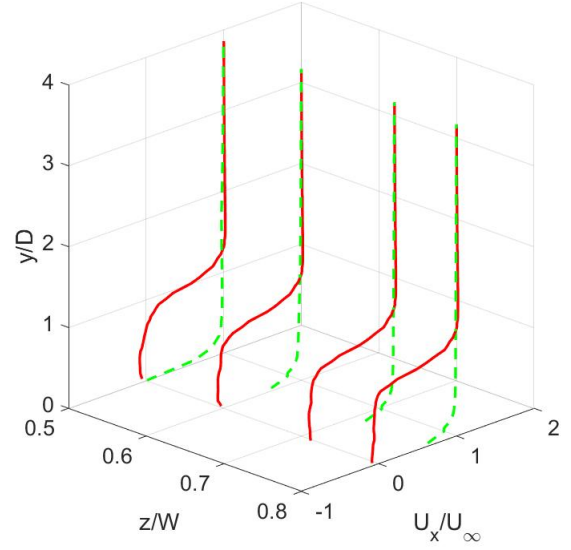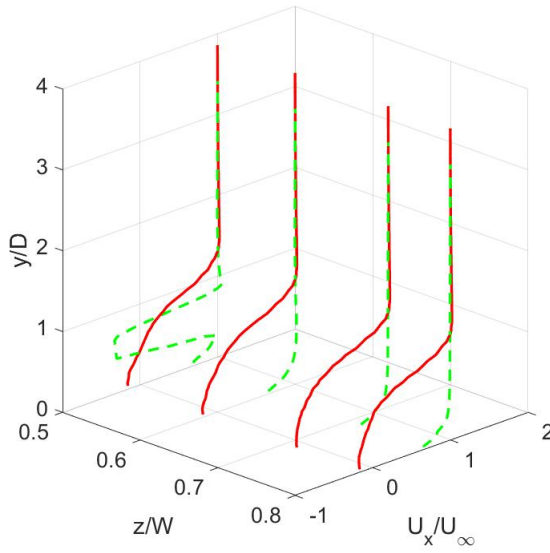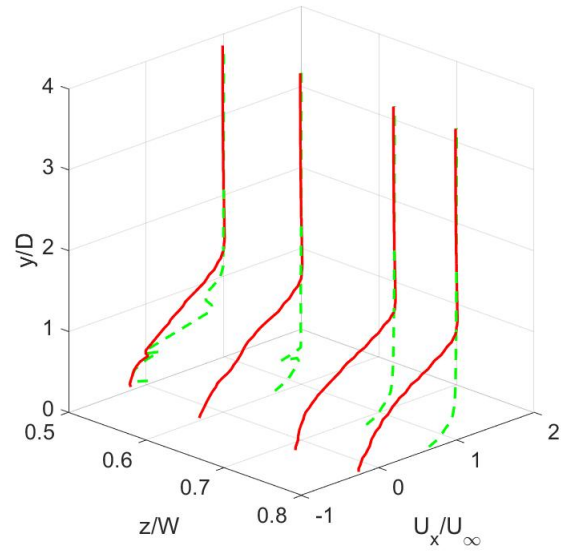
(h) $x/L = 0.54$
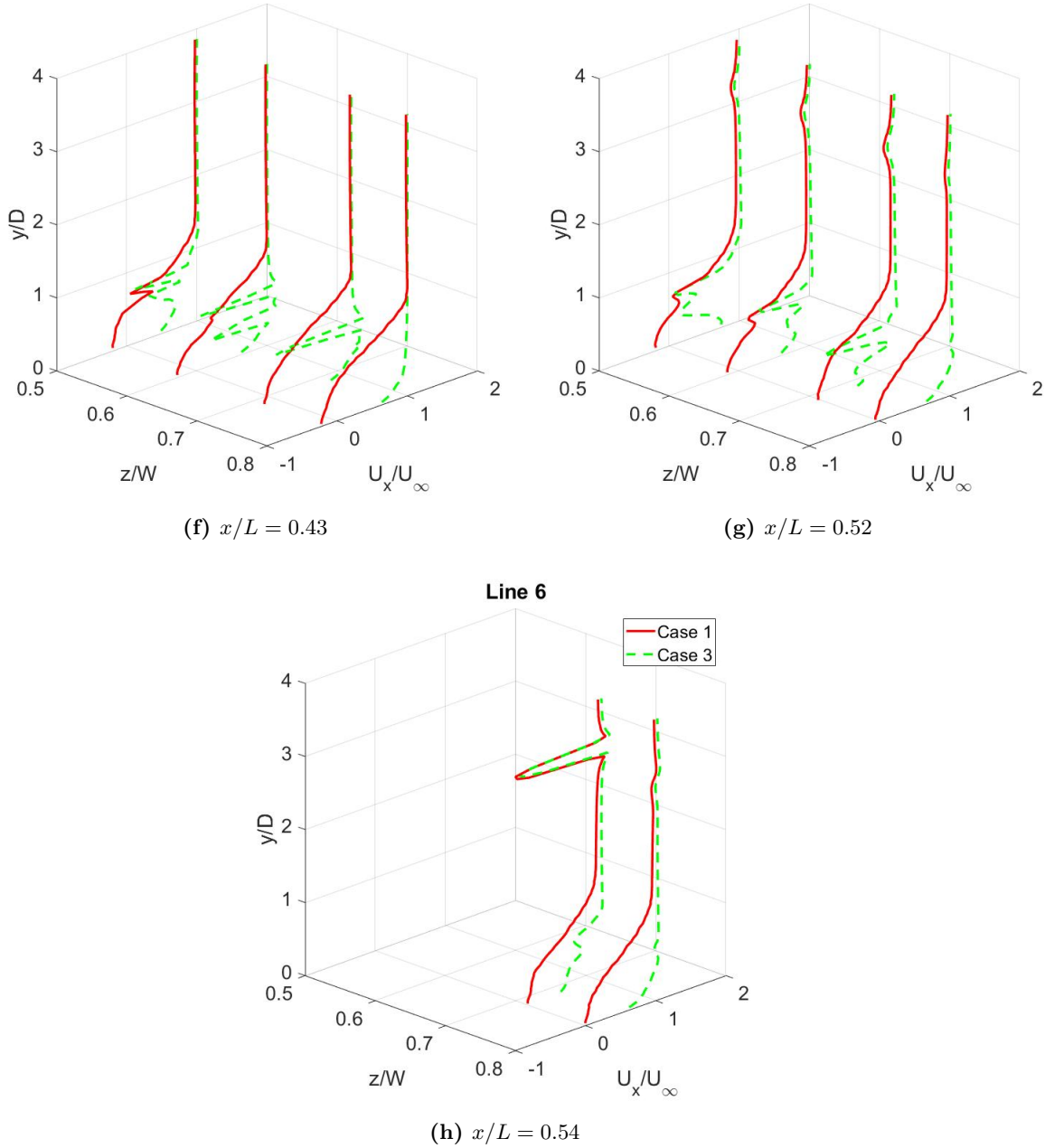
Figure 5.8: Streamwise time-averaged velocity U_x from cases 2 and 4.

5.2.3   RMS surface pressure

To help identify the main acoustic source regions, the wall pressure fluctuations on the pantographs are shown in Figures 5.9 (side view) and 5.10 (top view). These are shown as SPLs in decibels $L_p = 10\log_{10}(p_{\mathrm{rms}}^2/p_{\mathrm{ref}}^2)$, where p_{rms} is the rms value of pressure fluctuation and p_{ref} is the reference sound pressure (20 μPa).

The surface pressure fluctuations are generally large on the panhead, joint and top part of the lower arm for all four cases since those parts are either exposed to the freestream flow, where the flow speed is higher, or they interact with the shear layer. The downstream contact strip and horn of the raised pantograph display larger pressure fluctuations than the upstream contact strip for all cases, as shown in Figure 5.10. This is due to the shed vortices from the upstream contact strip impinging on the surface of the downstream one and the horn.

Comparing cases 1 and 2, the wall pressure on the lower arm and the control strut in case 1 has stronger fluctuations than in case 2 due to the impingement of the shear layer from the cavity leading edge. However, the surface pressure fluctuations on the joint in case 2 are larger than in case 1. This can also be found in a comparison between cases 3 and 4 since the highly unsteady flow generated from the upper part of the lower arms impinges on the joint surface. For cases 1 and 2, the rms pressure amplitude on the top surface of the panhead and arm of the folded pantograph is larger than on their side surfaces. This location is where the shear layer from the cavity leading edge impinges on the top surfaces. A large pressure fluctuation appears on the downstream contact strip of the folded pantograph for cases 3 and 4, see Figure 5.10(c) and (d). Compared with the contact strip of the pantograph, the surface pressure fluctuations in these areas are much larger. The folded pantograph for cases 3 and 4 is exposed to higher speed flow compared with cases 1 and 2, and therefore highly unsteady flow is generated from the upstream contact strip. This strong flow interacts with the downstream contact strip. For the rear pantograph in cases 3 and 4, there are large differences on the frame and foot regions where the pressure fluctuations are larger than for cases 1 and 2, as shown in Figure 5.9. This is due to the fact that a strong wake from the front pantograph frame and foot impacts on the rear one for cases 3 and 4, whereas the wake for cases 1 and 2 is weakened by the cavity. In general, the pressure fluctuations on the top surface of both the raised and the folded pantographs are larger than on their side surfaces for all cases. This suggests that the radiated noise in the vertical direction is stronger than that in spanwise direction.

(a) Case 1

(b) Case 2

(c) Case 3

(d) Case 4
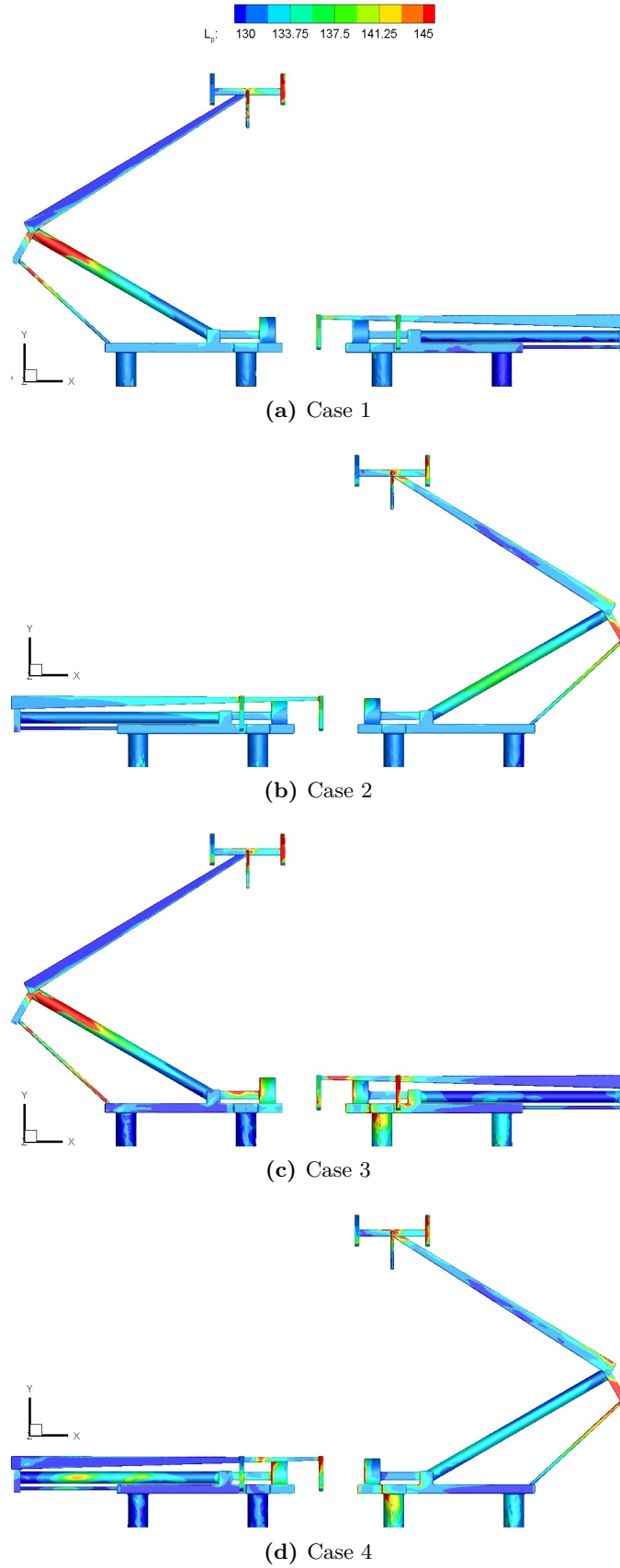
Figure 5.9: RMS surface pressure in decibels re 2×10^{-5} Pa

(a) Case 1

(b) Case 2

(c) Case 3

(d) Case 4
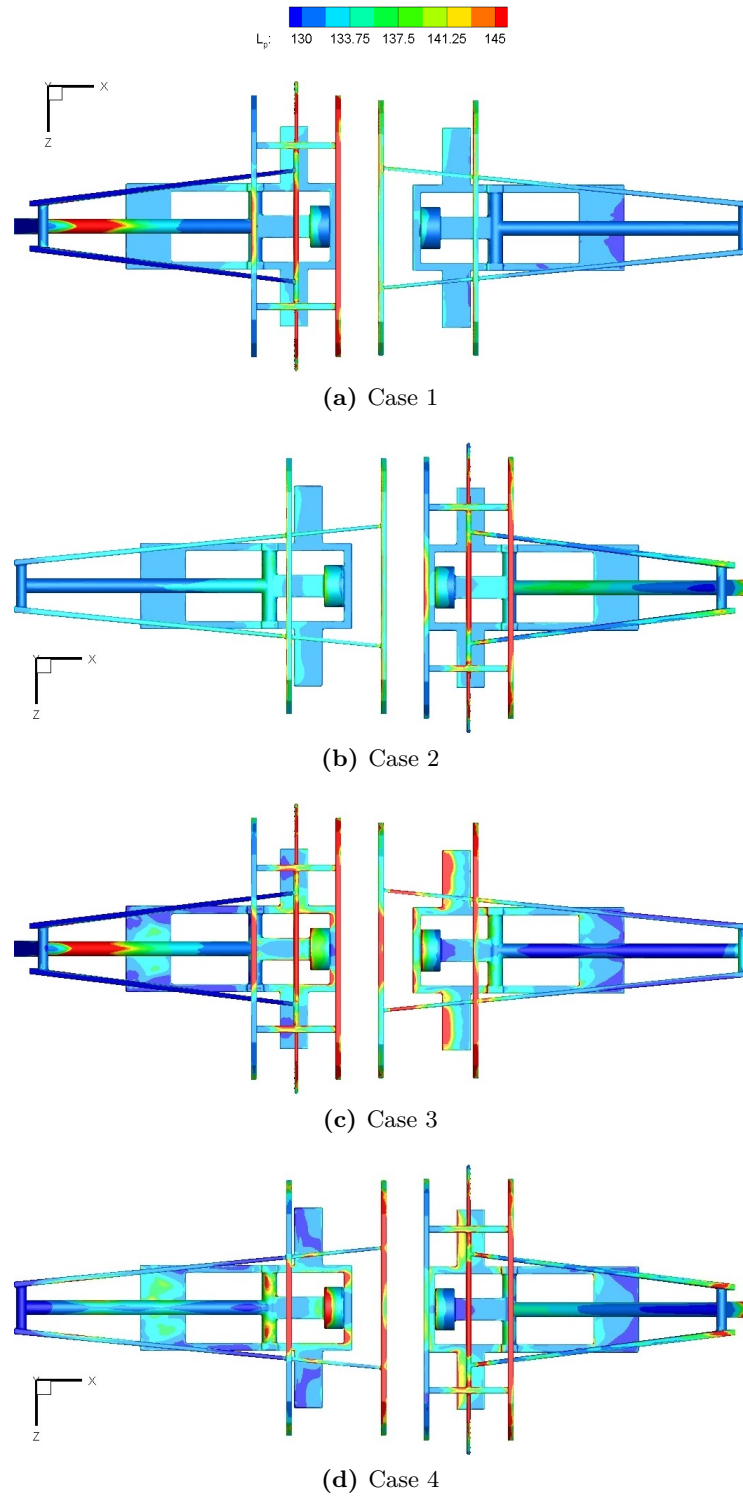
Figure 5.10: RMS surface pressure in decibels re 2×10^{-5} Pa

5.3   Aeroacoustic results

To calculate the far-field noise, the FW-H solver was used with the integration surface for the solver coinciding with the solid walls. The unsteady pressure data on the surface of the pantographs, the cavity and the train roof are used as the input. Thus, only the contributions from dipole sources are included, whereas the contributions from quadrupole sources in the wake are neglected. This is reasonable as the contribution from quadrupole sources is small at low Mach number. The convective effects are also neglected. Far-field narrowband sound pressure spectra obtained from the simulation are converted to 1/3 octave bands and then adjusted to give the equivalent results at full scale using Equations 4.2 and 4.3.

5.3.1   Sound pressure level

A total of 244 far-field receivers are used in the model, located on a sphere with radius 2.5 m (corresponding to a radius of 25 m at full scale) from the middle of the cavity floor. For both the side (azimuthal angle) and the the top (polar angle) directions, receivers are uniformly distributed with an interval of 4.5 degrees. The same receiver positions are used for all four cases. The all results in this section were not consider reflections from the train roof and only direct sound pressure are accounted. The results focus on the SPL at two receiver positions, at the side (an azimuthal angle $\theta = 90°$) and the top (a polar angle $\phi = 90°$). All current results are converted to full-scale level and the flow speed is kept as 83.3 m/s. Figure 5.11 shows the spectra at the side receiver of the radiated sound pressure from all components including the cavity and both pantographs (a), the raised pantograph (b), the folded pantograph (c), and only the cavity (d).

The differences between the noise radiated when the raised pantograph is in front (cases 1 and 3) and behind (cases 2 and 4) are not very large. The noise levels with the raised pantograph in front (knee-upstream) are around 1.5 dB higher than the levels with the raised pantograph at the back (knee-downstream). The total SPL for cases 3 and 4 is higher in most of the frequency range than for cases 1, 2 (with cavity). In Figure 5.11(b), the noise from the raised pantograph is similar to the total noise for frequencies above 250 Hz. For cases 1 and 2, two peaks are seen at 250 Hz and 500 Hz for the raised pantograph, whereas these peaks are seen at 315 Hz and 630 Hz for cases 3 and 4. These are produced by the upstream contact strip and the horn (H3 see Figure 4.18) respectively. The panhead is the most significant source of noise compared with other components. The amplitude of the first peak, associated with the contact strips, is highest for case 3 and lowest for case 2. This may be related to the reduced incoming flow velocity in the vicinity of the panhead due to the cavity flow.

Figure 5.11(c) shows the spectra of noise radiated from the folded pantograph. In each case, there are no strong tonal components. Furthermore, for cases 1 and 2 the folded pantograph is located in the cavity, where the flow velocity is significant lower and consequently the spectra of radiated noise are more than 10 dB lower than for cases 3 and 4. The noise levels of the folded pantograph are similar for cases 3 and 4, although in the low frequency region up to 300 Hz, the level for case 3 with the folded pantograph downstream is slightly higher. This may be due to the highly unsteady flow from the frame impinging on feet of the front pantograph and the rear folded pantograph.

Figure 5.11(d) shows the spectra of noise radiated from the cavity including the cavity wall and cavity aft wall for cases 1 and 2, and for comparison the empty cavity case. The tendency in all three cases is similar but in the high frequency region above 600 Hz the SPL for cases 1 and 2 is slightly higher. The noise radiated from the cavity is much lower than the other components, especially the raised pantograph, expect at low frequencies.

Figure 5.12 shows the corresponding spectra of radiated sound pressure at the top receiver position. In general, the SPL at this location is much higher than that at the side location, especially for the sound radiated by the cavity. A strong tonal peak at 500 Hz for cases 3 and 4 is observed in the spectra of the raised pantograph (Figure 5.12(b)) which is radiated by the horn bush. In Figure 5.12(d), it can be seen that the noise from the cavity for cases 1 and 2 is 10 dB higher than for the empty cavity in the frequency region between 200 Hz and 800 Hz. This suggests that flow downstream of the pantographs interacts with the cavity flow in the downstream region. This produces more unsteady flow and fluctuating pressure on the aft wall surface of the cavity which radiates to the top receiver.

Table 5.2: OASPL in dB at the side and the top.

At the side (azimuthal angle $\theta = 90°$)				
Simulation cases	Whole system	Raised pantograph	Folded pantograph	Cavity
Case 0	N/A	N/A	N/A	75.4
Case 1	86.3	85.9	71.0	74.5
Case 2	85.1	84.7	70.3	72.9
Case 3	89.4	88.3	84.0	N/A
Case 4	88.6	87.6	81.0	N/A
At the top (polar angle $\phi = 90°$)				
Case 0	N/A	N/A	N/A	91.0
Case 1	95.8	91.1	76.6	93.7
Case 2	96.3	93.8	76.5	95.2
Case 3	97.9	96.1	89.7	N/A
Case 4	98.5	97.0	90.2	N/A

Table 5.3: A-weighted OASPL in dB at the side and the top.

At the side (azimuthal angle $\theta = 90°$)				
Simulation cases	Whole system	Raised pantograph	Folded pantograph	Cavity
Case 0	N/A	N/A	N/A	50.3
Case 1	79.8	79.8	60.9	50.8
Case 2	78.4	78.4	59.3	50.7
Case 3	83.8	83.1	75.3	N/A
Case 4	82.2	91.3	74.3	N/A
At the top (polar angle $\phi = 90°$)				
Case 0	N/A	N/A	N/A	78.4
Case 1	90.6	85.7	66.9	88.3
Case 2	91.0	88.2	65.9	90.9
Case 3	93.1	91.3	82.2	N/A
Case 4	93.2	92.3	83.4	N/A

(a) Total

(b) Raised pantograph

(c) Folded pantograph

(d) Only cavity and empty cavity
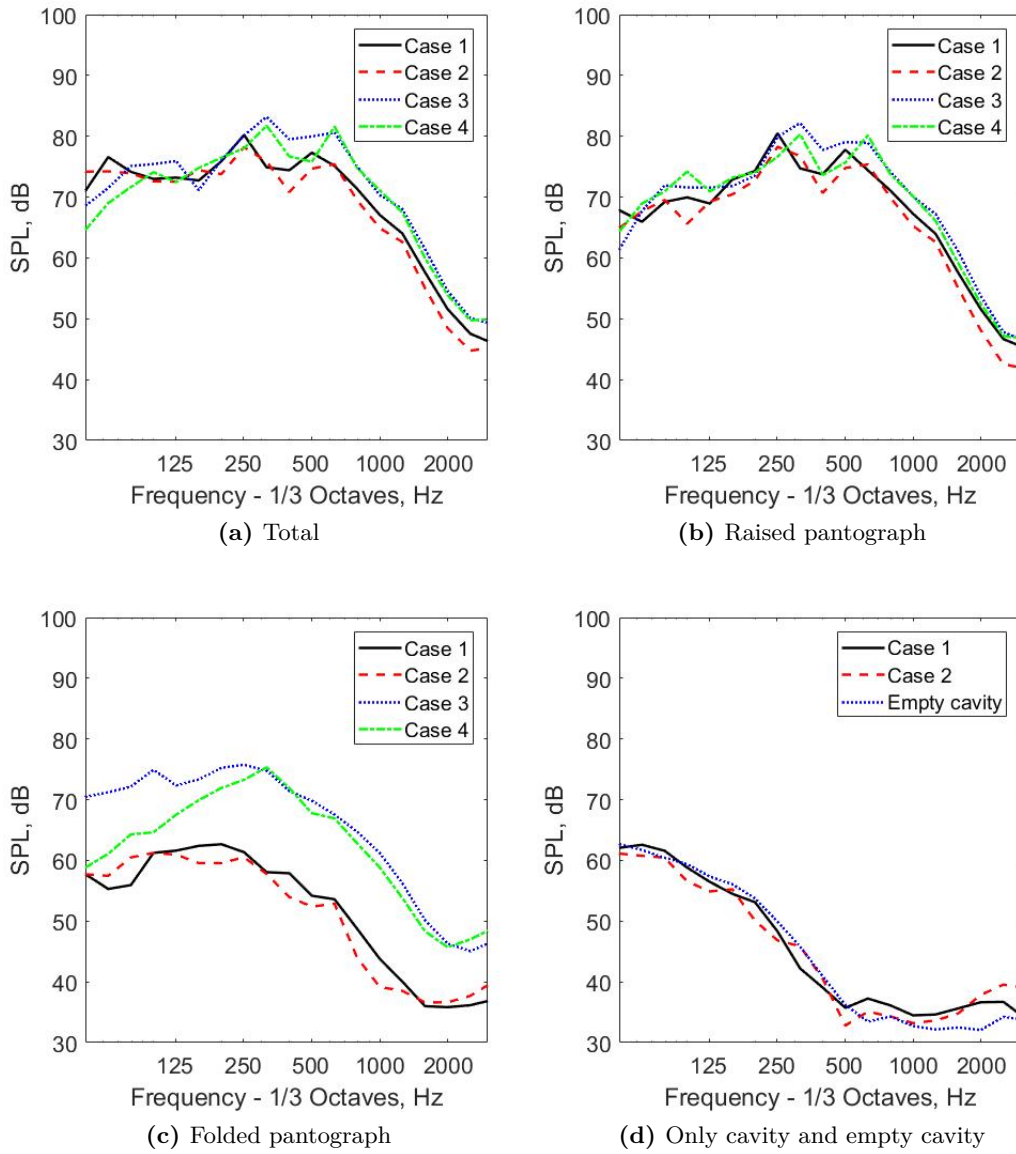
Figure 5.11: SPL at side receiver position.

(a) Total

(b) Raised pantograph

(c) Folded pantograph

(d) Only cavity and empty cavity
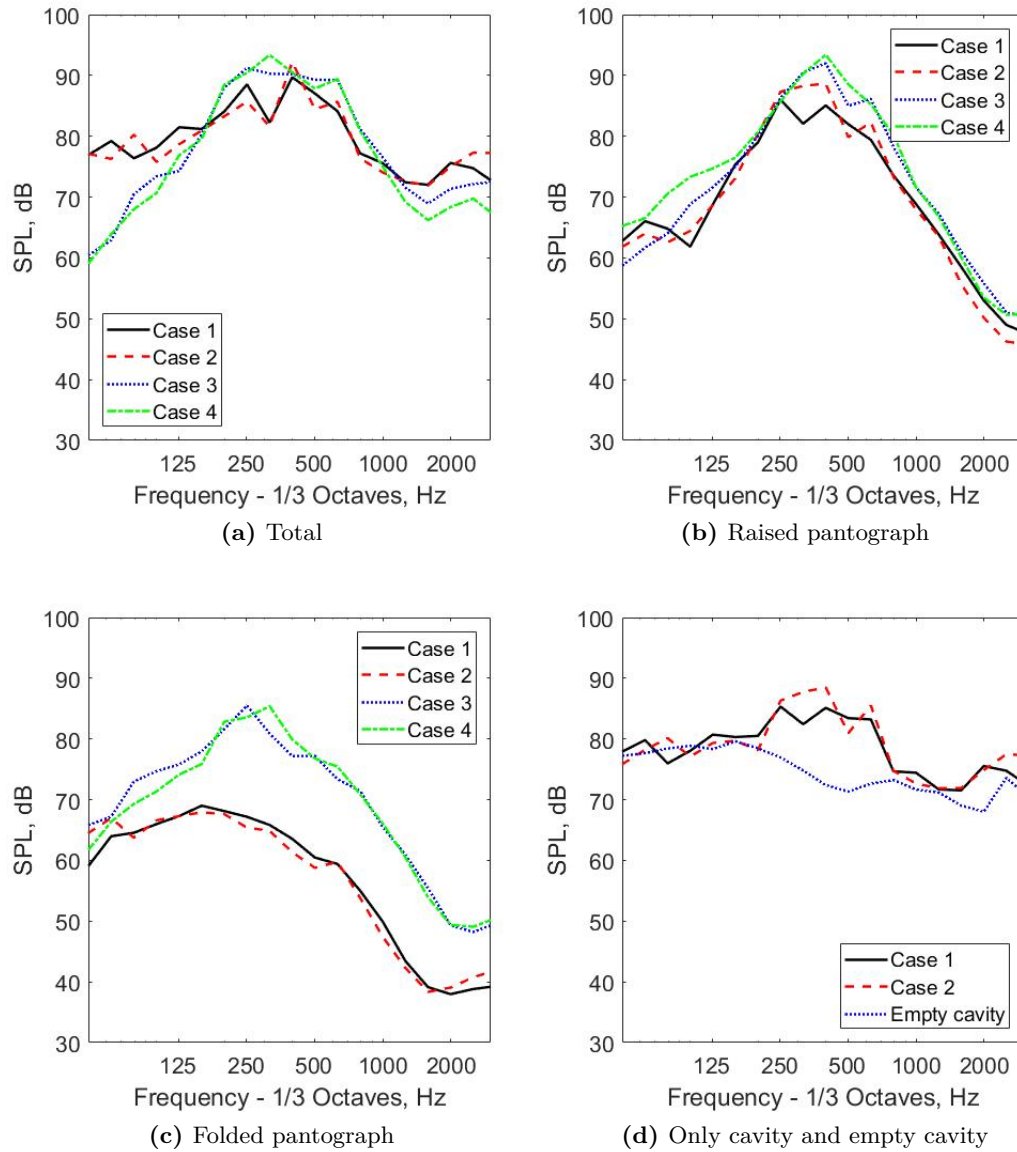
Figure 5.12: SPL at top receiver position.

5.3.2   Acoustic directivity

5.3.2.1   Three-dimensional (3D) directivity

Figure 5.13 shows the three-dimensional directivities for all cases. The OASPL is obtained by integrating the mean-square pressure over the frequency range up to 2500 Hz. To consider reflections from the train roof, receivers are also placed symmetrically below the cavity wall (or ground for cases 3 and 4), and the direct and reflected sound spectra are added accounting for their phase; the latter is taken from the direct radiated sound to the mirrored receiver. Furthermore, the inflow direction is only considered in streamwise direction (x-direction).

The other flow direction including crosswind is neglected in these results.

The OASPL is much higher above the pantograph than to the sides for all cases. Directly above the centre of the cavity floor the level is approximately 10 dB higher than that at the side position at $\theta = 90°$ for all cases. The levels downstream of the pantographs are generally greater than those in the upstream region even though convection effects are neglected.

The sound power is obtained for all cases by integrating over the full receiver grid:

$$W = \int_S \frac{p_{rms}^2}{\rho c} dS \qquad (5.1)$$

where p_{rms} is the rms acoustic pressure, ρ is the density, c is sound speed and S is the surface area. The sound power levels are listed in Table 5.4. These are given both as unweighted and A-weighted values. The sound powers for cases 1 and 2 are approximately 2 dB lower than for cases 3 and 4 due to the influence of the cavity flow as discussed in Section 5.2.

Table 5.4: Sound power levels (SWL) from case 0 with empty cavity, cases 1 and 2 with a rectangular cavity, and cases 3 and 4 without the cavity (P.R: Pantograph Raised).

Simulation cases	Unweighted SWL (dB re 10^{-12} W)	A-weighted SWL (dBA re 10^{-12} W)
Case 0 (Empty cavity)	106.5	91.8
Case 1 (Front P.R with cavity)	110.8	105.5
Case 2 (Rear P.R with cavity)	111.0	105.2
Case 3 (Front P.R without cavity)	112.7	107.9
Case 4 (Rear P.R without cavity)	112.8	107.8
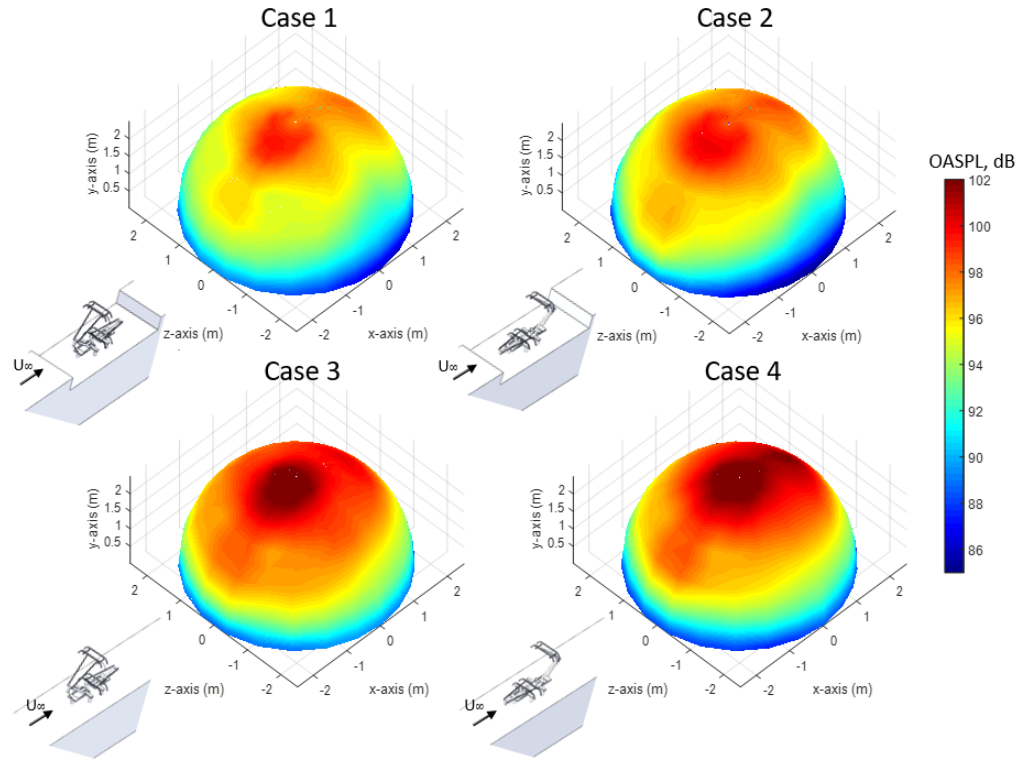
(a) Front part of isometric view
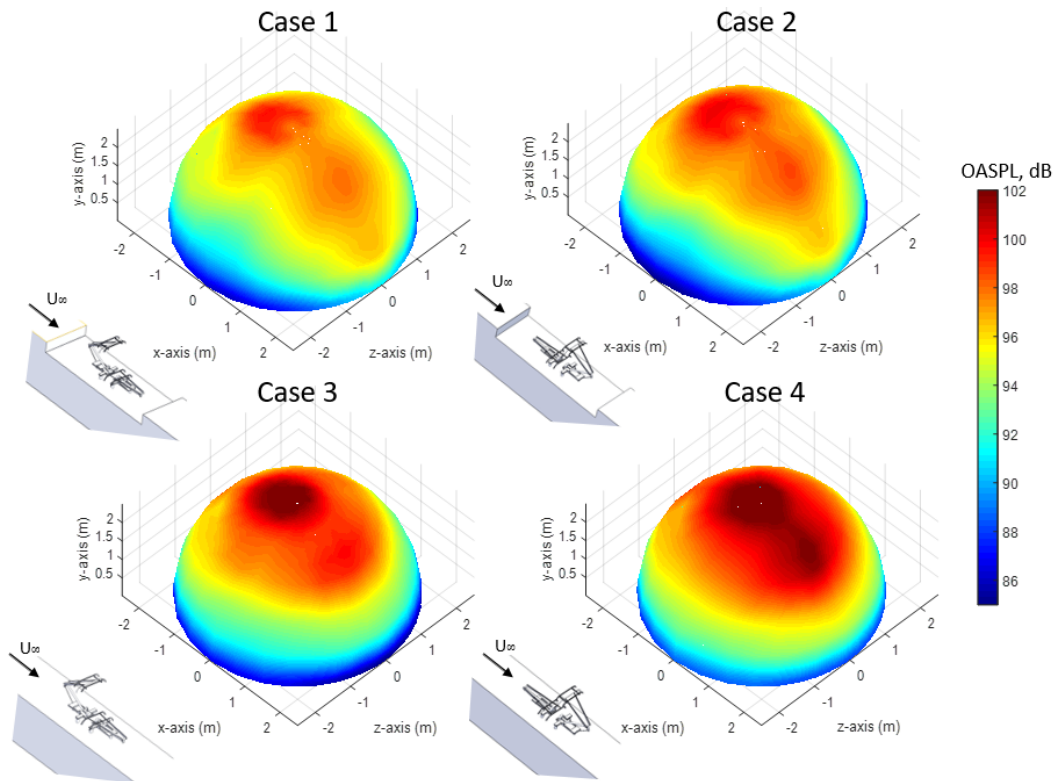
(b) Back part of isometric view

Figure 5.13: Three-dimensional noise directivity.

5.3.2.2   Two-dimensional (2D) lateral directivity

Figure 5.14 shows far-field directivities in a horizontal plane for the noise radiated from the whole system (a), the raised pantograph (b), the folded one (c) and the cavity (d). The directivity patterns for the noise radiated from the whole system are similar for all four cases. However, the maximum OASPL appears at $\theta = 180°$ for cases 1 and 2 and at $\theta = 90°$ for cases 3 and 4. The noise at $\theta = 90°$ has the highest level for case 3 at 89.4 dB and for case 4, it is similar at 89.0 dB. For case 2 at the same location, the level is lower at 85.1 dB. This is because the noise level of the raised and folded pantographs for cases 1 and 2 is reduced by the cavity flow, which causes lower incoming velocity at the pantographs, as discussed in Section 5.2.2. This can also be seen in Figure 5.14(b) and (c). At $\theta = 90°$, the noise level from the raised pantograph for case 3 is approximately 4 dB greater than for case 2. For the folded pantograph, there are large differences between the cases with and without the cavity; the noise level for case 3 is about 13 dB higher than that for case 2 at $\theta = 90°$. The noise radiated from the cavity is not significant compared with the pantographs at the lateral position. However, its levels are still quite large at $\theta = 180°$ and $\theta = 360°$.

(a) Total   **(b)** Raised pantograph

(c) Folded pantograph **(d)** Only cavity and empty cavity
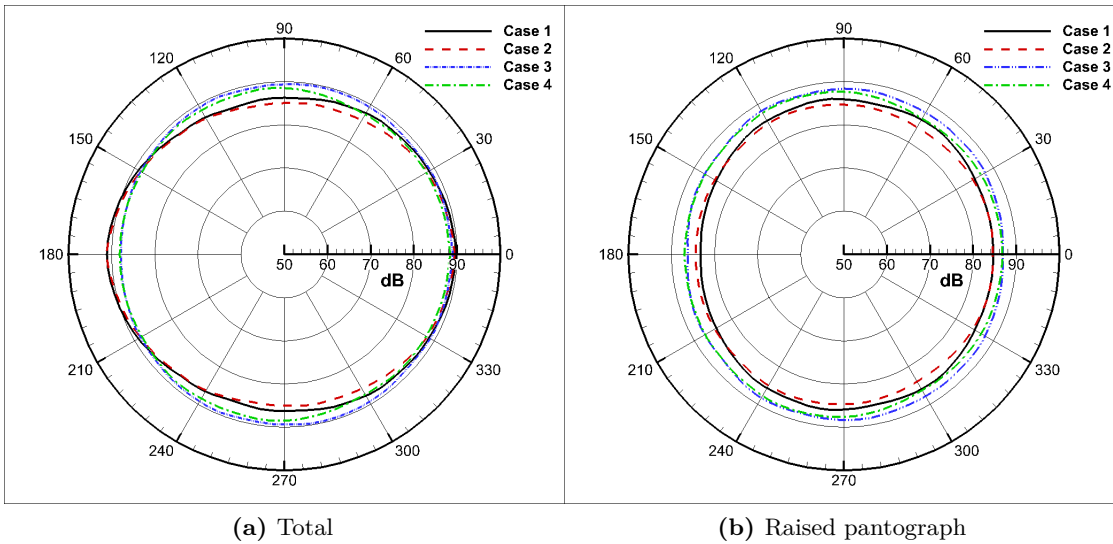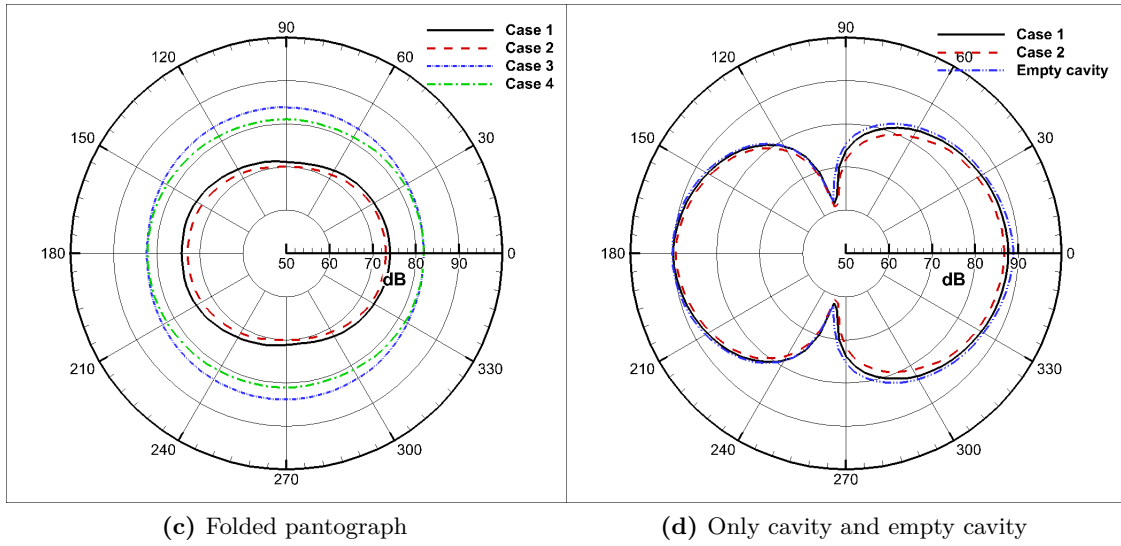
Figure 5.14: OASPL side directivity.

5.4 Summary

The flow field and radiated noise of two DSA 350 pantographs (one raised and one retracted) located in a cavity have been investigated and compared with those for the same pantographs installed on a flat surface without the cavity.

Highly unsteady flow is generated in the region of the cavity and the panhead of the raised pantograph. The separated shear layer from the cavity leading edge impinges on the pantographs and the cavity. This rolls up and becomes a spanwise vortical structure. The numerical flow visualisation shows interaction between the cavity shear layer and the pantograph. The flow separates again at the cavity trailing edge. Strong vortices are seen to be generated by the lower parts of the pantographs in cases without the cavity.

It is found that a slightly lower velocity occurs upstream of the panhead of the raised pantograph for cases with the cavity due to the effect of the cavity flow. Furthermore, the flow velocity inside the cavity is much lower than the freestream velocity. This leads to reduced surface pressure fluctuations on both the raised and the folded pantographs, and lower radiated noise levels. The largest pressure fluctuations occur on the contact strip and the horn of the raised pantograph and its lower arm for all cases. Furthermore, large fluctuations appear on the panhead and frame of the folded pantograph for cases without the cavity.

The radiated noise level is dominated by the panhead of the raised pantograph with strong tonal noise, whereas the noise radiated from the folded pantograph has no strong tonal component. A comparison between cases with and without the cavity shows that the noise

from the pantographs is reduced by the cavity flow. However, the cavity also generates highly unsteady flow. It is found that the OASPL above the pantographs is much higher than that at the side. Furthermore, the different train running directions have no significant impact on the total noise radiated, with differences of less than 1.5 dB in spectral levels and less than 1 dB in OASPL.

Chapter 6

Effect of cavity flow control on a high speed train pantograph noise

It was shown in Chapter 5 that the noise radiated from the cavity wall is considerable in the low frequency region. However, the noise reduction treatments for a closed cavity (of which the pantograph recess is an example) have been given less attention than a open cavity. This Chapter aims to study an efficient technique to control the cavity flow for the purpose of noise reduction. As most noise is generated by the shear layers from the leading edge and trailing edge of the cavity, and their impingement on other components. the effects of modifications to the leading edge and the trailing edge are investigated. Furthermore, this Chapter aims to provide understanding of the effect of the modified cavity flow on the pantographs (one raised and one folded). The Chapter is structured as follows: Section 6.1 describes the geometry of the cavity modification and details of the grid generation and the computational set-up. Section 6.2 presents the computational flow field results for the modified cavity, while far-field pressure results are presented in section 6.3. In Section 6.4, aerodynamic and acoustic simulations are presented for the best case of the modified cavity with pantographs installed. The findings are summarised in Section 6.5.

6.1   Computational set-up

6.1.1   Geometry

As in the previous chapter, the cavity geometry is chosen to represent a simplified 1/10 scale pantograph roof cavity of a TGV train. This is simplified to a rectangular cavity with length $L = 0.812$ m, depth $D = 0.07$ m and width $W = 0.29$ m, giving $L/D = 11.5$, W/D = 4.1. The cavity is then modified by sloping the upstream and downstream surfaces while retaining a fixed depth D and floor length L(Figure 6.1(a)). The angle θ is varied from 30° to 75°. In an alternative approach, the cavity leading and trailing edges are rounded

Table 6.1: Summary of the cases

Cavity edges treatments cases	
Cavity with rounded edges cases	Cavity with angled edges cases
$h/D = 0.2$	$\theta = 30°$
$h/D = 0.4$	$\theta = 45°$
$h/D = 0.6$	$\theta = 60°$
$h/D = 0.8$	$\theta = 75°$
Cavity with the pantographs cases	
Case 1	Baseline cavity with front pantograph raised
Case 2	Baseline cavity with rear pantograph raised
Case 3	Modified cavity with front pantograph raised
Case 4	Modified cavity with rear pantograph raised

with a radius h as shown in Figure 6.1(b) with the ratio h/D varying from 0.2 to 0.8. The modifications are the same for both front and rear as trains operate in both directions. All cases are summarised in Table 6.1.

(a) Side view

(b) Side view
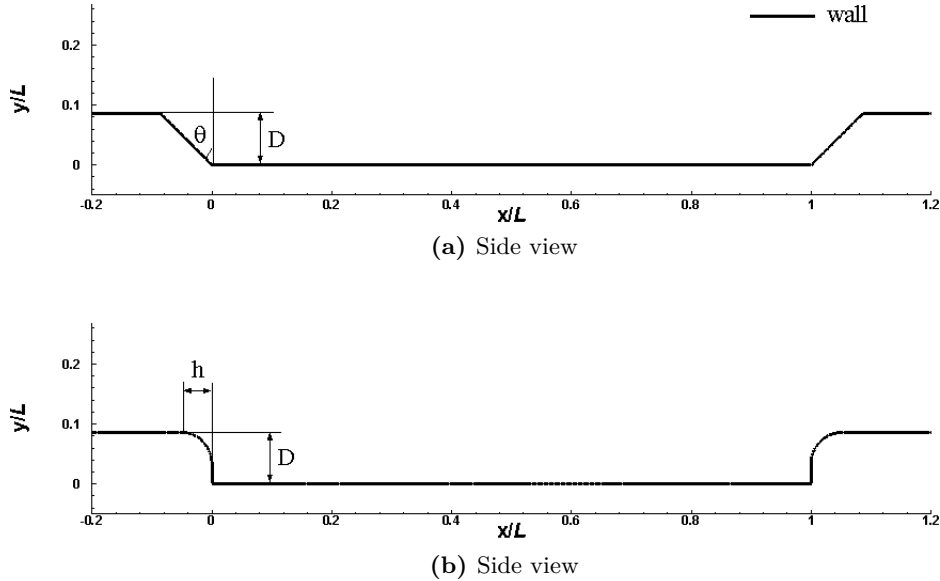
Figure 6.1: Description of the geometry.

6.1.2   Numerical test section

The computational domain is illustrated in Figure 6.2. It has dimensions of $71.5D$, $29D$ and $4.1D$ along the streamwise (x), vertical (y) and spanwise (z) directions, respectively. No-slip wall conditions are applied to the cavity walls, while symmetry conditions are used for the top boundary and a pressure outlet is imposed at the outlet boundary. Periodic boundary conditions are applied to the two side surfaces of the domain. The inflow boundary is set as a velocity inlet with incoming flow velocity $U_\infty = 83.3$ m/s (300 km/h). A hexa-dominated

mesh, generated using the STAR-CCM+ mesh generator, is used with several refinement zones. Different cell sizes are specified for each refinement zone. The cell aspect ratio near the wall is 200 (Δx / Δy, Δz / $\Delta y = 200$) as determined in Chapter 4. The details of the mesh around the cavity edges are shown in Figure 6.3 and the number of cells for each case is listed in Table 6.2. The non-dimensional cell size perpendicular to the wall y_1^+ is less than 1 on all wall surfaces. The non-dimensional time step is $U\Delta t/D = 0.0095$ ($\Delta t = 8 \times 10^{-6}$s), where D is depth of the cavity. The Reynolds number is $Re = 3.9 \times 10^5$ based on the cavity depth and the inflow velocity.
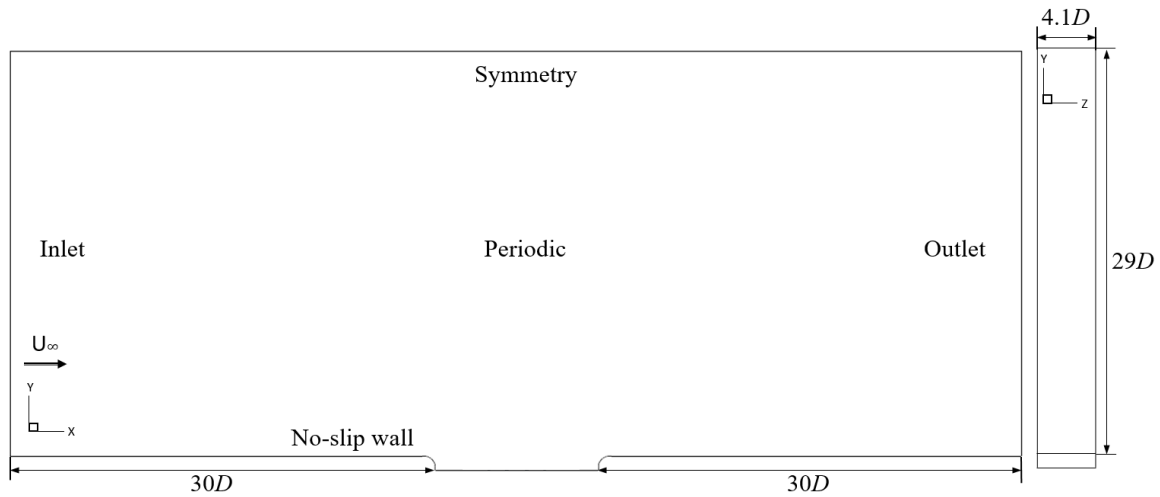
Figure 6.2: Computational domain and boundary conditions.

(a) Overall view of the cavity leading edge mesh **(b)** Detailed view of the cavity leading edge mesh

(c) Overall view of the cavity leading edge mesh **(d)** Detailed view of the cavity leading edge mesh
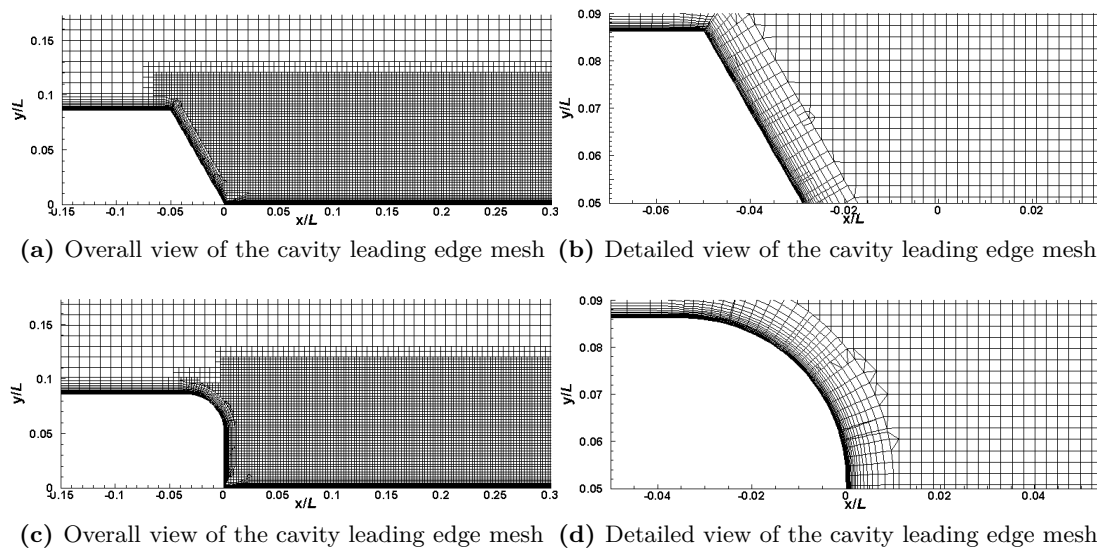
Figure 6.3: Overview and details of the meshes.

Table 6.2: The grid for each cases.

Simulation cases		Number of cells
Rounded edge cases	$h/D = 0.2$	7.3 million
	0.4	7.3 million
	0.6	7.4 million
	0.8	7.5 million
Angled edge cases	$\theta = 30°$	7.4 million
	45°	7.6 million
	60°	7.9 million
	75°	8.1 million

6.2   Aerodynamic results for the modified cavities

6.2.1   Forces

The coefficients of lift C_L and drag C_D ($C_F = \frac{2F}{\rho u^2 A}$ where F is force, ρ is density of air, and A is reference area) are shown in Figure 6.4 for the cavity with rounded (h/D cases) and angled (θ cases) treatments. Both the mean and the rms values are shown for each coefficient. The reference area for the force coefficients is the cavity cross-section $W \times D = 0.0196$ m^2. The force coefficients were calculated after 0.05s when the flow was deemed to be statistically steady from the force coefficients time history. The coefficient data were then collected at each time step for another 0.2s.

The treatment of the leading and the trailing edges of the cavity induces changes in the force coefficients. Both treatments show a reduction in the mean drag coefficient $\overline{C}_D$ with reductions of 54% for $h/D = 0.8$ and 20% for $\theta = 60°$, compared with the baseline case. The mean lift coefficients $\overline{C}_L$ show negative values for all cases. When the cavity edges are rounded, the negative mean lift coefficient is reduced by 34%, compared with the baseline case and it remains almost constant for all values of h/D. The angled edges cases also show a reduction in the negative mean lift coefficient, by 17% for $\theta = 30°$, 45° and 60° and 10% for $\theta = 75°$.

In all cases, the fluctuating lift coefficient (C_L^{rms}) is much larger than the fluctuating drag coefficient (C_D^{rms}). Both treatment methods of the cavity edges reduce the fluctuating lift and drag forces considerably. The largest reductions are the rounded edges. For $h/D = 0.8$, the fluctuating lift and drag forces are reduced by 89% and 88%, respectively, compared with the baseline case.

(a) $\overline{C}_L$

(b) $\overline{C}_D$

(c) C_L^{rms}

(d) C_D^{rms}
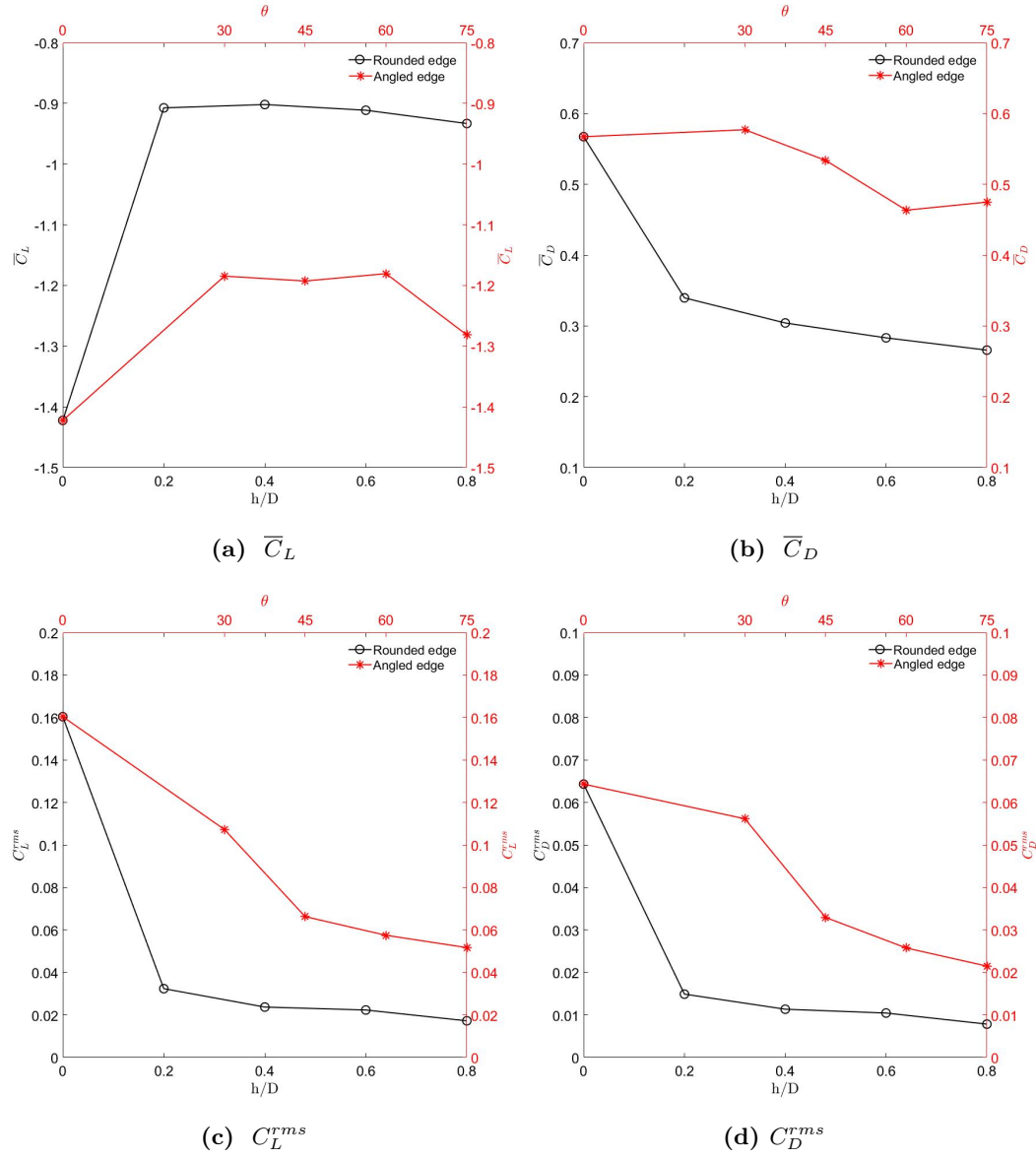
Figure 6.4: Force coefficients for different cavity edge treatment cases.

6.2.2   Q-criterion

Figure 6.5 and 6.6 shows three-dimensional instantaneous flow features around the cavity based on the *Q*-criterion, the second invariant of the velocity gradient [93] (see also Section 5.2.1). The iso-surfaces are coloured by the instantaneous velocity magnitude. For the baseline configuration shown in Figure 6.5(a) and 6.6(a), the incoming flow separates from the cavity leading edge. After the separation, Kelvin-Helmholtz (K-H) instabilities in the shear layer start to develop and a highly turbulent flow occurs in the cavity region and another highly unsteady flow region is seen at the cavity trailing edge and aft cavity wall region. When the cavity edges are rounded, the highly turbulent flow generated at the trailing edge of the cavity is significantly reduced as shown in Figure 6.5(b) - (e). This can also be seen in the turbulence kinetic energy which is shown in Figure 6.7. It can effectively diminish the unsteady flow in this region even when the trailing edge is only slightly modified (see Figure 6.5(b)). Furthermore, the shear layer from the cavity leading edge is weakened by the rounding.

Results for angled cavity walls are shown in Figure 6.6. Here also the highly unsteady flow is reduced. However, the reduction of the turbulent flow generated by the cavity trailing edge is much smaller than for the cases with the rounded cavity edges. The strength of the shear layer from the leading edge is similar to the baseline case.

(a) Baseline

(b) $h/D = 0.2$

(c) $h/D = 0.4$

(d) $h/D = 0.6$

(e) $h/D = 0.8$
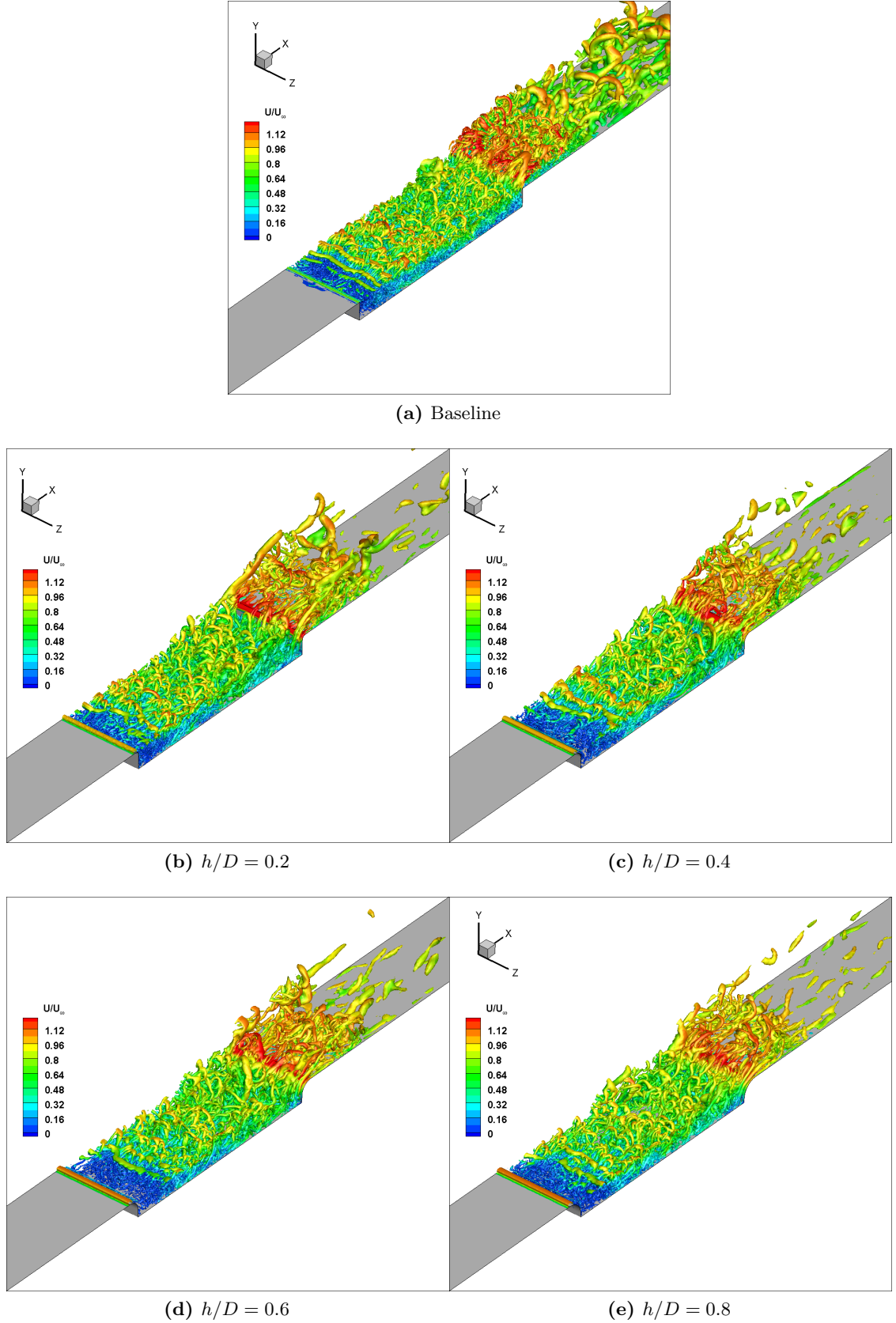
Figure 6.5: Flow structure demonstrated for the rounded cavity edge by iso-surface of Q-criterion with Q_{norm}=2.5.

(a) Baseline

(b) $\theta = 30°$

(c) $\theta = 45°$

(d) $\theta = 60°$

(e) $\theta = 75°$
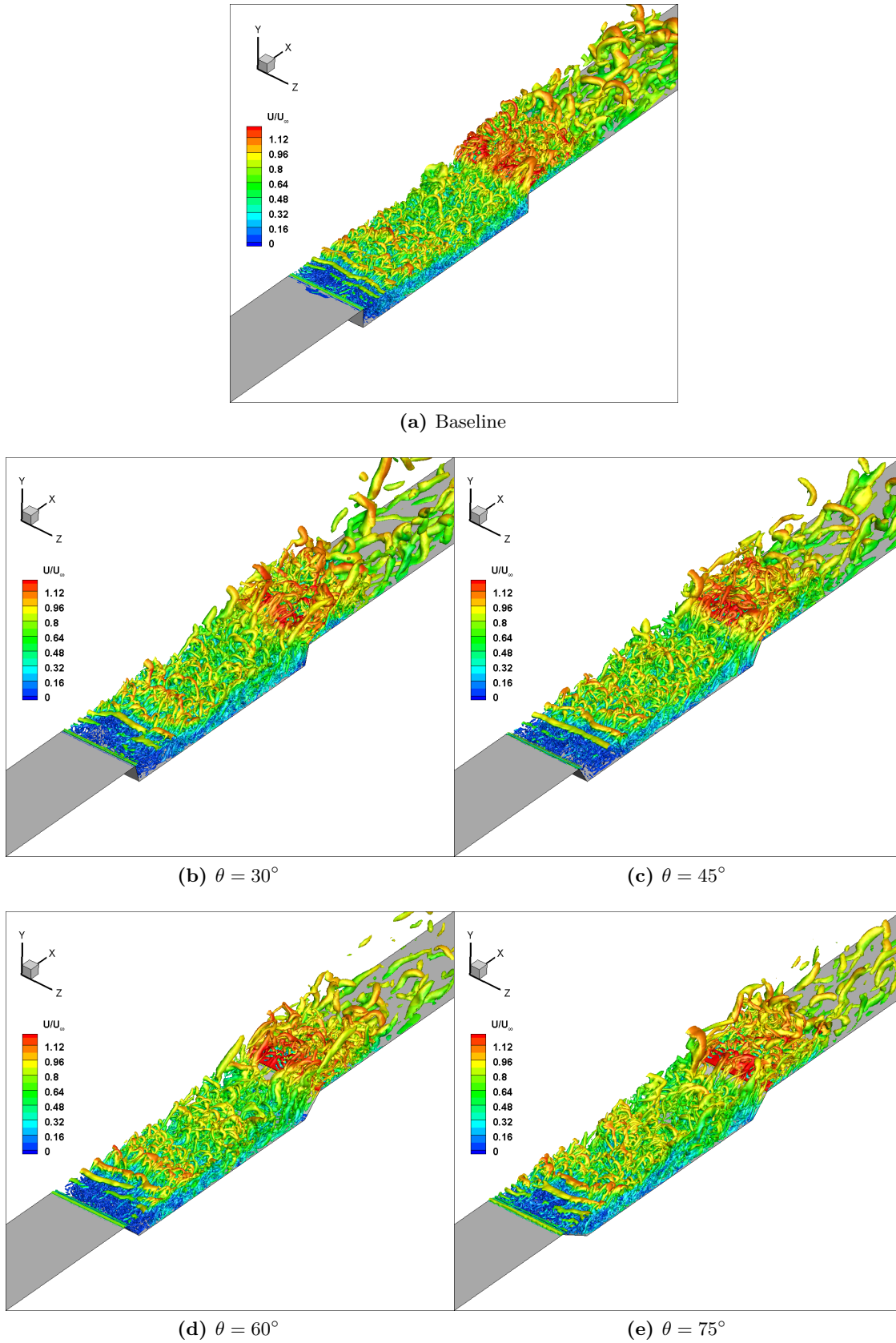
Figure 6.6: Flow structure demonstrated for the angled cavity edge by iso-surface of Q-criterion with Q_{norm}=2.5.

(a) Baseline

(b) $h/D = 0.8$

(c) $\theta = 75°$
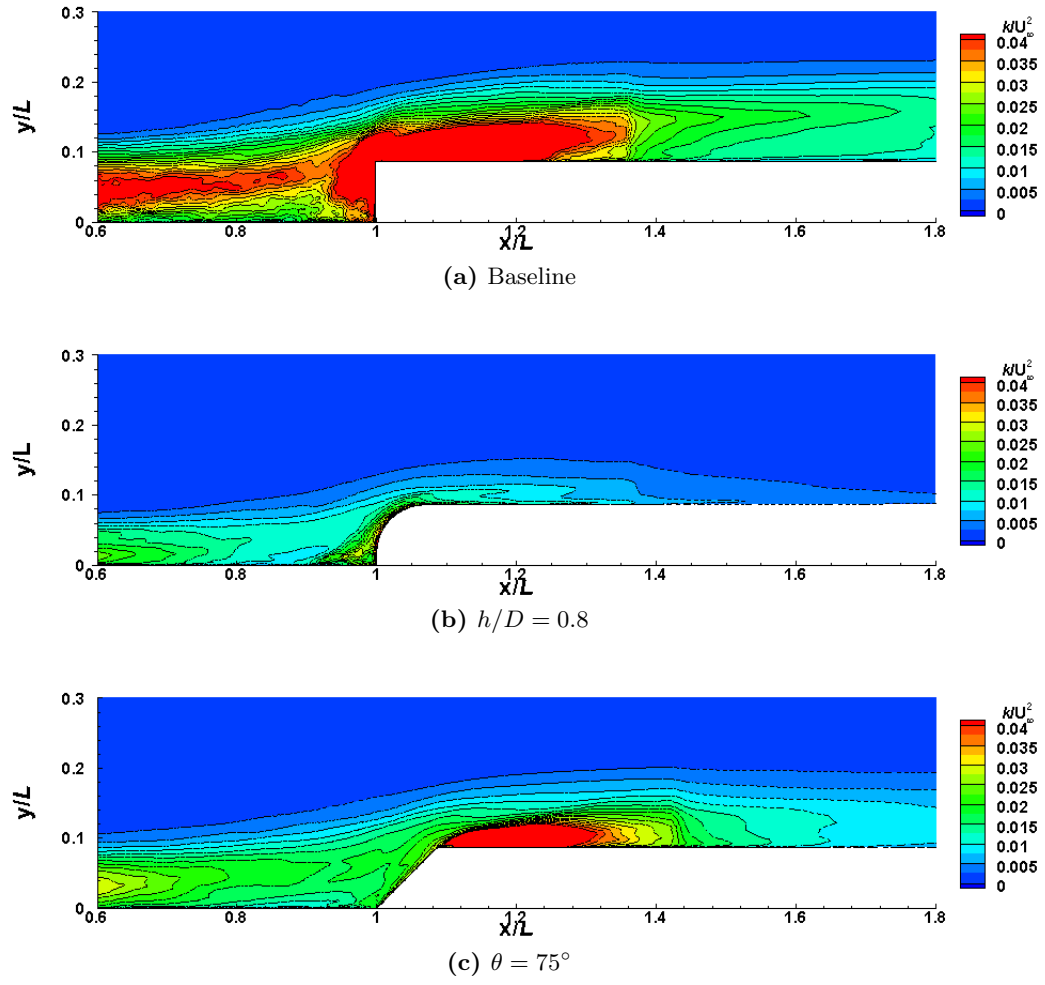
Figure 6.7: Comparison of turbulence kinetic energy for the baseline (a), $h/D = 0.8$ (b) and $\theta = 75°$ (c) in the cavity trailing edge region.

6.2.3   Time-averaged velocity field

Figure 6.8 and 6.9 displays contours of the time-averaged streamwise velocity at the mid-span plane together with two-dimensional sectional streamlines. For the baseline cavity shown in Figure 6.8(a) and 6.9(a), the incoming flow separates from the leading edge of the cavity and the shear layer begins to develop. This shear layer impinges on the cavity floor around $x/L = 0.6$, which introduces a recirculation region between $x/L = 0$ and $x/L = 0.6$. When the cavity edge is rounded, and the shear layer impingement point moves upstream. This recirculation region becomes smaller. For $h/D = 0.2$, the impingement point occurs at $x/L = 0.48$. The point moves further upstream on the cavity walls are rounded more and reaches $x/L = 0.4$ for $h/D = 0.8$. A similar flow pattern can be seen in the angled edge cases. By increasing the angle θ, the shear layer impingement point moves upstream and the recirculation region becomes smaller. However, the change is not as far as the rounded edge cases.

Another recirculation occurs in the vicinity of the trailing edge. The flow separated from the cavity trailing edge reattaches on the cavity aft wall at $x/L = 1.1$. This recirculation is eliminated for all rounded trailing edge cases, whereas it is only eliminated for sloped edge cases at large angles ($\theta = 60°$ and $75°$), and is reduced in size for the other sloping angles. The cavity edge treatments reduce unsteady flow from the cavity and the effect of these flow field changes on the far-field noise will be quantified in Section 6.3.
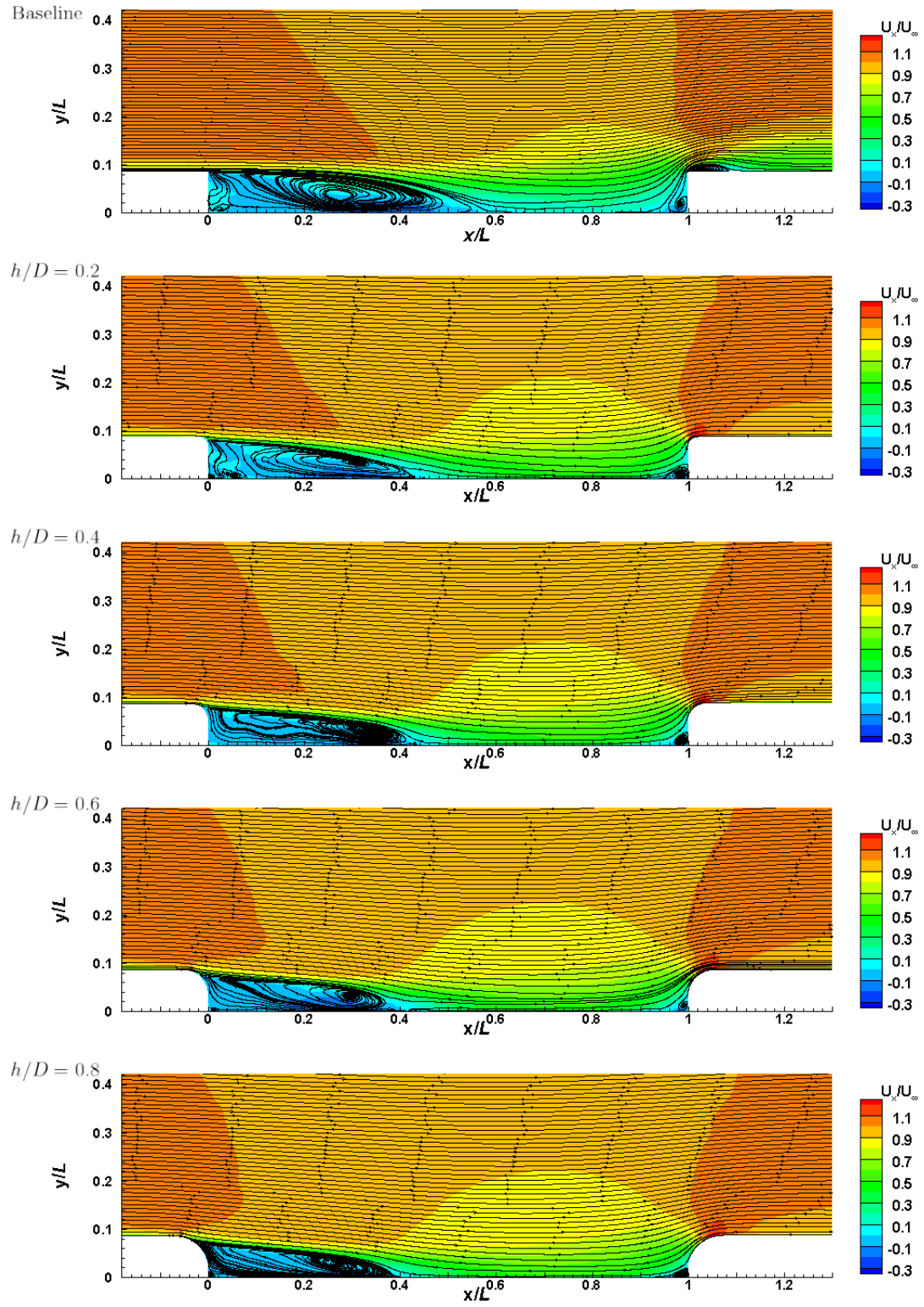
Figure 6.8: Mean streamline with time-averaged velocity contours for baseline cavity and the rounded cavity edge cases.
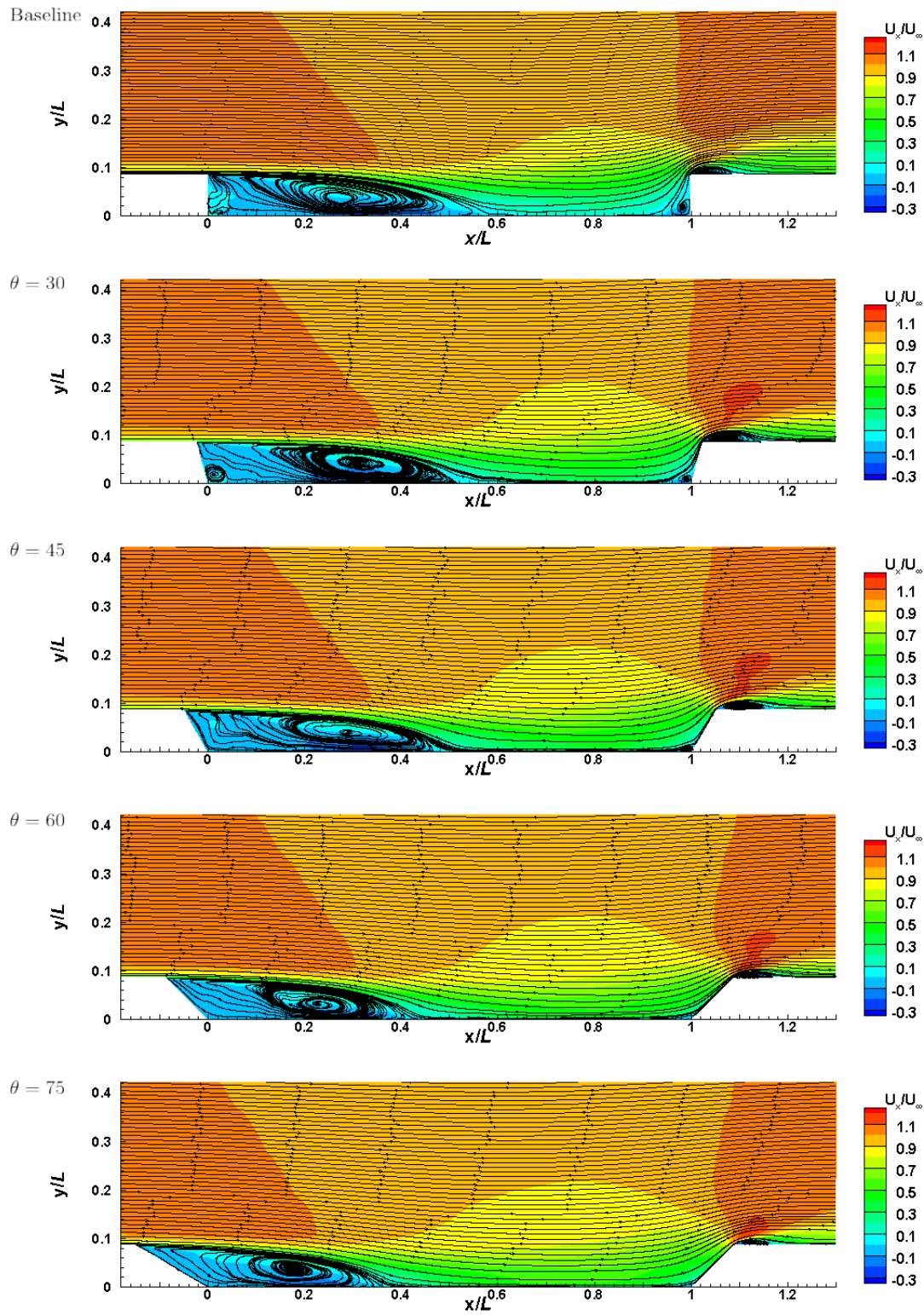
Figure 6.9: Mean streamline with time-averaged velocity contours for baseline cavity and the angled cavity edge cases.

6.3 Aeroacoustic results for the modified cavities

The radiated noise is predicted for two far-field receivers, located 2.5 m away from the centre of the cavity at the side and at the top. The far-field pressure sampling frequency was 125 kHz and a Hanning window with 50% overlap was used to determine the spectra [92]. All spectra are converted to full scale frequencies and amplitudes according to Equation 4.2 and 4.2 and are presented in one-third octave bands.

The spectra of the far-field pressure from the cavity is plotted in Figure 6.10. There are no strong tonal components as expected for a classic closed cavity [34]. By rounding the cavity edges, the SPLs at the side and the top receivers are reduced in the low frequency region below about 630 Hz, but they are unaffected at high frequency as shown in Figure 6.10 (a) and (b). Similarly, the spectra of the radiated noise from the angled edge configurations become lower in the low frequency region as the angle θ is increased. However, the spectra of the noise for $\theta = 60°$ and $75°$ are similar. These reductions are not as significant as for the rounded edge cavity configurations.

The OASPLs, calculated by integrating the spectra over frequency up to 2000 Hz, are given in Table 6.3. Compared with the noise levels for the baseline case, the case with rounded edges with $h/D = 0.8$ shows a reduction of 15.2 dB for the receiver at the side, and of 12 dB for the receiver at the top. The noise levels for the angled edge with $\theta = 75°$ are approximately 5.3 dB lower at the side, and 7.2 dB lower at the top than the levels for the baseline case. The rounded cavity edges with $h/D = 0.8$ have the largest effect on the noise from the cavity.

Table 6.3: OASPL at the side and the top receiver positions and values of the difference relative to baseline.

Simulation cases		Side (dB)	Difference	Top (dB)	Difference
Baseline		75.4		91.0	
Rounded edge cases	$h/D = 0.2$	66.3	9.1	85.6	5.4
	0.4	63.9	11.5	82.2	8.8
	0.6	62.0	13.4	80.6	10.4
	0.8	60.2	15.2	79.0	12
Angled edge cases	$\theta = 30°$	72.8	2.6	89.1	1.9
	45°	70.6	4.8	86.5	4.5
	60°	69.8	5.6	85.2	5.8
	75°	67.9	7.5	83.8	7.2

(a) Rounded edge cases at side

(b) Rounded edge cases at top

(c) Angled edge cases at side

(d) Angled edge cases at top
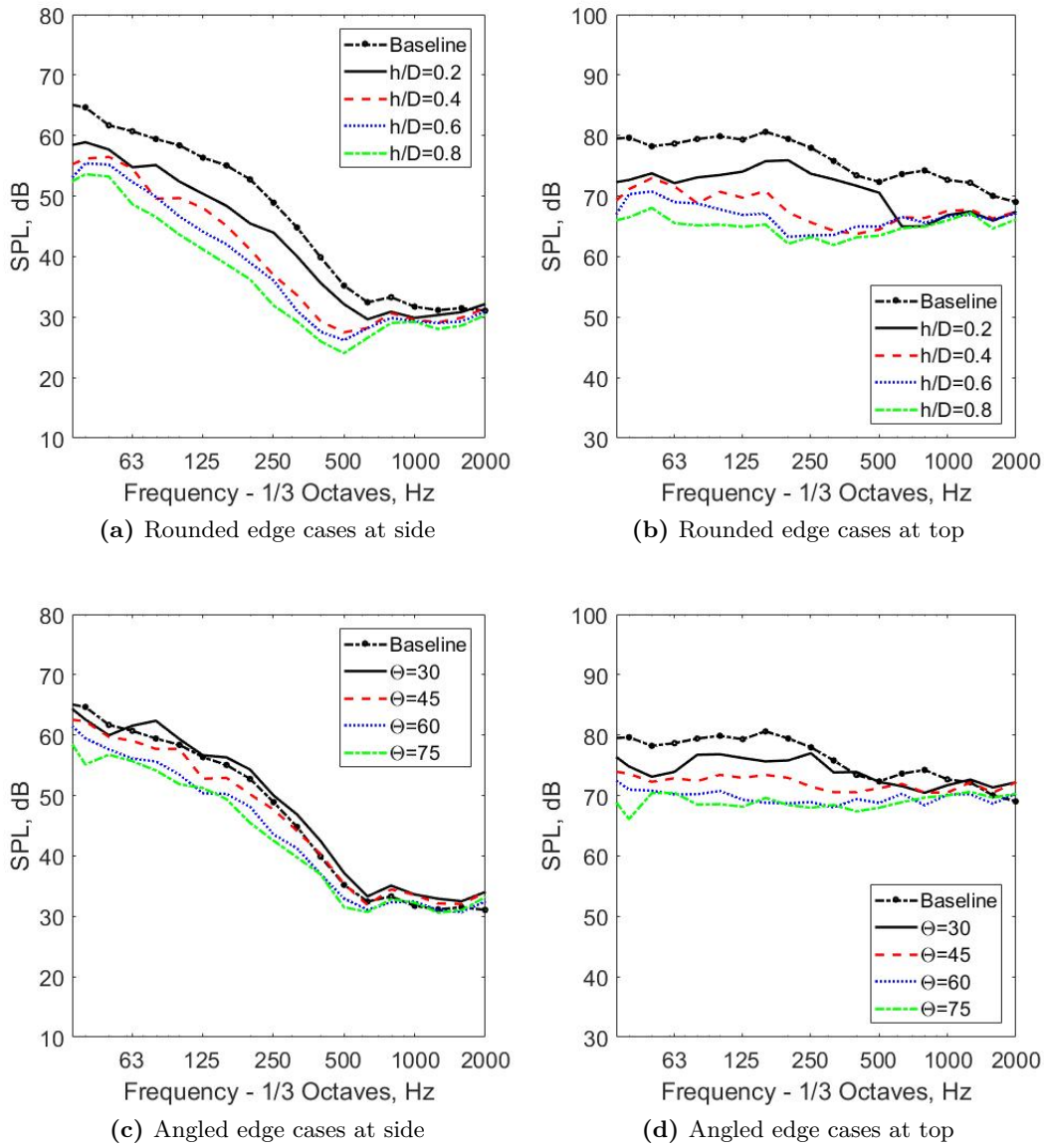
Figure 6.10: SPL at side and top receiver positions.

6.4 Effect of the cavity geometry on pantograph noise

6.4.1 Geometry

The influence of the cavity edge treatment on the flow and the noise of the pantographs is investigated here. In the previous Section, the rounded case with $h/D = 0.8$ shows the lowest level of noise from the cavity. This treatment is therefore chosen to investigate effects of the modified cavity on pantograph aerodynamic noise. Two DSA 350 pantographs (one raised and one folded) are installed inside the cavity and these cases (cases 3 and 4) are compared with a rectangular cavity (cases 1 and 2) as considered in Chapter 5. Furthermore, the effects of the train running direction are investigated. The freestream direction is set as the positive x-direction for cases 1 and 3, and as the negative x-direction for cases 2 and 4, as shown in Figure 6.11(a). The simplified pantograph shown in Figure 4.18(c) is again used. The origin of the coordinate system is at the cavity floor and the upstream wall edge corner, as shown in Figure 6.11.

(a) Side view
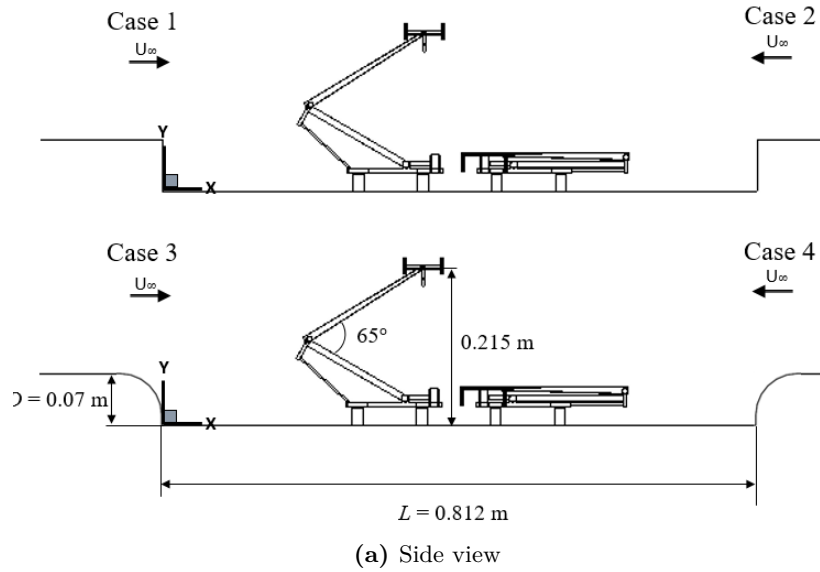
Figure 6.11: Description of the geometry of the baseline (cases 1 and 2) and the rounded cavity (cases 3 and 4 with the pantographs.

6.4.2 Numerical test section

The computational domain size and boundary conditions are identical with the previous cavity cases as shown in Figure 6.2. A Hexa-dominated mesh is also used for the pantographs. Different cell sizes are specified for each refinement zone. Several refinement zones are used for the pantograph components and wake regions. The total number of cells used for each case is listed in Table 6.6. It is verified that y_1^+ is less than 1 on all surfaces. As before, a non-dimensional time step $U\Delta t/D = 0.0095$ ($\Delta t = 8 \times 10^{-6}$s) is used.

Table 6.4: The grid for each cases

Cases	Description of the case	Number of cells
Case 1	Front pantograph raised with baseline cavity	30.4 million
Case 2	Rear pantograph raised with baseline cavity	29.4 million
Case 3	Front pantograph raised with the rounded cavity edges	31.5 million
Case 4	Rear pantograph raised with the rounded cavity edges	29.5 million

6.4.3   Aerodynamic results

6.4.3.1   Time-averaged velocity field

Figure 6.12 displays contours of the mean streamwise velocity at the mid-span plane ($z/W = 0.5$) together with two-dimensional in-plane streamlines. For the two cases in which the cavity edges are rounded (cases 3 and 4), the incoming flow follows and attaches initially to the rounded edge surface before separating at $\theta = 30°$, whereas the flow separates immediately at the leading edge for cases 1 and 2. Due to the delayed separation in cases 3 and 4, the separated shear layer reattaches earlier to the cavity floor and generates smaller recirculation regions, and only interacts with pantograph components in the foot part of the cavity. Variation of the flow separation changes the behaviour of the separated shear layer and its interaction with the pantographs and the cavity. The shear layer impinges onto the upstream part of the cavity ($x/L = 0.3$) and interacts with the front foot of the raised pantograph in case 3 and the joint of the folded pantograph in case 4. However, the shear layer impinges at the middle of the cavity floor and interacts with more parts of the pantographs in both cases 1 and 2. The separated flow impinges on most of the lower parts of the raised pantograph including the foot, the frame and the control strut in case 1. In case 2, most of the folded pantograph panhead is within the shear layer impingement region. These different impingement regions may generate different features of the surface pressure fluctuations of the pantographs, which will be discussed below.

(a) Case 1

(b) Case 2
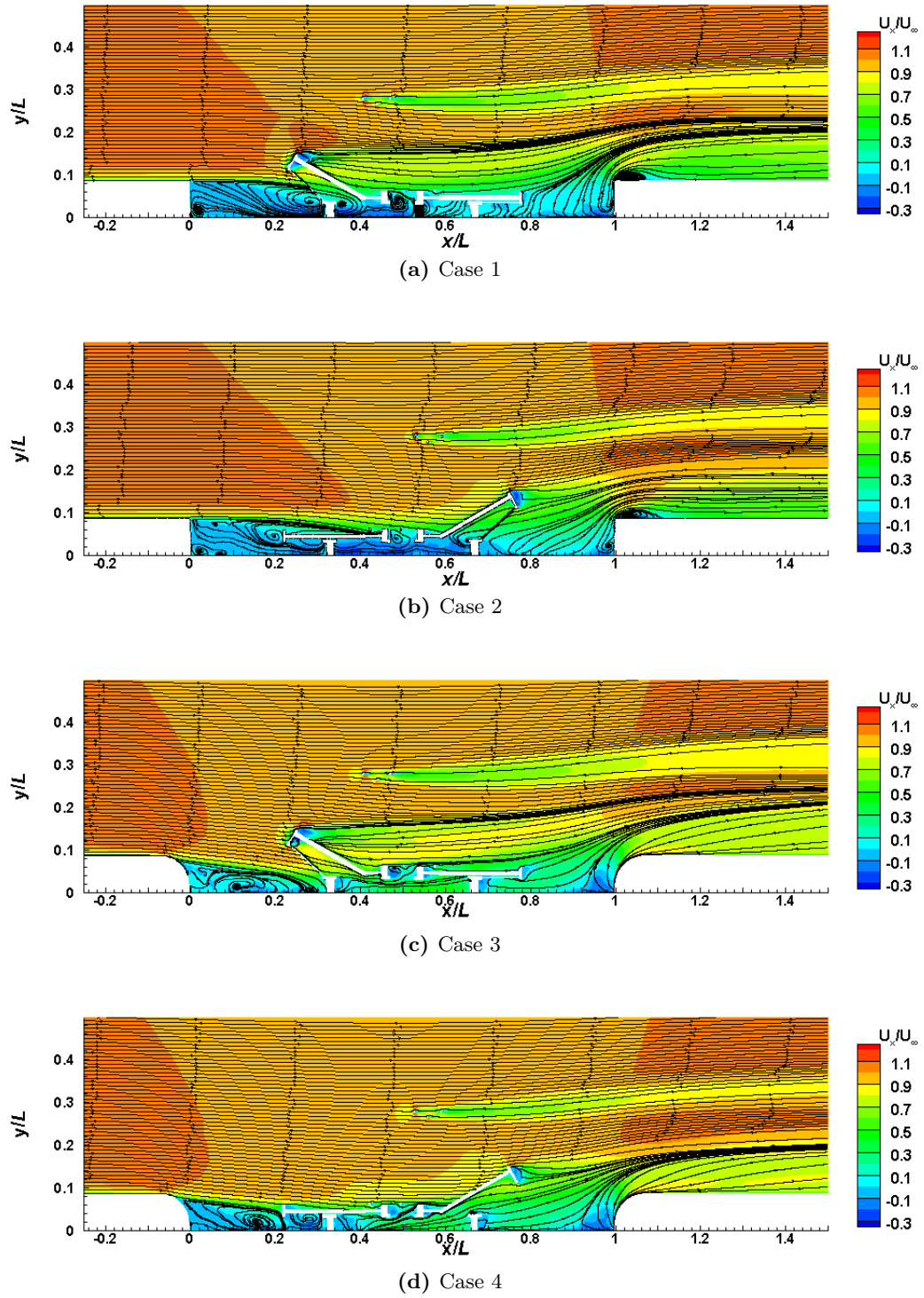
(c) Case 3

(d) Case 4

Figure 6.12: Mean streamline with time-averaged velocity contours, (a) case 1 (baseline cavity), (b) case 2 (baseline cavity), (c) case 3 (the rounded cavity edge), (d) case 4 (the rounded cavity edge).

Figures 6.13 and 6.14 display the profiles of the time-averaged streamwise velocity U_x at different streamwise and spanwise locations for the four cases with pantographs. The lines at $x/L = 0.43$ for cases 1 and 3 are located just before the upstream contact strip of the raised pantograph and the lines at $x/L = 0.45$ are just in front of the horn of pantograph. In cases 2 and 4, the lines at $x/L = 0.52$ and at $x/L = 0.54$ are located at the upstream contact strip and the horn of the raised pantograph.

The profiles in cases 1 and 3 are similar for all locations above the cavity region ($y/D = 1 \sim 4$), but for case 3, the flow speed in this region is approximately 3% lower that for case 1 at $x/L = 0.26$ and $x/L = 0.34$. For case 3, the flow speed outside the cavity region is generally smaller than case 1, whereas with rounded cavity edges the flow speed is higher in the cavity region than for the rectangular cavity. Similar flow features can be seen between cases 2 and 4 as shown in Figure 6.14. This means that the rounded cavity edge reduces the flow speed around the upper parts of the raised pantograph (the upper arms and the panhead), but increases the flow velocity around the lower parts of the raised pantograph and the whole folded pantograph.

At the locations just ahead of the panhead ($x/L = 0.43$) and the horn of the raised pantograph ($x/L = 0.45$), the values of U_x between $y/D = 3$ and 3.5 in case 3 are about 4% lower than case 1. A similar tendency is also seen at $x/L = 0.52$ and 0.54 in cases 2 and 4. The effect of the rounded cavity edge on the flow upstream of both the raised and folded pantographs will change the levels of the radiated noise from the pantographs, compared with cases 1 and 2. This will be discussed in more detail in the far-field results section.
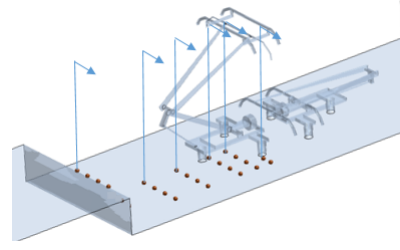
(a) Line positions
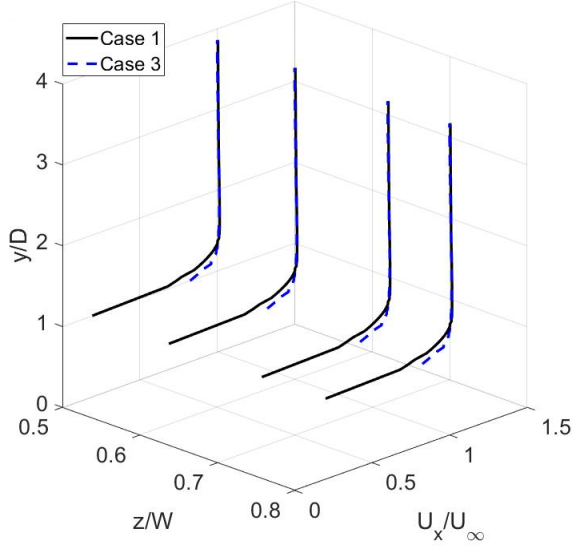
(b) $x/L = 0$
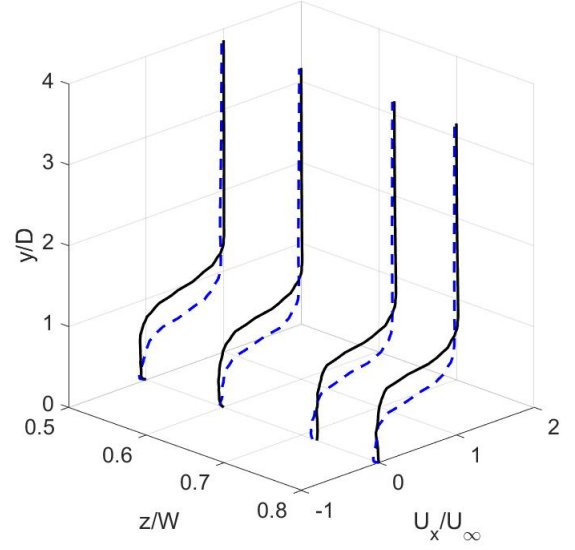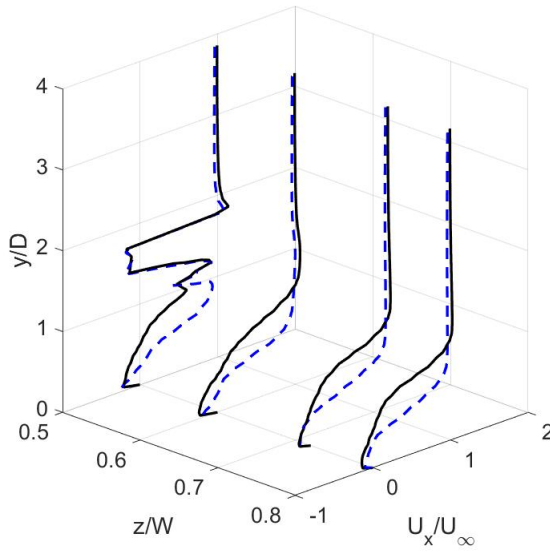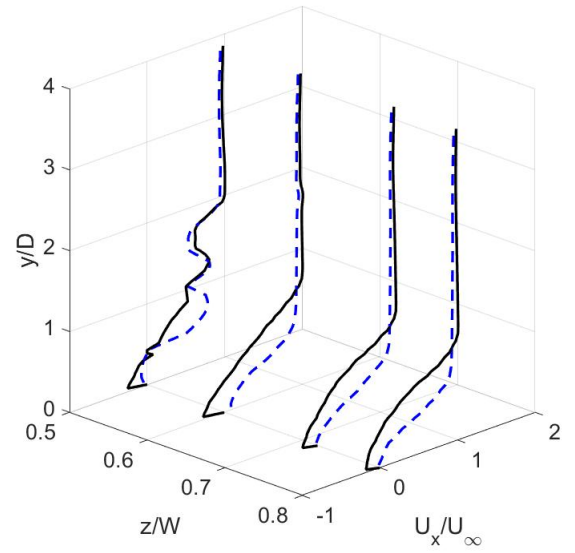
(c) $x/L = 0.17$
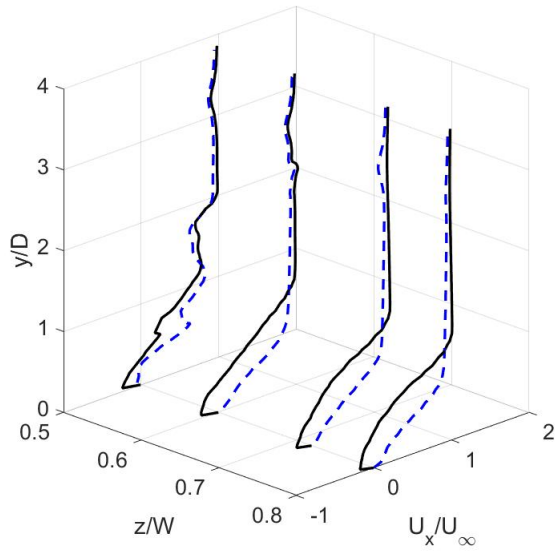
(d) $x/L = 0.26$

(e) $x/L = 0.34$

(f) $x/L = 0.43$
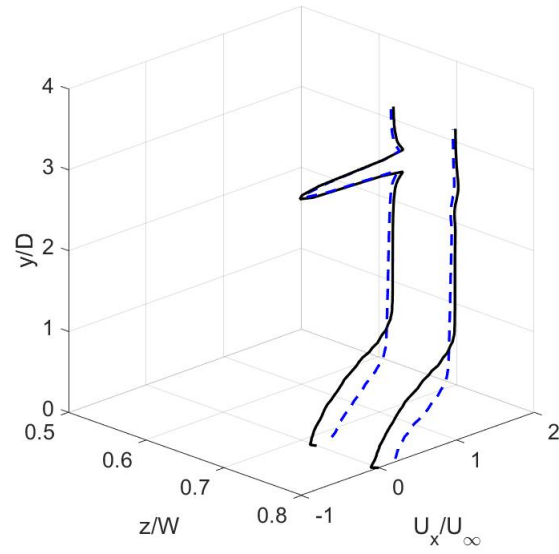
(g) $x/L = 0.45$

Figure 6.13: Time-averaged streamwise velocity U_x from case 1 with rectangular cavity and case 3 with rounded cavity.

(a) Line positions

(b) $x/L = 0$

(c) $x/L = 0.17$

(d) $x/L = 0.26$

(e) $x/L = 0.34$

(f) $x/L = 0.43$

(g) $x/L = 0.52$
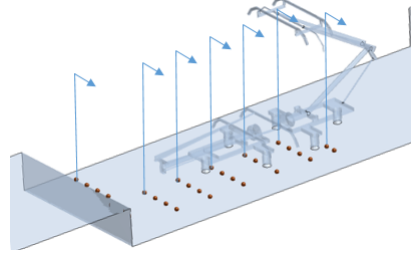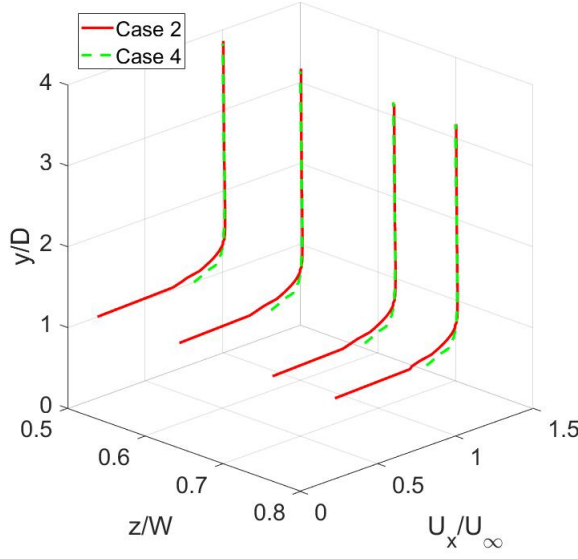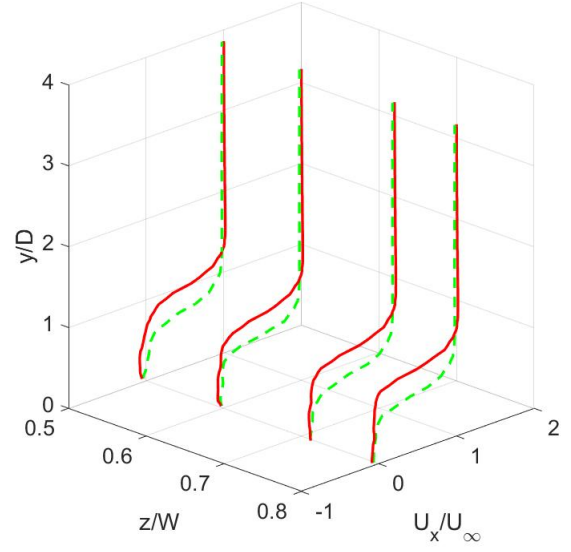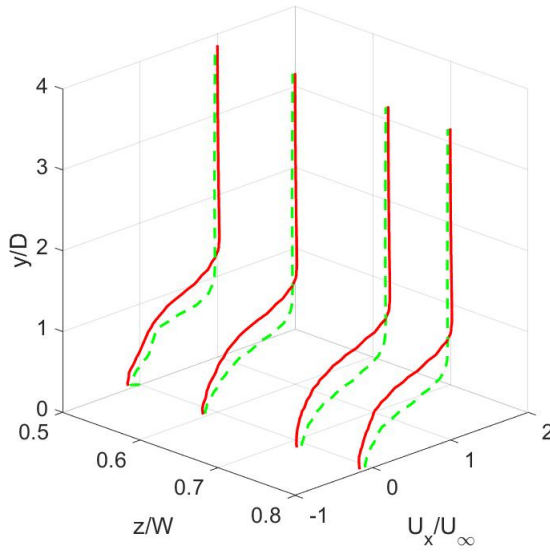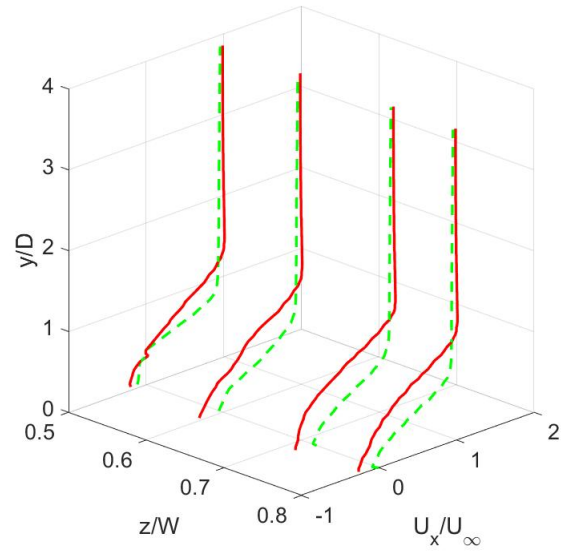
(h) $x/L = 0.54$
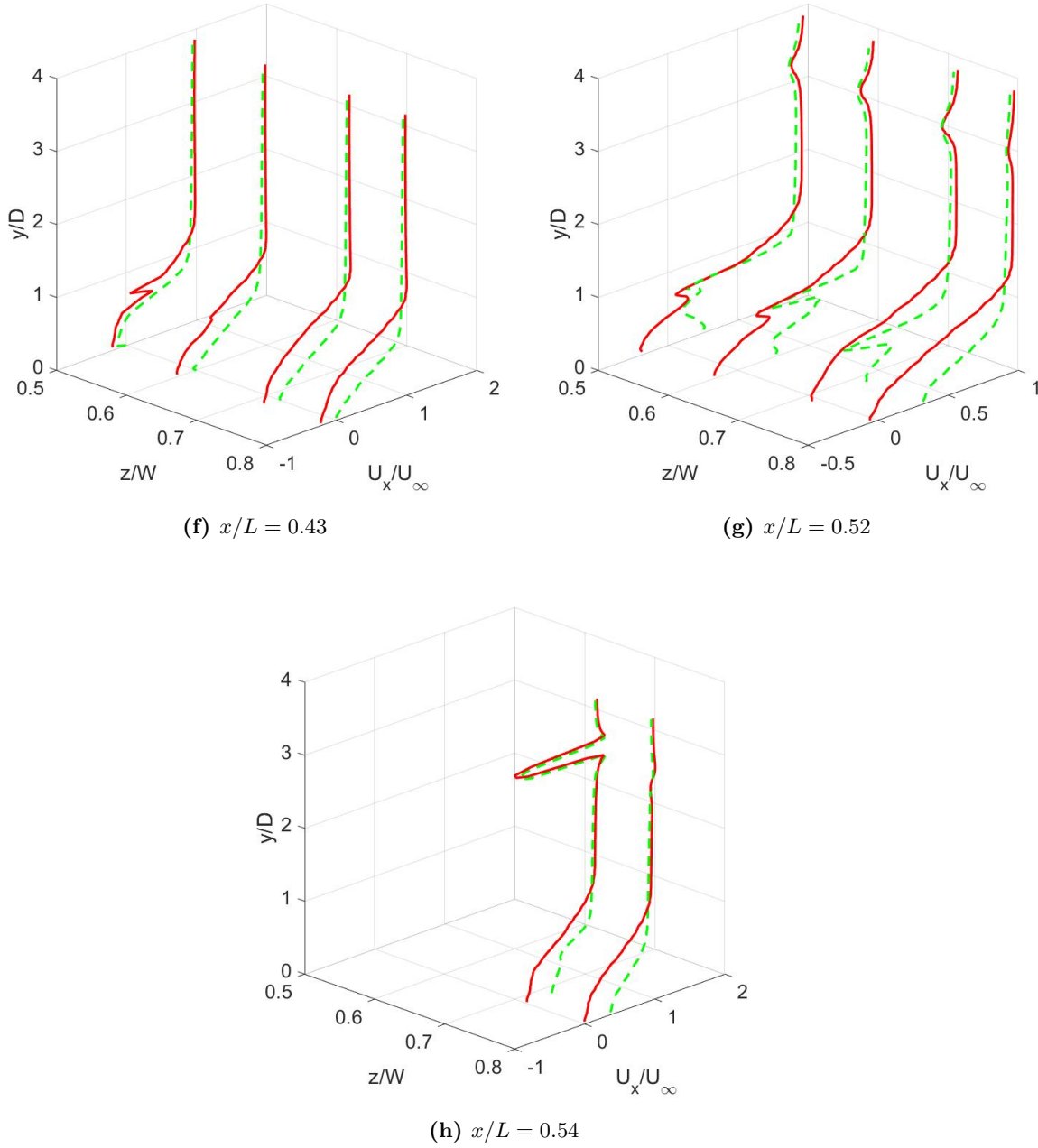
Figure 6.14: Time-averaged streamwise velocity U_x from case 2 with rectangular cavity and case 4 with rounded cavity.

6.4.4 Flow unsteadiness

6.4.4.1 RMS surface pressure

At low Mach number, dipole sources dominate the radiated noise; therefore the wall pressure fluctuation can be used to determine potential acoustic source regions. Figures 6.15 and 6.16

show the wall pressure fluctuations on the pantographs in side and top view, respectively, for all four cases. These are shown as SPLs in decibels $L_p = 10\log(p_{\text{rms}}^2/p_{\text{ref}}^2)$, where p_{rms} is the rms value of the pressure fluctuation and p_{ref} is the reference sound pressure (20 μPa).

The wall pressure fluctuations on the frame of the raised pantograph in case 3 are larger than in case 1 due to lower flow speed in this cavity region for case 1. However, the pressure fluctuations on the upper parts of the raised pantograph, including the joint, the lower arms and the panhead in case 3 are smaller than in case 1 as shown in Figure 6.15(a) and (c). Similarly, the wall pressure on the folded pantograph in case 4 has stronger fluctuations than in case 2, whereas the lower arm and the frame of the raised pantograph in case 4 has smaller surface pressure fluctuations than in case 2, as displayed in Figure 6.15(b) and (d).

A large pressure fluctuation appears on the downstream contact strip of the raised pantograph for all cases, see Figure 6.16. Comparing cases 1 and 3, the pressure fluctuations of the horn, the horn bush and the raised pantograph in case 3 are slightly smaller than in case 1. However, the surface pressure on the panhead of the folded pantograph in case 3 is greater than in case 1. This can also be seen in the comparison between cases 2 and 4. The horn, horn bush and downstream contact strip of the raised pantograph in case 4 have slightly weaker fluctuations than in case 2, apart from the upstream contact strip which has smaller fluctuations in case 2 than in case 4.

(a) Case 1

(b) Case 2

(c) Case 3

(d) Case 4
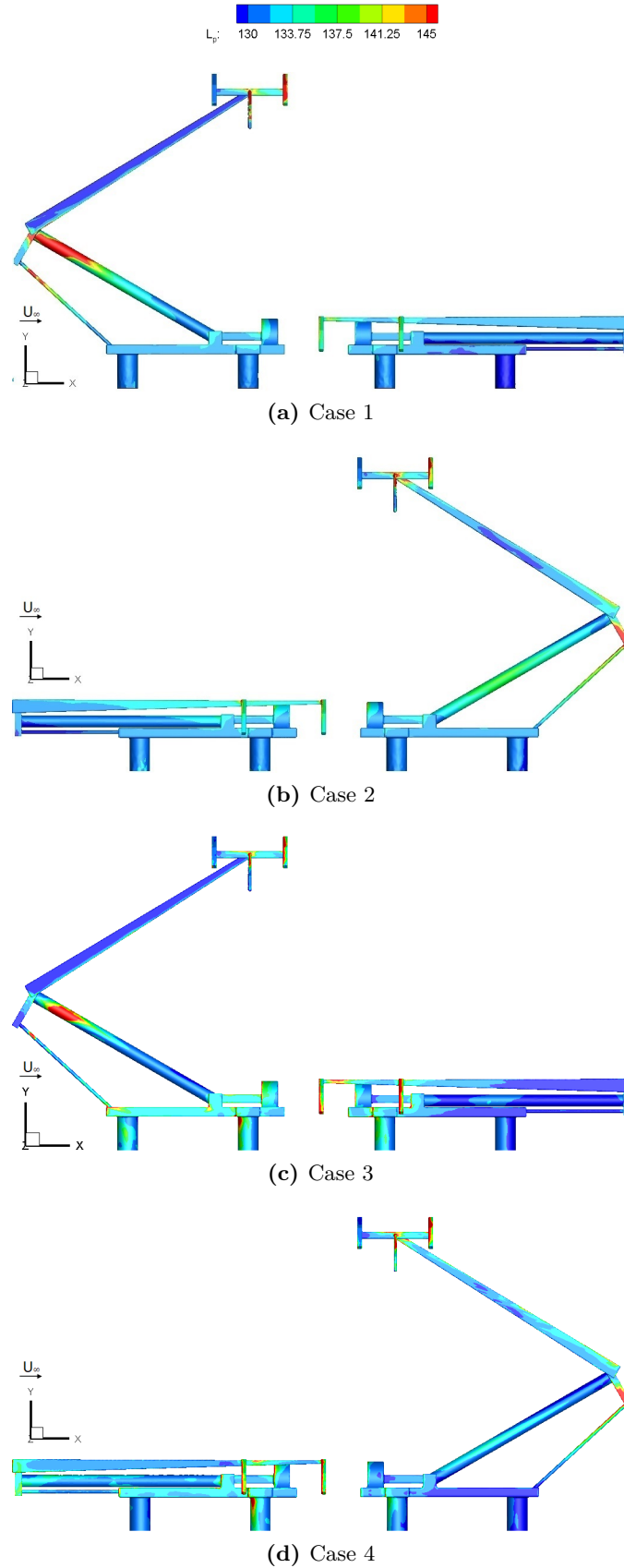
Figure 6.15: RMS surface pressure in decibels re 2×10^{-5} Pa

(a) Case 1

(b) Case 2

(c) Case 3

(d) Case 4
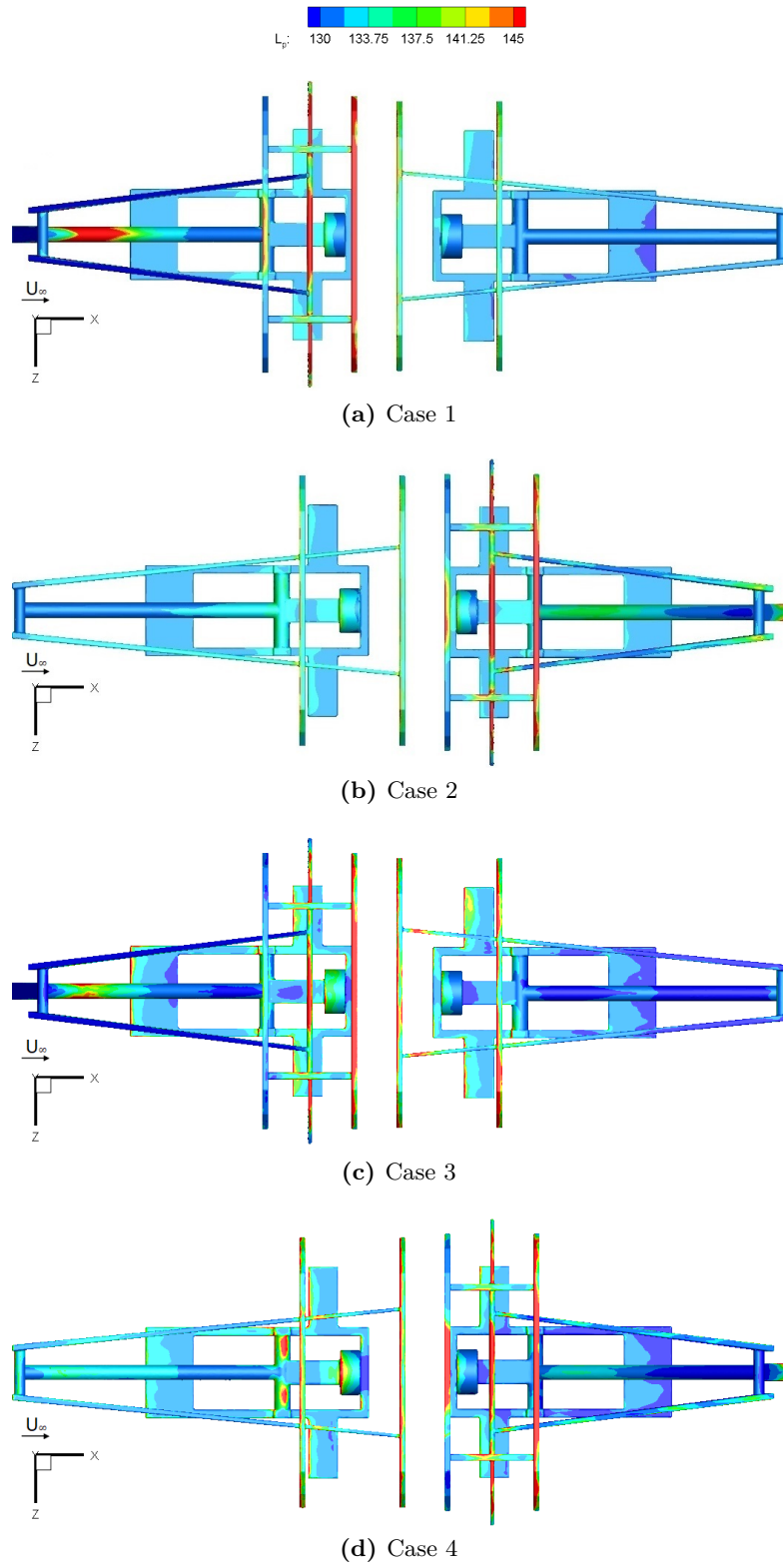
Figure 6.16: RMS surface pressure in decibels re 2×10^{-5} Pa

6.4.5   Aeroacoustic results of the modified cavity with pantographs

6.4.5.1   Sound pressure level

Two far-field receivers are used in the model, one directly to the side and one directly above the cavity at a distance of 2.5 m (corresponding to 25 m at full scale) from the centre of the cavity floor. The same method as in Section 6.3 is used for sampling the sound pressure and calculating the spectra. The all results in this section were not consider reflections from the train roof and only direct sound pressure are accounted. The results are converted to full scale from the 1/10 scale model for the current simulation, using Equation 4.2 and 4.3.

The spectra of the radiated sound pressure at the side receiver from the whole system, the raised pantograph, the folded pantograph and only the cavity walls, including the aft cavity wall, are shown in Figure 6.17. In the low frequency region below 160 Hz, there is a large difference between the rectangular cavity (cases 1 and 2) and the rounded cavity edges (cases 3 and 4) in the whole system noise. This is because the rounded cavity edge configuration reduces the noise radiated from the cavity at low frequency as shown in Figure 6.17 (d). Figure 6.17(b) shows the noise radiated from the raised pantograph where two peaks at 250 Hz and 500 Hz are seen for all cases. At the first peak generated by the contact strip the highest level happens in case 1 (80 dB) and the lowest level in case 4 (78 dB). The difference of the level between cases 1 and 4 at the second peak (500 Hz) is approximately 2.5 dB. The contribution from the raised pantograph dominates the overall sound spectrum.

The contributions from the folded pantograph (Figure 6.17(c)) are generally lower with no strong tonal components. As discussed in Section 6.2.3, for the rounded edges, the flow velocity within the cavity region is higher than for cases 1 and 2 and consequently the levels of the radiated noise from the folded pantograph are approximately 7 dB higher for cases 3 and 4. Figure 6.17(d) shows the noise radiated from the cavity walls. In the frequency region below 500 Hz, the differences between the rounded cavity cases and the baseline cases are significant (around 12 dB).

Figure 6.18 shows the corresponding spectra of radiated sound pressure at the top receiver position. In general, the SPL at this location is much higher than that at the side location, especially for the sound radiated by the cavity. Furthermore, the differences between the noise radiated when the cavity edges are rounded (cases 3 and 4) and without it are much less, compared with the levels at side position.

Table 6.5: OASPL in dB at the side and the top.

At the side (azimuthal angle $\theta = 90°$)				
Simulation cases	Whole system	Raised pantograph	Folded pantograph	Cavity
Case 1	86.3	85.9	71.0	74.5
Case 2	85.1	84.7	70.3	72.9
Case 3	85.9	85.0	78.1	62.5
Case 4	84.6	83.6	77.8	63.2
At the top (polar angle $\phi = 90°$)				
Case 1	95.8	91.1	76.6	93.7
Case 2	96.3	93.8	76.5	95.2
Case 3	95.6	91.0	85.5	92.6
Case 4	94.0	89.1	83.7	91.2

Table 6.6: A-weighted OASPL in dB at the side and the top.

At the side (azimuthal angle $\theta = 90°$)				
Simulation cases	Whole system	Raised pantograph	Folded pantograph	Cavity
Case 1	79.8	79.8	60.9	50.8
Case 2	78.4	78.4	59.3	50.7
Case 3	79.7	79.5	69.7	44.8
Case 4	78.4	77.9	67.9	44.6
At the top (polar angle $\phi = 90°$)				
Case 1	90.6	85.7	66.9	88.3
Case 2	91.0	88.2	65.9	90.9
Case 3	89.9	85.7	76.1	87.8
Case 4	89.2	84.3	74.0	86.8

(a) Whole system

(b) Raised pantograph

(c) Folded pantograph

(d) Cavity only
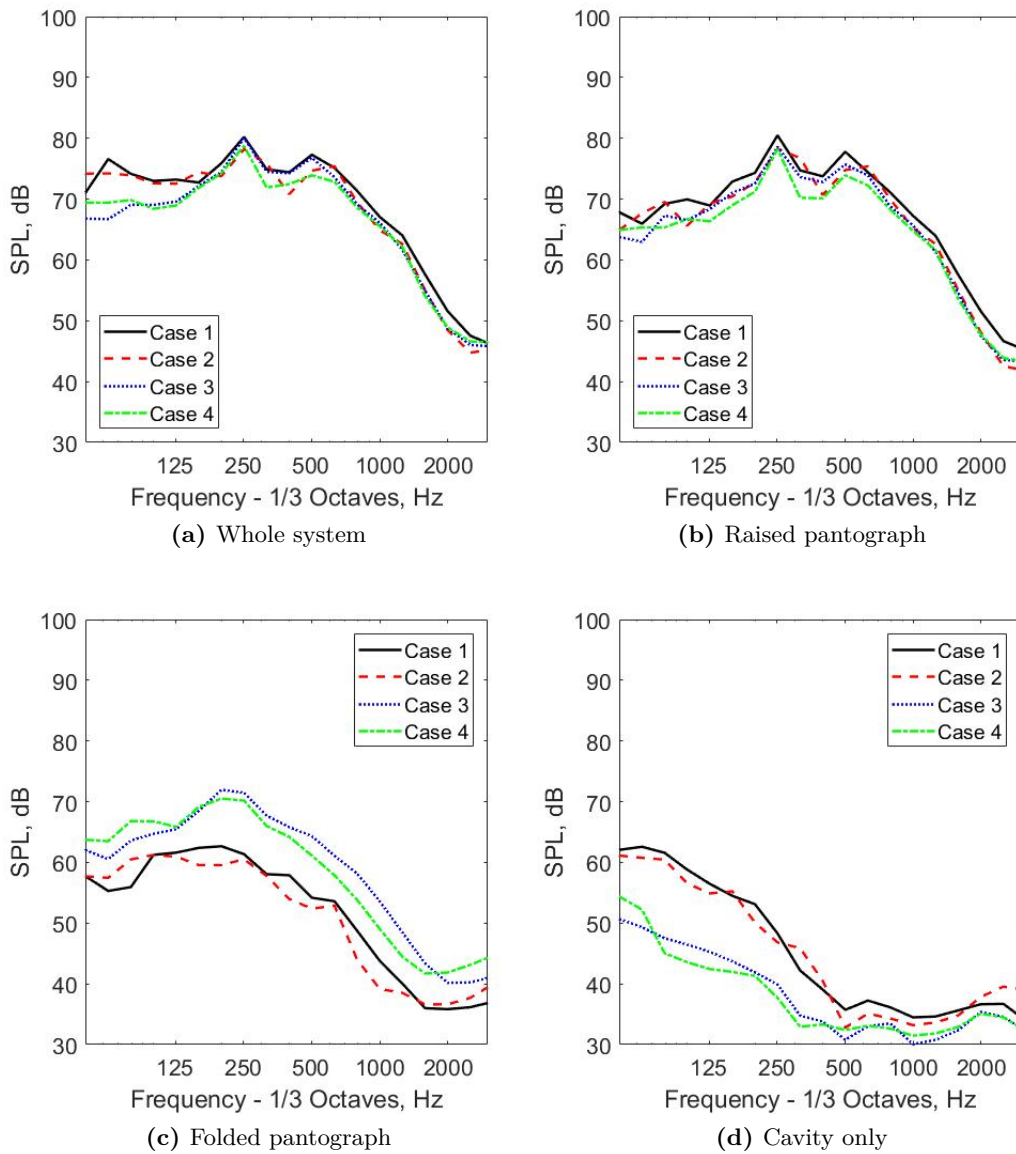
Figure 6.17: SPL at side receiver position.

(a) Total

(b) Raised pantograph

(c) Folded pantograph

(d) Cavity only
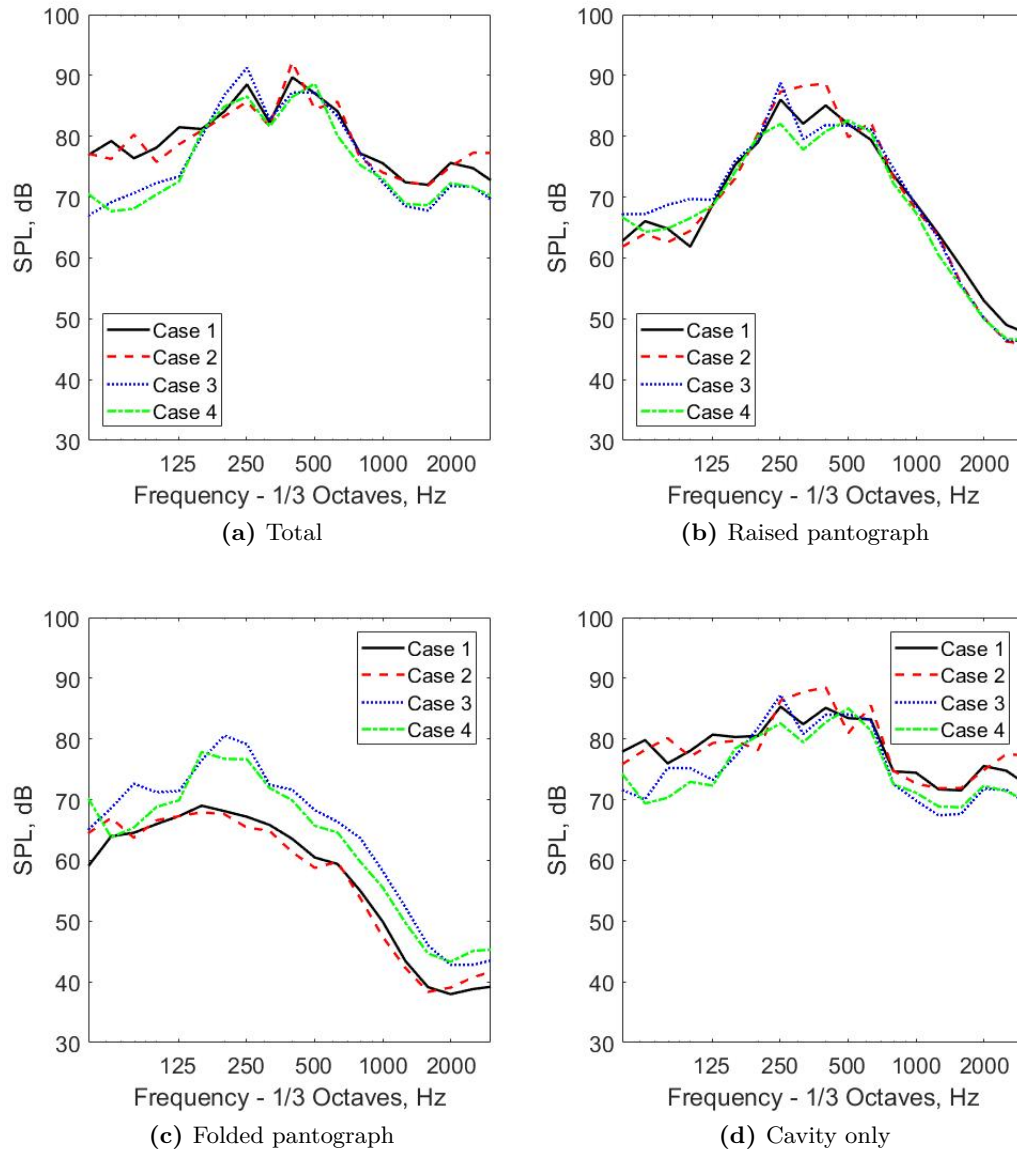
Figure 6.18: SPL at top receiver position.

6.4.5.2   2D lateral directivity

The OASPL is calculated by integrating the mean-square pressure over the frequency range up to 25000 Hz (2500 Hz at full scale). Far-field directivities in a horizontal plane are shown in Figure 6.19. The directivity patterns for the noise radiated from the whole system and the raised pantograph are similar for all cases, confirming that the raised pantograph is the main contributor to the far-field noise. The maximum OASPL locations are different for each case. For cases 1 and 2, the maximum OASPL appears at the side ($\theta = 180°$), whereas it appears in the upstream direction ($\theta = 90°$) for cases 3 and 4. The noise radiated from the whole system for case 2 has its highest level at $180°$. For case 1, it has a similar noise

level. For cases 3 and 4 at 90°, the levels are 85.9 dB and 84.6 dB, respectively. For the raised pantograph, the radiated noise for case 1 is slightly higher than for the other cases for $30° < \theta < 150°$ and the raised pantograph for case 4 has the lowest noise for most directions. The noise levels from the folded pantograph for cases 1 and 2 are lower than for cases 3 and 4, and at 90°, the level for case 2 is around 7.5 dB lower than for case 4. However, the noise levels from the cavity itself for cases 1 and 2 are greater than for cases 3 and 4 in all side directions. By rounding the cavity edges, there is benefit of reduced noise from the cavity and the raised pantograph, but it also causes slightly higher noise radiated from the folded pantograph.

(a) Total

(b) Raised pantograph

(c) Folded pantograph

(d) Only cavity
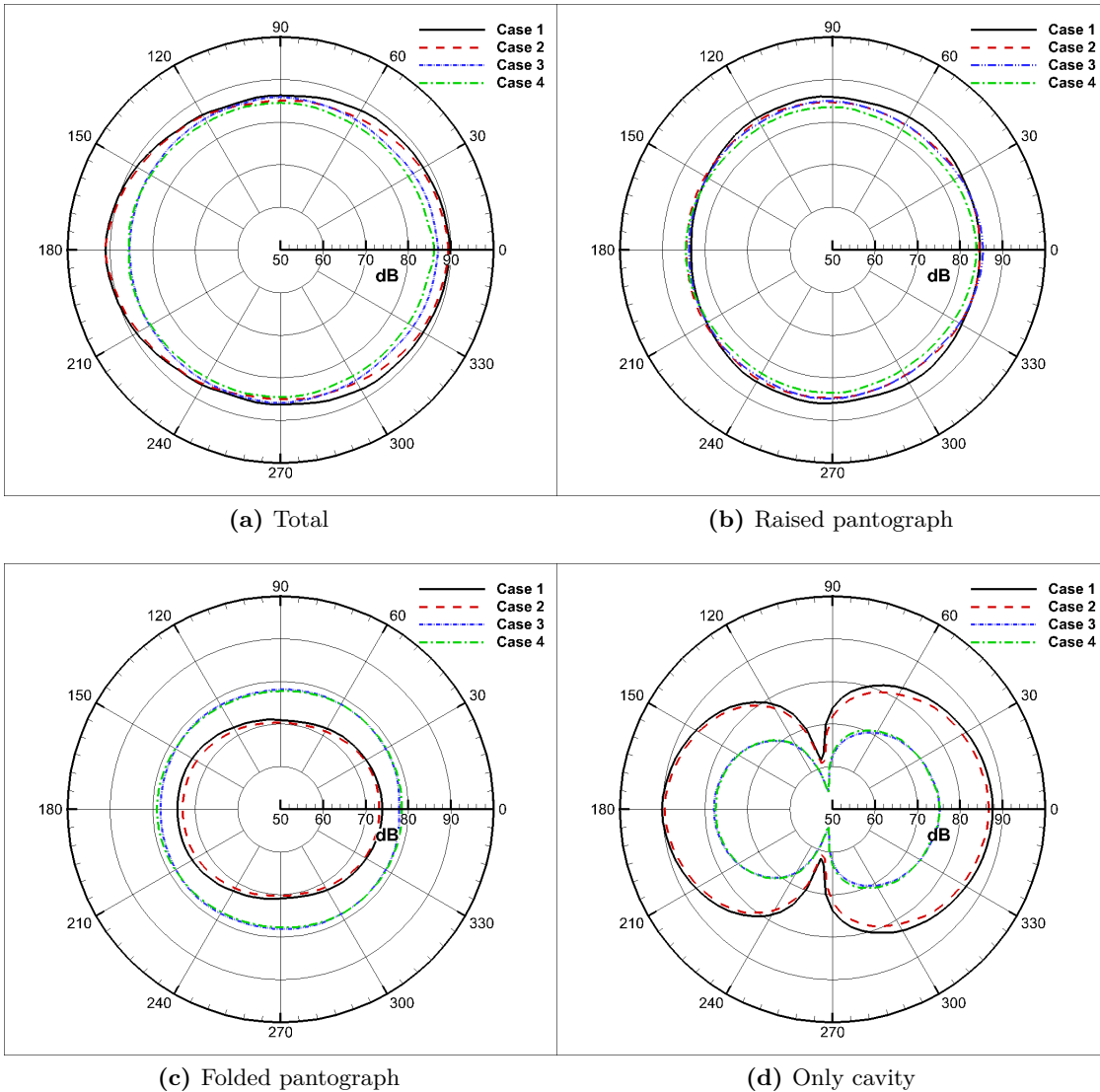
Figure 6.19: OASPL side directivity.

6.4.5.3 3D directivity

Figure 6.20 displays the three-dimensional directivities for all four cases. Receivers are also placed symmetrically below the cavity wall to consider reflections from the train roof. The direct and reflected sound pressure are summed in the time domain to account for their phase; the latter is taken from the direct radiated sound to the mirrored receiver. In general, the OASPL is much higher above the pantograph than to the sides for all cases, due mainly to noise radiated from the cavity and the panhead of the raised pantograph. Furthermore, most of the noise radiates towards the vertical and the downstream direction (polar angle $90° < \theta < 160°$).

The sound power can be obtained from,

$$W = \int_S \frac{p_{rms}^2}{\rho c} dS \qquad (6.1)$$

where p_{rms} is the rms acoustic pressure, ρ is the density, c is sound speed and S is the surface area of the hemisphere. The sound power levels for the four cases are listed in Table 6.7. Both unweighted and A-weighted levels are given. The sound powers from the rounded cavity edges configuration (cases 3 and 4) are around 2 dB lower than the cases without the treatment. This is due to mainly reduction of the noise radiated from the cavity wall by rounding the cavity edges.
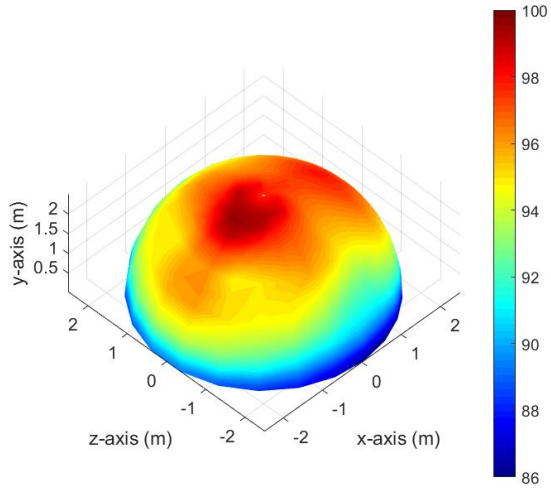
(a) Front case 1
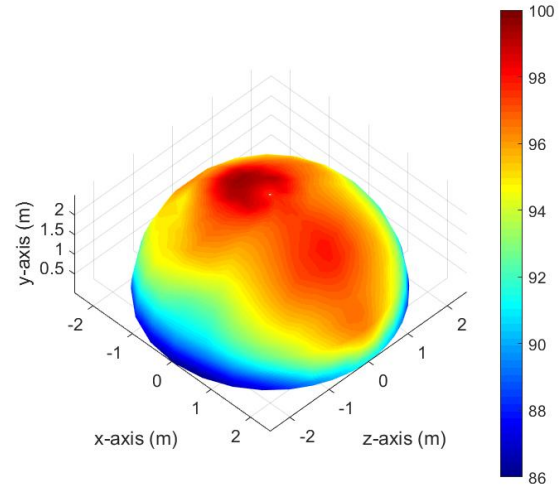
(b) Back case 1
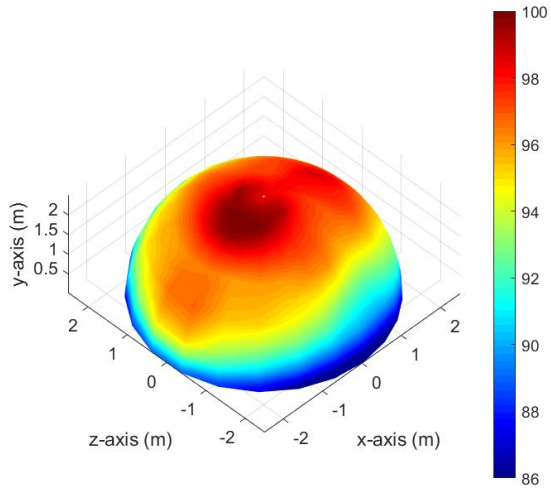
(c) Front case 2

(d) Back case 2

(e) Front case 3

(f) Back case 3

(g) Front case 4
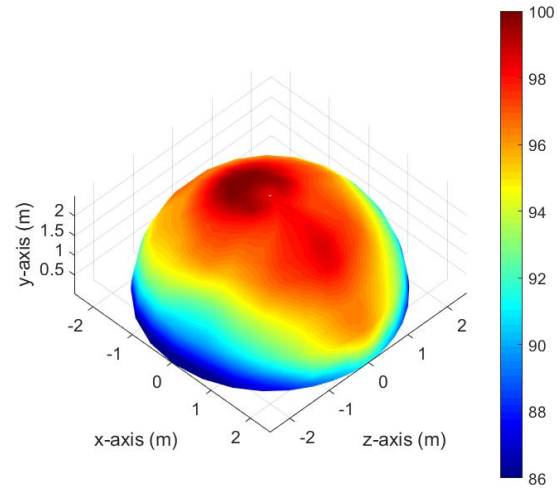
(h) Back case 4
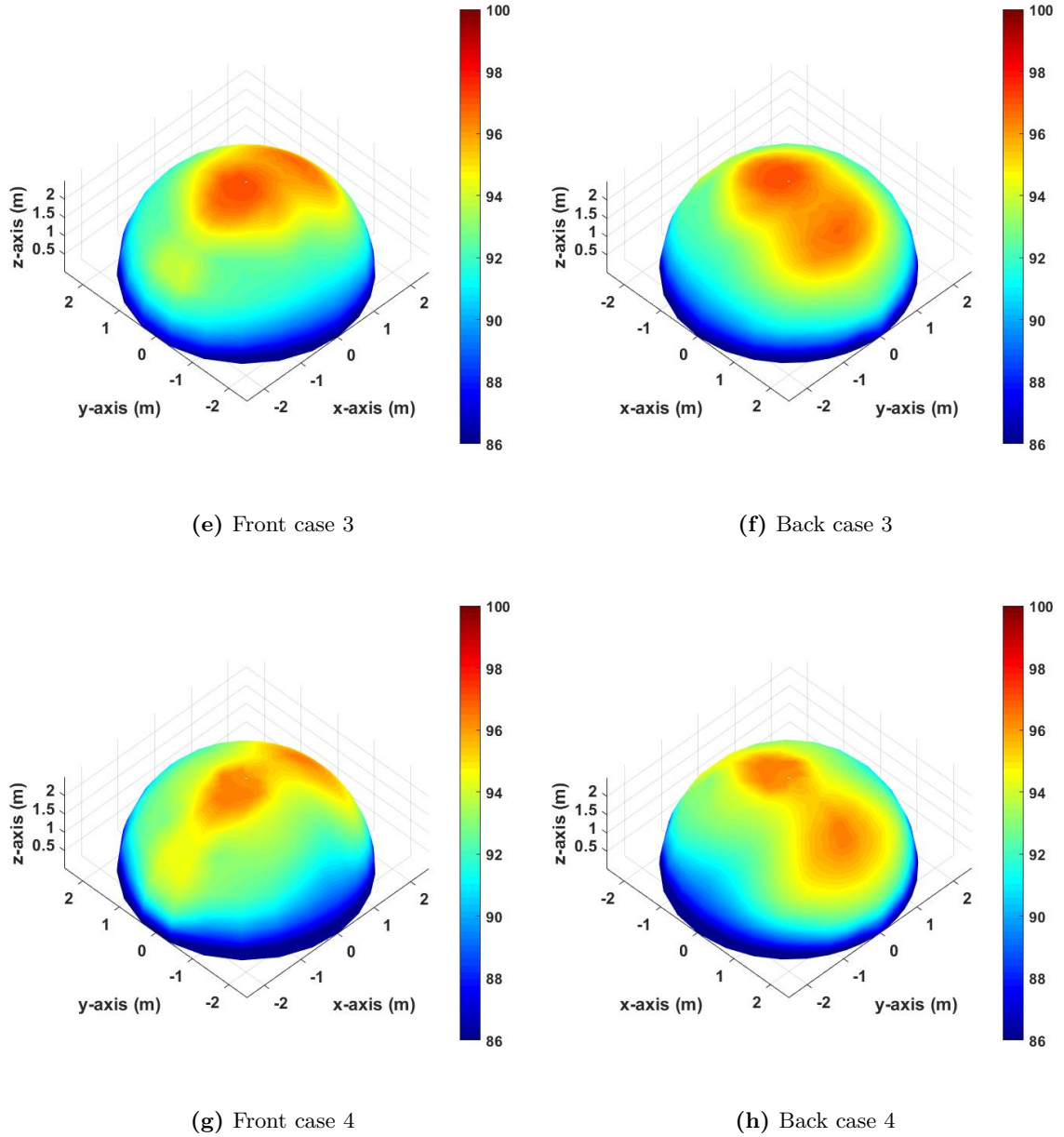
Figure 6.20: 3D side directivity.

6.5   Summary

Numerical simulations have been performed to investigate effects on the flow features and
far-field acoustics of different cavity edge configurations by rounding and angling the cavity
edges. Both these cavity edge treatments show a reduction in the mean drag and the
(negative) lift coefficients. When the cavity edges are rounded, the RMS values of the drag
and the lift coefficients are also significantly reduced. Both treatments (the rounded and

Table 6.7: Sound power levels from cases 1 and 2 with a rectangular cavity , and cases 3 and 4 with the rounded cavity.

| | Sound power level (re 10^{-12} W) | |
Simulation cases	Whole system (dB)	Whole system (dB(A))
Case 1	110.8	105.5
Case 2	111.0	105.2
Case 3	108.6	103.3
Case 4g	108.5	103.2

angled trailing edges) of the cavity show a significant reduction of the unsteady flow in the cavity trailing edge region. By rounding the cavity edges, the recirculation in the upstream region is reduced and the small recirculation region generated by the cavity trailing edge is eliminated. Consequently, the rounded cavity edge configuration with $h/D = 0.8$ gives a 15.2 dB reduction in noise at the side receiver position and a 12 dB reduction at the top receiver position, compared with the baseline case.

Furthermore, the flow and noise characteristics of two DSA 350 pantographs located in a cavity with the rounded cavity edge have been investigated and compared with those for the same pantographs installed in a rectangular cavity. It is found that when the cavity edges are rounded, a slightly lower velocity occurs upstream of the upper parts of the raised pantograph than in the baseline case. However, the rounded cavity edge configuration causes higher velocities inside the cavity region. Consequently, the noise radiated from the raised pantograph with the rounded edge cavity is approximately 1 dB lower than for the baseline at the side receiver, whereas the noised radiated from the folded pantograph increases by 7.5 dB compared with the baseline case. However, its contribution to the total noise is still negligible. Furthermore, the noise radiated from only the cavity itself is significantly reduced. When the cavity edges are rounded with radius $h/D = 0.8$, a total reduction of 0.5 dB at the side and, 1.7 dB at the top are achieved.

Chapter 7

Effect of different high speed train roof configurations

The pantographs are installed on the train roof in a variety of configurations. As well as the plain cavity considered in earlier chapters, a ramped cavity raised about the roof is sometimes used. Some trains use side insulation plates placed next to the pantograph region without a cavity. This Chapter aims to provide an insight into the aerodynamic phenomena and noise generation mechanisms from these three different types of train roof configurations and their effects on the flow around the pantograph and the radiated noise. Unlike the previous chapters, the side walls of the train body are included in the models. This chapter is structured as follows: Section 7.1 describes the train roof geometries and followed by the computational set-up. Section 7.2 presents the computational aerodynamics results, and Section 7.3 the aeroacoustic results. A summary is given in Section 7.4.

7.1 Computational set-up

7.1.1 Geometry

A simplified 1/10 scale high-speed train model is used to reduce the complexity and computational resource requirements. This has two pantographs (a front retracted one and a rear raised one) of the same type as studied in previous chapters. Three different roof configurations are represented by the three cases illustrated in Figure 7.1. The first (Figure 7.1(a)) is a flat roof with a pantograph recess, modelled as a rectangular cavity, which is a widely used configuration for different trains, such as TGV (France). The ramped roof cavity type (case 2, Figure 7.1(b)) was developed in Japan to shield noise from the pantograph, and used for Shinkansen 500 (Japan) and HEMU-430X (Korea). Case 3 shown in Figure 7.1(c) represents trains with side insulation plates which are also commonly used in Japan and China, such as Shinkansen E5 (Japan) and CRH 380A (China). However, the geometries

135

used here do not represent any particular train.

The pantograph cavity in cases 1 and 2 is simplified as a rectangular cavity with dimensions $L = 0.812$ m (length), $D = 0.07$ m (depth) and $W = 0.27$ m (width), giving $L/D = 11.5$, and $W/D = 3.9$. For cases 2 and 3, the ramps or side insulation plates have an angle of 30 degrees at both ends as shown in Figure 7.1(b) and 7.1(c). For case 3, the height of the side insulation plates is the same as the cavity depth in cases 1 and 2. A simplified DSA 350 pantograph model is used for the current study, as shown in Figure 4.18(c). The origin of the coordinate system is at the cavity or roof floor and outside insulation plate as shown in Figure 7.1. The side walls of the train are included with a height of approximately half that of the whole train.

(a) Case 1   (b) Case 2   (c) Case 3
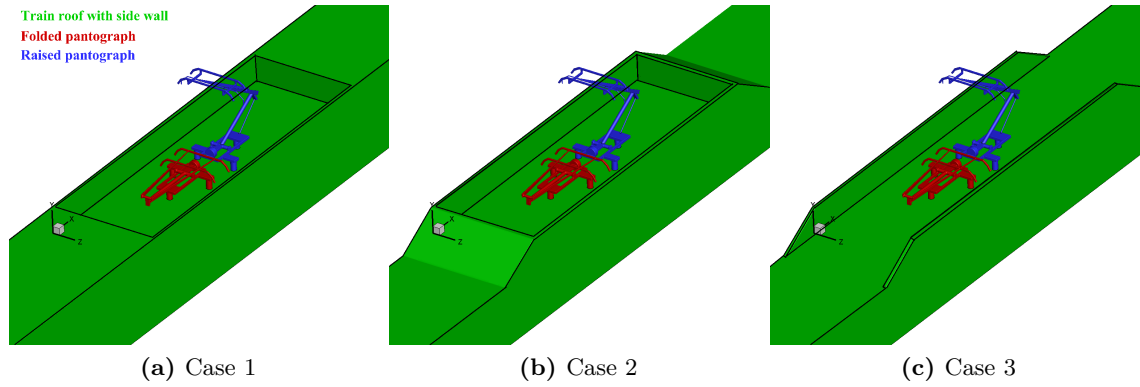
Figure 7.1: Description of the geometry.

7.1.2 Solver and numerical setup

The computational domain, as shown in Figure 7.2, extends 3.99 m ($57D$), 2.1 m ($30D$), and 1.16 m ($16.5D$) in the streamwise (x), vertical (y) and spanwise (z) directions, respectively. The upstream length of the train roof is set to 1.4 m ($20D$), which is equivalent to the actual length in a high-speed train from the nose to the first pantograph recess, and the downstream length is $25.5D$. The outlet and top boundaries are sufficiently far away from the cavity and the pantograph in order to have negligible effect on the flow. The cavity, the pantographs, the plate and the train body surfaces are defined as no-slip wall conditions, whereas the bottom surface is set to be a slip wall boundary with the same velocity as the inflow to model the moving ground. Symmetry boundary conditions are applied to the top and the spanwise sides of the domain. The outlet boundary is set be a pressure outlet. A velocity inlet is applied at the inflow boundary. The simulation is performed for a flow speed of 83.3 m/s (300 km/h).

A hexa-dominated mesh is used for all cases, generated by the STAR-CCM+ mesh generator with several refinement zones. Different cell sizes are applied for each refinement zone as

summarised in Table 7.1. Ten different refinement zones are used for the cavity and the side wall regions. Furthermore, 38 refinement regions are used for the pantographs, including regions around all components and in the wake of the panhead and the arms of the raised pantograph similar to previous chapter. The cavity downstream and trailing edge regions are refined with a minimum cell size of 1.2 mm, the panhead region is refined to 0.4 mm, while the size for the insulation plate edge regions is 2 mm. All refinement regions have a surface growth rate of 1.1. Furthermore, 14 - 40 prism layers are used to resolve the boundary layer near the solid surfaces. The first layer non-dimensional wall distance y^+ given previously is smaller than 1.0 and a grid stretching ratio of 1.12 in the wall normal direction is used. A non-dimensional time step $U\Delta t/D = 0.0095$ ($\Delta t = 8 \times 10^{-6}s$) is used, where D is the depth of the cavity, which ensures that the CFL number is less than 1 for all cases.

Table 7.1: The refinement zones and mesh criteria for each zone.

Refinement region	No. zones	Cell size (mm)	No. boundary layers
Cavity leading edge	1	6.0	40
Cavity trailing edge	2	1.2	40
Cavity inside	2	2.0	40
Cavity overall	5	8.0	N/A
Insulation plate edge	2	2.0	30
Raised pantograph panhead wake	4	1.0 - 1.8	N/A
Raised pantograph upper arm wake	2	1.5	N/A
Raised pantograph joint wake	1	1.5	N/A
Raised pantograph lower arm wake	1	1.8	N/A
Around pantograph components	30	0.4 - 0.8	14
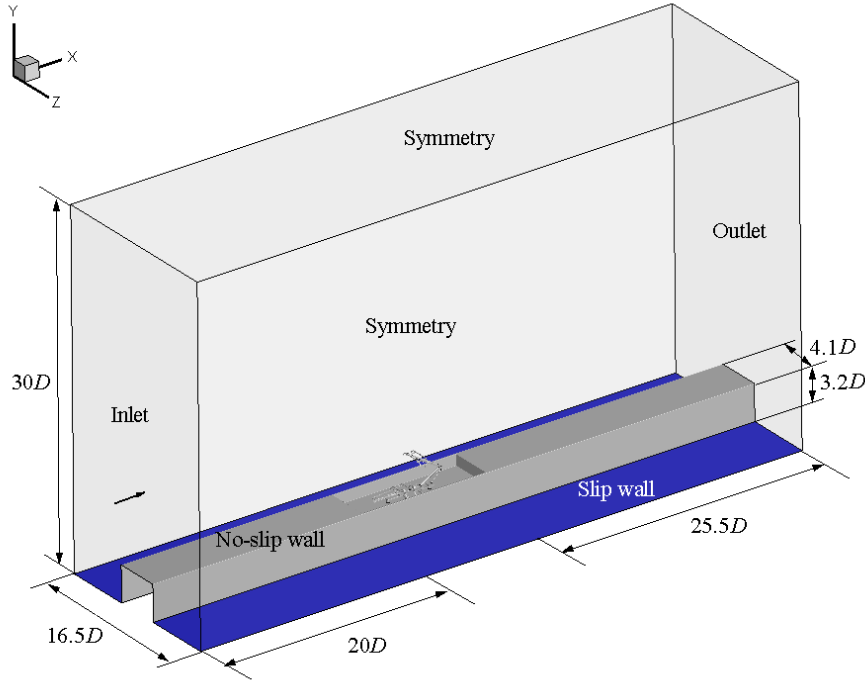
Figure 7.2: Computational domain and boundary conditions.

Table 7.2: The case description and the grid number.

Cases	Description of the case	Number of cells
Case 1	Cavity with side insulation plates	56.2 million
Case 2	Ramped cavity with side insulation plates	57.8 million
Case 3	Side insulation plates only	53.1 million

7.2   Aerodynamic results

7.2.1   Forces

The mean and rms values of the coefficients of lift C_L, and drag C_D from the whole model, the raised pantograph, the folded pantograph and the roof and insulation plates are shown in Figure 7.3. The cavity cross section $W \times D = 0.0196$ m^2 is used as the reference area to calculate each of the force coefficients. The force coefficients were obtained after running the cases for 0.05 s when the flow is deemed to be statistically steady by checking the time history of the force coefficients. Data were then collected at each time step for 0.15 s. For all cases, the mean lift coefficients $\overline{C}_L$ of the whole system are negative. The cavity roof configuration (case 1) has the highest negative lift force. The ramped roof cavity configuration (case 2) induces a higher mean drag force coefficient $\overline{C}_D$ than cases 1 and 3 by 35% and 55% respectively. The mean drag and lift forces from the pantographs are significantly smaller

than those from the roof and insulation plates. For all cases, the mean drag force of both the raised and the folded pantographs is larger than the corresponding mean lift and side forces. Furthermore, the mean side force coefficient $\overline{C}_S$ is significantly small compared with other forces because the geometries for all cases are symmetric with respect to the central vertical plan ($z/W = 0.5$). For all three roof configurations, the fluctuating lift (C_L^{rms}) and the fluctuating drag force (C_D^{rms}) for case 3 are higher than the fluctuating side force (C_s^{rms}). However, the fluctuating side force for cases 1 and 3 is slightly higher than the fluctuating lift and drag forces.

The PSDs of C_L, C_D, and C_s are displayed in Figure 7.4. These are obtained based on Welch's method using a Hanning window with a 50% overlap between segments and have been adjusted to full scale frequencies.

For all three force spectra of the whole system, the results for cases 1 and 2 are higher than those for case 3 at low frequencies up to 200 Hz. This is due to fact that the cavity and ramped roof components are the main contributors to those force fluctuations. These are produced by large-scale flow structures at low frequency (below 200 Hz) and produce higher forces than for the side insulation plate configuration, as shown in Figure 7.4(j) - (l). For cases 1 and 2, a broad peak appears in the lift coefficient spectrum at 635 Hz in Figure 7.4(j). This peak is generated by the insulation plate edges due to vortex shedding from the plates. Comparing cases 1 and 2, the three force coefficients the spectra of the roof and the insulation are similar in most of the frequency range, except below 20 Hz where the amplitude of the spectra for case 2 is higher than for case 1. Furthermore, in the spectra of the drag force coefficient C_D of the roof and insulation plates shown in Figure 7.4(k), there is very large difference between case 3 and the other two cases. For the raised pantograph in Figure 7.4(d) and (e), there are tonal peaks at 280 Hz and 450 Hz in the spectra of the lift force, and at 270 Hz and 550 Hz in the spectra of the drag force. These peaks are associated with vortex shedding from the upstream contact strip (270 Hz) and the horn (550 Hz). These two peaks can also be seen in the spectra of far-field pressure as will be discussed later. In the side force spectrum of the raised pantograph, another tonal component at 610 Hz is produced by the horn. For all three force spectra of the folded pantograph in Figure 7.4(g) - (i), the spectra for case 2 are lower than those for cases 1 and 3 in the most of frequency region. The spectra for case 1 are higher than those for cases 2 and 3 at low frequencies up to 50 Hz, whereas the folded pantograph for case 3, as it is exposed in the freestream flow, has higher force fluctuations for case 3 than for cases 1 and 2 in the high frequency region, i.e. over 210 Hz for lift and drag force, and 240 Hz for side force.
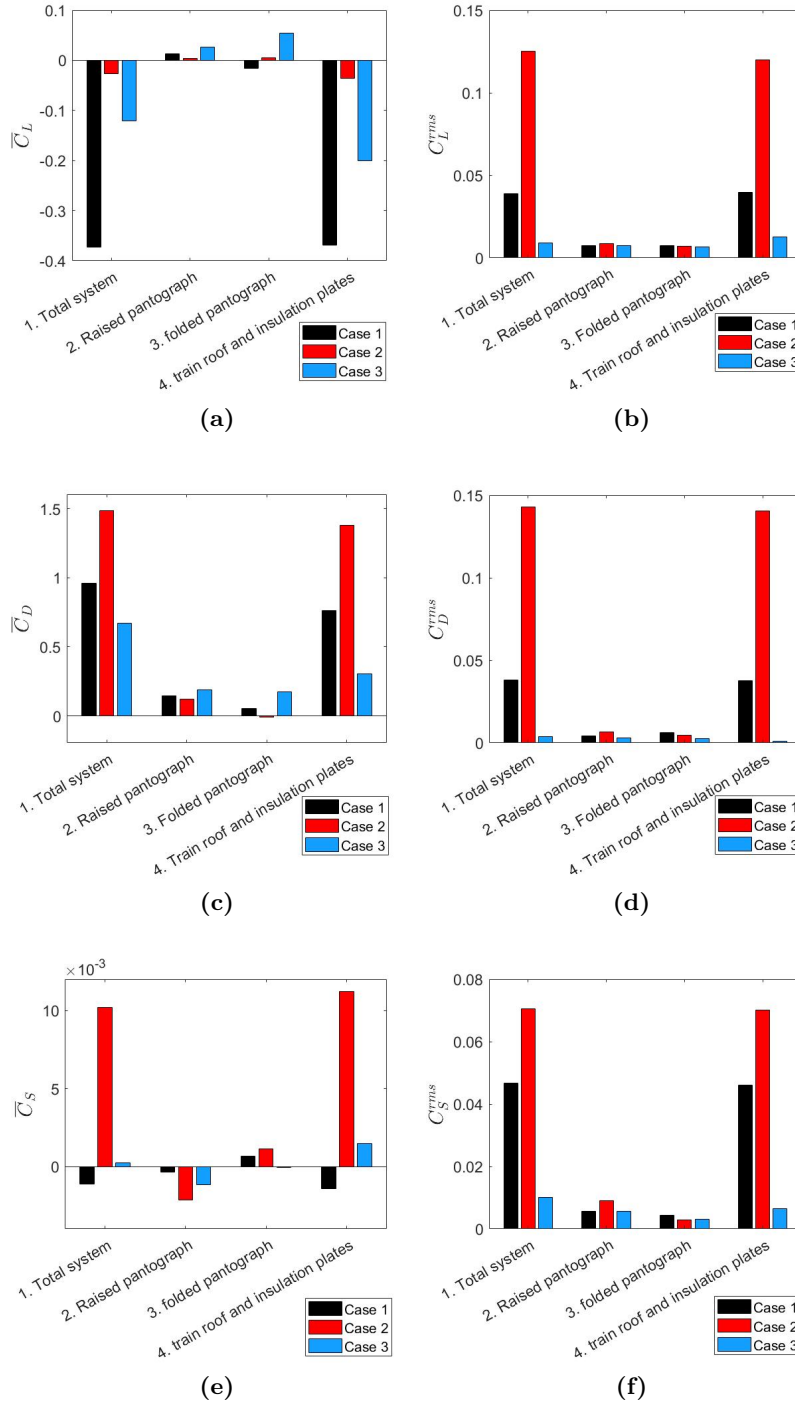
Figure 7.3: Force coefficients for different roof geometry configurations. (a) Mean lift coefficient $\overline{C}_L$; (b) rms lift coefficient C_L^{rms}; (c) mean drag lift coefficient $\overline{C}_D$; (d) rms drag coefficient C_D^{rms}; (e) mean side force coefficient $\overline{C}_D$; (f) rms side force coefficient C_D^{rms}

(a) C_L of whole system   **(b)** C_D of whole system   **(c)** C_S of whole system

(d) C_L of raised pantograph   **(e)** C_D of raised pantograph   **(f)** C_S of raised pantograph

(g) C_L of folded pantograph   **(h)** C_D of folded pantograph   **(i)** C_S of folded pantograph

(j) C_L of roof and insulation plates   **(k)** C_D of roof and insulation plates   **(l)** C_S of roof and insulation plates
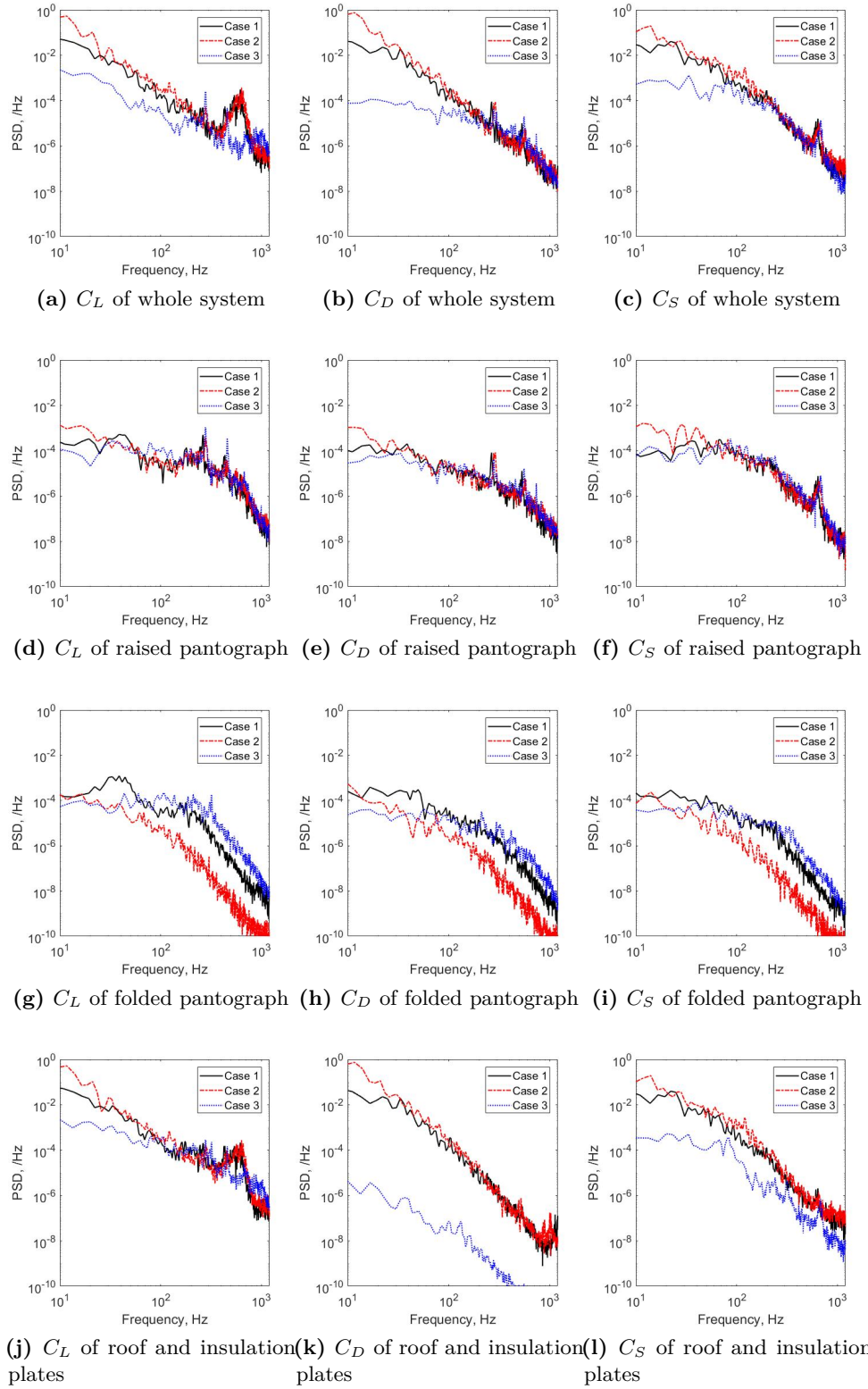
Figure 7.4: PSD of force coefficients for different roof geometry configurations.

7.2.2   General unsteady flow features

Figure 7.5 visualises three-dimensional vortical structures around the pantographs, the cavity and the insulation plates. The iso-surfaces are coloured by the non-dimensional instantaneous velocity magnitude. In general, large vortices are present in the region downstream of the cavity in cases 1 and 2, while vortices are also generated in the wakes of the raised pantograph panhead for all cases.

When the pantographs are placed in the cavity (cases 1 and 2), the shear layer, due to the flow separation from the cavity leading edge, rolls up and generates spanwise vortical structures in a recirculation region between the upstream wall of the cavity and the front pantograph and these vortical structures evolve and become hairpin vortices as they are convected downstream of the reattachment of the shear layer. This detail of coherent vortical structures can be seen in Figure 8. The spanwise vortical structure in case 2 is dissipated earlier than in case 1 due to the presence of the ramped cavity shape which reduced the flow velocity inside the cavity upstream region. In cases 1 and 2, highly unsteady flows occur in the cavity downstream region due to flow separation at the cavity trailing edge. Compared with cases 1 and 2, much stronger vortices are generated in the downstream region of the cavity. This is due to the fact that the strong vortices are generated by the front ramp side edges and these merge with vortices from the insulation plates. The merged vortices interact with the shear layer from the leading edge of the ramped cavity and vortices at its trailing edge. This interaction generates a highly unsteady flow in the rear ramp region. It is also seen that vortices are generated by the insulation plates as well the train upper body edges. For case 3, highly unsteady flows are generated by the pantographs. Small vortices generated by the insulation plates can be observed at the upstream and upper edges of the plates. These results suggest that the ramped roof cavity (case 2) produces a much stronger unsteady flow than cases 1 and 3 and that the side insulation plate configuration (case 3) produces the least unsteady flow.
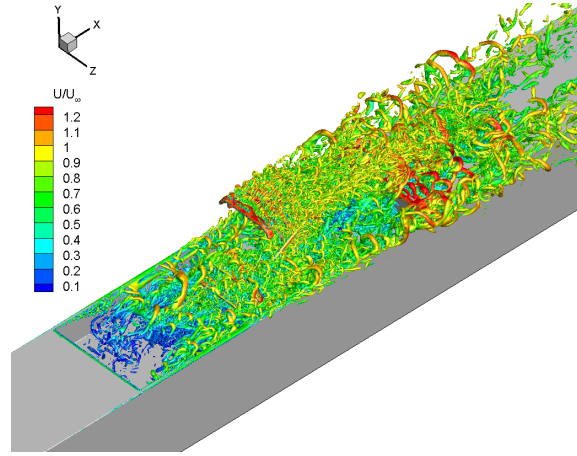
(a) Case 1
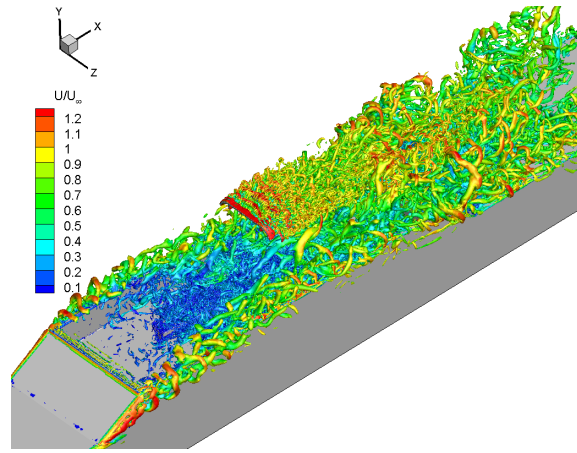
(b) Case 2
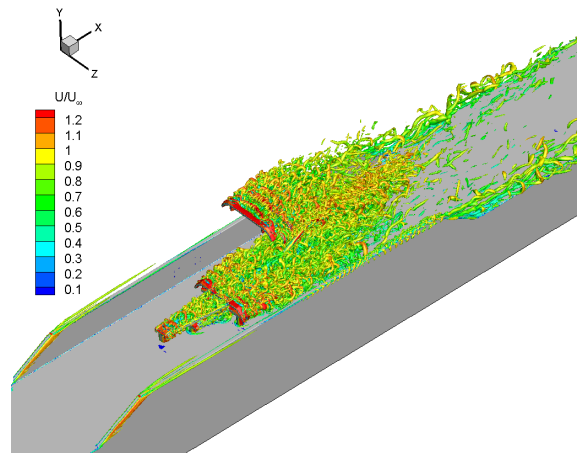
(c) Case 3

Figure 7.5: Flow structures for different train roof configurations, demonstrated by iso-surface of Q-criterion with Q_{norm}=2.5, contoured by the instantaneous velocity magnitude.

7.2.3 Time-averaged velocity field

Figure 7.6 shows contours of the time-averaged streamwise velocity streamlines at the mid-span plane ($z/W = 0.5$). In plane streamlines are also shown. In both cases 1 and 2, incoming flow separates at the cavity leading edge and generates a recirculation region within the cavity. Due to the ramp in case 2, the shear layer, its impingement on the pantograph and the resulting recirculation region are different from case 1. For case 1, the recirculation region appears between the cavity leading edge and the folded pantograph, which is in front of the raised pantograph; the shear layer impinges on the folded pantograph panhead region. For case 2, the incoming flow at the cavity leading edge is directed upward by the ramp and it causes a larger recirculation region which appears above the folded pantograph; the shear layer then impinges on the lower arm of the raised pantograph. Furthermore, another recirculation region is seen in the cavity downstream region for both cases 1 and 2. The recirculation is generated due to flow separation at the cavity trailing edge. This recirculation region is significantly larger in case 2 than in case 1 due to the ramped slope. In case 3, only small recirculation regions appear at the back of the feet, the joint and the frame of the pantographs.

Figure 7.7 compares the profiles of streamwise velocity U_x at various streamwise locations along the middle of the train roof ($z/W = 0.5$) for the three cases. Parts of the pantographs are shown to indicate the relative position. For cases 1 and 2, the incoming flow separates at the cavity leading edge ($x/L = 0$). For $0.1 < x/L < 0.3$ in these cases, negative velocity appears due to the recirculation zone formed in the cavity. Compared with cases 1 and 3, lower velocity occurs for case 2 in the region $0 < y/L < 0.16$ between the leading edge and $x/L = 0.7$. This is because the separated flow from the leading edge produces a large recirculation region above the folded pantograph as shown in Figure 7.6. This low velocity will reduce the noise radiated from the folded pantograph and the lower part of the raised pantograph compared with case 3.

Figure 7.8 shows the profiles of the streamwise velocity U_x at $x/L = 0.5$ located just before the upstream contact strip and at $x/L = 0.54$ located just in front of the horn of the raised pantograph. The roof cavity configuration (case 1) has the lowest incoming flow velocity at the upstream contact strip in the region $0.25 < y/L < 0.3$ due to the influence of the cavity flow, whereas the ramped cavity roof configuration (case 2) has the highest velocity, which is 7% higher than for case 1. However, in terms of the incoming flow velocity at the horn at $0.265 < y/L < 0.275$, the velocity in case 2 is the lowest and is 20% lower than for case 3, which has the highest velocity in this region. These influences may affect the noise radiated from the panhead of the raised pantograph. This will be discussed later.

(a) Case 1

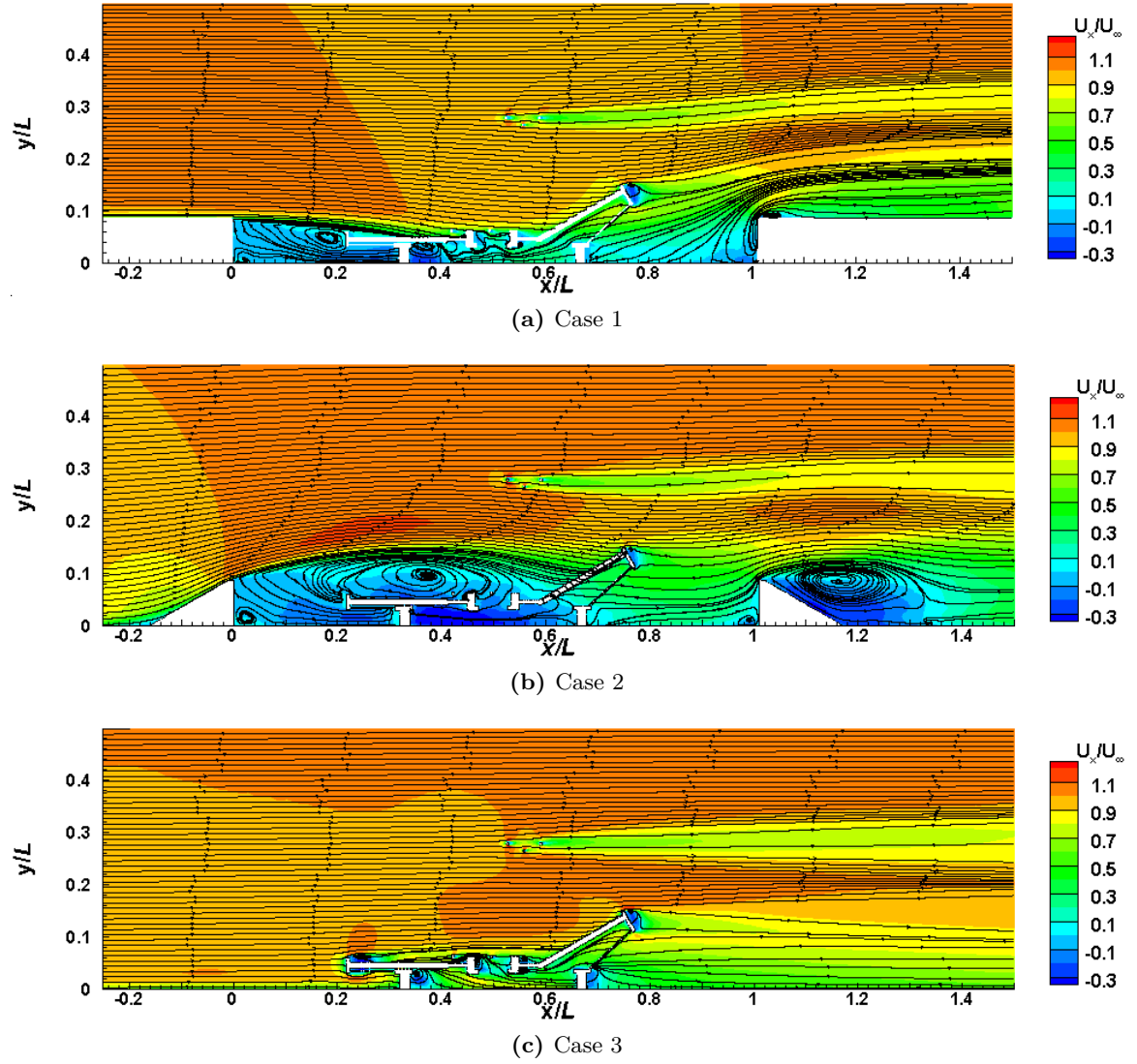
(b) Case 2

(c) Case 3

Figure 7.6: Time-averaged 2D streamlines and the mean streamwise velocity contours.
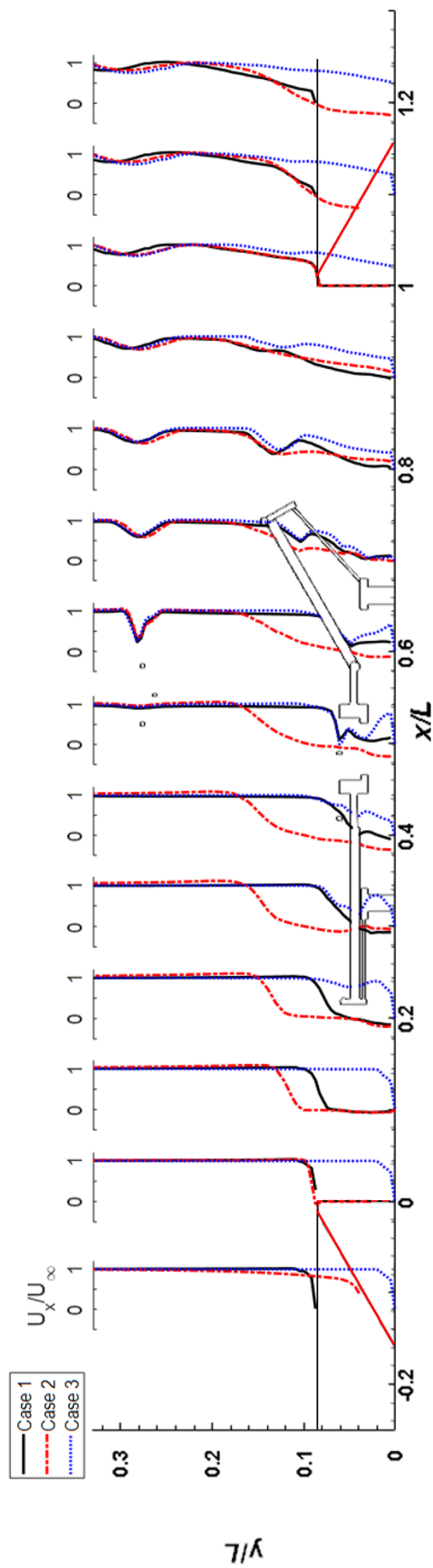
Figure 7.7: Time-averaged streamwise velocity over roof and pantographs.
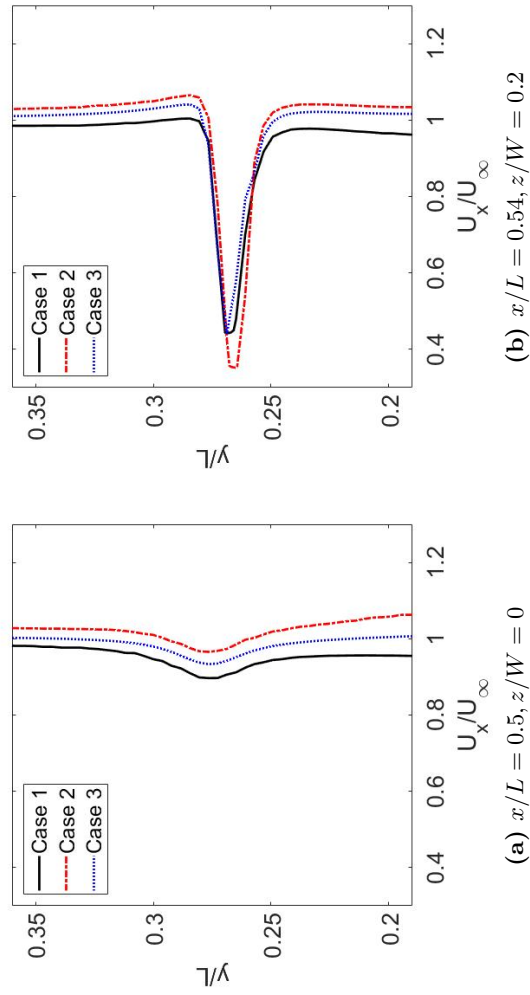
Figure 7.8: Time-averaged streamwise velocity in front of the upstream contact strip (a) and the horn (b) of the raised pantograph.

7.2.4   Near-wall flow pattern

When flow separation happens, the recirculating flow interacts with the wall, resulting in strong unsteady wall pressure fluctuations. Therefore flow separation and attachment can be used to identify potential noise sources [95]. The wall shear stress lines, plotted by the linear integral convolution [94], are used to identify the near-wall flow characteristics. The separation, attachment patterns and critical points are determined from the wall shear stress lines according to Lazos [95] and Perry et al. [96].

Figure 7.9 shows the surface flow features on the side wall including the outside of the insulation plates. For case 1, flow over the train roof separates from the cavity side edge and reattaches later, forming a recirculation region on the side wall towards the rear part of the cavity, as shown in Figure 7.9(a) by the reattachment line. For case 2, flow separation and attachment occur at both the upstream and downstream edges of the insulation plate. The separated flow at the upstream ramp side edges introduces strong vortices which impinge on the side wall, causing a large separation on the insulation plate. This also happens at the rear edge, where vortical flow from the ramped cavity introduces a large separation on the insulation plate. Flow separation at the front edge of the insulation plate is much smaller for case 3 than for case 2. The flow remains attached on other parts of the insulation plate surface.

These flow features over the insulation plate are shown in Figure 7.10 by streamlines initiated upstream from a line from $(x, y, z) = $ (-0.2 m, 0.01 m, 0.2 m) to $(x, y, z) = $ (-0.2 m, 0.01 m, 0.31 m). For case 1, the incoming flow in the middle of the train roof (red arrows) attaches on the cavity floor after separating from the cavity leading edge. It continues over the cavity, the insulation plate edge and reattaches on the insulation plate outside surface and merges with the flow (blue arrows) from outside the cavity. For case 2, the flow pattern is similar to case 1 for the incoming flow in the middle part of the roof (red arrows). The flow separated from the ramped roof edge (blue arrows) attaches on the side plate surface and goes inside the cavity and separates at the cavity trailing edge. In case 3, due to the absence of the cavity, the flow is fully attached to the side plate, except for a small separation region at the insulation plate front edge (Figure 7.10(c)).

Figure 7.11 shows the near-wall surface flow patterns with critical points as defined by Lazos [95] and Perry et al. [96]. For case 1, there are two primary attachment lines on the floor and the aft wall of the cavity, as shown in Figure 7.11(a). The shear layer separates from the leading edge of the cavity and reattaches to the cavity floor at $x/L = 0.43$, near the rear feet of the front folded pantograph. The flow separating from the cavity trailing edge reattaches on the aft wall, forming a separation region, which is $0.6D$ long at the middle ($z/W = 0.5$) and $1.1D$ long at $z/W = 0.25$ and 0.75. For case 2, a favourable pressure gradient occurs in front of the upstream ramp with a stagnation point (unstable node point).

The flow separated from the ramped cavity leading edge reattaches with two unstable nodes and a saddle of attachment in the middle of the cavity floor at $x/L = 0.68$. The flow separates again downstream of the cavity forming two stable focus points. This separated flow reattaches on the aft wall of the ramped cavity with two unstable node points and one saddle of attachment point. Furthermore, two separation lines are observed along the cavity side corner. For case 3, a common feature is found at the front and rear parts of the pantograph feet (cylinder) forming two corner separations in which the flow structure is characterised by two saddle points (one in the front and one in the rear of the feet). Furthermore, the separation lines occur at the front and side of the feet and the attachment lines are observed at the downstream of each foot.

(a) Case 1
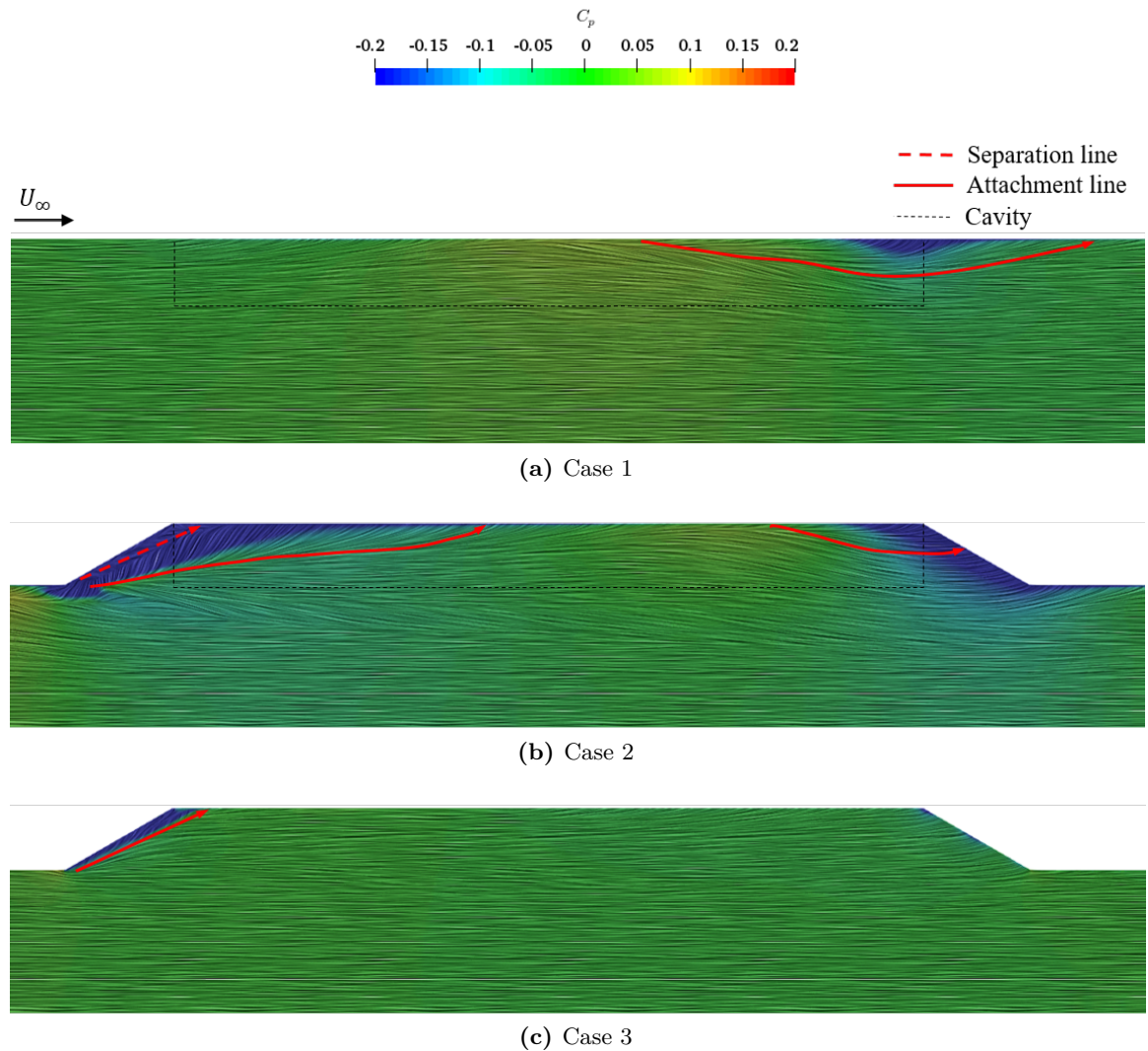
(b) Case 2

(c) Case 3

Figure 7.9: Mean wall shear stress lines coloured by the mean pressure coefficient.
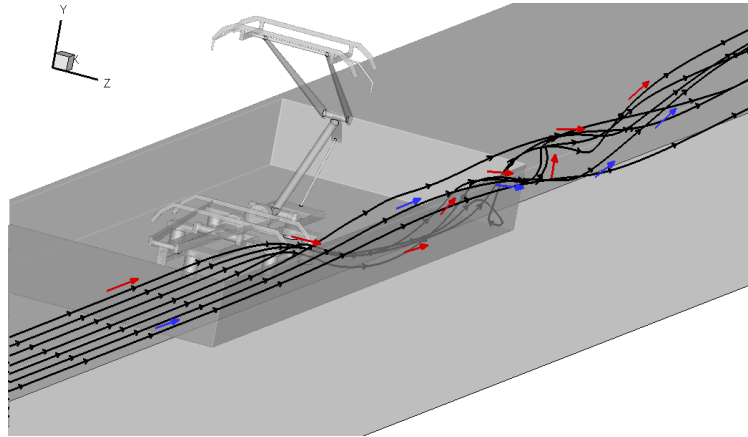
(a) Case 1
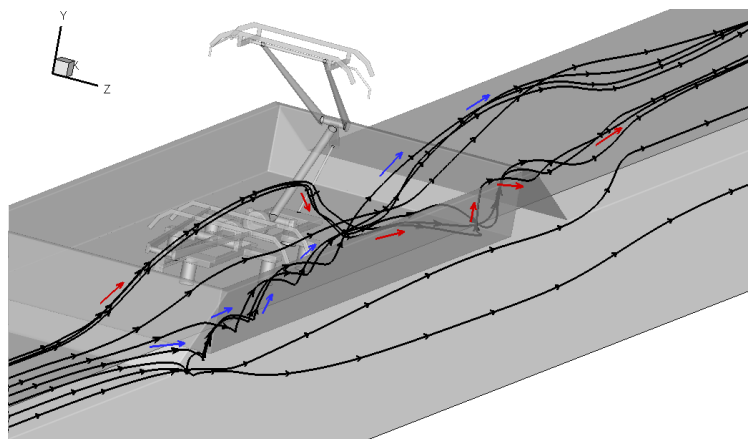
(b) Case 2
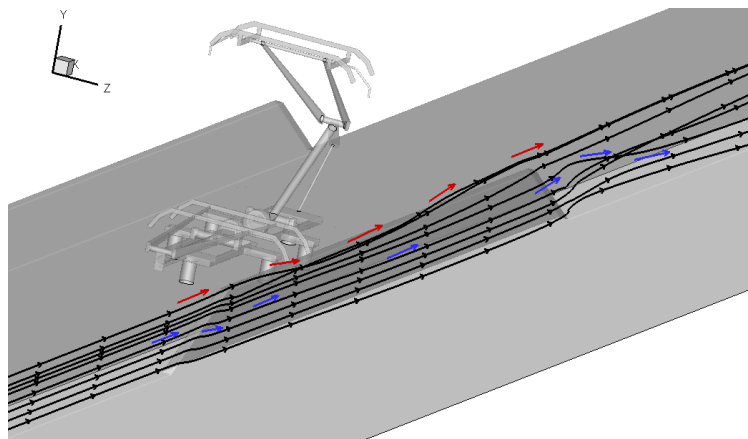
(c) Case 3

Figure 7.10: Time-averaged 3D streamlines for flow over the side of the train.

(a) Case 1

(b) Case 2

(c) Case 3
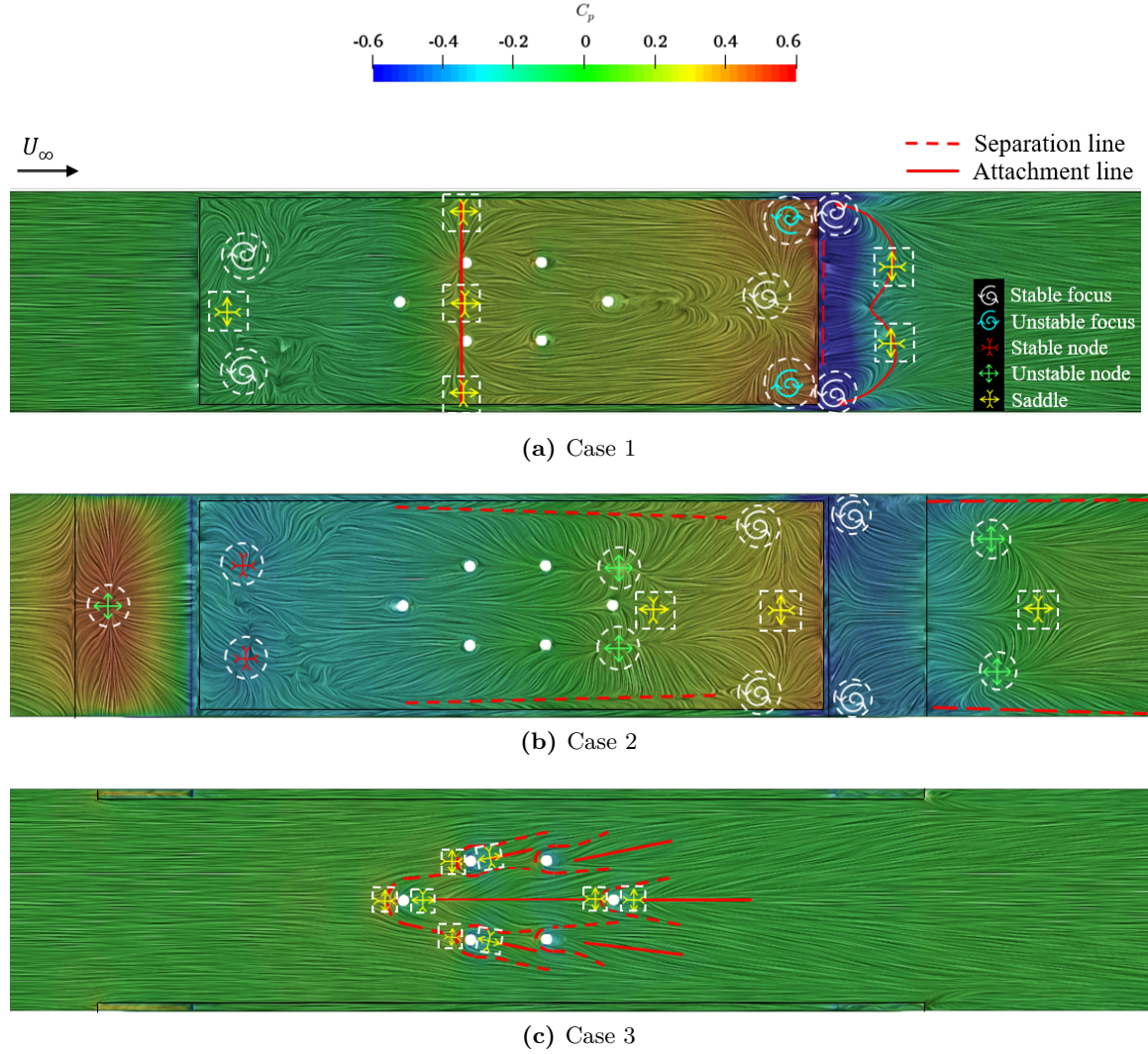
Figure 7.11: The wall shear stress lines coloured by the mean pressure coefficient. White circles are the feet of the pantographs.

7.2.5 Surface pressure fluctuations

Figure 7.12 displays the fluctuating wall pressure level in decibels, $L_p = 10\log(p_{rms}^2/p_{ref}^2)$, where p_{rms}^2 is the mean-square pressure fluctuation and p_{ref} is a reference sound pressure (20 μPa). These results show that surface pressure fluctuations are generally large in the highly unsteady flow regions, where strong vortical flow exists. For case 1, large fluctuations occur in the region downstream of the cavity, especially in the cavity trailing edge region, which is typical for a 'closed' cavity ($L/D > 10$) [37]. It is also seen that large fluctuating pressures appear around the middle of the cavity floor, the folded pantograph and the middle of the insulation plates. This is because the shear layer from the cavity leading edge impinges on the surfaces of those components. The results for case 2 also show a similar pattern in which large pressure fluctuations generally appear on the surface of the rear ramp and aft

wall. The surface pressure fluctuations on the region downstream of the cavity in case 2 are larger than in case 1. Large fluctuations appear in the downstream region of the plates due to vorticity generated by the plate edges. A moderately large pressure fluctuation appears in the plate upstream region (on the outside surface of the plates). This is due to vortices generated by the front ramp edge impinging on the surface, as can be seen from Figure 7.5. For case 3, the pressure fluctuations on the side surfaces of the insulation plates and the train body are lower than for cases 1 and 2. However, the surface pressure fluctuations are generally large on the pantographs as they are exposed to higher flow speed.
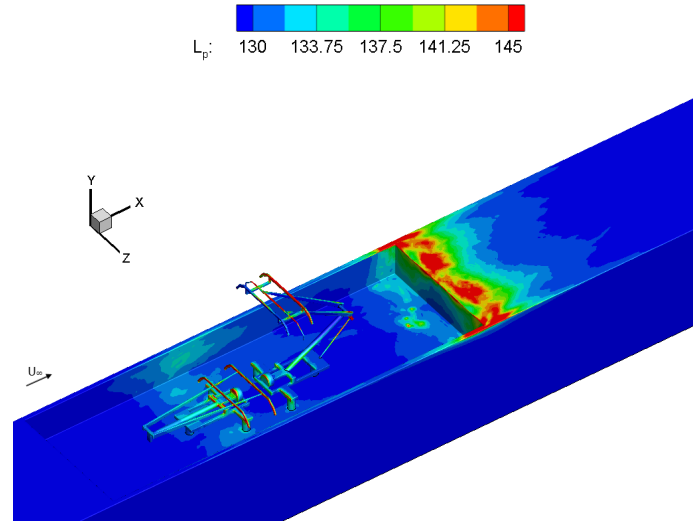
(a) Case 1
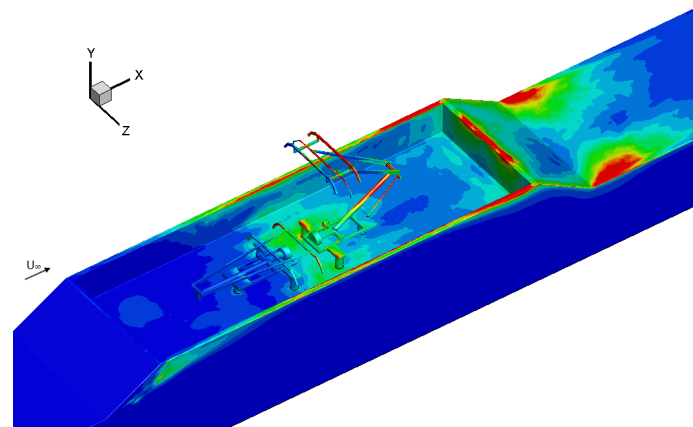
(b) Case 2
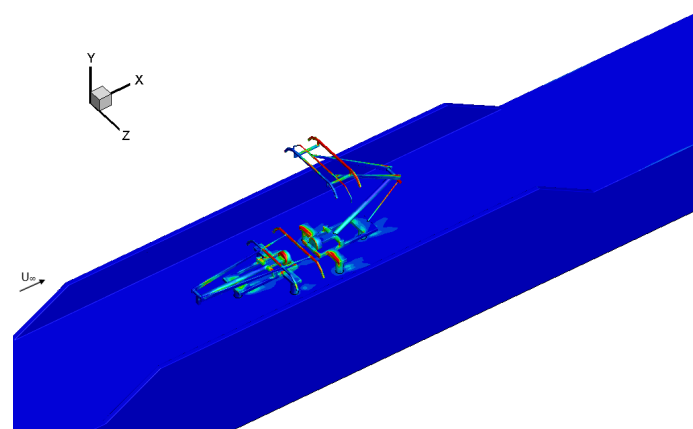
(c) Case 3

Figure 7.12: RMS surface pressure fluctuations in decibels, re 2×10^{-5} Pa.

7.3　Aeroacoustic results

7.3.1　Far-field sound pressure level

A total of 244 far-field receivers are defined in the model, located on a sphere with radius 2.5 m (corresponding to radius 25 m at full scale) centred at the middle of the cavity floor. For both the side (azimuthal angle) and the the top (polar angle) directions, receivers are uniformly distributed with an interval 4.5 degrees. The sampling frequency of the far-field noise was 125 kHz at 1/10 scale. A segmental average using a Hanning window with 50% overlap was used [92] to calculate the narrow band spectra, which were converted to 1/3 octave bands and adjusted to full scale using Equation 4.2 and 4.3. It is note that the current method for prediction of far-field pressure is not taken into account the acoustic shielding and diffraction effects of the side insulation plates.

Figure 7.13 shows the spectra of the radiated sound pressure at a receiver directly to the side as well as the contributions from different components. The corresponding OASPL values are listed in Table 7.3. The SPL from the whole system for case 2 is higher in the low frequency region (below 250 Hz) than for cases 1 and 3, as shown in Figure 7.13(a). This is due to stronger noise radiation from the ramped cavity itself (see Figure 7.13(d)). Figure 7.13(b) shows the spectra of radiated noise from the raised pantograph. Two strong tonal components are seen in the 250 Hz and 500 Hz band. The first peak is associated with the upstream contact strip of the panhead and the second is generated by the horn of the panhead see Section 4.4 [29]. In general, the SPL for case 1 is slightly lower in most of the frequency range than for cases 2, and 3.

Figure 7.13(c) shows the spectra of the noise radiated from the folded pantograph, which are generally lower. There are no strong tonal components and the radiated noise is broadband for all cases. The noise for cases 1 and 2 is lower than for case 3, as the folded pantograph for these cases is placed inside the cavity, where the flow speed is generally much lower than the freestream velocity. The radiated noise from the folded pantograph for case 2 has the lowest level, which is 12 dB lower than for case 3 because the folded pantograph in case 2 is completely within the cavity recirculation flow region without being impinged by the shear layer from the cavity leading edge. This would be the motivation of using a ramp to redirect the shear layer.

Figure 7.13(d) shows the spectra of noise radiated from the train roof and the insulation plates. In the low frequency region (up to 315 Hz), the radiated noise for cases 1 and 2 is higher than for case 3. In these spectra, a peak is seen at 500 Hz for cases 1 and 2, and 630 Hz for case 3. This is generated by vortex shedding from the insulation plates. However, the folded pantograph does not have a significant contribution to the total level.

Figure 7.14 shows the spectra of the radiated sound pressure at a receiver directly above the configuration. In general, the SPL at this location is much higher than that at the side location, especially the sound radiated from the raised pantograph and the train roof and insulation plates (see Table 7.3). The second tonal peak for the raised pantograph at 500 Hz in case 3 is approximately 4 dB higher than for cases 1 and 2, as shown in Figure 7.14(b). In Figure 7.14(d), it can be seen that the noise from the train roof and insulation plates for case 3 is about 11 dB higher than at side receiver position. The SPL from case 3 (the insulation plate only configuration) is slightly lower in the lower frequency range below 250 Hz, whereas it is slightly higher in the high frequency region between 630 Hz and 1250 Hz.

From Table 7.3, it can be seen that at the side position, the OASPL from case 3 is lower than that from cases 1 and 2. However, at the top position, the OASPL from case 3 is approximately 2 dB higher than that from case 1 and 2. This is mainly due to the radiated noise from the raised pantograph, most of which is exposed to the freestream flow. The results of applying the A-weighting to the OASPL are also listed in Table 7.4. As the A-weighting attenuates significantly the contributions at low frequencies, the tonal peaks from the horn and insulation plate at higher frequencies become more important for the OASPL. Therefore, the A-weighted levels from case 3 become similar to those of case 2 at the side and are the highest at the top.

Table 7.3: OASPL in dB at the side and the top.

Simulation cases	Whole system	Raised pantograph	Folded pantograph	Roof and insulation plates
At the side (azimuthal angle $\theta = 90°$)				
Case 1	90.1	85.2	77.5	89.0
Case 2	93.6	86.0	69.0	93.1
Case 3	88.5	86.4	81.7	81.2
At the top (polar angle $\phi = 90°$)				
Case 1	94.5	93.4	84.0	91.7
Case 2	94.7	94.6	70.8	92.9
Case 3	97.5	95.6	91.0	92.0

Table 7.4: A-weighted OASPL in dB at the side and the top.

Simulation cases	Whole system	Raised pantograph	Folded pantograph	Roof and insulation plates
At the side (azimuthal angle $\theta = 90°$)				
Case 1	81.2	77.0	68.9	77.8
Case 2	83.1	78.4	57.1	81.0
Case 3	82.9	78.7	75.5	77.1
At the top (polar angle $\phi = 90°$)				
Case 1	87.8	85.0	74.9	83.7
Case 2	88.8	86.6	59.8	84.9
Case 3	91.7	88.5	84.4	86.7

(a) Total

(b) Raised pantograph

(c) Folded pantograph

(d) Roof and insulation plates
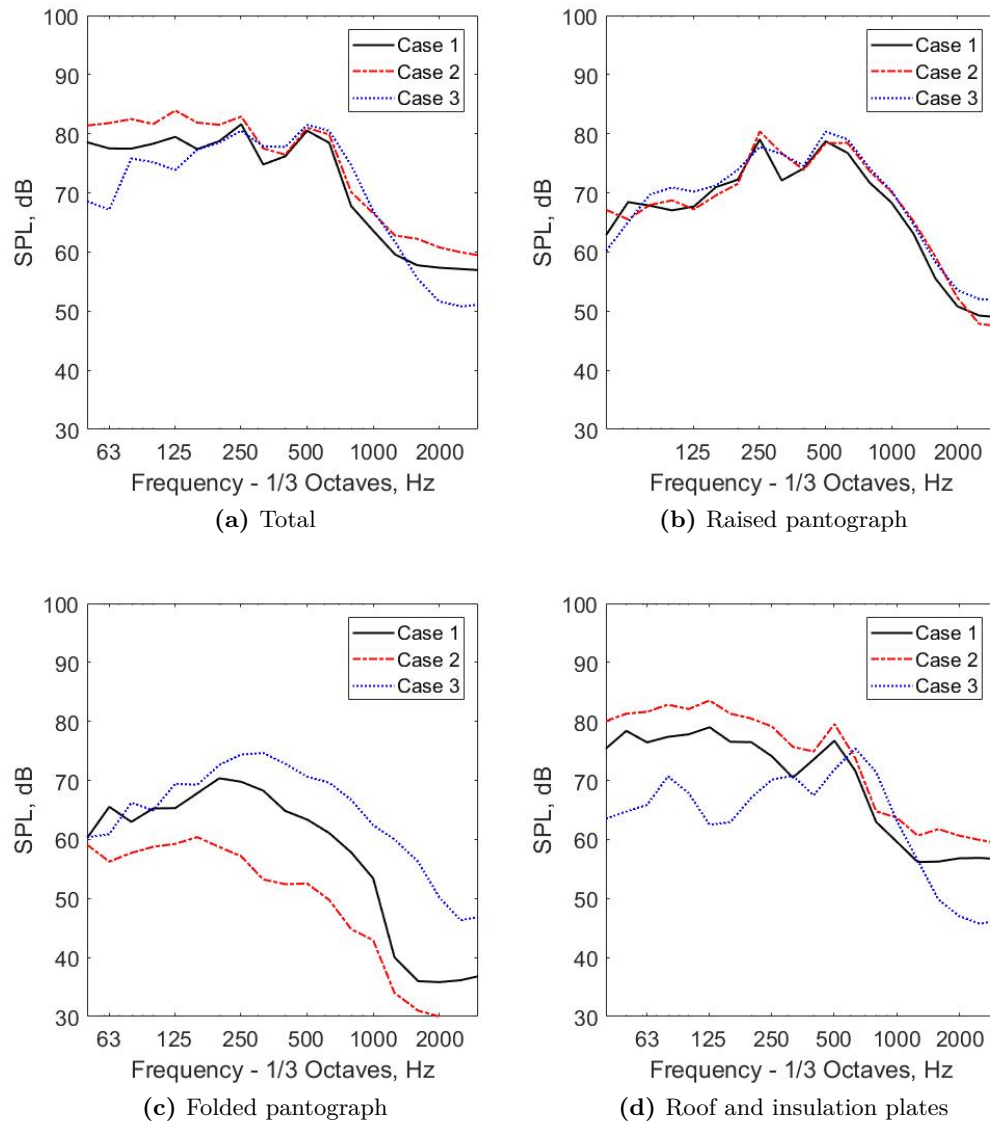
Figure 7.13: SPL at the side receiver position.

(a) Total

(b) Raised pantograph

(c) Folded pantograph

(d) Roof and insulation plates
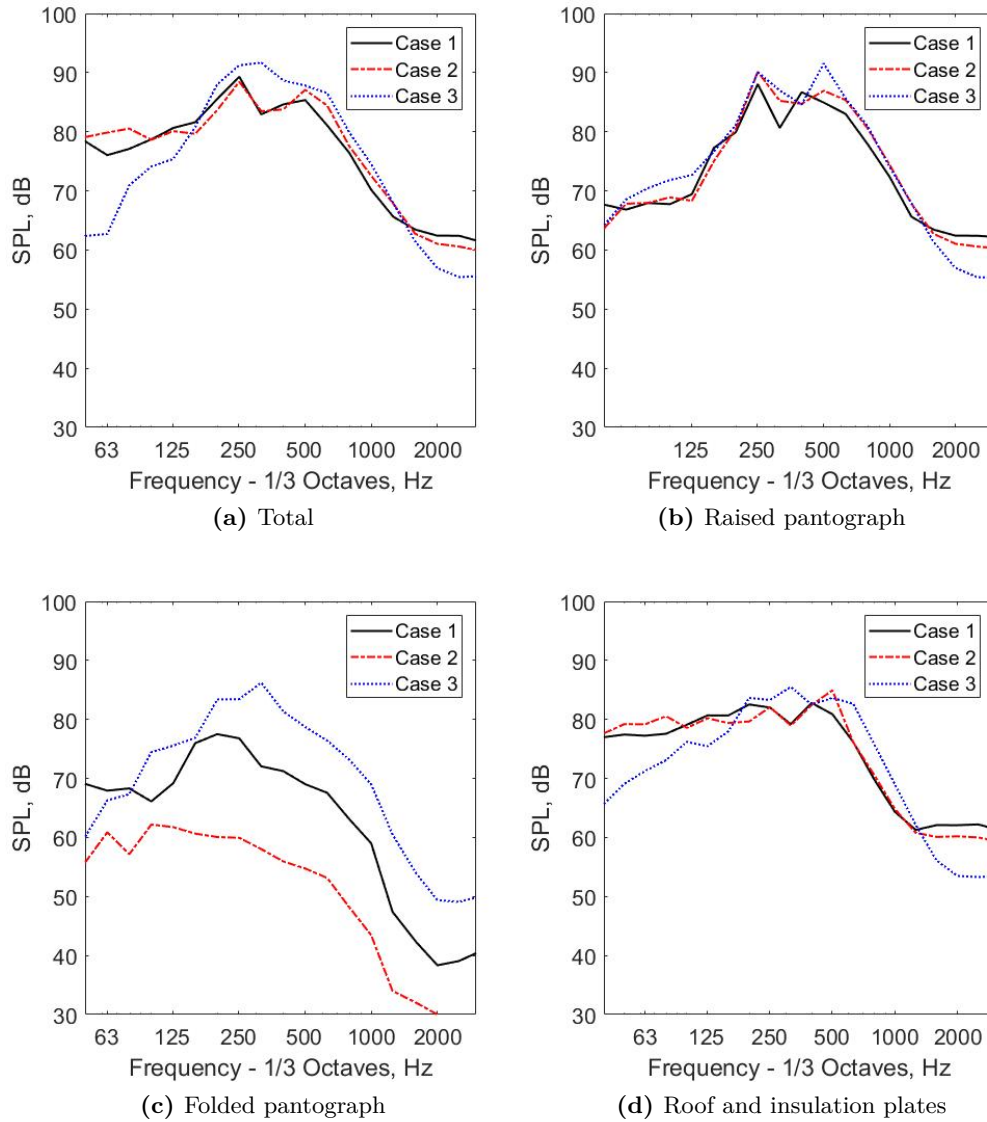
Figure 7.14: SPL at the top receiver position.

7.3.2   2D lateral directivities

Figure 7.15 shows far-field directivities in the horizontal plane for noise radiated from the train roof and pantograph system and also contribution from the various components. The A-weighted levels are shown in Figure 7.15(b). The noise radiated from the whole system for case 2 is higher than for cases 1 and 3 in all directions. It is seen that the maximum OASPL appears in different directions for different cases. The maximum OASPL for case 1 appears at $\theta = 108°$. The maximum OASPL for case 2 is seen at $\theta = 171°$, whereas the OASPL for case 3 is at $\theta = 94.5°$.

However, the directivity of the A-weighted OASPL shows a different pattern. The noise radiated from the whole system for cases 1 and 2 is higher than for case 3 for $300° < \theta < 60°$ and $110° < \theta < 250°$. At $\theta = 90°$, the cavity configuration (case 1) has the lowest OASPL. For the raised pantograph, the directivity patterns are similar for all cases. However, the radiated noise for case 3 is slightly higher than for cases 1 and 2, especially between $\theta = 60°$ and $\theta = 180°$. For both cases 1 and 2, the minimum OASPL appears at $\theta = 36°$. Furthermore, the minimum OASPL for case 3 occurs at $\theta = 0°$. In terms of the roof and the insulation plates, there are large differences between cases 2 and 3. In general, the SPL for case 3 is higher than for the other two cases, especially the noise radiated from the roof (including ramped cavity) and the insulation plates.

(a) Total

(b) Total with A-weighting

(c) Raised pantograph

(d) Folded pantograph

(e) Train roof and insulation plates
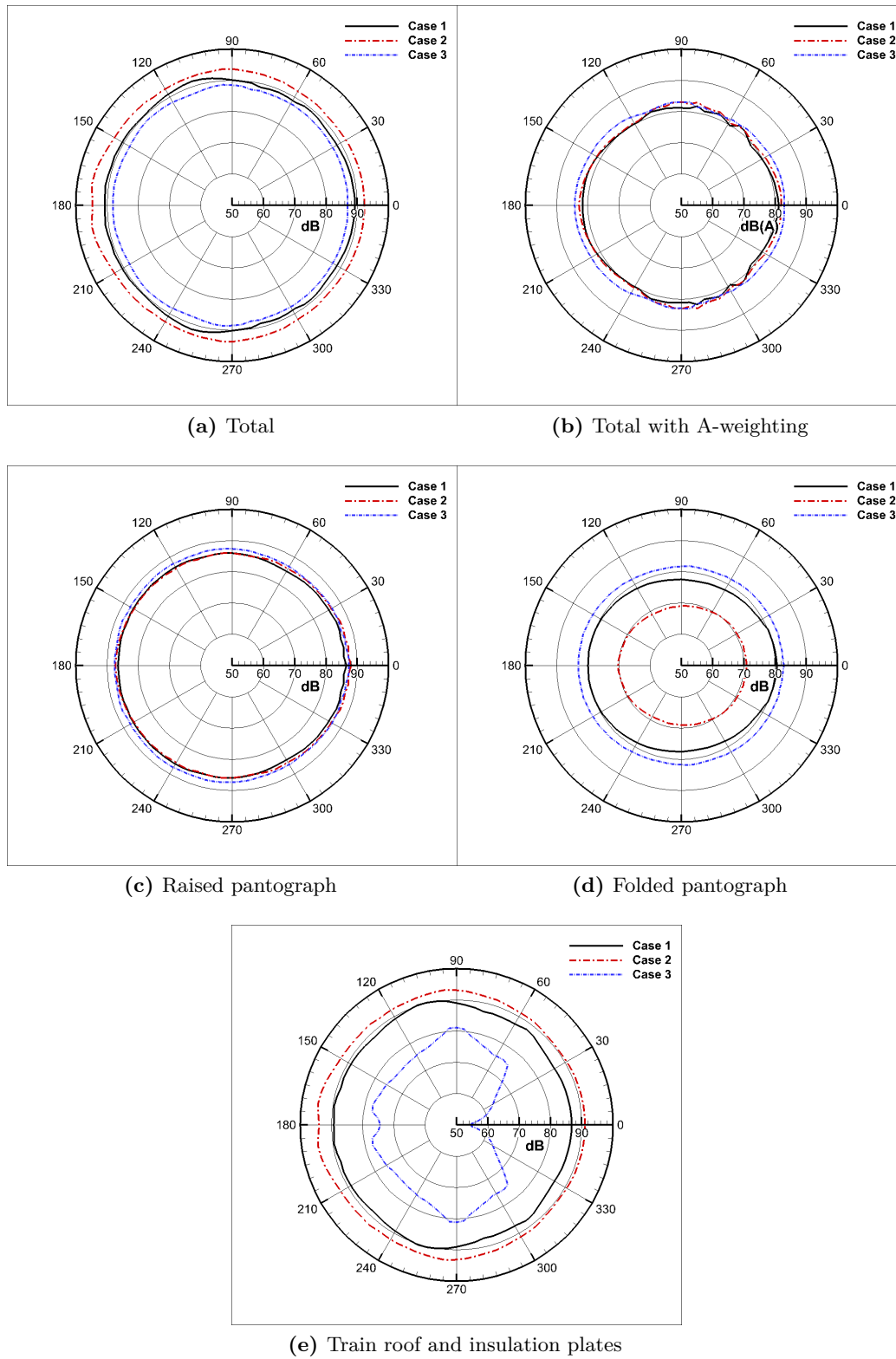
Figure 7.15: Noise directivity in the horizontal plane from the whole pantograph system and various components.

7.3.3 3D directivities

Figure 7.16 shows the 3D directivities of noise radiated from the whole system for all cases. To consider reflections from the train roof, receivers are also placed symmetrically below the train roof, and the direct and reflected sound noise are added coherently. In general, the OASPL is much higher above the pantograph than to the sides for all cases. For case 3, there is a difference of about 9 dB between the level at the side position at azimuthal angle $\theta = 90°$ and at the top position. Furthermore, the majority of the noise is radiated towards the downstream direction. The noise above the centre of the roof (an azimuthal angle $\theta = 90°$, a polar angle $\theta = 90°$) has the highest level for case 3. For case 1 and 2, the highest level occurs on the top and downstream direction

The sound power levels are listed in Table 7.5 and the A-weighted levels in Table 7.6. The unweighted sound power for case 1 is approximately 2 dB lower than for case 2 and 1 dB lower than for case 3. This is due to the influence of the cavity flow and the ramped cavity configuration causing higher levels in the low frequency region up to 250 Hz. However, when the A-weighting is applied, the sound power level of the whole system for case 3 becomes around 2 dB larger than for cases 1 and 2. This is mainly due to tonal noise from the horn and the insulation plates at high frequency as discussed in Section 7.3.1.

Table 7.5: Sound power levels from case 1 with the cavity, case 2 with the ramped cavity and case 3 with the side plate only.

Simulation cases	Sound power level (dB re 10^{-12} W)		
	Whole system	Raised pantograph	Folded pantograph
Case 1	110.6	106.4	99.6
Case 2	112.5	109.4	88.1
Case 3	111.6	109.4	105.9

Table 7.6: A-weighted sound power levels from each case.

Simulation cases	Sound power level (dB(A) re 10^{-12} W)		
	Whole system	Raised pantograph	Folded pantograph
Case 1	103.6	103.3	91.1
Case 2	104.4	104.2	77.6
Case 3	106.0	105.7	99.5
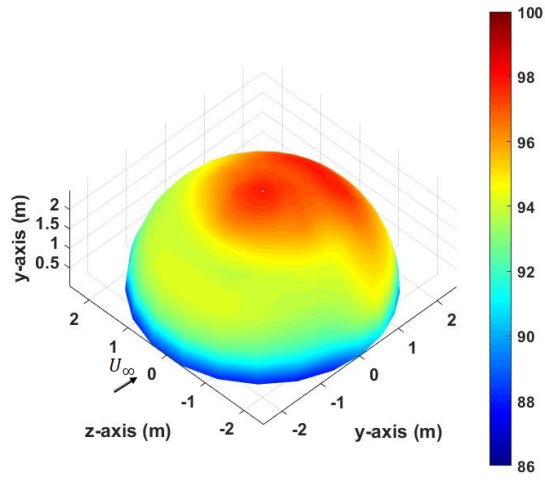
(a) Front part of isometric view, case 1
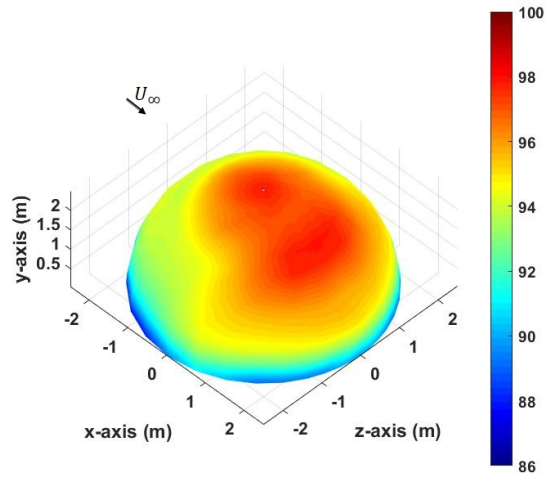
(b) Back part of isometric view, case 1
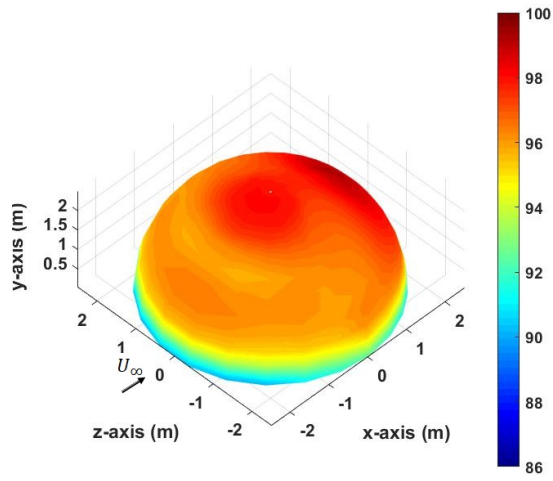
(c) Front part of isometric view, case 2
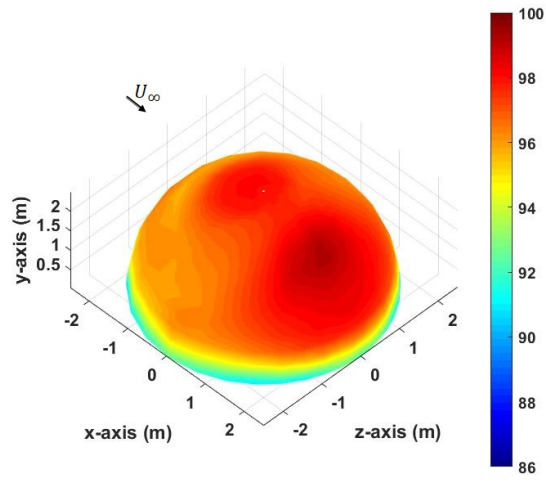
(d) Back part of isometric view, case 2
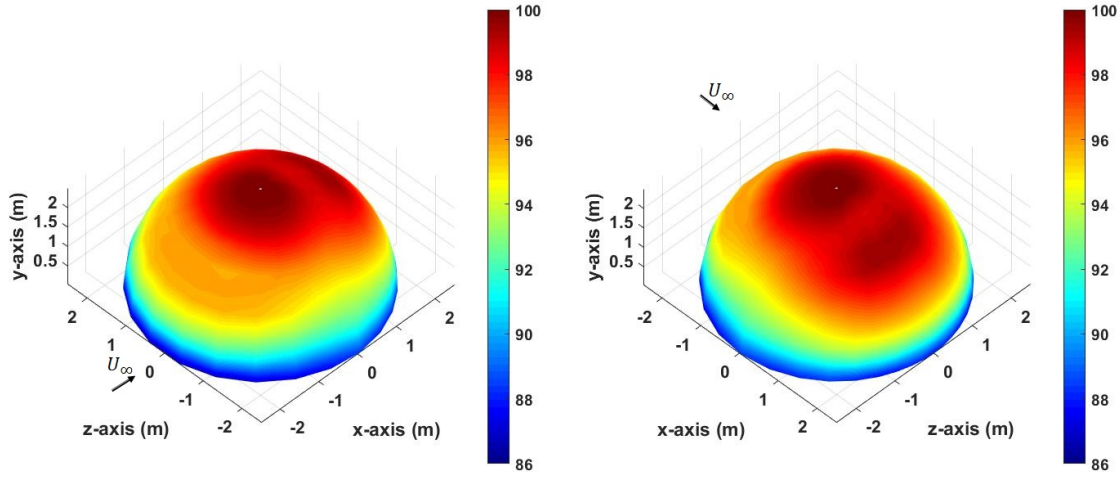
(e) Front part of isometric view, case 3   **(f)** Back part of isometric view, case 3

Figure 7.16: 3D noise directivity.

7.4 Summary

The flow and noise characteristics of three different high-speed train roof configurations including a folded and a raised pantograph have been investigated.

For the roof cavity and the ramped cavity configurations, highly unsteady flow is seen in the region downstream of the roof cavity due to flow separation and reattachment. For the ramped cavity configuration, vortices are generated by the upstream ramp edge and the insulation plates. Furthermore, highly unsteady flow is also observed in the wake regions of the raised pantograph panhead for all cases. It is found that a slightly lower velocity occurs upstream of the horn of the raised pantograph for the ramped cavity roof configuration due to interaction with the cavity flow.

Furthermore, the flow velocity inside the cavity and the ramped cavity is much lower than the freestream velocity. This leads to reduced surface pressure fluctuations on both the folded pantograph and lower parts of the raised pantograph, and therefore lower radiated noise levels from these components.

Furthermore, for the ramped cavity configuration, a large flow separation occurs at the upstream edge of the insulation plate, whereas for configuration with only side insulation plates, small flow separation occurs at the front plate edge and the flow attaches on other regions of the plate. For the cavity and the ramped cavity configurations, the primary

attachment line and points are found on the middle of cavity floor due to the shear layer impingement. Furthermore, a primary attachment line and points also appear on the cavity aft wall due to flow separation at the trailing edge.

Large wall pressure fluctuations occur on the aft wall of the cavity for the roof cavity and the ramped cavity configurations due to flow separation at the cavity trailing edge. This is also seen in slightly larger pressure fluctuations on the outside surface of the insulation plates for the ramped cavity configuration.

For the roof cavity and the ramped cavity configurations, the radiated noise level is dominated by the raised pantograph, the roof cavity and insulation plates. The ramped cavity configuration has the highest noise level in all directions and there is around 5 dB difference between the ramped cavity and side plate configurations at the side. The flat roof with side insulation plates has the lowest overall noise levels. However, in terms of A-weighted OASPLs, the roof configuration with only the side insulation plates has similar levels with the ramped cavity roof configuration at the side.

Chapter 8

Conclusions and Recommendations

8.1 Conclusions

A computational investigation has been carried out to study the aerodynamic and aeroacoustic characteristics of the pantograph roof cavity and pantograph components of a high speed train. The aim of this study is to understand the noise generation mechanisms of the roof cavity including the raised and the folded pantographs and its effects on the noise from the pantographs. Furthermore, modified shape have been introduced for the cavity to reduce the radiated noise. This numerical investigation was based on Computational Fluid Dynamics simulations in STAR-CCM+. For the near-field calculation of the aerodynamic characteristics, the Navier-Stokes (N-S) equations were solved using the IDDES model and for the far-field acoustics calculations, the FW-H equations based on Farassat's Formulation 1A were employed.

Experiments were carried out in a wind tunnel at the University of Southampton and in ISVR's anechoic chamber to validate the numerical methodology used. The mean pressure coefficient measured on the cavity floor and aft wall was used to validate numerical results at a flow speed of 30 m/s. Far-field pressures from the numerical and experimental results were also compared. In both cases, good agreement has been found between the numerical results and the measurements. A grid sensitivity study has been carried out from which a maximum cell aspect ratio 200 is chosen for generating meshes for the cavities. Furthermore, the numerical results of the mean pressure coefficient have been validated against other measurements on a 'closed' cavity floor at a Mach number of 0.2. In addition, the raised pantograph model has been validated by comparison with published experimental results from a wind tunnel for a full-scale DSA350 pantograph. The numerical predictions of the pantograph noise show good agreement with the experimental data up to 800 Hz but the agreement at higher frequencies is affected by the omission of small components in the

computational model.

The effects of the cavity flow on the pantograph noise have been investigated and results have been compared with those for the pantographs installed on a flat surface without the cavity. Highly unsteady flow occurred in the region of the cavity and the panhead of the raised pantograph. Interactions were seen between the separated shear layer flow and the pantographs. Highly unsteady flow also occurred at the cavity trailing edge due to the separated flow. In the spectra of noise radiated from the raised pantograph, two strong tonal components were seen at 250 Hz and 500 Hz when the pantograph was mounted in the cavity, whereas these peaks occurred at 315 Hz and 630 Hz when the pantograph placed on the flat surface. These peaks are generated by the upstream contact strip and the horn, respectively. It was found that lower streamwise velocities occurred upstream of the contact strip and the horn of the raised pantograph due to the cavity flow. This led to reductions in the noise radiated from the panhead of the raised pantograph, which is the main noise source of the pantograph. At the side receiver, the difference in OASPL between the pantographs with and without the cavity was approximately 4 dB. Furthermore, it was found that the effect of the train running direction on the noise radiated from the pantographs was not significant, with a difference of 1.5 dB. The noise radiated from the raised pantograph in front (knee-upstream) was higher than that when the raised pantograph was at the rear (knee-downstream).

Numerical simulations were performed to investigate effects on the flow features and far-field acoustics of different cavity edge configurations by rounding or angling the cavity leading and trailing edges. It was found that both treatments reduced the mean drag and (negative) lift as well as the RMS drag and lift. Cavities with treated edges effectively eliminated unsteady flow inside the cavity and aft wall regions. The rounded cavity edges reduced the size of the recirculation zone, which occurred between the cavity leading edge and middle of the cavity floor, and eliminated the recirculation in the cavity trailing edge region. The largest rounded cavity edge configuration with a radius of 80% of the cavity depth showed the best performance in reducing both the unsteady flow and the noise radiated from the cavity. Compared with a rectangular cavity, a 15.2 dB reduction in OASPL was achieved at the side and 12 dB at the top receivers. Furthermore, the effect of the cavity with the rounded edges on the pantograph has also been investigated and compared with a rectangular cavity. It was found that the overall noise radiated from the raised pantograph with the rounded cavity edges is about 1 dB lower than that from the pantograph with the rectangular cavity at the side receiver. However, by rounding the cavity edges, the flow velocity inside the cavity is increased, and consequently, the noise radiated from the folded pantograph is increased by 7.5 dB compared with the case with a rectangular cavity. In terms of the OASPL, a total reduction of 0.5 dB at the side and 1.7 dB at the top are achieved by rounding the cavity

edges with this radius.

Numerical simulations have been performed to investigate three different high speed train roof configurations with insulation plates and pantographs. Highly unsteady flow was seen in the region downstream of the roof cavity and ramped cavity. Vortices were generated by the edges of the insulation plates and the separated flow reattached on the surfaces of the insulation plates. Furthermore, the streamwise velocity inside the cavity and the ramped cavity was much lower than the freestream velocity, especially for the ramped cavity configuration. This led to reduced surface pressure fluctuations on both the folded pantograph and lower parts of the raised pantograph. Consequently, the overall noise radiated from the folded pantograph in the ramped cavity at the side receiver was 12 dB lower than for the side plate configuration, in which the pantographs were exposed to the freestream velocity. However, for the ramped cavity configuration, a large flow separation occurred at the upstream edge of the insulation plate and large surface pressure fluctuations appeared on the cavity aft wall. For the configuration with side insulation plates, small flow separations were found at the front plate edge and small pressure fluctuations occurred on the roof wall. This led to increased radiated noise from the roof and insulation plates for the ramped cavity configuration; the noise level was 12 dB higher than for the side plate configuration. For the noise radiated from whole system, the ramped cavity roof configuration was 5 dB higher than side plate configurations at the side. The flat roof with side insulation plates had the lowest overall noise levels. However, in terms of A-weighted levels, the flat roof configuration with the side insulation plates had similar levels to the ramped cavity roof configuration at the side receiver.

8.2 Recommendations for future work

In current study, it was found that strong tonal noise is generated from the panhead in the high frequency region. The tonal noise from the panhead is a significant contributor to the total pantograph noise. Therefore, it would be used to study the geometrical shapes of the panhead or flow control to reduce the turbulence level from the panhead.

The modification of the cavity edges reduced the unsteady flow around the cavity and led to reduced noise radiated from both the cavity and the raised pantograph. Other potential noise reduction techniques could be applied to the cavity and the pantographs. Another way to reduce the noise could be to use porous materials [11, 18, 105]. The main noise sources of the cavity are in vicinity of the trailing edge region, including the cavity downstream and aft walls. The introduction of porous material could reduce the strength of

the acoustic source in this region.

More studies can also be carried out for the effect of incoming flow. In current study, it was found that the incoming flow speed influenced on the radiated noise from the raised pantograph. In the current study, it is assumed that the pantographs and the recess are placed on the top of the leading coach where boundary layer thickness is thin and may not have an effect on the noise from the raised pantograph. However, some high speed trains have them in the middle of the coach. Therefore, it is noted that the boundary layer in front of the cavity could be thicker than for the cases in this study [106, 107]. This will mainly influence the flow speed and turbulence levels around the raised pantograph. It would be interesting to study more realistic and detailed train geometry including the leading coach and several other vehicles. The effects on the incoming flow at the pantographs may affect the radiated noise. In particular the pantograph noise may vary depending on which vehicle of the train it is mounted on. Furthermore, crosswind is important factor for high-speed train design. It would be also interesting to investigate the effect of the different direction of incoming turbulent flow and it may result different characteristics of radiated noise, including acoustic directivity from the pantographs and the recess compared with upwind cases.

In current study, the effect of the side insulation plates has been studied without considering the acoustic shielding and diffraction effects of the plates. When those are considered, it may be show different results compared with the result from current study. Therefore, it will be important to investigate effects to obtain more precise noise predictions and understanding of the mechanism of the noise generation. Compressible flow simulation may be used to take account to these effects, but it requires high computational cost. Finite elements method or boundary element could be used as an alternative method.

Due to the computational cost, the geometries of the cavity and the pantograph were simplified in the current study. The details of the pantograph geometry are considerable so they would require a much finer mesh and smaller time step. If possible, the model should be extended to include this detail. This is because small slender parts, including springs, strips, and wire arms generate the high frequency peaks which can be important noise sources, especially in the A-weighted noise level.

More studies can be carried out for different cavity length-to-depth ratios (L/D) for example with a single pantograph. In the current study, only a 'closed' rectangular cavity with $L/D = 11.5$ was investigated, but some high speed trains have recesses with smaller L/D ratio and just one pantograph. It will be interesting to investigate the flow features and noise generation mechanisms of an 'open' cavity including a pantograph and the compare them with the 'closed' cavity case.

More noise measurements for raised and folded pantographs in a wind tunnel are recommended for further validation including directivities. Furthermore, Particle Image Velocimetry (PIV) and force balance measurements for both raised and folded pantographs are recommended to provide more validation of the current simulation with regard to the flow features and force coefficients. Comparisons with field measurements carried out using microphone arrays would be useful.

In the current simulations, 1/10 scale models are used for the recess and the pantograph. However, the Reynolds number is smaller than at full scale. Although some phenomena (flow features and force coefficients) can be expected to remain unchanged and the cylindrical struts of the pantograph are in the sub-critical flow regime, it is necessary to investigate whether the scale model can be used reliably for estimation of noise radiated from the pantographs and the recess. Numerical investigation should be conducted for the full-scale pantograph and the recess separately due to high computational costs.

Bibliography

[1] A. Jehanno, D. Palmer, and C. James, "High Speed Rail and Sustainability", Systra Corp., Paris, Nov. 2011.

[2] D. J. Thompson, *"Railway noise and vibration: mechanisms, modelling and means of control",* Oxford: Elsevier, 2008.

[3] C. Talotte, "Aerodynamic noise: a critical survey",*Journal of Sound and Vibration*, vol. 231, pp. 549-562, 2000.

[4] C. Mellet, F. Létourneaux, F. Poisson, and C. Talotte, "High speed train noise emission: Latest investigation of the aerodynamic/rolling noise contribution", *Journal of sound and vibration*, vol. 293(3-5), pp. 535-546, 2006.

[5] V. V. Krylov, *"Noise and vibration from high-speed trains"*, Thomas Telford, 2001.

[6] C. Talotte, P.E. Gautier, D. J. Thompson, and C. Hanson, "Identification, modelling and reduction potential of railway noise sources: a critical survey", *Journal of Sound and Vibration*, vol. 267, pp. 447-468, 2003.

[7] H. Noh, S. Choi, S. Hong, and S. Kim, "Investigation of noise sources in high-speed trains", Proceedings of the Institution of Mechanical Engineers, Part F: *Journal of Rail and Rapid Transit*, 228(3), pp.307-322, 2013.

[8] S. Lei, Z. Chengchun, W. Jing and R. Luquan, "Numerical analysis of aerodynamic noise of a high-speed pantograph", in *2013 Fourth International Conference on Digital Manufacturing & Automation*, pp. 837-841, 2013.

[9] F.R. Grosche and G. Meier, "Research at DLR Göttingen on bluff body aerodynamics, drag reduction by wake ventilation and active flow control", *Journal of Wind Engineering and Industrial Aerodynamics*, vol. 89, pp. 1201-1218, 2001.

[10] H. H. Yu J. C. Li, and H. Q. Zhang, "On aerodynamic noises radiated by the pantograph system of high-speed trains",*Acta Mechanica Sinica*, vol. 29, pp. 399-410, 2013.

[11] M. Ikeda, T. Mitsumoji, T. Sueki, and T. Takaishi, "Aerodynamic noise reduction in pantographs by shape-smoothing of the panhead and its support and by use of porous material in surface coverings", Quarterly Report of RTRI, vol. 51, pp. 220-226, 2010.

[12] M. Ikeda and T. Mitsumoji, "Numerical estimation of aerodynamic interference between panhead and articulated frame", Quarterly Report of RTRI, vol. 50, pp. 227-232, 2009.

[13] M. Ikeda and T. Mitsumoji, "Evaluation method of low-frequency aeroacoustic noise source structure generated by Shinkansen pantograph", Quarterly Report of RTRI, vol. 49, pp. 184-190, 2008.

[14] J. Lee and W. Cho, "Prediction of low-speed aerodynamic load and aeroacoustic noise around simplified panhead section model", *Proceedings of the Institution of Mechanical Engineers, Part F: Journal of Rail and Rapid Transit*, vol. 222, pp. 423-431, 2008.

[15] K. Sato, R. Machida, and T. Aoki, "Aerodynamic Sound and Flow Field Generated from Combinational Inclined Tapered Cylinder", *Open Journal of Fluid Dynamics*, vol. 2, pp. 222-227, 2012.

[16] X. Liu, D.J. Thompson, Z. Hu, and V. Jurdic, "Aerodynamic noise from a train pantograph", *The 21st International Congress on Sound and Vibration, ICSV 21*, Beijing, China, 2014.

[17] T. Kurita, M. Hara, H.Yamada, Y.Wakabayashi, F. Mizushima, H. Satoh, and T. Shikama, "Reduction of pantograph noise of high-speed trains", *Journal of Mechanical Systems for Transportation and Logistics*, vol. 3, pp. 63-74, 2010.

[18] T. Sueki, M. Ikeda, T. Takaishi, T. Kurita, and H. Yamada, "Reduction of aerodynamic noise from high-speed pantograph using porous materials", *Journal of Environment and Engineering*, vol. 5, pp. 469-484, 2010.

[19] Y. Moritoh, Y. Zenda, and K. Nagakura",Noise control of high speed Shinkansen", *Journal of Sound and Vibration*, vol. 193, pp. 319-334, 1996.

[20] T. Kitagawa and K. Nagakura, "Aerodynamic noise generated by Shinkansen cars", *Journal of Sound and Vibration*, vol. 231, pp. 913-924, 2000.

[21] Y. Zhang, J. Zhang, T. Li, L. Zhang and W. Zhang, "Research on Aerodynamic Noise Reduction for High-Speed Trains", *Shock and Vibration*, pp. 21, 2016.

[22] W. Q. Dai, X. Zheng, Z. Y. Hao, Y. Qiu, H. Li and L. Luo, "Aerodynamic noise radiating from the inter-coach windshield region of a high-speed train. *Journal of Low Frequency Noise Vibration and Active Control*, 37(3), pp.590-610, 2016.

[23] H. Noh, "Noise-source identification of a high-speed train by noise source level analysis", Proceedings of the Institution of Mechanical Engineers, Part F: *Journal of Rail and Rapid Transit*, 231(6), pp.717-728, 2016.

[24] C. Hanson and B. Barsikow, "Noise sources on Amtrak's high-speed train", *Proceedings of the 29th International Congress and Exhibition on Noise Control Engineering, InterNoise 2000*, Nice, France, August 27-30, 2000.

[25] A. Martens, J. Wedemann, N. Meunier, A. Leclere, A.G. Deutsche Bahn, and D. B. Systemtechnik, "High speed train noise-sound source localization at fast passing trains", Deutsche Bahn AG, Sociedad Espanola de Acoustica, SEA, 2009.

[26] K. Nagakura, "Localization of aerodynamic noise sources of Shinkansen trains", *Journal of Sound and Vibration*, vol. 293, pp. 547-556, 2006.

[27] C. Zhu, H. Hemida, D. Flynn, C.Baker, X. Liang, and D. Zhou, "Numerical simulation of the slipstream and aeroacoustic field around a high-speed train", *Proceedings of the*

Institution of Mechanical Engineers, Part F: Journal of Rail and Rapid Transit, vol. 231(6), pp.740-756, 2016.

[28] D. J. Thompson, E. L. Iglesias, X. Liu, J. Zhu, and Z. Hu, "Recent developments in the prediction and control of aerodynamic noise from high-speed trains", *International Journal of Rail Transportation*, vol. 3, pp. 119-150, 2015.

[29] T. Lölgen, "Wind tunnel noise measurements on full-scale pantograph models", *The Journal of the Acoustical Society of America*, 105(2) 1136. doi: 10.1121/1.425410, 1999.

[30] H. Brick, T. Kohrs, E. Sarradj, T. Geyer "Noise from high-speed trains: Experimental determination of the noise radiation of the pantograph", In *Forum Acusticum.*, 2011.

[31] E. Latorre Iglesias, D. J. Thompson, M.G Smith, "Component-based model to predict aerodynamic noise from high-speed train pantograph", *Journal of Sound and Vibration*, 394, pp.280-305, 2017.

[32] H. Noh, "Numerical analysis of aerodynamic noise from pantograph in high-speed trains using lattice Boltzmann method", *Advances in Mechanical Engineering*, 11(7), 1687814019863995, 2019.

[33] Y. Zhang, J. Zhang, T. Li, and L. Zhang, "Investigation of the aeroacoustic behavior and aerodynamic noise of a high-speed train pantograph", *Science China Technological Sciences*, 60(4), pp.561-575, 2017.

[34] C. Noger, J. C. Patrat, J. Peube, and J. L. Peube, "Aeroacoustical study of the TGV pantograph recess", *Journal of Sound and Vibration*, 231(3), pp.563-575, 2000.

[35] Y. Yao, Z. Sun, G. Yang, W. Liu, and P. Prapamonthon, "Analysis of Aerodynamic Noise Characteristics of High-Speed Train Pantograph with Different Installation Bases", *Applied Sciences*, 9(11), pp. 2332, 2019.

[36] R. L. Stallings Jr and F. J. Wilcox Jr, "Experimental cavity pressure distributions at supersonic speeds", NASA Langley Res. Cent., Hampton, VA, Tech. Paper-2683, 1987.

[37] E. B. Plentovich, R. L. Stallings, and M.B. Tracy, "Experimental cavity pressure measurements at subsonic and transonic speeds. Static-pressure results", NASA Langley Res. Cent., Hampton, VA, Tech. Paper-3358, 1993.

[38] K. Krishnamurty, "Acoustic radiation from two-dimensional rectangular cutouts in aerodynamic surfaces", California Inst. of Tech., Washington, DC, NACA Tech. Note-3487, 1955.

[39] L. Chatellier, "Modélisation et contrôle actif des instabilités aéroacoustiques en cavité sous écoulement affleurant", PhD diss., Université de Poitiers, 2002.

[40] Y. Ng, "Characterising low-speed, transitional cavity flow." *The Aeronautical Journal*, vol. 116, pp. 1185-1199, 2012.

[41] D. Rockwell and E. Naudascher, "Review self-sustaining oscillations of flow past cavities", *Journal of Fluids Engineering*, vol. 100(2), pp. 152-165, 1978.

[42] ESDU, "Aerodynamics and aero-acoustics of rectangular planform cavities. Part 1: time-averaged flow", ESDU Data Item 02008. Pub IHS ESDU, London, 2004.

[43] H. Plumblee, J. Gibson, and L. Lassiter, "A theoretical and experimental investigation of the acoustic response of cavities in an aerodynamic flow", Lockheed Aircraft Corp Marietta GA, 1962.

[44] J. Rossiter, "Wind tunnel experiments on the flow over rectangular cavities at subsonic and transonic speeds", Ministry of Aviation; Royal Aircraft Establishment; RAE Farnborough, 1964.

[45] M. Gharib and A. Roshko, "The effect of flow oscillations on cavity drag", *Journal of Fluid Mechanics*, vol. 177, pp. 501-530, 1987.

[46] D. Rockwell and E. Naudascher, "Self-sustained oscillations of impinging free shear layers", *Annual Review of Fluid Mechanics*, vol. 11(1), pp. 67-94, 1979.

[47] M. Tracy and E. Plentovich, "Characterization of cavity flow fields using pressure data obtained in the Langley 0.3-meter transonic cryogenic tunnel", NASA, Washington, NASA-TM-4436, March 01, 1993.

[48] V. Koschatzky, R. Delfos, B. Boersma and J. Westerweel, "Boundary layer influence on cavity noise generation", *Advances in Turbulence XII*, pp. 847-850, 2009.

[49] K. Ahuja and J. Mendoza, "Effects of cavity dimensions, boundary layer, and temperature on cavity noise with emphasis on benchmark data to validate computational aeroacoustic codes", 1995

[50] V. Togiti, M. Breuer and J. Longo, "Influence of Boundary Layer on Supersonic Cavity Flow Dynamics", In ESA Special Publication, vol. 659, 2009

[51] G. Yang, J. Sun, Y. Liang, and Y. Chen, "Effect of Geometry Parameters on Low-speed Cavity Flow by Wind Tunnel Experiment", *AASRI Procedia*, vol. 9, pp. 44-50, 2014.

[52] H. L. Helmholtz and A. J. Ellis, *On the Sensations of Tone as a Physiological Basis for the Theory of Music*. New York: Cambridge University Press, 1912.

[53] M. B. Tracy and E. B. Plentovich, "Cavity unsteady-pressure measurements at subsonic and transonic speeds", NASA Langley Res. Cent., Hampton, VA, Tech. paper TP-3669" 1997.

[54] X. Zhang, X. X. Chen, A. Rona, and J.A. Edwards, "Attenuation of cavity flow oscillation through leading edge flow control", *Journal of Sound and Vibration*, 221(1), pp.23-47, 1999.

[55] Y. Wang, H. Lee, K. Li, Z. Gu and J. Chen, "Experimental and numerical study of flow over a cavity for reduction of buffeting noise", *Acta Acustica united with Acustica*, vol. 98(4), pp. 600-610, 2012.

[56] B. Henderson, "Third computational aeroacoustics (CAA) workshop on benchmark problems: Category 6 Automobile Noise Involving Feedback-Sound Generation by Low Speed Cavity Flows", Glenn Res. Cent. Cleveland, OH, NASA/CP-2000-209790, 2000.

[57] J. D. Anderson Jr, *"Fundamentals of Aerodynamics"*,, New York: McGraw-Hill Education, 2010.

[58] ANASYS, "ANSYS Fluent Tutorial Guide", ANSYS, Inc. Canonsburg, PA, 2014.

[59] D. C. Wilcox, *Turbulence Modeling for CFD vol. 2*, Canada, CA: DCW industries, Inc., 1998.

[60] P. R. Spalart, "Detached-eddy simulation", *Annual Review of Fluid Mechanics*, vol. 41, pp. 181-202. 2009.

[61] P. R. Spalart, S. Deck, M. L. Shur, K. D. Squires,M. K. Strelets and A. Travin, "A new version of detached-eddy simulation, resistant to ambiguous grid densities", *Theoretical and Computational Fluid Dynamics*, vol. 20(3), pp.181-195. 2006.

[62] M. L. Shur, P. R. Spalart, M.K. Strelets, A.K. Travin, "A hybrid RANS-LES approach with delayed-DES and wall-modelled LES capabilities", *23rd AIAA/CEAS Aeroacoustics Conference*, vol. 28(6), pp. 1638-1649, 2008.

[63] P. Holoborodko, "Central Differences", *Pavel Holoborodko Applied mathematics and beyond*, [Online] Available: http://www.holoborodko.com/pavel/numerical-methods/numerical-derivative [Accessed: 11 Jul 2016]

[64] S. C. Chapra and R. P. Canale, *Numerical Methods for Engineers vol. 2* New York: McGraw-Hill, 2012.

[65] M. Zeltkevic, "Forward and Backward Euler Methods", *Numerical Solution of Ordinary Differential Equations*, [Online] Available: http://web.mit.edu/10.001/Web/Course-Notes/Differential-Equations-Notes [Accessed: 11 Jul 2016]

[66] H. K. Versteeg and W. Malalasekera, *An introduction to computational fluid dynamics: the finite volume method.* New York: Pearson Education, 2007.

[67] H.J. Aguerre, S.M. Damian, J.M. Gimenez, and N.M. Nigro, "Modeling of compressible fluid problems with openfoam using dynamic mesh technology", *Mecánica Computacional*, vol. 32, pp. 955-1011, 2013.

[68] M. J. Lighthill, "On sound generated aerodynamically. I. General theory", *Proceedings of the Royal Society of London A: Mathematical, Physical and Engineering Sciences*, vol. 211(1107), pp. 564-587, 1952.

[69] N. Curle, "The influence of solid boundaries upon aerodynamic sound", *Proceedings of the Royal Society of London A: Mathematical, Physical and Engineering Sciences*, vol. 231(1187), pp. 505-514, 1955.

[70] A. P. Dowling and J. F. Williams, "Sound and sources of sound", Ellis Horwood Ltd., Chichester: J. Wiley and Sons, 1983.

[71] J. F. Williams and D. L. Hawkings, "Sound generation by turbulence and surfaces in arbitrary motion", *Philosophical Transactions of the Royal Society of London A: Mathematical*, Physical and Engineering Sciences, vol. 264, pp. 321-342, 1969.

[72] Hövelmann, Andreas. "Aerodynamic investigations of noise-reducing high-lift systems for passenger transport aircraft", Diploma Thesis, Dept. of Aeronautical and Vehicle Eng., Royal Inst. of Techno., Stockholm, 2011.

[73] D. P. Lockard, M. M. Choudhari, M. D. O'Connell, B. M. Duda, E. Fares, "Noise Simulations of the High-Lift Common Research Model", *23rd AIAA/CEAS Aeroacoustics Conference*, pp. 3362, 2017.

[74] L. Wen, "Numerical Investigation of Landing Gear Noise", Ph.D. Thesis, Faculty of Eng. and Environ., Univ. of Southampton., Southampton, 2011.

[75] P. R. Spalart, M. L. Shur, M. K.Strelets, A. K. Travin, "Towards noise prediction for rudimentary landing gear", *Procedia IUTAM*, pp.283-292, 2010.

[76] N. Paradot, E. Masson, F. Poisson, R. Grégoire, E. Guilloteau, H. Touil, P. Sagaut, "Aero-acoustic methods for high-speed train noise prediction", *Proceedings of the World Congress in Railway Research (WCRR)*, Seoul, Korea, 2008

[77] J. Y. Zhu, Z. W. Hu, D. J. Thompson, "The flow and flow-induced noise behaviour of a simplified high-speed train bogie in the cavity with and without a fairing", *Proceedings of the Institution of Mechanical Engineers, Part F: Journal of Rail and Rapid Transit*, 232(3), pp.759-773, 2018

[78] F. Farassat, "Acoustic radiation from rotating blades—the Kirchhoff method in aeroacoustics", *Journal of Sound and Vibration*, vol. 239, pp. 785-800, 2001.

[79] K. S. Brentner and F. Farassat, "An analytical comparison of the acoustic analogy and Kirchhoff formulation for moving surfaces", *The American Helicopter Society 53rd Annual Forum*, Virginia Beach, VA, May 1, 1997.

[80] K. S. Brentner and F. Farassat, "Modeling aerodynamically generated sound of helicopter rotors", *Progress in Aerospace Sciences*, vol. 39, pp. 83-120, 2003.

[81] C. Wagner, T. Hüttl and P. Sagaut, *"Large-eddy simulation for acoustics Vol. 20"*, . Cambridge University Press, 2007.

[82] P. Batten, E. Ribaldone, M. Casella and S. Chakravarthy, "Towards a generalized non-linear acoustics solver", *In 10th AIAA/CEAS Aeroacoustics Conference*, p. 3001, 2004

[83] P. R. Spalart, "Strategies for turbulence modelling and simulations", *International Journal of Heat and Fluid Flow*, vol. 21, pp. 252-263, 2000.

[84] W. K. Blake, *Mechanics of flow-induced sound and vibration vol. 1*, London : Academic Press, 1986.

[85] Y. Kim, *Sound Propagation: an impedance based approach*, Singapore : J. Wiley and Sons, 2010.

[86] B. Ganapathisubramani, Class Lecture, Topic: "Turbulence: Physics and Modelling", SESA6061, Faculty of Engineering and the Environment, University of Southampton, Southampton, 2014.

[87] R. N. Meroney D. E. Neff, "Reynolds Number Independence of the Wind-tunnel Simulation of Transport and Dispersion about Buildings", Unpublished internal memorandum, 1996.

[88] V. Thangamni, K. Knowles, and A. J. Saddington, "Effects of Scaling on High Subsonic Cavity Flow Oscillations and control", *Journal of Aircraft.*, 2014.

[89] A. Iida, T. Otaguro, H. Nagarekawa, A. Torii, and I. Naruse, "Similarity law of aerodynamic noise generation", in *6th AIAA Aeroacoustics Conference and Exhibit Conf.*, Lahaina.,2000, pp.2000-2012.

[90] R. D. Knowles, M. V. Finnis, A. J. Saddington, K. Knowles, "Planar visualization of vortical flows", in *Proceedings of the Institution of Mechanical Engineers, Part G: Journal of Aerospace Engineering.*, 2006, 220(6), pp.619-627.

[91] T. Chong, P. Joseph, P. Davies, "Design and performance of an open jet wind tunnel for aero-acoustic measurement", in *Applied Acoustics.*, 2009, 70(4), pp.605-614.

[92] Z. Hu, C.L. Morfey, and N.D. Sandham, "Wall pressure and shear stress spectra from direct simulations of channel flow", *AIAA Journal*, vol 44(7), pp.1541-1549, 2006.

[93] V. Kolář, "Vortex identification: New requirements and limitations", *International Journal of Heat and Fluid Flow*, vol. 28(4), pp.638-652, 2007.

[94] B. Carbral, L. C. Leedom, "Imaging vector fields using line integral convolution", *Proceedings of the 20th annual conference on Computer graphics and interactive techniques*, pp.263-270, 1993.

[95] B. Lazos, "Surface topology on the wheels of a generic four-wheel landing gear", *AIAA Journal*, vol 40(12), pp.2402-2411, 2002.

[96] A. E. Perry, M. S. Chong, "A description of eddying motions and flow patterns using critical-point concepts", *Annual Review of Fluid Mechanics*, vol 19(1), pp.125-155, 1987.

[97] X. Gloerfelt, "Cavity noise", VKI lecture series, 3. 2009.

[98] L. East, "Aerodynamically induced resonance in rectangular cavities", *Journal of Sound and Vibration*, vol. 3(3), pp. 277-287, 1966

[99] K. Karamcheti, A. Bauer, W. Shields, G. Stegen and J. Woolley",Some features of an edge-tone flow field", *NASA Special Publication*, vol. 207, p.275, 1969

[100] H. Heller, D. Holmes and E. Covert, "Flow-induced pressure oscillations in shallow cavities", *Journal of sound and Vibration*, vol. 18(4), pp.545-553, 1971.

[101] G. Ashcroft, K. Takeda, and X. Zhang, "A numerical investigation of the noise radiated by a turbulent flow over a cavity", *Journal of Sound and Vibration*, vol. 265, pp. 43-60, 2003.

[102] C. Y. Loh, "Computation of low speed cavity noise", Teitech, Inc., Beavercreek, OH, Tech. paper NASA/CR-2004-212892, 2004.

[103] U. Oza, Z. Hu, and X, Zhang, "Effect of Cavity Flow on Landing Gear Aerodynamic Loads", *In 22nd AIAA Computational Fluid Dynamics Conference* pp. 2288, 2016.

[104] M. Dahl, "Third computational aeroacoustics (CAA) workshop on benchmark problems", *Third CAA Workshop on Benchmark Problems of Conf. Proceedings*, Cleveland, United States, NASA/CP-2000-209790, August 01, 2000.

[105] Y. Yuan, K. Xu, and K. Zhao, "Numerical analysis of transport in porous media to reduce aerodynamic noise past a circular cylinder by application of porous foam", *Journal of Thermal Analysis and Calorimetry*, pp.1-12, 2019

[106] M. Carnevale, A. Facchinetti, L. Maggiori, D. Rocchi "Computational fluid dynamics as a means of assessing the influence of aerodynamic forces on the mean contact force acting on a pantograph", *Proceedings of the Institution of Mechanical Engineers, Part F: Journal of Rail and Rapid Transit*, 230(7), pp.1698-1713, 2016

[107] L. Jia, D. Zhou, J. Niu, "Numerical calculation of boundary layers and wake characteristics of high-speed trains with different lengths", *PloS one*, 12(12), e0189798, 2017.